

A Study into the Internal Energy
Distributions of Molecules Liberated from
an *In Vacuo* Liquid Surface

Olivia Jayne Maselli



*A thesis submitted in total fulfilment of the requirements for the
degree of Doctor of Philosophy*

July 2010

School of Chemistry and Physics
The University of Adelaide

Affidavit

This work contains no material which has been accepted for the award of any other degree or diploma in any university or other tertiary institution and, to the best of my knowledge and belief, contains no material previously published or written by another person, except where due reference has been made in the text.

I give consent to this copy of my thesis, when deposited in the University Library, being available for loan and photocopying, subject to the provisions of the Copyright Act 1968. I also give permission for the digital version of my thesis to be made available on the web, via the University's digital research repository, the Library catalogue, the Australasian Digital Theses Program (ADTP) and also through web search engines, unless permission has been granted by the University to restrict access for a period of time.

Olivia Jayne Maselli

Abstract

We use the liquid micro-jet technique coupled with laser spectroscopy to measure the rotational and vibrational energy content of benzene liberated from an *in vacuo* water-ethanol solution. A comparison is made between the internal temperatures of benzene molecules that spontaneously evaporate from the liquid surface and those that are laser desorbed by resonant IR light. In both cases it was found that rotations are cooled significantly more than the lowest vibrational modes and that the rotational energy distributions were Boltzmann. Within error, the rotational temperatures of the vibrationally excited molecules were the same as the vibration-less ground state in both systems.

Independent, collision-induced, gas phase energy transfer measurements reveal that benzene undergoes fast rotational relaxation, from which we deduce that the rotational temperature measured in the evaporation experiments (200-230 K) are an indication of the translational energy of the evaporate. Conversely, relaxation of ν_6 is found to be very inefficient, suggesting that the ν_6 temperature (260-270 K) is an indication of the surface temperature of the liquid. Modelling the relaxation of ν_{16} indicates that $>10^2$ collisions are occurring during the transition from liquid to vacuum, an order of magnitude more than have been reported to occur in the gas phase immediately above the liquid surface.

The temporal distribution of internal temperatures within the plume of laser desorbed molecules reveals that the coldest molecules are found close to the front of the expansion, and reach temperatures 60 to 100 K lower than the liquid surface temperature. Spectroscopic analysis of the mass spectra of desorbed products revealed that clusters were formed post benzene ionisation, in ion-dipole association reactions. The position of maximum cluster formation within the desorption plume was found to be a compromise between the point of maximum internal cooling and the highest translational velocities. Best estimates of the

translational temperature of the desorption plume were achieved through 3D Monte Carlo simulations of the gas expansion. The simulation revealed the plume can be described with a temperature of ~ 200 K and travelling with a bulk velocity of ~ 100 m.s⁻¹.

Acknowledgments

I would first like to thank my supervisor Professor Mark Buntine for his enthusiasm, encouragement and the advice that he has given me over the years. Mark's generous nature and strong sense of fair-mindedness have made him stand out as both a supervisor and as a person on significantly more than a handful of occasions. In particular I am grateful for the independence he has allowed me as a researcher. He has helped me to achieve all the work that I present here and more.

Dr Jason Gascooke has been a great mentor and friend throughout my PhD. He has taught me to have patience and perseverance with my research whilst at the same time advocating that life shouldn't be taken too seriously. Without his input I am sure that I would have written up this thesis years ago!

Thanks also to Professor Warren Lawrance for his help in the analysis of much of the data presented here. He curbed many a wild tangent that we often found ourselves riding.

The technical expertise of Peter Apoeffis were invaluable in building and maintaining the technical equipment for this project. I appreciate Pete's patience and enthusiasm in teaching me how to do the same.

To all the other members of the lab that I have had the pleasure of working and socialising with over the years – thanks. Special thanks to Vik Dryza who took pleasure in jumping out to scare me at any opportunity. Vik, sleep with one eye open...

Lastly I need to thank my family who have continued to support me in all facets of my life. Particularly my partner Matt, whose patience, loving and chai making skills have kept burning that light at the end of the PhD tunnel.

Publications to Date

Rotational Energy Distributions of Benzene Liberated from Aqueous Liquid Micro-jets: A Comparison between Evaporation and Infrared Desorption.

Maselli, O. J., Gascooke, J. R., Kobelt, S. L., Metha, G. F., Buntine, M. A., *Australian Journal of Chemistry*, 2006, 59,104-108

Benzene Internal Energy Distributions Following Spontaneous Evaporation from a Water-Ethanol Solution.

Maselli, O. J., Gascooke, J. R., Lawrance, W. D., Buntine, M. A., *Journal of Physical Chemistry C*, 2009, 113, (2), 637-643

Measuring the Internal Energy Content of Molecules Transported Across the Liquid-Gas Interface.

Maselli, O. J., Gascooke, J. R., Lawrance, W. D., Buntine, M. A., *The 8th Asian International Seminar on Atomic and Molecular Physics, Journal of Physics, Conference series*, 2009, 185, 012027

Abbreviations

L μ J	Liquid Micro-Jet
UV	Ultraviolet
IR	Infrared
TOF-MS	Time-of-Flight Mass Spectrometry
MALD	Matrix Assisted Laser Desorption
MALDI	Matrix Assisted Laser Desorption/Ionisation
1+1 R2PI	One-colour Resonant Two Photon Ionisation
REMPI	Resonance Enhanced Multiphoton Ionisation
FC	Frank Condon factor
LIF	Laser Induced Fluorescence
LIDF	Laser Induced Dispersed Fluorescence
FWHM	Full Width Half Maximum
OOP	Out-of-Plane
IP	In-Plane

List of Figures

Figure 2.1: (A) Assembly drawing of the TOF-MS used for the reported experiments. (B) Isometric view of the Source Chamber of the TOF-MS. -----5

Figure 2.2: Experimental setup for performing absorption spectroscopy of molecules IR desorbed or evaporating (only UV laser employed) from a L μ J. The inline bubble filter before the HPLC pump acts to degas the solution, collecting any bubbles that may try to enter the system. -----8

Figure 2.3: (A) Photograph of a L μ J created by a solution passing through a Pico Tip Emitter at atmospheric pressure. The exit aperture of the capillary is 15 μ m in diameter. The long stable, laminar flow region of the jet is illustrated here, and continuous for over 6 cm. Shorter laminar flow distances, typically 2-3 cm, are observed under high vacuum conditions. (B) Observation of the diffraction pattern produced when the UV laser is incident upon the stable *in vacuo* liquid filament. The diffraction patterns were viewed on fluorescent card at the exit to the chamber. Observation of a stable diffraction pattern is used to align the UV onto the centre of the jet. -----10

Figure 2.4: Diffraction patterns produced when the UV laser is incident upon the *in vacuo* L μ J at increasing distance from the capillary orifice. The diffraction patterns were viewed on a fluorescent card at the exit to the Source Chamber. The black background has been removed from each image so that the diffraction bands can be clearly seen. The white dots are equally spaced marks that have been included to help in the comparison of the length and position of each diffraction band. The diameter of the L μ J dictates the distance between the diffraction bands. In this example, the diameter of the jet appears to remain constant between 0-2 mm. The diffraction pattern is absent at a distance of 2.5-3 mm from the orifice - indication that the L μ J has begun to disintegrate at this distance.-----11

Figure 2.5: Scheme for resonant photon absorption. The probability of photon absorption is high when the energy of the photon is equal to the transition energy to a resonant intermediate state. The longer lifetimes of resonant intermediate states compared with virtual intermediate states increases the probability of absorbing a second photon. If the second photon is the same colour as the first then stimulated emission from the resonant intermediate state can occur instead of absorption. In the absence of collisional deactivation or other non-radiative relaxation processes, fluorescence can also be observed starting from the original resonant intermediate state. In the low pressure conditions inside the TOF-MS collisional deactivation is minimal. Boesl has found the absorption cross-sections, σ_α and σ_β , for benzene are 2.7×10^{-17} and 3.4×10^{-18} cm², respectively [18].-----14

Figure 2.6: Intensity of benzene parent ion signal produced by R2PI via the 6^1 resonant intermediate state. The wavelength of the ionising laser was 258.93 nm and the laser collimated into a spot with FWHM of $\sim 150 \mu\text{m}$. At fluences below $9 \times 10^6 \text{ W.cm}^{-2}$ the ion signal displays a quadratic dependence on the fluence of the UV laser. Above this value the photon absorption process is saturated reducing the relationship to a direct proportionality between ion signal and UV fluence. This saturation point is consistent with $1 \times 10^7 \text{ W.cm}^{-2}$ reported by Boesl *et al* [18].-----16

Figure 2.7: (A) Assembly drawings of the electrode stack designed to be used with the $\text{L}\mu\text{J}$ injector. The different stages of the assembly have the following dimensions: (s) has a length of 18 mm, (d) a length of 70 mm and (D) a length of $\sim 1 \text{ m}$. The brass, cone-shaped cap that covers the protruding $\text{L}\mu\text{J}$ capillary has not been included in the assembly drawings. (B) Schematic of a 2 stage acceleration stack. $E_x (\text{V.mm}^{-1})$ is the electric field strength across the stage x . The ions are created in the first stage, (s), and accelerated by E_s toward the second stage, (d). Further acceleration in (d) pushes the ions into the field-free flight tube, (D). When the ions reach the end of (D) they are detected. Tuning of E_s/E_d can force the space focus to occur at the point of detection (see text for details). -----19

Figure 2.8: Demonstration of the difference between Maxwellian velocity distributions typical of a supersonic expansion (3K, 300 m.s^{-1} bulk velocity) and the thermal distribution of molecules photo-desorbed from a $\text{L}\mu\text{J}$ (350 K, no bulk velocity). It is expected that higher desorption laser fluences will increase the flux of desorbed molecules and thus increase the number of gas-phase collisions. This phenomenon would tend to narrow the molecular velocity distribution to a hybrid between that of a supersonic and of a thermal expansion. --21

Figure 2.9: Illustration of Time-lag Focusing. Two same mass positive ions are born at position S_0 . Initially they are travelling in opposite directions but once a potential is created across the electrodes at time (t), the ion travelling toward the higher potential, Repeller electrode is forced to turn around. The closer this ion gets to the repeller electrode before the potential is applied, the faster the velocity of the ion will be when it passes S_0 again. At some point later this ‘turn-around’ ion will catch-up to the other ion – eliminating the effect of the initial velocity differences on the resultant resolution. The optimal delay between ion creation and extraction is dependent upon the initial relative kinetic energies of the molecules.--24

Figure 2.10: Demonstration of the changing shape of a single mass peak (m/z 78 - benzene monomer) as a function of Time-lag Delay. The mass spectra here are produced by benzene molecules that have evaporated from the surface of an *in vacuo* $\text{L}\mu\text{J}$.-----26

Figure 3.1: Reference frames for analysis of rotational and vibrational motion of benzene. The blue axes (ξ, η, ζ) are laboratory fixed axes with origin at the centre of mass of the molecule. The magnitude of the transition dipole vector, μ_A , along these axes is used in the rovibronic transition selection rules. The Euler angles (θ, ϕ, χ) are the angles between the

laboratory fixed axis and the (x,y,z) molecule fixed axis. The magnitude of the transition dipole along the molecule's fixed axes is used when determining vibronic transition selection rules. -----34

Figure 3.2: Electronic states of neutral benzene [15]. The electronic transition of interest to this study is the Herzberg-Teller transition, ${}^1B_{2u} \leftarrow {}^1A_{1g}$. Mixing of the ${}^1B_{2u}$ state with the neighbouring ${}^3E_{1u}$ is thought to be the reason why this electronically forbidden transition is unusually intense. -----37

Figure 3.3: Assignment of rotational angular momentum quantum number, k . -----45

Figure 3.4: Allowed rovibrational transitions within the $6_0^1 16_1^1$, ${}^{ev}E_{1g} \leftarrow {}^{ev}E_{2u}$ vibronic transition. Rovibrational levels are labelled with Hougen's quantum number, g . Allowed transitions are those that involve $\Delta g = 0 \pmod n$. In degenerate vibronic states such as ${}^{ev}E_{1g}$, Coriolis effects destroy the energetic degeneracy of the rovibronic state. The lower rovibronic states in this case do not display Coriolis splitting since the vibronic state is made from ν_{16} which has $\zeta_{16} = 0$. The symmetry of each rovibronic state has been assigned according to Wilson's theory [6] and summarised in Table 3.4.-----50

Figure 3.5: Allowed rovibrational transitions within the $6_0^1 16_1^1$, ${}^{ev}B_{1g} \leftarrow {}^{ev}E_{2u}$ vibronic transition. There are several important differences to note with Figure 3.4 - now that the transitions are between a degenerate and a non-degenerate vibronic state. Firstly the rovibrational levels in the non-degenerate excited electronic state are not split by Coriolis effects even though the vibronic state is the result of the product of two degenerate vibrations (ν_6 and ν_{16}). Also, note the alternating symmetries of the $k = 0$ states in ${}^{ev}B_{1g}$ as a consequence of the odd or even nature of J . Finally, symmetry restrictions prevent any transitions from the ground B_2 rovibronic state when $k = 1$, whilst allowing transitions out of the B_1 state. This is important to note when calculating the line strength of this transition.-----51

Figure 3.6: The effect of the magnitude of χ on the shape of a rovibrational contour. These examples have been calculated by changing the value of ζ'_{eff} for the 6_0^1 transition. Atkinson and Parmenter [10] established a general rule for contour shapes based on Equation 3.2.1.--57

Figure 3.7: 1+1 REMPI spectrum of benzene generated in a room temperature gas phase static cell. Band assignments are in agreement with those of Stephenson [1], Atkinson [2] and Fischer [3]. -----61

Figure 3.8: (A) ν_1 : In-plane ring stretch, (B) ν_6 : Degenerate in-Plane ring squash, (C) ν_{16} : Degenerate out-of-plane ring deformation, (D) ν_{11} : Out-of-plane C-H wagging.-----62

Figure 3.9: Zoom in of the P branch of the 6_0^1 absorption contour; experimental spectrum (black) and simulated spectrum (red). (A) The experimental absorption contour was generated by 1+1 REMPI of benzene vapour in a static cell. This technique is not mass selective so the absorption contour of $^{13}\text{C}^{12}\text{C}_5\text{H}_6$ is simultaneously generated, appearing blue shifted from the $^{12}\text{C}_6\text{H}_6$ 6_0^1 contour. However, it does appear as a small shoulder on the high energy side of the $^{12}\text{C}_6\text{H}_6$ 6_0^1 band. This is marked with an asterisk (*). The simulated contour is only the 6_0^1 band of $^{12}\text{C}_6\text{H}_6$, hence the poor fit between experimental and simulated contours at the (*) position. (B) The experimental spectrum generated from room temperature background signal in the TOF-MS. By performing 1+1 REMPI in the TOF-MS, mass selection of the ions allows the $^{12}\text{C}_6\text{H}_6$ molecules to be analysed independently of the $^{13}\text{C}^{12}\text{C}_5\text{H}_6$ isomer. Comparison with the simulated spectrum shows that the shoulder caused by the $^{13}\text{C}^{12}\text{C}_5\text{H}_6$ isomer is no longer present. The absorption contours generated after mass selection were used in the best temperature fit analyses.-----64

Figure 3.10: Simulation of 6_0^1 absorption feature. In Figure (A) the simulated contour (red) is fit to an experimental spectrum (black) generated by 1+1 REMPI in the Source of a TOF-MS. In Figure (B) the simulated contour is fit to an experimental spectrum generated in free-jet expansion of benzene and nitrogen. The best-fit temperatures were found by using the spectroscopic constants reported in Table 3.12. The reported errors are 1 standard deviation of the best-fit temperature. -----68

Figure 3.11: Illustration of the perturbation of vibrational state energies due to both anharmonic interaction and fermi resonances between vibronic states. The result is the distortion of predicted intensities of the rovibrational contours as well as displacement from their unperturbed origins. The levels in bold are those that are thought to be involved in the transitions. -----71

Figure 3.12: Figure (A) is an overlay of the simulated (red) contour with the experimentally obtained REMPI spectrum (black) of room temperature benzene vapour. The tail of the adjacent 16_0^2 and 6_0^1 bands were removed as a baseline from the experimental spectrum before fitting. The small bump on the tail on the contour has been assigned by Lyman as the $6_0^1 18_1^1$ band [33]. This band was not included in the simulations. Figure (B) identifies the three sub-bands that contribute to the overall contour. The blue and green bands are identical except that they are split by fermi resonance (see Figure 3.11). Figure (C) is an overlay of the simulated (red) contour with the experimental spectrum obtained from a free-jet expansion of benzene in nitrogen (black). The temperatures quoted are the best temperature fits to the experimental contours using the spectroscopic constants from Table 3.16.-----73

Figure 3.13: Figure (A) is an overlay of the simulated (red) contour with the experimentally obtained REMPI spectrum (black) of room temperature benzene vapour. The temperatures quoted are the best temperature fits to the experimental contours using the spectroscopic constants from Table 3.20 Table 3.20 and Table 3.21. Figure (B) identifies the sub-bands that contribute to the overall contour. Figure (C) is an overlay of the simulated (red) contour with the experimental spectrum (black) obtained from a free-jet expansion of benzene in nitrogen. The unknown feature at $\sim 38434 \text{ cm}^{-1}$ was also simulated assuming it was also a type I band. -----80

Figure 3.14: Experimental setup for recording the 2D - LIDF spectrum of room temperature benzene.-----84

Figure 3.15: Typical dispersed fluorescence spectrum generated by the imaging spectrometer. This image was collected over 10,000 laser shots with a slit size of $100 \mu\text{m}$, giving a resolution of 0.5 cm^{-1} . This image was generated by exciting warm benzene with 260.1 nm light which corresponds to the absorption transition $6_0^1 16_1^1 / 6_0^1 11_1^1$. The observed dispersed fluorescence is $1_1^0 6_0^1 16_1^1 / 1_1^0 6_0^1 11_1^1$. -----86

Figure 3.16: (A) Laser Induced Fluorescence. The energy of the excitation photon remains constant whilst the spectrum of emitted photons is collected. (B) Dispersed Fluorescence. The energy of the excitation laser is scanned whilst monitoring the intensity of the emitted photons. A single fluorescence energy can be monitored or the total summed fluorescence. The LIDF technique simultaneously records both the Laser Induced and Dispersed Fluorescence spectra. -----87

Figure 3.17: Experimental LIDF spectrum of the 6_0^1 absorbance / 6_0^1 fluorescence transition. Absorption step size 0.001 nm , Fluorescence energy/pixel 0.13 cm^{-1} (fluorescence slit width of $25 \mu\text{m}$). This spectrum has not been normalised to laser power. The intensity fluctuations of the absorption contour are due to fluctuations in laser power.-----89

Figure 3.18: Experimental LIDF spectrum of the $6_1^2 / 6_1^0 11_0^2$ absorption/ $6_1^2 / 6_1^0 11_0^2$ fluorescence transition. The spectrum has not been normalised to laser power. Absorption step size 0.001 nm , Fluorescence energy/pixel 0.13 cm^{-1} (fluorescence slit width of $25 \mu\text{m}$). The presence of the $6_0^1 18_1^1$ can clearly be seen half-way along the main diagonal feature. A more detailed schematic of the transitions involved in the absorption step of this LIDF spectrum is shown in Figure 3.11. -----90

Figure 3.19: Simulated LIDF spectrum based on the 6_0^1 absorbance/ 6_0^1 fluorescence transition. The ζ_{eff} in the excited state has been set to $+0.6$, generating absorption and fluorescence spectra both with shape of type I. The absorption points are convoluted with a

Gaussian of 0.001 nm FWHM. Whilst the fluorescence points are convoluted with a Gaussian of 0.004 nm FWHM. -----92

Figure 3.20: Simulated LIDF spectrum based on the 6_0^1 absorbance/ 6_0^1 fluorescence transition. The ζ_{eff} in the excited state has been set to 0, generating absorption and fluorescence spectra both with shape of type II.-----93

Figure 3.21: Simulated LIDF spectrum based on the 6_0^1 absorbance/ 6_0^1 fluorescence transition. The ζ_{eff} in the excited state has been set to -0.6 , generating absorption and fluorescence spectra both with shape of type III.-----94

Figure 3.22: Simulated LIDF spectrum based on the 6_0^1 absorbance/ 6_0^1 fluorescence transition. The ζ_{eff} in the excited state has been set to -1.2 , generating absorption and fluorescence spectra both with shape of type IV.-----95

Figure 3.23: Simulated image based upon absorption through a third-order transition and fluorescence through a first-order transition. The features marked with ♣, are unique features to a LIDF spectrum that involves this type of transition pathway. The complimentary process, absorption through a first-order transition and fluorescence through a third-order transition, produces an identical LIDF spectrum except it is reflected about the main diagonal.-----96

Figure 3.24: Experimental, room temperature LIDF spectrum of the $6_0^1 16_1^1 / 6_0^1 11_1^1$ absorption $1_1^0 6_0^1 16_1^1 / 1_1^0 6_0^1 11_1^1$ fluorescence transition.-----99

Figure 3.25: Experimental, room temperature LIDF spectrum of the $6_0^1 16_1^1 / 6_0^1 11_1^1$ absorption $1_1^0 6_0^1 16_1^1 / 1_1^0 6_0^1 11_1^1$ fluorescence transition. The sharp dip in signal seen in the fluorescence profile is due to a damaged pixel in the detector. See Section 3.4.4 for explanation of marker symbols.-----100

Figure 3.26: Experimental, cold LIDF spectrum of the $6_0^1 16_1^1 / 6_0^1 11_1^1$ absorption $1_1^0 6_0^1 16_1^1 / 1_1^0 6_0^1 11_1^1$ fluorescence transition generated in a free-jet expansion of benzene in helium.---101

Figure 3.27: Schematic of the transition pathways that were used to create the simulated LIDF spectrum. Absorption transitions are in blue and fluorescence transitions are in red. (A) and (B) are all the allowed pathways within the $6_0^1 16_1^1$ absorption/ $1_1^0 6_0^1 16_1^1$ fluorescence

process. The varying energy of the excited states is due to the magnitude of the Coriolis and vibrational coupling constants. The transitions marked with (*) are third-order transitions and have a much lower transition probability than the other, first-order transitions. (C) shows the allowed transitions for the $6_0^1 11_1^1$ absorption/ $1_1^0 6_0^1 11_1^1$ fluorescence process.-----104

Figure 3.28: Best-fit simulation of the room temperature $6_0^1 16_1^1 / 6_0^1 11_1^1$ absorption, $1_1^0 6_0^1 16_1^1 / 1_1^0 6_0^1 11_1^1$ fluorescence LIDF spectrum. (A) Simulated LIDF spectrum using the spectroscopic constants from Table 3.22. The labelling of the bands is explained in Section 3.4.4. (B) Difference spectrum highlighting the discrepancies between the experimental and simulated spectra. The black areas indicate that the experimental spectrum is more intense, and the white areas indicate that the simulated spectrum is more intense.-----105

Figure 3.29: (A) Best-fit simulation of the rotationally cold $6_0^1 16_1^1 / 1_1^0 6_0^1 16_1^1$ LIDF spectrum shown in Figure 3.26. The rotational temperature of the spectrum was determined to be 8 ± 1 K. The labelling of the bands is explained in Section 3.4.4. (B) Difference spectrum highlighting the discrepancies between cold experimental and simulated spectra.-----106

Figure 3.30: (A) An overlay of the simulated (red) absorption contour with the experimentally obtained REMPI spectrum (black) of room temperature benzene vapour. The spectroscopic constants used to generate the simulated contour are the result of best-fits to the LIDF spectrum presented in Table 3.22. (B) Identification of the sub-bands that contribute to the overall contour. In comparison with the results of Figure 3.13(B) the shape of the $6_0^1 l_0^{\mp 1} 11_1^1 l_0^0$ contour (blue) is now definitely of type I and sits directly under the $6_0^1 l_0^{\mp 1} 16_1^1 l_{\pm 1}^{\pm 1}$ sub-band (orange). The type III contour of the third-order transition, $6_0^1 l_0^{\pm 1} 16_1^1 l_{\pm 1}^{\mp 1}$ (pink), now appears centred between the two main absorption features.-----107

Figure 4.1: (A) Schematic of the TOF-MS with $L\mu J$ source. (B) Illustration of the relative laser position for evaporation experiments. The blue arrow represents the collimated UV laser. The laser is positioned perpendicular to both the $L\mu J$ and TOF axes and between the $L\mu J$ and detector. Only those evaporating molecules that have an initial velocity component along the TOF axis will reach the laser ionisation volume, be ionised and then detected.-----125

Figure 4.2: Example of best temperature fits to the 3 rovibrational contours of interest. Each experimental spectrum (black) is the convolution of at least 4 consecutive wavelength scans and overlaid with the best-fit simulated spectrum (red). Temperatures of simulated spectra are displayed with error bars indicating 1 standard deviation from the mean. When fitting spectrum (C) it was assumed that 16_1 and 11_1 vibrational levels were at the same rotational temperature. The justification for this assumption is provided later in this chapter. --

Figure 4.3: (A) Rotational temperatures of different vibrational modes of benzene as a function of surface residence time in the vacuum. Residence time is determined by the vertical distance of the ionising laser from the L μ J nozzle and the flow rate of the L μ J. (B) Rotational temperatures of different vibrational modes of benzene as a function of radial distance from the liquid surface. Vibrationless rotational temperatures are represented by the solid circles (\bullet), whilst rotational temperatures for ν_6 , ν_{16} (and ν_{11}) are represented by the solid squares (\blacksquare) and open circles (\circ), respectively. The error bars represent 3 times the weighted error of the mean, 3σ .-----131

Figure 4.4: Benzene 1+1 REMPI absorption spectrum produced under various experimental conditions. (A) In a room-temperature static cell. The integrated intensities of the hot bands relative the 6_0^1 are indicated under each band. (B) Evaporation of benzene from an *in vacuo* L μ J. The ionising laser was positioned 1 mm from the nozzle and 300 μ m from the jet surface. (C) Benzene seeded into a free-jet expansion of nitrogen. The expansion conditions are reported in Section 4.4.2. The intensity of all spectra at energies less than 38535 cm^{-1} have been enhanced ten-fold for display purposes.-----137

Figure 4.5: (A) Vibrational temperatures of benzene as a function of residence time in the vacuum. (B) Vibrational temperatures of the different vibrational modes as a function of distance from the liquid surface. The vibrational temperatures for ν_6 , ν_{16} and ν_{11} are represented by the solid squares (\blacksquare), open circles (\circ) and open squares (\square), respectively. The error bars represent 3 times the weighted error of the mean, 3σ .-----140

Figure 4.6: Illustration of the collisional cooling experienced in the nitrogen free-jet expansion as a function of binary collision number. The translational temperature of benzene is determined by the expansion properties of the 3D jet, including the orifice diameter and the heat capacity of the carrier gas [85]. Under the experimental conditions reported here the translational temperature asymptotes to a maximum of 360 binary collisions. The collisional cooling efficiencies of the other modes were varied until their temperature at 360 collisions was equal to that observed experimentally. The collisional cooling efficiencies required to achieve these temperatures are given in Table 4.2.-----146

Figure 4.7: General description of rates of energy transfer into and out of state ψ_i -----150

Figure 4.8: The 17 transitions included in the Master Equation (ME) kinetic model.----153

Figure 4.9: Modelling the change in temperature of the different degrees of freedom of benzene as a function of binary, hard-sphere collision number. The results of the TG model are indicated using the red lines whilst the ME results are indicated with the blue lines.----158

Figure 5.1: (A) Schematic of the TOF-MS with L μ J Source Chamber. (B) Illustration of the relative laser positions for desorption experiments. The blue arrow represents the collimated UV laser and the red arrow the focused IR laser. Both lasers are positioned perpendicular to both the L μ J and TOF axes. The IR laser is focused onto the surface of the L μ J, whilst the UV laser is positioned 300 μ m from the liquid surface between the L μ J and ion detector. Only those desorbed (or evaporating) molecules which leave the liquid surface with a velocity component along the TOF axis will reach the ionisation volume, be ionised and then detected.-----176

Figure 5.2: Comparison between mass spectra generated under different experimental conditions. IR only: Only the IR laser is incident upon the L μ J. $\lambda_{\text{IR}} = 2.85 \mu\text{m}$. UV only: The UV laser is position 300 μ m from the liquid surface, UV photon energy is 38611 cm^{-1} . The only ion signal observed is from benzene monomer that has evaporated from the liquid surface. IR + UV: The IR laser is fired and then the UV laser is fired. In this example spectrum the IR-UV delay is 10 μ s. Inset: zoom in on the baseline of the mass spectra show that the two-laser technique has greatly increased the number of fragment ions to be produced.-----178

Figure 5.3: 1+1 REMPI spectra of the fragments identified in Figure 5.2 These spectra were generated with an IR-UV delay of 1.3 μ s. Each fragment shows the same wavelength dependence - they all portray the 6_0^1 rovibronic spectrum of the benzene monomer.-----180

Figure 5.4: Dependence of ion signal on IR laser fluence. (●) Integrated intensity of benzene monomer ion signal (78 amu). (○) Integrated intensity of all benzene fragment ion signals. The UV laser is positioned 300 μ m from the liquid surface. UV photon energy is 38611 cm^{-1} , where the first absorption step is via the 6_0^1 absorption band. λ_{IR} is 2.85 μ m. The IR-UV delay is 10 μ s. The fragment intensities show an IR fluence dependence similar to that of the monomer. When the data are fitted with Equation 5.1 the monomer ion signal shows an n value of 0.8 ± 0.1 , and the fragment ion signal an n value of 1.2 ± 0.1 .-----182

Figure 5.5: Mass spectrum of benzene (m/z 78) desorbed from a 25% ethanol/water L μ J. UV photon energy is 38611 cm^{-1} and UV fluence is 0.014 J.cm^{-1} . IR wavelength is 2.85 μ m and IR fluence is 0.9 J.cm^{-2} . IR-UV delay is 0.5 μ s. Under these conditions the monomer ion signal has been enhanced by a factor of 4.3 by the introduction of the IR laser. The maximum enhancement of the monomer ion signal is seen at $\sim 3 \mu$ s delay, where the two-laser setup has enhanced the pure evaporation signal sixfold. There is no signal from the IR laser alone so it is not included in the figure. The observed clusters consist only of benzene ions clustered to solvent molecules or their fragments. Ethanol molecules are abbreviated as EtOH. No benzene dimer is seen.-----184

Figure 5.6: Changes in the observed TOF mass spectrum with time-lag delay. UV photon energy is 38611 cm^{-1} . IR wavelength is $2.85 \text{ }\mu\text{m}$. IR fluence is $0.9 \text{ J}\cdot\text{cm}^{-2}$. IR-UV delay is $2.5 \text{ }\mu\text{s}$. The time-lag delay between ionisation and ion extraction is 1.1 , 0.69 and $0.39 \text{ }\mu\text{s}$ for spectrum (A),(B) and (C), respectively. Each spectrum is shifted to shorter flight times as the extraction delay time is decreased. The increase in cluster signal with time-lag delay is evidence that the clustering process is occurring post-ionisation of the benzene. At even longer time-lag delays, distortion of the mass peak shape occurs for all masses due to spatial limitations of the electrode assembly (see Chapter 2).-----186

Figure 5.7: 1+1 REMPI spectra of selected clusters seen in the mass spectra with an IR-UV delay of $0.5 \text{ }\mu\text{s}$. Each cluster shows the same wavelength dependence - they all portray the 6_0^1 vibronic spectrum of the benzene monomer. The best-fit ground state rotational temperatures of each contour are indicated with 1 standard deviation error (1σ). Within error, all of the clusters show the same rotational temperature as the monomer.-----187

Figure 5.8: (A) The effect of changing IR-UV delay on the monomer TOF ion signal. The TOF peak displayed here belongs to the C_6H_6^+ ion. Each peak has been fitted to the sum of two Gaussians. The relative intensities of each component changes with IR-UV delay times. The identity of each component is confirmed by determining the rotational temperature of each component. (B) 6_0^1 vibronic spectrum of the benzene monomer generated with IR-UV delay of $1 \text{ }\mu\text{s}$. The green spectrum was generated by monitoring the intensity of the fast component of the mass peak. The blue spectrum was generated by monitoring the slow component.-----190

Figure 5.9: Monomer and cluster intensity as a function of IR-UV delay. (●) Benzene monomer, C_6H_6^+ , (●) two component (binary) clusters, $\text{C}_6\text{H}_6^+\bullet\text{X}$, (●) three component (tertiary) clusters, $\text{C}_6\text{H}_6^+\bullet\text{X}\bullet\text{Y}$. (A) The monomer achieves maximum desorption signal at an IR-UV delay of $\sim 3 \text{ }\mu\text{s}$, whilst the binary cluster signal is maximised at a delay of $\sim 1 \text{ }\mu\text{s}$. Data points in (A) are the average of the results from several mass spectra. Error bars represent 1σ error. (B) Zoom in on the overlay of monomer and cluster temporal profiles generated from a single mass spectrum. The tertiary clusters are now included. The plot demonstrates that stable cluster formation occurs early in the desorption plume (at short IR-UV delay). The maximum intensity of the tertiary clusters is seen at an IR-UV delay of $\sim 0.5 \text{ }\mu\text{s}$.-----192

Figure 5.10: Fit of two Maxwell-Boltzmann distributions to (A) the benzene monomer ion signal and (B) the binary cluster ion signal. Plots were produced by transforming the data of Figure 5.9(A) using Equation 5.2. The fits have been weighted by the displayed error in the data points. Both best-fits describe a velocity distribution that has zero drift velocity perpendicular to the jet axis (u_\perp). All distributions use a mass of 78 amu (benzene monomer). In both plots the red curve is the summation of both of the underlying components. The ionising laser energy is 38611 cm^{-1} corresponding to the maximum in the 6_0^1 absorption band of the monomer.-----194

Figure 5.11: Schematic of the conditions of the 3D Monte Carlo simulation. Different length arrows represent molecules released from the liquid surface with different initial velocities. The volume of the ionisation region runs into the page, perpendicular to the $L_{\mu J}$ axis. The different width arrows represent different initial masses emerging from the $L_{\mu J}$ – this is used in the mass-independent velocity distribution simulations.-----200

Figure 5.12: Demonstration of the effects of the diameter of the ionisation volume on the shape of the IR-UV delay distribution created by the 3D Monte Carlo simulations. The translational temperature and bulk velocity used in the simulations were 200 K and 100 $\text{m}\cdot\text{s}^{-1}$, respectively. The diameter of the UV volume is 150 μm (blue line), diameter of the UV volume is 1.5 μm (red line). The signal/noise is worse when the UV volume is smaller since fewer molecules find themselves within the region at the time of ionisation. Larger ionisation volumes distort the maximum in the distribution to shorter delay times since molecules with a larger range of molecular velocities can reach the ionisation volume at the shorter delays. The distribution created with 1.5 μm diameter has been fitted with a function of the form of Equation 5.4 but without the pre-exponential factor, C/t^4 (black line). The best fit predicted a \bar{u} of $88 \pm 1 \text{ m}\cdot\text{s}^{-1}$ and a T_{\perp} of $19 \pm 1 \text{ K}$.-----201

Figure 5.13: Simulated IR-UV delay distributions overlaid with the experimentally observed benzene monomer ion signal (\bullet) distribution. All the simulations in (A) have a bulk velocity of 200 $\text{m}\cdot\text{s}^{-1}$ but vary in translational temperature: (red line) 300 K, (black line) 200 K, (green line) 100 K. (B) shows the effects of changing the drift velocity in the simulations with a temperature of 200 K. (red line) 300 $\text{m}\cdot\text{s}^{-1}$, (green line) 200 $\text{m}\cdot\text{s}^{-1}$, (black line) 100 $\text{m}\cdot\text{s}^{-1}$.-----203

Figure 5.14: Simulated IR-UV delay distributions of different masses included in the 3D Monte Carlo simulation. (A) C_6H_6 , 78 amu (black line), $\text{C}_6\text{H}_6\bullet 2\text{H}_2\text{O}$, 114 amu (blue line), $\text{C}_6\text{H}_6\bullet 4\text{H}_2\text{O}$, 150 amu (green line). (B) When the distributions from each mass are summed together the resultant IR-UV delay is broader at the maximum which more closely resembles the shape of the experimentally observed distribution maximum. Only C_6H_6 (black line), C_6H_6 and $\text{C}_6\text{H}_6\bullet 2\text{H}_2\text{O}$ (red line), C_6H_6 , $\text{C}_6\text{H}_6\bullet 2\text{H}_2\text{O}$ and $\text{C}_6\text{H}_6\bullet 4\text{H}_2\text{O}$ (green line). Experimental data (\bullet).-----206

Figure 5.15: Rovibrational contours of benzene molecules IR desorbed from the $L_{\mu J}$. These spectra were produced with an IR-UV delay time of 3.9 μs . Temperature fits are displayed with error indicating 1 standard deviation from the mean. The lower signal/noise and larger fitting error of (C) is due to the dramatic decrease in the intensity of the band under desorption conditions. (*) See text for a discussion of this feature.-----209

Figure 5.16: Comparison of the benzene absorption spectrum generated under different experimental conditions. See text for details. The rotational temperatures of benzene molecules are also quoted for each experimental environment. The IR-UV delay used to

generate the desorption spectrum shown here was $4 \mu\text{s}$. The intensity of all spectra has been magnified ten-fold at energies less than 38535 cm^{-1} . -----211

Figure 5.17: Temporal evolution of the internal temperatures of neutral benzene molecules laser desorbed from the surface of the $L\mu\text{J}$. (A) Rotational temperatures as a function of IR–UV delay. It is assumed that the rotational temperatures of molecules excited with vibration ν_{16} and ν_{11} are equal. Vibrationless rotational temperatures are represented by the solid circles (\bullet), whilst rotational temperatures for ν_6 , ν_{16} (and ν_{11}) are represented by the solid squares (\blacksquare) and open circles (\circ), respectively. (B) Vibrational temperatures as a function of IR-UV delay. Vibrational temperatures for ν_6 , ν_{16} and ν_{11} are represented by the solid squares (\blacksquare), open circles (\circ), and open squares (\square), respectively. The error bars on all points represent 3 times the weighted error of the mean (3σ). The temperatures at 0 IR-UV delay are the temperatures of benzene molecules that are naturally evaporating into the vacuum from the $L\mu\text{J}$.-----214

Figure 5.18: Comparison between the rates of change of ground state rotational temperatures (\bullet) and the observed intensity of the benzene monomer ion signal (\bullet) as a function of IR-UV delay. The temperature scale has been reversed to aid in the overlay. The data at 0 IR-UV delay are from benzene molecules that are naturally evaporating into the vacuum from the $L\mu\text{J}$. -----216

List of Tables

Table 3.1: Symmetries and frequencies of benzene vibrational modes. The vibrations are labelled according to the convention introduced by Wilson [3]. Descriptions of the vibrations are taken from Muller [4]. Unless otherwise indicated, frequencies are taken from Atkinson [5]. (χ) Page [6], (δ) Stephenson [7], (ϵ) Muller [4].-----39

Table 3.2: Determination of the vibronic symmetries for excitation of the vibrations ν_6 and ν_{16} in the excited electronic state ${}^1B_{2u}$ of benzene. Both ν_6 and ν_{16} have symmetry E_2 , so both θ_6 and θ_{16} equal $4\pi/6$.-----42

Table 3.3: Determination of allowed vibrational angular momentum transitions within the vibronic transition $6_1^0 11_0^2$. The only allowed transition here is shown to be $6_1 l_{\pm 1} 11_0 l_0 \leftrightarrow 6^0 l^0 11^2 l^0$ since it involves $\Delta\theta_{ev} = \mp 4\pi/6$.-----42

Table 3.4: Rovibronic symmetries of states involved in the $6_0^1 16_1^1$ transition. (\ddagger) Rotational symmetries, $\Gamma(\psi_r)$, are taken from Wilson [3]. Not all states are involved in each $\Delta k = \pm 1$ transition. -----45

Table 3.5: Determination of Hougen's Quantum number for the $6^1 16^1$ vibronic state in the ${}^1B_{2u}$ excited electronic state of benzene. (\ddagger) The symmetries were calculated in Table 3.2.--48

Table 3.6: Assignment of rovibronic symmetries using Hougen's quantum number, g . ----48

Table 3.7: $\pm l$ selection rules for rovibronic transitions. -----53

Table 3.8: Hönl-London factors for a perpendicular transition [11]. $K = |k|$. J and K values are from the initial rotational states involved in the rotational transition. The upper signs are for $\Delta K = -1$ transitions, lower signs are for $\Delta K = +1$ transitions. (*) If $K=0$ and $\Delta K = +1$, then the factor must be multiplied by 2. -----59

Table 3.9: Examples of statistical weights calculated for some of the rovibronic transitions allowed within the vibronic transition ${}^{ev}B_{1g} \leftarrow {}^{ev}E_{2u}$, and displayed in Figure 3.5. (‡) Note that although the total symmetry of ψ''_{evr} is $B_1 + B_2$ when $k = 1$, only the wavefunctions of symmetry B_1 can undergo the $\Delta k = -1$ transition due to symmetry restrictions. The statistical weight reflects only the degeneracy of states that are involved in the transition. -----59

Table 3.10: The vibronically induced transitions simulated in this study and their symmetry according to Mills' polar co-ordinate assignment. (*) These transitions were only used in the 2D simulated spectra discussed in Section 3.4. -----62

Table 3.11: Vibrational anharmonicity energy factors and effective Coriolis constant involved in the 6_0^1 transition. -----67

Table 3.12 Spectroscopic constants used in the simulation of $6_0^1 l_0^{\mp 1}$. All rotational constants and the Coriolis constant were taken from Okruss [23]. The anharmonic constants are taken from Atkinson [5].-----67

Table 3.13: Vibrational anharmonicity energy factors and effective Coriolis constant for states involved in the transition 6_1^2 . -----69

Table 3.14: Vibrational anharmonicity energy factors and effective Coriolis constant for states involved in the transition $6_1^0 11_0^2$. -----69

Table 3.15: Vibrational anharmonicity energy factors and effective Coriolis constant from states involved in the 16_0^2 transition. -----72

Table 3.16: Spectroscopic constants used in the simulation of $6_1^2/6_1^0 11_0^2$. (*)Ground state rotational constants were taken from Hollenstein [25]. (†) The value for the ground state Coriolis constant was taken from Weber [18] The anharmonic constants are taken from Atkinson [5]. The excited state rotational constants were determined by fitting of the room temperature experimental spectrum with a simulated spectrum. The standard deviation is given in parenthesis in units of the last digit. -----74

Table 3.17: Comparison of rotational defects for molecules vibrating in the ${}^1B_{2u}$ electronic state of benzene. All rotational constants are the best-fit values from fitting of the room temperature absorption spectrum. $\Delta\nu$ given in units of $\text{amu}\cdot\text{\AA}^2$. For comparison literature values of rotational constants and $\Delta\nu$ are included in the bottom half of the table. These values were taken from the following sources: (*) Riedle [19], (¥) Weber [33], (†) Sieber [37].-----76

Table 3.18: Vibrational anharmonicity energy factors and Effective Coriolis constant for states involved in the transition $6_0^1 16_1^1$.-----77

Table 3.19: Vibrational anharmonicity energy factors and effective Coriolis constant for states involved in the transition $6_0^1 11_1^1$.-----78

Table 3.20: Spectroscopic constants used in the simulation of the $6_0^1 16_1^1$ contour. (*) Ground state rotational constants were taken from Hollenstein [25]. The anharmonic constants are taken from Atkinson [5]. The excited state rotational constants were determined by fitting of the room temperature experimental spectrum with a simulated spectrum. It was assumed that the intensity of the third-order component (the $6_0^1 l_0^{\pm 1} 16_1^1 l_{\pm 1}^{\mp 1}$ transition) was negligible during the fitting process. Allowing the rotational constants of the excited states to be different did not produced any improvements in the fit. The results reported here were generated assuming that the rotational constants in the excited state were equal. The standard deviation is given in parenthesis in units of the last digit for constants determined in this study.-----79

Table 3.21: Spectroscopic constants used in the simulation of the $6_0^1 11_1^1$ contour. (*) Ground state rotational constants were taken from Hollenstein [25]. The anharmonic constants are taken from Atkinson [5]. The excited state rotational constants were determined by fitting of the room temperature experimental spectrum with a simulated spectrum. The standard deviation is given in parenthesis in units of the last digit for constants determined in this study.-----79

Table 3.22: Summary of spectroscopic constant values generated from best-fit to the LIDF spectrum in Figure 3.25. (*) Value taken from Hollenstein [25]. (†) Values calculated from the rotational defects reported by Jagod [35]. All other rotational constants are the result of best-fit simulations performed in this study. 1 standard deviation is given in parentheses in units of the last digit. $\Delta\nu$ given in units of $\text{amu}\cdot\text{\AA}^2$, all other constants have units cm^{-1} . (★) When calculated from the shape of the third-order transition, $1_1^0 l_0^0 6_0^1 l_0^{\pm 1} 16_1^1 l_{\pm 1}^{\mp 1}$, the best-fit was a $\Delta\nu$ value of -0.497 and $\zeta_{eff} = 0.484(3)$.-----103

Table 4.1: Temperatures of the different internal degrees of freedoms of benzene molecules evaporating from an in vacuo aqueous surface.-----139

Table 4.2: Mode-specific collisional energy transfer efficiencies ($k_{i\infty}$) of benzene in N₂.--
-----148

Table 4.3: Summary of possible levels to be included in the ME model of relaxation rates in S₀ benzene. †Degeneracies correlate will those quoted in Ref [98]. *Populations are relative to the vibrationless ground state at 295 K. Highlighted rows are the transitions that were included in the model. Of the 36 possible transitions only 17 are included in this model; the other transitions were discarded upon enforcement of the simplifications as stated in the text. Δ, Ω, ∞: these transitions were given equivalent rate constants, (k_{ij}), as they involve the same number of quanta change of a particular vibration. This leaves 11 independent rate constants to be calculated using the series of differential equations.-----152

Table 4.4: k_{ij} values obtained using the Master Equation model.-----155

Table of Contents

Affidavit	II
Abstract	III
Acknowledgments	V
Publications	VI
Abbreviations	VII
List of Figures	VIII
List of Tables	XX
Table of Contents	XXIV
1. Outline	1
1.1 References	3
2. Experimental Technique	4
<i>Design and Implementation of a TOF-MS with Liquid Micro-Jet Source</i>	
2.1 Introduction	4
2.2 Apparatus	4
2.3 Creating an <i>in vacuo</i> Liquid Micro-jet	9
2.4 One-colour Resonant Two Photon Ionisation (1+1 R2PI)	13
2.5 Time-of-Flight Mass Spectrometry	17
2.6 References	29
3. Spectral Simulation	32
<i>Simulation of the ${}^1B_{2u} \leftarrow {}^1A_{1g}$ Gas Phase Absorption spectrum of Benzene</i>	
3.1 Introduction	32
3.2 Theory of Optical Transitions	33
3.2.1 Selection Rules for Allowed Vibronic Transitions	35
3.2.2 Simulating Rovibronic Transitions	43

3.2.3	Energy of a Rovibronic State	54
3.2.4	Intensity of a Rovibronic Transition	58
3.3	Simulation of the Vibronic Transitions within ${}^1B_{2u} \leftarrow {}^1A_{1g}$	60
3.3.1	Simulation of the 6_0^1 Absorption Feature	66
3.3.2	Simulation of the 6_1^2 and $6_1^0 11_0^2$ Absorption Features	69
3.3.3	Simulation of the $6_0^1 16_1^1$ and $6_0^1 11_1^1$ Absorption Features	76
3.4	Laser Induced Dispersed Fluorescence (LIDF)	82
3.4.1	Experimental Technique	83
3.4.2	Interpretation of a LIDF Image	88
3.4.3	De-convolution of the $6_0^1 16_1^1 / 6_0^1 11_1^1$ absorption band	97
3.4.4	Analysis of $6_0^1 16_1^1 / 6_0^1 11_1^1$ Absorption, $1_1^0 6_0^1 16_1^1 / 1_1^0 6_0^1 11_1^1$ Fluorescence LIDF Spectrum	108
3.5	Conclusion	114
3.6	References	115
 4. Molecular Evaporation		 119
<i>The Dynamics of Evaporation from a Liquid Surface</i>		
4.1	Introduction	119
4.2	Experimental Method	124
4.3	Results and Discussion	127
4.3.1	Rotational Temperatures	127
4.3.2	Vibrational Temperatures	136
4.4	Determination of collision numbers upon evaporation from an <i>in vacuo</i> liquid surface	142
4.4.1	Collisional Energy Transfer	142
4.4.2	Modelling Collisional Energy Transfer Rates	144
4.4.3	Temperature Gap Model of Collisional Relaxation Rates	147
4.4.4	Master Equation Model of Collisional Relaxation Rates	148
4.4.5	Results of Master Equation Modelling	154
4.4.6	Estimate of Collisional Numbers upon Evaporation	156
4.5	Conclusion	159
4.6	References	161

5. Infrared Desorption	169
<i>Partitioning of Internal Energy within Benzene Molecules Thermally Desorbed from a Liquid Surface</i>	
5.1 Introduction	169
5.2 Experimental Method	173
5.3 Features of the Desorption Mass Spectrum	175
5.4 Translational Velocity Distributions of the Desorption Process	191
5.5 Distribution of Internal Energy by the Desorption Process	196
5.6 Conclusion	216
5.7 References	218

Chapter 1. Thesis Outline

The adiabatic process of the phase change between liquid and gas is an integral part of many natural and industrial processes. Everyone has experienced the cooling sensation of water evaporating from their skin, but a fundamental understanding of the dynamics of the evaporation process is yet to be completely understood at the molecular level. The approach used here to research this fundamental process is a multifaceted one. Physical measurements are collected and their interpretation dependent upon correlations between simulations, or theoretical recreations, of the results.

This thesis reports on experiments which elucidate the distribution of internal energy amongst an ensemble of molecules directly after they have escaped from an aqueous liquid surface. A comparison is made between the state distributions that occur as a result of spontaneous molecular evaporation and laser-stimulated desorption. In order to minimise the poisoning effects of post desorption gas phase collisions on the nascent molecular energy distribution, the liquid surface is interrogated under vacuum. The difficulty with sustaining an *in vacuo* aqueous environment arises because the adiabatic process of evaporation is so rapid and the molecular densities so high that a liquid placed under vacuum will tend to freeze before it can be interrogated. However, in 1988 Faubel pioneered the use of a micron-diameter, fast moving liquid jet as a source for the *in vacuo* liquid surface [1]. The sharp curvature of the jet's liquid surface decreases the likelihood that an evaporating molecule will collide and thus condense with other evaporating molecules. Time-of Flight analysis of evaporating water molecules allowed Faubel to establish the velocity distribution and thus an estimate of the internal energy distribution of the evaporating molecules. In this study we are able to directly measure the internal energies of molecules evaporating from the surface of an aqueous liquid micro-jet (L μ J) using molecular spectroscopy.

Chapter 2 contains a description of the apparatus built specifically for performing experiments using the *in vacuo* liquid micro-jet (L μ J). The experiments were performed in a Time-of-Flight Mass-Spectrometer (TOF-MS) with a Source Chamber that was modified to accommodate the L μ J system at low pressures. Combining the mass selectivity of a TOF-MS with the state-selective ionisation of Resonance Enhanced Multiphoton Ionisation (REMPI) has allowed us to perform molecule-specific spectroscopy. The spectroscopic techniques used here extract the molecular information in the form of absorption spectra of ‘spy’ molecules that have been seeded into the liquid system.

Chapter 3 outlines the theory required to simulate the REMPI spectrum of benzene, our molecular ‘spy’ molecule. Since the values of many of the spectroscopic constants needed to define benzene’s rovibronic band contours are unknown, these had to be determined before the simulations could be performed. The optimum values for these constants were found by non-linear least squares comparison of the simulated spectra to thermally equilibrated, room temperature examples of the same absorption bands. We also introduce a high resolution, 2D spectroscopy that simultaneously records a molecule’s absorption and dispersed fluorescence spectrum. The technique is labelled Laser Induced Dispersed Fluorescence (LIDF). These 2D spectra were also simulated. Examples are given that show the accuracy of the simulations in reproducing the absorption bands and LIDF spectra at different rotational temperatures. The simulated spectra were then used in the analysis of the experimental observations reported in Chapters 4 and 5.

The final two chapters report results of experiments performed with the L μ J TOF-MS. In Chapter 4 the rotational and vibrational temperatures of benzene molecules that spontaneously evaporate from the *in vacuo* aqueous surface are reported. The temperatures were measured at varying distances from the surface and after different residence times of the liquid being exposed to the vacuum. After establishing the collisional cooling efficiencies of the different

molecular degrees of freedom we estimate the number of collisions the benzene ‘spy’ undergoes as it traverses the liquid-vacuum interface.

Finally, in Chapter 5, we explore the dynamics of the laser desorption process whereby benzene molecules are forced into the gas phase when the water matrix absorbs resonant IR photons. The temporal characteristics of the desorption plume such as molecular density, translational velocity and the propensity for ion-molecule reactions are explored. In addition, the rotational and vibrational temperatures of the benzene molecules entrained in the desorption plume are recorded. Significant cooling of the internal degrees of freedom of benzene is observed inside the expansion. This result justifies the IR desorption process being labelled as a mild supersonic expansion.

1.1 References

- (1) Faubel, M.; Schlemmer, S.; Toennies, J. P. *Zeitschrift Fur Physik D-Atoms Molecules and Clusters* **1988**, *10*, 269.

Chapter 2. Experimental Technique

Design and Implementation of a TOF- MS with Liquid Micro-Jet Source

2.1 Introduction

A Time-of-flight Mass spectrometer (TOF-MS) was designed and built for the express purpose of performing mass spectrometry and laser spectroscopy on molecules liberated from an *in vacuo* liquid surface. The experiments performed here focus specifically on neutral organic molecules (e.g. benzene) leaving the surface of an ethanol/water solution. The liquid surface is presented to the vacuum in the form of a high-speed thin liquid filament or liquid ‘micro-jet’. Once in the vacuum, the molecules leave the liquid surface either by the natural process of evaporation or are stimulated by a laser desorption technique. In the gas phase, these molecules are interrogated by a combination of mass spectrometry and laser spectroscopy. The following sections outline the design of the mass spectrometer, highlighting the special features required for producing and studying neutral molecules liberated from the *in vacuo* liquid micro-jet (L μ J).

2.2 Apparatus

The L μ J TOF-MS is illustrated in Figure 2.1. The TOF-MS consists of a large ‘Source’ chamber in which the L μ J injection system and ion acceleration electrodes are housed. Adjacent to the Source Chamber is the Ion Drift Tube – a region free of electric fields which would disturb an ion’s trajectory on the way to the detection system.

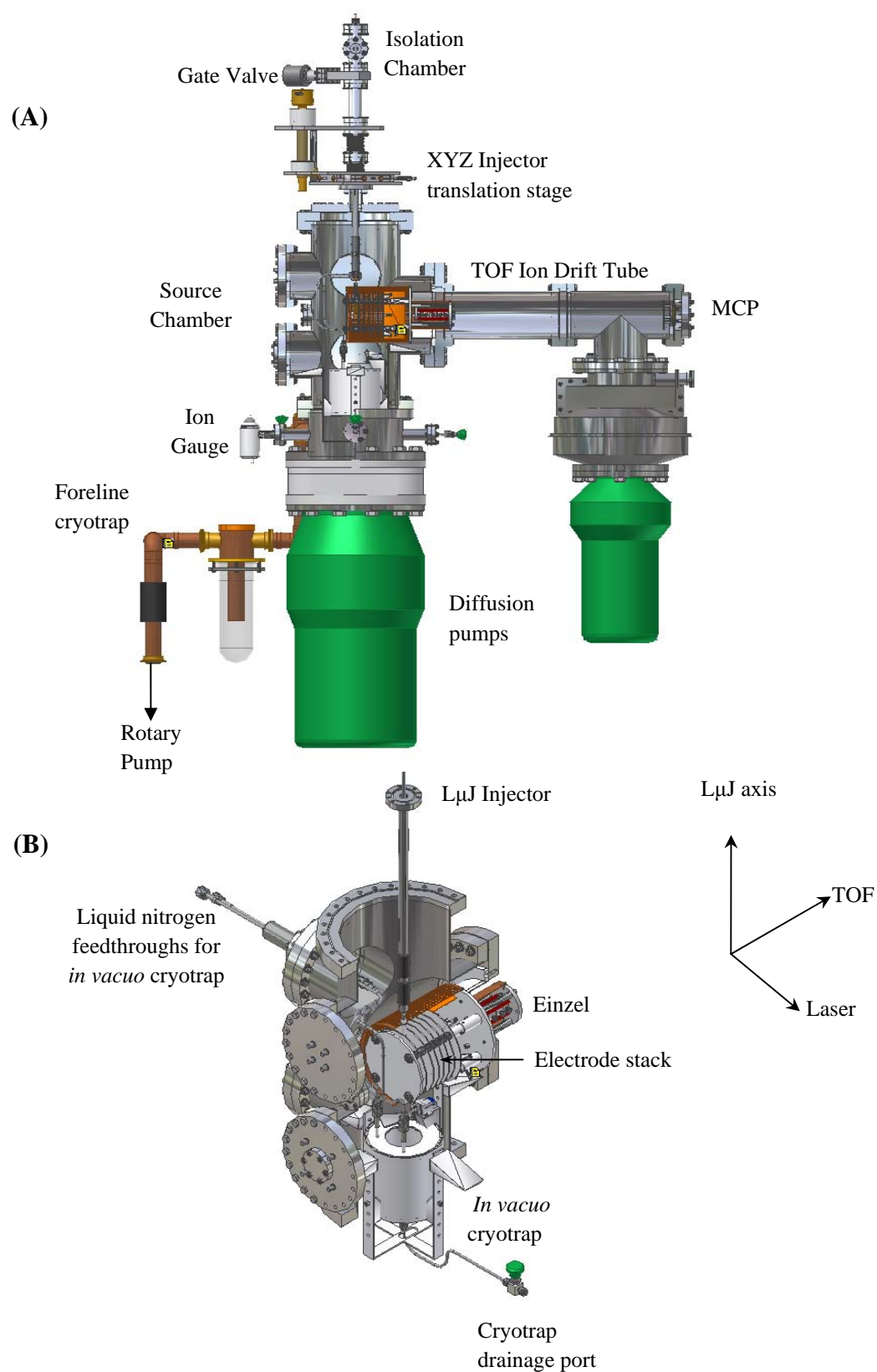


Figure 2.1: (A) Assembly drawing of the TOF-MS used for the reported experiments. (B) Isometric view of the Source Chamber of the TOF-MS.

The entire Liquid Injection System is mounted on an XYZ translation stage. This is used to position the jet in the centre of the chamber and along the TOF axis. A small isolation vacuum chamber is mounted on top of the translation stage and isolated from the Source Chamber via a small gate valve. The injector is first introduced into this small chamber at atmospheric pressure with the jet flowing. The chamber is then evacuated by a mechanical pump before a gate valve is opened so that the injector can be inserted into the Source Chamber. The use of the Isolation Chamber means that the flowing jet can be introduced or removed from the Source Chamber without the requirement of bringing the whole Source Chamber up to atmospheric pressure. The jet cannot be made to start flowing whilst inside the evacuated Source Chamber since the stationary liquid inside the tip freezes, preventing the jet from forming properly, if at all. The use of the Isolation Chamber proves to be greatly beneficial if the injector has to be removed several times from the Source Chamber during the course of an experiment.

After travelling vertically for 15 cm in the evacuated Source Chamber, the jet of solution reaches a cryotrap. Freezing out of the excess liquid is essential to keeping the working pressure of the system low. A mechanical chopper regularly sweeps across the top of the cryotrap removing any icicles that grow back toward the injector and block it.

The Source Chamber is evacuated by two diffusion pumps. The cryotrap sits directly above the mouth of a 1600 L.s⁻¹ diffusion pump (VHS-10) and the secondary diffusion pump (VHS-6) beneath the electrode assembly. Both diffusion pumps are backed with rotary pumps and an in-line cryotrap sits in the foreline of the Source Chamber pumping system to reduce the amount of high volatility vapour entering the rotary pump. The operating pressure in the Source Chamber is typically between 2-8x10⁻⁶ Torr depending upon the jet composition and diameter. Without the jet flowing the Source Chamber base pressure is typically ~5x10⁻⁷ Torr.

Molecules evaporate (or desorb) radially from the $L\mu J$ surface, but only those with a velocity component along the TOF axis reach the detector. The detector is a dual micro-channel plate (MCP) ion detector (El Mul MCP-M585) shielded from the TOF region by a grounded nickel mesh. Typical voltages of 2 KV are placed across the micro-channel plates. The output of the MCP is directed into a digital oscilloscope (LeCroy Model 9350AM, 500 MHz) and the resultant mass spectra downloaded to a computer. The communication programs between oscilloscope, laser and computer systems were designed and written in our laboratory. The schematic layout of the experimental apparatus is illustrated in Figure 2.2.

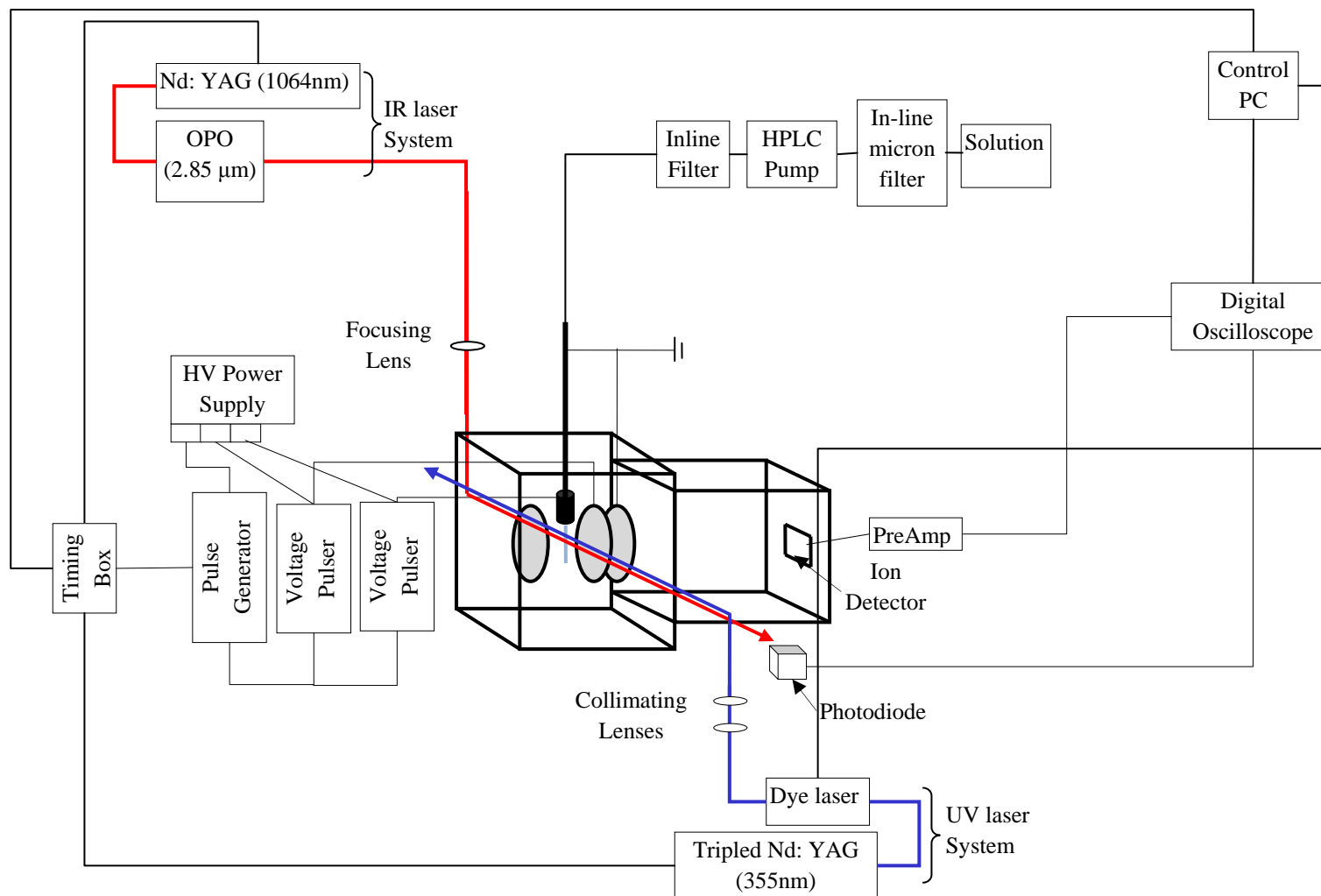


Figure 2.2: Experimental setup for performing absorption spectroscopy of molecules IR desorbed or evaporating (only UV laser employed) from a μJ . The inline bubble filter before the HPLC pump acts to degas the solution, collecting any bubbles that may try to enter the system.

2.3 Creating an *In vacuo* Liquid Micro-jet

When a liquid surface is exposed to the vacuum, the endothermic process of evaporation occurs at a fast rate causing the liquid to freeze. However, if the exposure time of the surface to the vacuum is kept short and the number for gas-phase collisions kept to a minimum, then stable *in vacuo* liquid surfaces can be created [1]. In the experiments reported here, the L μ J is produced by forcing liquid at high pressure through a tapered silica capillary with an exit aperture of typically 15 μ m in diameter (New Objective Pico Tip Emitter, coated SilicaTip, P/N:FS360-75-15-N), see Figure 2.3(A). Platinum apertures are commonly used by other groups but we have found capillaries to be more favourable because, although they are not as mechanically strong as the apertures, they are cheaper, can be unblocked more easily and typically produce a stable jet of greater length. The SilicaTip capillary is typically cut to a length of \sim 3 cm for ease of handling.

Figure 2.3(B) shows the diffraction of a UV laser beam from an *in vacuo* L μ J. Diffraction of the laser light is only observed when the jet is a stable filament. The diffraction patterns are visible for 2-3 cm downstream from the tip of the capillary which indicates the length of the laminar flow region for the micro-jet. Analysis of the diffraction pattern shows that at these downstream distances the diameter of the jet is the same as that of the exit aperture (see Figure 2.4). The distance at which the jet starts to disintegrate is directly proportional to the jet diameter to the power of 1.5 and the jet velocity whilst being inversely proportional to the square root of the surface tension [2,3]. In the experiments reported here, ethanol was added to the solution not only to solubilise the organic analyte, but its addition also lowered the surface tension of the solution, helping to stabilise the L μ J.

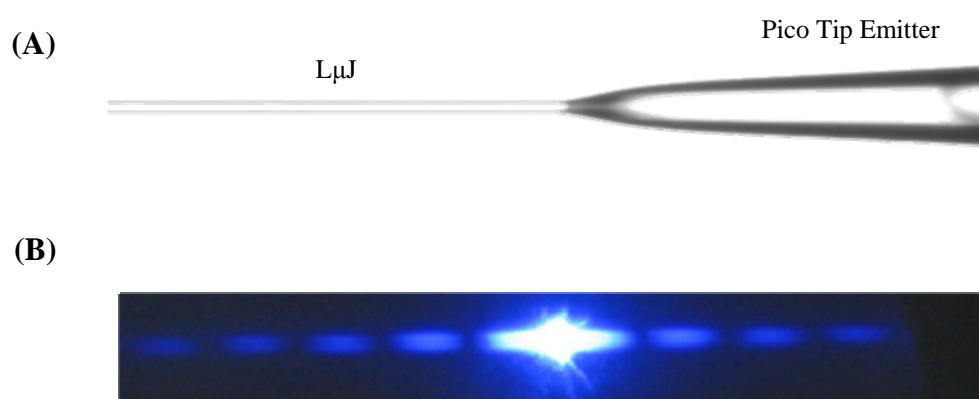


Figure 2.3: (A) Photograph of a L μ J created by a solution passing through a Pico Tip Emitter at atmospheric pressure. The exit aperture of the capillary is 15 μ m in diameter. The long stable, laminar flow region of the jet is illustrated here, and continuous for over 6 cm. Shorter laminar flow distances, typically 2-3 cm, are observed under high vacuum conditions. (B) Observation of the diffraction pattern produced when the UV laser is incident upon the stable *in vacuo* liquid filament. The diffraction patterns were viewed on fluorescent card at the exit to the chamber. Observation of a stable diffraction pattern is used to align the UV onto the centre of the jet.

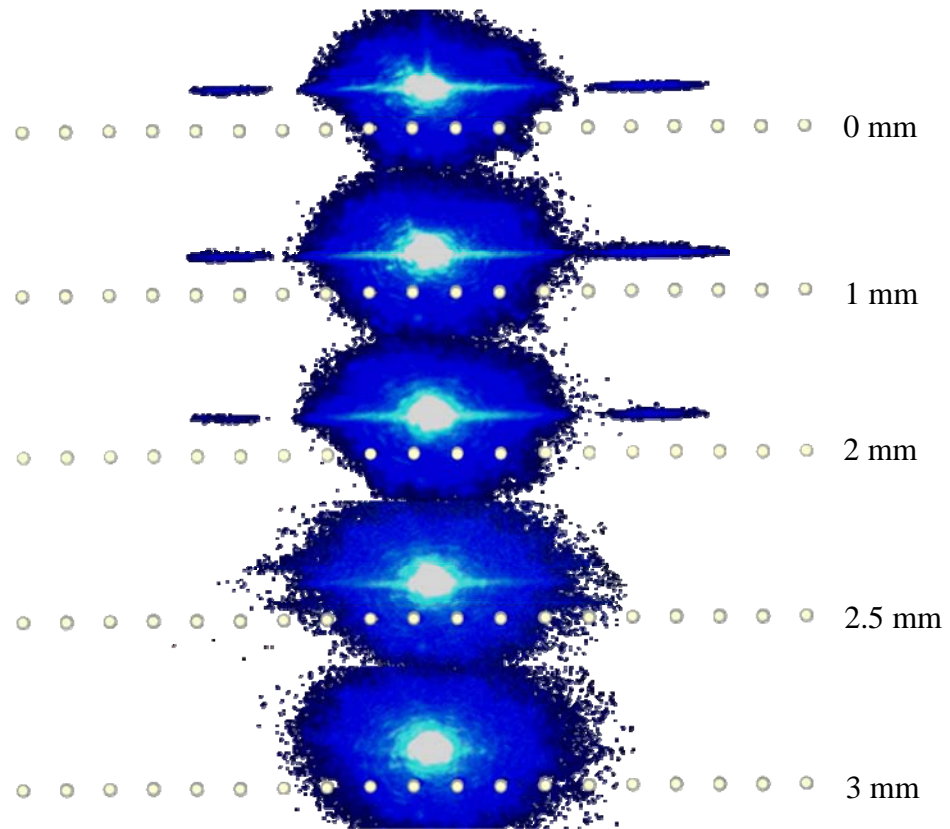


Figure 2.4: Diffraction patterns produced when the UV laser is incident upon the *in vacuo* L μ J at increasing distance from the capillary orifice. The diffraction patterns were viewed on a fluorescent card at the exit to the Source Chamber. The black background has been removed from each image so that the diffraction bands can be clearly seen. The white dots are equally spaced marks that have been included to help in the comparison of the length and position of each diffraction band. The diameter of the L μ J dictates the distance between the diffraction bands. In this example, the diameter of the jet appears to remain constant between 0-2 mm. The diffraction pattern is absent at a distance of 2.5-3 mm from the orifice - indication that the L μ J has begun to disintegrate at this distance.

The capillary is attached to 1/16" stainless steel tubing by a compression sleeve inside a PEEK union (Upchurch Scientific, Microtight Adapter, P770). The solution is pumped through the injection system using a HPLC pump (Dionex P680) at pressures of typically (200-500 psi) for a 25% v.v. ethanol solution - achieving a flow rate of 0.25 mL.min⁻¹. For the 15 µm diameter capillaries this flow rate equates to a liquid velocity of ~24 m.s⁻¹. At this velocity, laminar flow is established within the capillary which ensures that a stable jet exits the aperture. The requirement for the establishment of laminar flow is that the Reynolds Number, R_e , be less than 2000. The Reynolds number is defined as [4]:

$$R_e = \frac{2r\bar{u}\rho}{\eta}, \quad \text{Equation 2.1}$$

where \bar{u} is the average speed of the fluid, ρ the fluid density, η the fluid viscosity and r is the radius of the capillary. For the experimental conditions reported here, the Reynolds number for fluid flowing at 24 m/s within a 15 µm diameter capillary is 354. This is sufficiently low enough to ensure that the flow of liquid exiting the capillary is laminar.

The HPLC is routinely flushed with isopropanol after experiments to rinse and wet the surface of the internal components of the HPLC. The main components of the solutions (i.e. ethanol and water) are vacuum filtered separately using a 0.2 µm pore size nylon filter (Pall, Nylaflo, P/N:66602) before mixing. Separate pre-filtering is required since the different volatilities of the components results in a change in the volume ratio if the solution is vacuum filtered with the components mixed. Filtering also successfully degasses the solution which prevents bubbles forming in the pump and adversely affecting the flow rate.

2.4 One-colour Resonant Two Photon Ionisation (1+1 R2PI)

In vacuo L μ J have been successfully created from aqueous solutions containing both neutral [5-11] and charged [12-17] analytes. In the experiments outlined herein, the molecules of interest are neutral in solution and remain so when they are ejected into the vacuum. The analytical technique of Time-Of-Flight Mass spectrometry is only sensitive to charged particles since it works to separate and identify species according to their mass-to-charge ratio. Consequently, the liberated molecules must be ionised in order to be detected. This is achieved by directing an ionising laser beam into the Source Chamber perpendicular to both the L μ J and TOF axes (see Figure 2.2). Since molecules desorb radially from the jet surface, only those that pass through the ionisation volume of the laser and with a velocity component along the TOF axis are ionised and detected.

The ionisation technique used here is known as Resonant Two-Photon Ionisation (R2PI) (see Figure 2.5). Discrimination between different molecules of the same mass becomes possible when the molecules are selectively ionised by the resonant absorption of photons. In contrast to collisional ionisation techniques, R2PI is described as “soft”, since at low fluences the photon absorption can result in minimal fragmentation of the parent mass. The probability of a molecule absorbing two photons depends upon the absorption coefficients of the first and second steps as well as the lifetime of the intermediate state [18]. The absorption coefficients for each step are dependent upon the degree of overlap between vibrational wavefunctions in the initial and final states (Frank Condon Factor (FC)) and transition selection rules [19].

When the energy of the first absorbed photon is resonant with an electronic transition to a stationary state, the probability of absorption of the second photon is increased dramatically, since the lifetimes of these states can be quite long. If absorption of a second photon does not occur, then the molecules relax into the high vibrational levels of the ground state by radiative or non-radiative processes. In the studies reported herein benzene is the primary chromophore

and the first absorption step is always into the ${}^1B_{2u}$ electronic state*. Selinger and Ware report stationary state lifetime of ~ 80 ns within ${}^1B_{2u}$ [20]. This lifetime is much larger than the duration of the 7 ns laser pulse so absorption of a subsequent photon is likely. If the absorption of the second photon takes the energy of the excited electron above the ionisation potential (IP) of the molecule then the electron dissociates and the molecule is left as a cation.

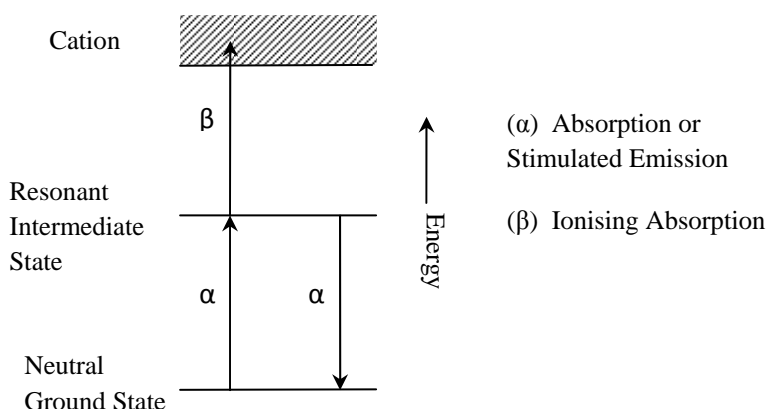


Figure 2.5: Scheme for resonant photon absorption. The probability of photon absorption is high when the energy of the photon is equal to the transition energy to a resonant intermediate state. The longer lifetimes of resonant intermediate states compared with virtual intermediate states increases the probability of absorbing a second photon. If the second photon is the same colour as the first then stimulated emission from the resonant intermediate state can occur instead of absorption. In the absence of collisional deactivation or other non-radiative relaxation processes, fluorescence can also be observed starting from the original resonant intermediate state. In the low pressure conditions inside the TOF-MS collisional deactivation is minimal. Boesl has found the absorption cross-sections, σ_{α} and σ_{β} , for benzene are 2.7×10^{-17} and 3.4×10^{-18} cm², respectively [18].

* The spectroscopy specific to benzene is discussed in greater detail in Chapter 3.

As a cation the molecule can now be detected by mass spectrometry[†]. The probabilities of transitions into the manifold of cationic states are also subject to selection rules and a FC factor. For this reason absorption spectra generated by monitoring the fluorescence yield after absorption to the intermediate state may differ slightly from absorption spectra generated by monitoring R2PI products. In this study the ionisation of benzene is possible using two one-colour photons of wavelength ~260 nm (1+1 R2PI) since the energy of the electronic state, $^1B_{2u}$, is more than half way to the IP.

In general, the two-photon absorption cross-section is strong for benzene in the ultra-violet region around 260 nm - especially considering the transitions we are observing are electronically forbidden [18]. As a result, care was taken to ensure that the photon flux did not saturate the absorption process as this would result in a distortion of the resultant absorption spectrum. Saturation occurs when the magnitude of the population of molecules that have been excited to the resonant intermediate state approaches that which remains in the ground state. Since the rate at which molecules can be stimulated to emit energy and return to the ground state is equal to the reverse process of absorption (see Figure 2.5), when the system is saturated adding more photons to the system does not increase the chance of a second photon being absorbed. Consequently, when a system is completely saturated, the probability of ionisation no longer has a quadratic dependence on laser power. Boesl *et al* showed that benzene saturates at laser intensities greater than 10^7 W.cm⁻² for a two-photon process [18]. Figure 2.6 illustrates the intensity of benzene ion signal observed as a function of laser fluence in our system. The deviation from quadratic photon flux signal dependence was observed above 9×10^6 W.cm⁻². This is considerably larger than the saturation intensity of $\sim 10^4$ that Riedle observed for one-photon transitions in benzene [22] but is consistent with Boesl's

[†] Chewter *et al* found the Ionisation Potential of benzene to be 74555 cm⁻¹ (21) Chewter, L. A.; Sander, M.; Mullerdethlefs, K.; Schlag, E. W. *Journal of Chemical Physics* **1987**, *86*, 4737.

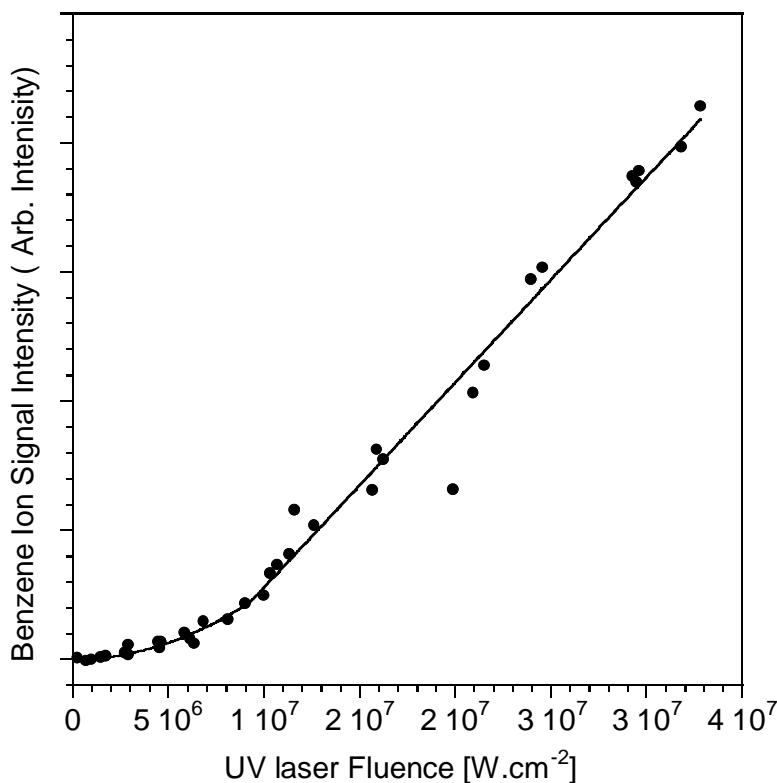


Figure 2.6: Intensity of benzene parent ion signal produced by R2PI via the 6^1 resonant intermediate state. The wavelength of the ionising laser was 258.93 nm and the laser collimated into a spot with FWHM of ~ 150 μm . At fluences below 9×10^6 $\text{W}\cdot\text{cm}^{-2}$ the ion signal displays a quadratic dependence on the fluence of the UV laser. Above this value the photon absorption process is saturated reducing the relationship to a direct proportionality between ion signal and UV fluence. This saturation point is consistent with 1×10^7 $\text{W}\cdot\text{cm}^{-2}$ reported by Boesl *et al* [18].

report for R2PI [18]. All experiments performed here employed fluences under the observed saturation threshold of $9 \times 10^6 \text{ W.cm}^{-2}$.

When the photo-ion current of a particular mass is monitored as a function of the frequency of the absorbed photons, an absorption spectrum of the molecule is mapped out. This simple variation of the TOF-MS technique allows us to distinguish between structural isomers as well as study electronic spectra free from poisoning species such as isotopologues. For example, combining TOF-MS with laser spectroscopy allows us to generate the UV spectrum of $^{12}\text{C}_6\text{H}_6$ independently of $^{13}\text{C}^{12}\text{C}_5\text{H}_6$. The addition of laser spectroscopy adds another dimension to the analytical capabilities of mass spectrometry.

2.5 Time-of-Flight Mass Spectrometry

A TOF-MS was designed and built specifically for use with the $\text{L}\mu\text{J}$ source. The advantages of Time-of-Flight Mass Spectrometry include its ‘unlimited’ mass range[‡] and high duty factor[§] which make for a very versatile analytical instrument [23]. When a uniform electric field is created between two electrodes a positively charged particle will travel toward the electrode with the lower potential. Newton’s second law of motion states that the acceleration the particle experiences in the uniform electric field is proportional to both its mass and its charge. This means that ions that start at the same position within an electric field but have different mass-to-charge ratios will reach zero potential at different times. It is this phenomenon that allows for the temporal separation and consequent identification of different masses within a TOF-MS experiment. For best overall mass resolution ($M_{S,\theta}$) both spatial (M_S) and velocity (M_θ) resolution must be considered since [24]:

[‡] The mass range is in fact only limited by the signal resolution obtainable.

[§] Duty Factor is the percentage of ions formed that are actually detected.

$$\frac{1}{M_{S,\theta}} = \frac{1}{M_S} + \frac{1}{M_\theta} . \quad \text{Equation 2.2}$$

The design of the electrode assembly used in this study was based upon the Wiley-McLaren setup [24,25]. This involves a two-stage ion source with electrode potential chosen such that first-order focusing conditions are produced. The relationship below describes the conditions required for first-order spatial focusing of the ion packet [24]:

$$D = 2S_0K_0^{3/2} \left[1 - \frac{1}{\left[K_0 + K_0^{1/2} \right] S_0} d \right] , \quad \text{Equation 2.3}$$

where D is the length of the field-free drift region, d is the length of the second stage of the electrode assembly, S_0 is the ion start position within region s (see Figure 2.7). Furthermore,

$$K_0 = \frac{S_0E_s + dE_d}{S_0E_s} , \quad \text{Equation 2.4}$$

where E_x is the electric field strength across stage x .

Two-stage sources have the advantage that the space focus of the ions can be tuned by changing the ratio E_s / E_d (see Figure 2.7). First order focusing conditions were chosen since the position of the space focus can be changed more dramatically than with second order focusing. This flexibility of space focus position means that extensions such as a reflectron

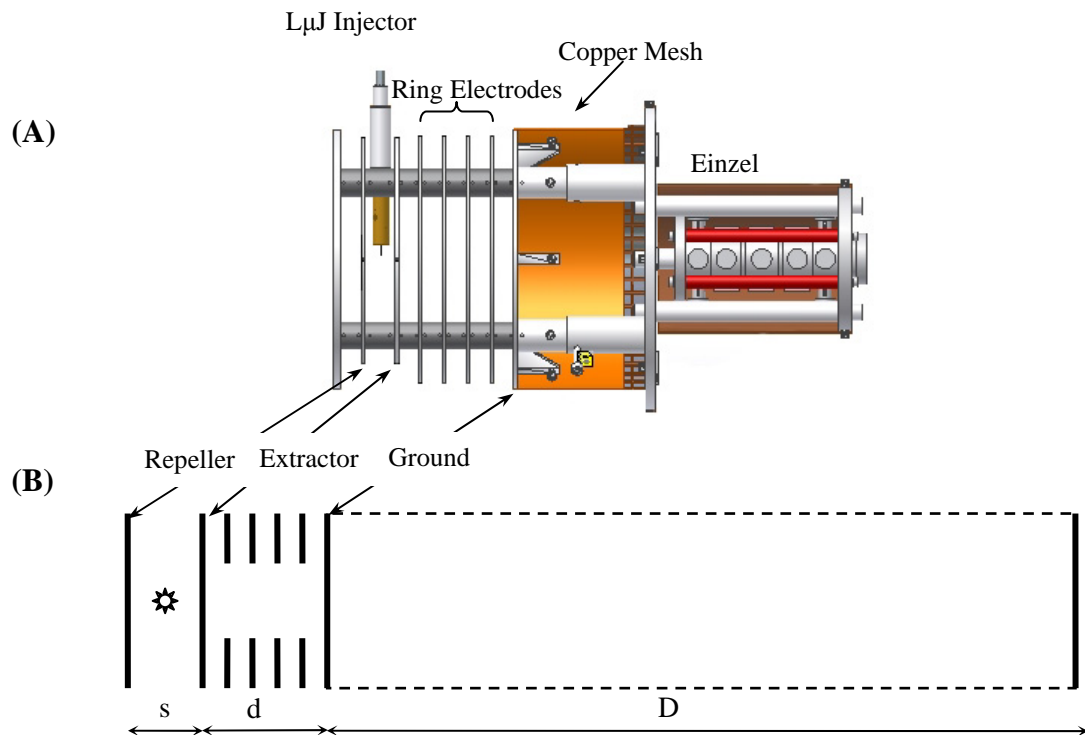


Figure 2.7: (A) Assembly drawings of the electrode stack designed to be used with the L μ J injector. The different stages of the assembly have the following dimensions: (s) has a length of 18 mm, (d) a length of 70 mm and (D) a length of ~ 1 m. The brass, cone-shaped cap that covers the protruding L μ J capillary has not been included in the assembly drawings. (B) Schematic of a 2 stage acceleration stack. E_x ($\text{V}\cdot\text{mm}^{-1}$) is the electric field strength across the stage x . The ions are created in the first stage, (s), and accelerated by E_s toward the second stage, (d). Further acceleration in (d) pushes the ions into the field-free flight tube, (D). When the ions reach the end of (D) they are detected. Tuning of E_s/E_d can force the space focus to occur at the point of detection (see text for details).

could be added to the system. Computer simulations aided the design of the assembly to maximise the resolution of a masses produced from the L μ J source [26].

The length of the Ion Drift region (D) was set at approximately 1m. Repeller and extractor plates are circular electrodes of diameter 200 mm and are separated by 18 mm - the distance dictated by the fact that the L μ J injector must sit between these two electrodes. The lower halve of both these electrodes was removed so that if the L μ J begins to spray there is no chance of icicles forming on the electrodes and distorting the electric fields. Simulation of the ion trajectories showed no significant perturbation of the ion trajectories when the cut-outs of the electrodes were introduced. The whole electrode assembly was surrounded by copper mesh with a small opening for the injector to enter and the L μ J to exit. Without the mesh it was observed that the large amount of ice that collects in the cryotrap could cause a decrease in the observed ion signal by building up a charge and perturbing the field between the electrodes.

The temporal and spatial spread of same mass ions as they reach the end of the field-free drift region determines the mass resolution of the instrument. The best mass resolution is achieved when there is baseline separation between adjacent mass peaks and the spread (Full Width Half Max) of the ion signal is small. The mass resolution of a TOF-MS is dependent upon several factors – most dramatically the spatial, temporal and velocity (energy) distribution of the ions when they are placed in the electric field. The spatial distribution of same mass ions born inside an electric field collapses to a minimum at the space focus of a TOF-MS. Ions which are born far from the zero potential will experience the accelerating force over a longer distance than those born closer to the zero potential. Consequently ions that are born far from the zero potential will achieve a greater energy and faster final velocity than those born closer to the zero potential. As the ions travel through the field-free Ion Drift Region, the faster ions will catch up to the slower ions – this point in space is called the space focus. By placing the

detector at the space focus the impact on mass resolution caused by the initial spatial distribution can be minimised, as all the ions of the same mass will be detected simultaneously. Initial spatial distribution effects are also minimised by creating the ions in the smallest region possible. When using a laser to ionise the molecules within the electric field this is usually achieved by focusing the laser spot to a minimal beam waist. However, care must be taken to keep the photon density low enough so that the ion packet does not expand due to space-charge repulsion, as this would further degrade the resolution [25].

The temporal distribution at ion birth within an electric field has a minimal effect on resolution if the length of time in which the ions are created is much shorter than the ideal final separation of the ion packets at detection. The use of nanosecond laser pulses to ionise the molecules within the electric field creates a negligible temporal distribution of the ion packets compared to the microsecond timescale over which the different ion masses are finally detected.

As with Matrix Assisted Laser Desorption/Ionisation (MALDI), the major factor limiting the resolution for ions emerging from a $L\mu\text{J}$ source is the large initial velocity distribution [27,28]. An initial velocity distribution of ions results in a temporal broadening of the ion signal at the detector. When a skimmed supersonic expansion is used as the source of a TOF-MS, the spread in initial molecular velocities is very small, resulting in a translation temperature of a few Kelvin [29] (Figure 2.8). Consequently velocity distribution effects on the mass resolution are minimal. Although not firmly established, the distribution of velocities leaving the surface of a $L\mu\text{J}$ are reported to be much greater than a purely gas phase expansion.

Faubel's studies of water evaporating from a $15\ \mu\text{m}$ diameter *in vacuo* water micro-jet found a velocity spread of the molecules which could be represented by a translational temperature $\sim 130\ \text{K}$ [1]. Hydroquinone molecules photo-desorbed from a $L\mu\text{J}$ surface were reported by Otten *et al* to have a translational temperature of $\sim 350\ \text{K}$ [7].

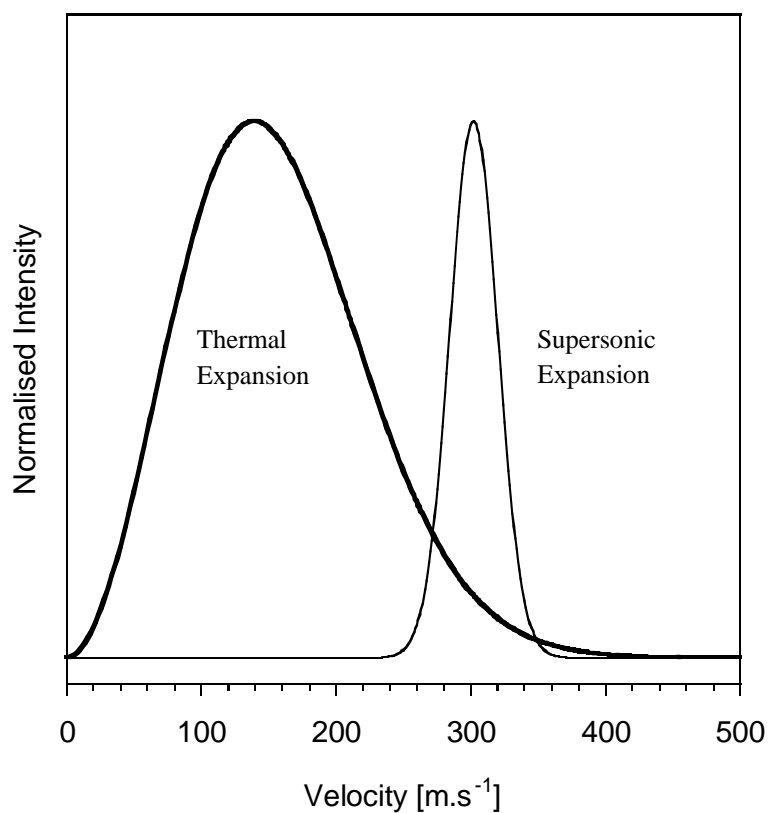


Figure 2.8: Demonstration of the difference between Maxwellian velocity distributions typical of a supersonic expansion (3K, 300 m.s⁻¹ bulk velocity) and the thermal distribution of molecules photo-desorbed from a 1 μ J (350 K, no bulk velocity). It is expected that higher desorption laser fluences will increase the flux of desorbed molecules and thus increase the number of gas phase collisions. This phenomenon would tend to narrow the molecular velocity distribution to a hybrid between that of a supersonic and of a thermal expansion.

In the extreme example of ions travelling away from the detector just prior to the electric field being created, the ions must first be decelerated by the electric field then re-accelerated in the right direction before they can hit the detector. The time taken for the turn-around is called the lag-time and is proportional to the initial velocity of the ion away from the detector [24,25]. This lag-time manifests as a temporal spacing between the two ions at the zero potential position. At the point of detection, the ions that have been turned around cause a temporal tailing of the ion signal. A technique called Time-lag Focusing developed by Wiley and McLaren can be employed to address this problem [25,27,30,31]. The technique is described in detail in Figure 2.9. Essentially, tuning of the time between ionisation and ion extraction (creation of the electric field) can achieve a focusing effect of the ion packet.

In the experimental setup used here, the ionising laser is placed between the $L\mu\text{J}$ surface and the ion detector. As such, the extreme example of ions travelling away from the zero potential would not be encountered since, with this setup, only molecules that are ejected from the liquid surface with a velocity component aimed toward the detector can be ionised and potentially detected. However, Lag-time focusing was found to still have a positive effect on the mass resolution for the $L\mu\text{J}$ source.

The Time-lag delay technique is performed here by simultaneously increasing the voltage on the Repeller electrode and the brass cap surrounding the Injector after a set delay from the firing of the ionisation laser. Initially, the Repeller, Injector and Extractor electrodes are all held at +2 kV. The repeller and injector are then pulsed up to +2.4 kV and +2.2 kV, respectively, by high voltage pulsing units (DEI, PVM-4140 +/- 3KV Pulser Module). The timing between laser firing and electrode pulsing is controlled by a digital delay generator (Griffith University, TARDIS II). The extractor electrode is maintained at 2 kV and is resistively linked via four ring electrodes to ground. The purpose of the ring electrodes is to

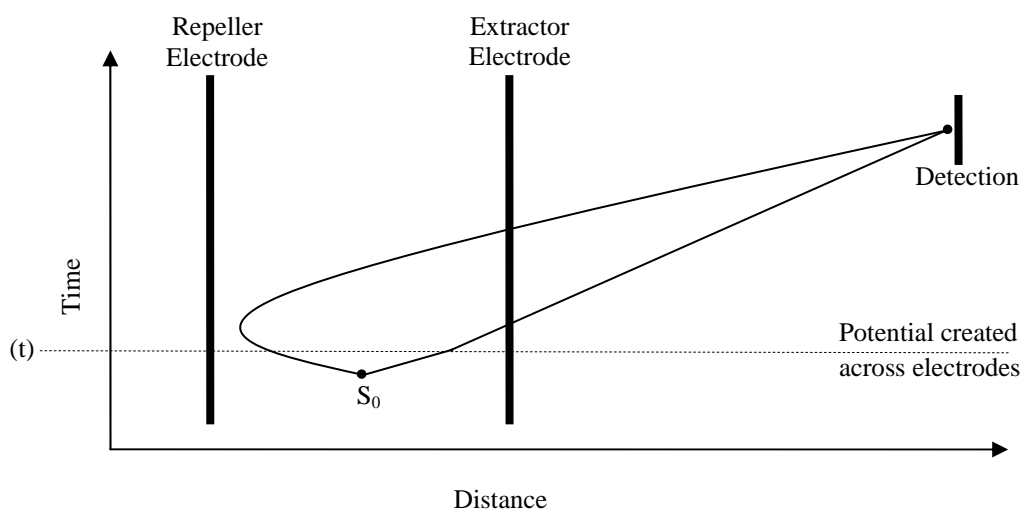


Figure 2.9: Illustration of Time-lag Focusing. Two same mass positive ions are born at position S_0 . Initially they are travelling in opposite directions but once a potential is created across the electrodes at time (t), the ion travelling toward the higher potential, Repeller electrode is forced to turn around. The closer this ion gets to the repeller electrode before the potential is applied, the faster the velocity of the ion will be when it passes S_0 again. At some point later this 'turn-around' ion will catch-up to the other ion – eliminating the effect of the initial velocity differences on the resultant resolution. The optimal delay between ion creation and extraction is dependent upon the initial relative kinetic energies of the molecules.

help maintain a smooth potential gradient over the large distance from extractor plate to ground.

Figure 2.10 shows the effect of Time-lag focusing on the ion mass peak produced from evaporating benzene molecules. The mass resolution, seen as a decrease in peak width, changes with delay time. In this example the maximum resolution is achieved at 1500 ns. However, at large time delay a slow shoulder appears on the mass peaks, distorting the shape from Gaussian. This distortion is attributed to fast moving ions that have been able to travel past the extractor plate into the second acceleration region, (d), before the extraction voltage is applied. These ions do not experience the same accelerating voltage as those left behind in the first extraction region, (s), and so are detected later in the TOF mass spectrum. This phenomenon is a consequence of the broad velocity distribution of molecules leaving the μJ . The delay times used in the experiments performed here are a compromise between mass resolution and minimisation of the mass peak distortion. A future modification to the electrode assembly used here would be to increase the length of the first acceleration region, (s), so that all the ions remain inside the region before the extraction pulse is applied.

The delay between ionisation and ion extraction that achieves the best focusing is slightly different for each mass and as a consequence a particular Time-lag Delay works well over only a limited mass range. For the majority of experiments discussed here this is not an issue since only baseline separation of the benzene parent mass peak and its carbon-13 isotope is routinely required. The optimum time delay for focusing should also vary according to the conditions at the time of ion creation. However, in practise it was found that both the evaporation and desorption experiments typically use Time-lag Delays of $\sim 0.5 \mu\text{s}$.

The disadvantage of applying a voltage directly to the μJ injector is that electrolytic solutions (for example, strong acids or salt solutions) cannot be flowed through the system

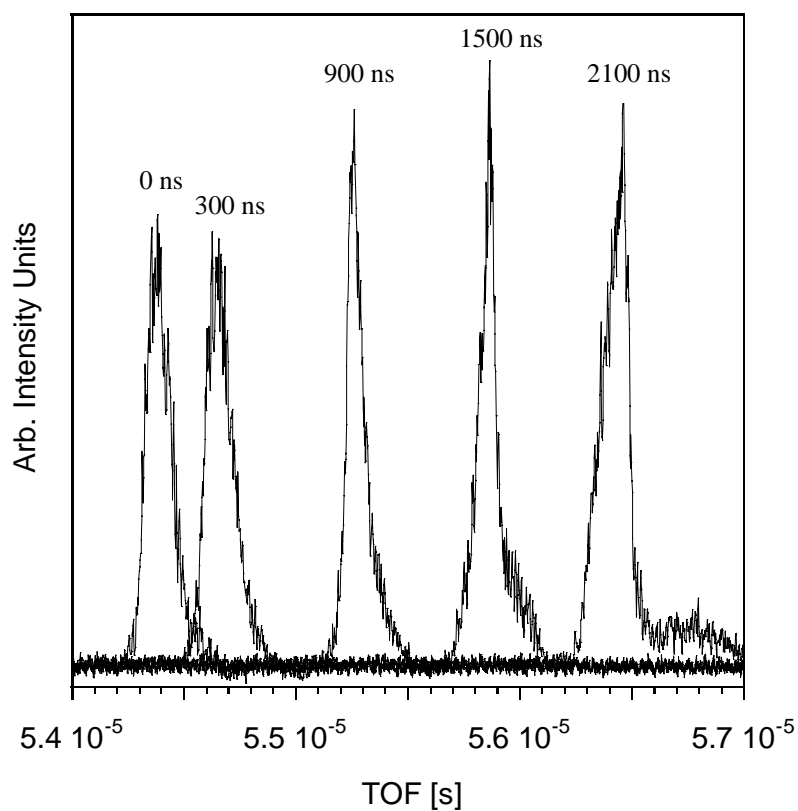


Figure 2.10: Demonstration of the changing shape of a single mass peak (m/z 78 - benzene monomer) as a function of Time-lag Delay. The mass spectra here are produced by benzene molecules that have evaporated from the surface of an *in vacuo* L μ J.

since they conduct electricity up the length of the injector. It was found that when a voltage is applied there is electrical arcing between different parts of the injector followed by the joints of the injector exploding apart. The explosions would usually produce carbonaceous material inside the silica capillary. Also, when the jet of the electrolytic solution passes through the electric field, electrostatic forces on the aqueous ions cause the jet to disintegrate into a spray. However, if the length of time for which the electric field is applied is short, then jets of weakly electrolytic solutions were found to be stable within the region of the electrodes. In the experiments reported here, the voltage on both the repeller and extractor electrodes are pulsed on for only $\sim 1.25 \mu\text{s}$ - just enough time for the ions to be accelerated into the second ionisation region.

An einzel and ion deflectors were also included in the experimental setup; positioned after the electrode assembly. An einzel is designed to spatially focus the ion packet perpendicular to the flight trajectory. In practise, however, the einzel showed no positive effect on the intensity on the ion signal recorded by the detector, which implies that the dimensions of the ion packet at the space focus was smaller than the active face of the detector.

Vertical deflection of the ions away from the TOF axis can also jeopardise mass signal intensity. The $L\mu\text{J}$ surface is travelling at $\sim 24 \text{ m}\cdot\text{s}^{-1}$ ** inside the vacuum, so molecules that leave the surface will likely retain a component of their velocity parallel to the $L\mu\text{J}$ axis. However, when the molecules are accelerated along the TOF axis by the applied potential gradient, this vertical component of the velocity becomes negligible. The main factor which proved to perturb the ion trajectory in the vertical direction was the presence of the asymmetric injector between the Repeller and Extractor electrodes. However, tuning of the voltage on the injector relative to the electrodes allowed the ions to be steered onto the face of

** The surface velocity is $\sim 24 \text{ m}\cdot\text{s}^{-1}$ for a $15 \mu\text{m}$ jet flowing at $0.25 \text{ mL}\cdot\text{min}^{-1}$.

the detector and the mass signal maximised. In this was the injector acts as a more effective ion optic than the ion deflectors located after the einzel.

2.6 References

- (1) Faubel, M.; Schlemmer, S.; Toennies, J. P. *Zeitschrift Fur Physik D-Atoms Molecules and Clusters* 1988, 10, 269.
- (2) Kowalewski, T. A.; Hiller, W. J.; Behnia, M. *Physics of Fluids A* 1993, 5.
- (3) Collantes, G. O.; Yariv, E.; Frankel, I. *Journal of Fluid Mechanics* 2003, 474, 95.
- (4) Giancoli, D. C. *Physics*, 3rd ed.; Prentice-Hall International: London, 1991.
- (5) Faubel, M.; Steiner, B.; Toennies, J. P. *Journal of Chemical Physics* 1997, 106, 9013.
- (6) Maselli, O. J.; Gascooke, J. R.; Kobelt, S. L.; Metha, G. F.; Buntine, M. A. *Australian Journal of Chemistry* 2006, 59, 104.
- (7) Otten, D. E.; Trevitt, A. J.; Nichols, B. D.; Metha, G. F.; Buntine, M. A. *Journal of Physical Chemistry A* 2003, 107, 6130.
- (8) Wilson, K. R.; Rude, B. S.; Smith, J.; Cappa, C.; Co, D. T.; Schaller, R. D.; Larsson, M.; Catalano, T.; Saykally, R. J. *Review of Scientific Instruments* 2004, 75, 725.
- (9) Wilson, K. R.; Schaller, R. D.; Co, D. T.; Saykally, R. J.; Rude, B. S.; Catalano, T.; Bozek, J. D. *Journal of Chemical Physics* 2002, 117, 7738.
- (10) Winter, B.; Faubel, M. *Chemical Reviews* 2006, 106, 1176.
- (11) Holstein, W. L.; Hammer, M. R.; Metha, G. F.; Buntine, M. A. *International Journal of Mass Spectrometry* 2001, 207, 1.
- (12) Charvat, A.; Abel, B. *Physical Chemistry Chemical Physics* 2007, 9, 3335.
- (13) Kohno, J.; Toyama, N.; Buntine, M. A.; Mafune, F.; Kondow, T. *Chemical Physics Letters* 2006, 420, 18.
- (14) Saykally, R. J. *Abstracts of Papers of the American Chemical Society* 2004, 228, U243.
- (15) Faubel, M.; Kisters, T. *Nature* 1989, 339, 527.

-
- (16) Kondow, T.; Mafuné, F. *Annual Review of Physical Chemistry* 2000, 51, 731.
- (17) Charvat, A.; Lugovoj, E.; Faubel, M.; Abel, B. *European Physical Journal D* 2002, 20, 573.
- (18) Boesl, U.; Neusser, H. J.; Schlag, E. W. *Chemical Physics* 1981, 55, 193.
- (19) Harris, D. C.; Bertolucci, M. D. *Symmetry and Spectroscopy*; Dover Publications: New York, 1989.
- (20) Selinger, B. K.; Ware, W. R. *Journal of Chemical Physics* 1970, 53, 3160.
- (21) Chewter, L. A.; Sander, M.; Mullerdethlefs, K.; Schlag, E. W. *Journal of Chemical Physics* 1987, 86, 4737.
- (22) Riedle, E.; Knittel, T.; Weber, T.; Neusser, H. J. *Journal of Chemical Physics* 1989, 91, 4555.
- (23) Weinkauff, R.; Walter, K.; Weickhardt, C.; Boesl, U.; Schlag, E. W. *Journal of Physical Sciences* 1989, 44a, 1219.
- (24) Wiley, W. C.; McLaren, I. H. *The Review of Scientific Instruments* 1955, 26, 1150.
- (25) Guilhaus, M. *Journal of Mass Spectrometry* 1995, 30, 1519.
- (26) Dahl, D. A.; Delmore, J. E. *The Simion PC/PS2 User's Manual Version 4.0*; Idaho National Engineering Laboratory, 1988.
- (27) Damaschin, I. *International Journal of Mass Spectrometry* 2001, 206, 211.
- (28) Guilhaus, M.; Mlynski, V.; Selby, D. *Rapid Communications in Mass Spectrometry* 1997, 11, 951.
- (29) Miller, D. R. *Atomic and Molecular Beam Methods*; Oxford University Press: New York, 1991; Vol. 1.
- (30) Mafune, F.; Kohno, J.; Nagata, T.; Kondow, T. *Chemical Physics Letters* 1994, 218, 7.

- (31) Chandezon, F.; Huber, B.; Ristori, C. Review of Scientific Instruments 1994, 65, 3344.

Chapter 3. Spectral Simulation

Simulation of the ${}^1B_{2u} \leftarrow {}^1A_{1g}$ Gas Phase Absorption Spectrum of Benzene

3.1 Introduction

In this study we use benzene as a spectroscopic probe to explore the dynamics of a molecule leaving an *in vacuo* liquid surface. The features and shapes of bands that appear in a molecule's absorption spectrum are sensitive to the molecule's environment since the environment influences the molecule's internal energy distribution. By recording and analysing the absorption spectrum of a molecule as it leaves the liquid surface, we can start to learn about the interfacial environment. Benzene is an ideal candidate to use as a dynamical probe since its spectroscopy is extremely well characterised, and it has strong absorption cross-sections in regions which are easily accessible with modern laser systems. The shape of an individual rovibrational contour gives an indication of the rotational temperature on the molecules, including those which are vibrationally excited. Fitting of simulated spectra to those which are experimentally observed allows for the determination of the rotational temperature of the benzene molecules. The vibrational temperature of the molecules can also be determined by considering the changes in relative intensities of the rovibronic bands.

Section 3.2 is a detailed account of the spectroscopic theory required to simulate the rovibronic contours of a symmetric top. Simulation of the identified contours requires an understanding of the selection rules that determined the allowed rovibronic transitions, their energies and their relative intensities. Section 3.3 looks in detail at the results of simulating the absorption bands of benzene in the region $\sim 38400\text{-}38700\text{ cm}^{-1}$. In Section 3.4 a two-dimensional spectroscopic technique is introduced that allows for the refinement of

spectroscopic constants of bands that are overlapped in the absorption dimension. By fitting the simulated spectra to spectra obtained from gas phase benzene equilibrated at a known temperature, the value of several rotational constants and frequencies of vibrationally excited benzene are determined. The success of this procedure gives confidence to then fit the simulated spectra to those generated from the benzene molecules liberated from an *in vacuo* liquid surface and thus used to determine both rotational and vibrational temperature for these liberated molecules.

3.2 Theory of Optical Transitions

In general, a transition between two rovibronic wavefunctions, ψ'_{evr} and ψ''_{evr} , will occur with the absorption or emission of electromagnetic radiation if the matrix element between the two wavefunctions does not vanish. *i.e.*

$$\langle \psi'_{evr} | \boldsymbol{\mu}_A | \psi''_{evr} \rangle \neq 0, \quad \text{Equation 3.1}$$

where $\boldsymbol{\mu}_A$ is the component of the electric dipole along the ξ, η or ζ axis (see Figure 3.1). Here the subscript *evr* denotes the wavefunction as rovibronic. These axes belong to a co-ordinate system which is laboratory fixed with an origin at the centre of mass of the molecule. It is necessary to project the molecular co-ordinates onto the laboratory framework since molecular rotations cannot be observed within a molecule-based reference frame. Equation 3.1 is called a 'selection rule' since it describes the necessary relationship between two wavefunctions if an optical transition is to occur between them.

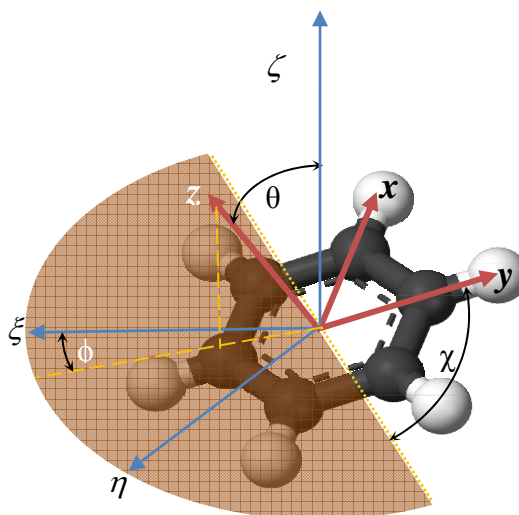


Figure 3.1: Reference frames for analysis of rotational and vibrational motion of benzene. The blue axes (ξ, η, ζ) are laboratory fixed axes with origin at the centre of mass of the molecule. The magnitude of the transition dipole vector, μ_A , along these axes is used in the rovibronic transition selection rules. The Euler angles (θ, ϕ, χ) are the angles between the laboratory fixed axis and the (x, y, z) molecule fixed axis. The magnitude of the transition dipole along the molecule's fixed axes is used when determining vibronic transition selection rules.

3.2.1 Selection Rules for Allowed Vibronic Transitions

Using the Born-Oppenheimer, harmonic oscillator and rigid-rotor approximations, rovibronic wavefunctions can be separated into their electronic, vibrational and rotational components*. This partitioning allows us to distinguish between the symmetry requirements for a purely vibronic or a rovibronic transition. Equation 3.1 can now be rewritten as:

$$\langle \psi'_e \psi'_v \psi'_r | \boldsymbol{\mu}_A | \psi''_e \psi''_v \psi''_r \rangle \neq 0 . \quad \text{Equation 3.2}$$

Here the subscripts e , v , and r refer to the independent electronic, vibrational and rotational wavefunctions. $\boldsymbol{\mu}_A$ is related to the component of the dipole along the molecule fixed axis, μ_α , ($\alpha = x, y$ or z) through the relationship [1]:

$$\boldsymbol{\mu}_A = \lambda_{xA} \mu_x + \lambda_{yA} \mu_y + \lambda_{zA} \mu_z , \quad \text{Equation 3.3}$$

where $\lambda_{\alpha A}$ are the direction cosine matrix elements that depend only upon the Euler angles (see Figure 3.1).

So the selection rule for a vibronic transition therefore becomes:

* Nuclear spin symmetries are not considered in this work since the dipole moment is independent of the spin coordinates (1) Bunker, P. R.; Jensen, P. *Fundamentals of Molecular Symmetry*; Institute of Physics Publishing: London, 2005.

$$\langle \psi'_e \psi'_v | \mu_\alpha | \psi''_e \psi''_v \rangle \neq 0. \quad \text{Equation 3.4}$$

A non-zero integrand will result if the symmetries of the wavefunctions involved, $\Gamma(\psi)$, satisfy one of the following conditions:

$$\Gamma(\psi'_e) \otimes \Gamma(\psi'_v) \otimes \Gamma(\psi''_e) \otimes \Gamma(\psi''_v) \supset \Gamma(\mu_\alpha) \equiv \{\Gamma(T_z) \text{ or } \Gamma(T_{x,y})\}, \quad \text{Equation 3.5}$$

since the component of the molecular dipole along the α molecular axis has the same symmetry as the translation operator, T_α .

Benzene is an oblate symmetric top of D_{6h} symmetry. In the D_{6h} point group the $\Gamma(T_z) \equiv A_{2u}$ and $\Gamma(T_{x,y}) \equiv E_{1u}$. Transitions between wavefunctions whose product is of A_{2u} symmetry are called parallel transitions since the dipole change is parallel to the principle rotation axis (z), and conversely wavefunctions whose product is of E_{1u} symmetry are called perpendicular transitions because the dipole change is perpendicular to the principle rotation axis (x or y).

The symmetries of the electronic states, $\Gamma(\psi_e)$, of neutral benzene are shown in Figure 3.2. The strongest transition observed in the benzene ultraviolet spectrum is the purely electronic perpendicular transition ${}^1E_{1u} \leftarrow {}^1A_{1g}$ [2]. Symmetry forbidden electronic transitions can be observed as well, by combining vibrational symmetry changes with the electronic changes such that the overall *vibronic* change is of symmetry $\Gamma(\mu_\alpha)$. The electronic transition ${}^1B_{2u} \leftarrow {}^1A_{1g}$ is electronically forbidden, but it can be vibronically induced by accompanying the electronic change with a change in vibration of symmetry e_{2g} since:

NOTE:

This figure is included on page 37 of the print copy of the thesis held in the University of Adelaide Library.

Figure 3.2: Electronic states of neutral benzene [15]. The electronic transition of interest to this study is the Herzberg-Teller transition, ${}^1B_{2u} \leftarrow {}^1A_{1g}$. Mixing of the ${}^1B_{2u}$ state with the neighbouring ${}^3E_{1u}$ is thought to be the reason why this electronically forbidden transition is unusually intense.

$${}^e B_{2u} \otimes {}^v e_{2g} \otimes {}^e A_{1g} \supset E_{1u} \equiv \Gamma(T_{x,y}). \quad \text{Equation 3.6}$$

Here the superscript e labels the symmetry as belonging to an electronic, v a vibrational and ev a vibronic wavefunction. The symmetries of benzene's vibrations can be found in Table 3.1. Vibrationally induced transitions, also known as "Herzberg-Teller" transitions, are the feature of the benzene ultraviolet spectrum that are of interest in this study. In particular we are interested in the absorption features between 38400-38700 cm^{-1} .

The active vibration in this region of the benzene absorption spectrum is predominantly the degenerate vibration, ν_6 . The symmetry of ν_6 is e_{2g} . The involvement of degenerate vibronic wavefunctions in transitions increases the complexity of selection rules significantly. Vibronic wavefunctions that are generated from two (or more) quanta of a degenerate vibration(s) can have their energetic degeneracy lifted by the effects of vibrational angular momentum. Vibrational angular momentum is generated by interaction between each member of the degenerate pair. Vibrational angular momentum effects can split vibronic degeneracy and also make the selection rules different for each member of the pair. Each member of the pair is labelled with a unique vibrational angular momentum quantum number, l_i . For a degenerate state where ν_i is the quantum number of the vibrational mode, l_i is related to ν_i by $l_i = \nu_i, \nu_i - 2, \dots, -\nu_i$. For example, if a state is composed of two quanta of the degenerate vibration, ν_{16} , the possible l_{16} values are 2, 0, -2.

Table 3.1: Symmetries and frequencies of benzene vibrational modes. Benzene has 30 vibrations, 10 of which are degenerate. The vibrations are labelled according to the convention introduced by Wilson [3]. Descriptions of the vibrations are taken from Muller [4]. Unless otherwise indicated, frequencies are taken from Atkinson [5]. (χ) Page [6], (δ) Stephenson [7], (ϵ) Muller [4].

Vibration			Observed Frequency [cm^{-1}]	
Mode	Symmetry	Type	${}^1A_{1g}$	${}^1B_{2u}$
1	a_{1g}	Ring stretching	993.1	923.0
2	a_{1g}	C-H Stretching	3073	3130.1
3	a_{2g}	C-H Bending (parallel)	1350	1327 χ
4	b_{2g}	Ring deformation	707	365
5	b_{2g}	C-H Bending (vertical)	990	744.6
6	e_{2g}	Ring deformation	608.3	521.4
7	e_{2g}	C-H Stretching	3056	3077.2
8	e_{2g}	Ring stretching	1599	1516 δ
9	e_{2g}	C-H Bending (parallel)	1178	1147.7
10	e_{1g}	C-H Bending (vertical)	846	580.7
11	a_{1g}	C-H Bending (vertical)	674.0	515-518
12	b_{1u}	Ring deformation	1010	936
13	b_{1u}	C-H Stretching	3057	3159 ϵ
14	b_{2u}	Ring stretching	1309	1570
15	b_{2u}	C-H Bending (parallel)	1146	1148
16	e_{2u}	Ring deformation	398.8	237.5
17	e_{2u}	C-H Bending (vertical)	967	718.2
18	e_{1u}	C-H Stretching	1037	919
19	e_{1u}	Ring stretching and Ring deformation	1482	1405 χ
20	e_{1u}	C-H Bending (parallel)	3064	3084 χ

The polar co-ordinate representation of vibronic symmetry established by Mills can be used to distinguish between states of the same vibronic symmetry but different vibrational angular momentum components [8]. This assignment technique is outlined below. The vibronic wavefunction, ψ_{ev} , can be classified by its transformation properties under the symmetry operation C_n , where n is the order of the principle molecular rotation axis [2]. Benzene belongs to the C_6 rotational point group, so all of its vibronic wavefunctions must obey the relationship:

$$C_6\psi_{ev} = e^{-i\theta}\psi_{ev} . \quad \text{Equation 3.7}$$

The value of the angle θ is used to classify the symmetry of the vibronic wavefunctions [2,8] :

$\theta = 0$	A species
$\theta = \pm 2\pi/n$	E_1 species
$\theta = \pm 4\pi/n$	E_2 species
$\theta = \pi$	B species.

The individual components of a degenerate vibronic wavefunction (E_x) are classified as:

$$\begin{aligned} \psi_{ev}(a) & \text{ if } 0 < \theta < \pi \\ \psi_{ev}(b) & \text{ if } -\pi < \theta < 0. \end{aligned}$$

An example of the classification of the vibronic symmetry for one of the electronically excited states studied here, 6^116^1 , is outlined below and summarised in Table 3.2.

The notation 6^116^1 refers to the excitation of one quantum of the degenerate species ν_6 (e_{2g} symmetry) and one quantum of the degenerate species ν_{16} (e_{2u} symmetry) in the electronic state (${}^1B_{2u}$). The product of these three wavefunctions produces three unique vibronic wavefunctions, one of which is degenerate:

$${}^e B_{2u} \otimes {}^v e_{2g} \otimes {}^v e_{2u} \supset {}^{ev} B_{1g} + {}^{ev} B_{2g} + {}^{ev} E_{1g}. \quad \text{Equation 3.8}$$

Table 3.2 shows the use of Mills' polar co-ordinates to distinguish between the vibronic states which differ only by their vibrational angular momentum components [8]. All possible combinations of vibrational angular momentum components of the different vibrational species are considered. The vibrational angular momentum values also affect the effective value of the Coriolis constant (see Section 3.2.3). From Table 3.2 it is clear that the assignment of a degenerate wavefunction as being of type (a) or type (b) is dependent upon vibrational angular momentum quantum numbers.

Once the polar co-ordinate for a state has been established we can use the difference in θ_{ev} between that wavefunction and another to determine whether an optical transition between the two wavefunctions is symmetry allowed. In benzene, as described above, in order for the ${}^1 B_{2u} \leftarrow {}^1 A_{1g}$ transition to be seen, a change in vibration equivalent to e_{2g} must accompany the transition. The polar co-ordinate representation of species E_2 is $\pm 4\pi/6$, so according to Equation 3.7, the C_6 fold axis transforms the wavefunction as $\mp 4\pi/6$. Thus, a $\Delta\theta_{ev}$ change of $\mp 4\pi/6$ upon going from ${}^1 B_{2u} \leftarrow {}^1 A_{1g}$ will make the transition vibronically allowed. This method was introduced by Atkinson and Parmenter for determining allowed vibrational transitions involving degenerate species that are distinguished only by their angular momentum components [9]. The application of this technique to one of the transitions relevant to this study is presented in Table 3.3.

Table 3.2: Determination of the vibronic symmetries for excitation of the vibrations ν_6 and ν_{16} in the excited electronic state ${}^1B_{2u}$ of benzene. Both ν_6 and ν_{16} have symmetry E_2 , so both θ_6 and θ_{16} equal $4\pi/6$.

Vibrational angular momentum quantum number		Polar coordinate representation of ψ				Total symmetry species
l_6	l_{16}	$l_6\theta_6$	$l_{16}\theta_{16}$	θ_e	θ_{ev}	ψ_{ev}
-1	-1	$-4\pi/6$	$-4\pi/6$	π	$-2\pi/6$	$E_1(B)$
+1	+1	$+4\pi/6$	$+4\pi/6$	π	$+2\pi/6$	$E_1(A)$
-1	+1	$-4\pi/6$	$+4\pi/6$	π	π	B
+1	-1	$+4\pi/6$	$-4\pi/6$	π	π	B

Table 3.3: Determination of allowed vibrational angular momentum transitions within the vibronic transition $6_1^0 11_0^2$. The only allowed transition here is shown to be $6_1 l_{\pm 1} 11_0 l_0 \leftrightarrow 6^0 l^0 11^2 l^0$ since it involves $\Delta\theta_{ev} = \mp 4\pi/6$.

Vibrational angular momentum quantum number		Polar coordinate representation of ψ				Total symmetry species
Ground state						
l_6	l_{11}	$l_6\theta_6$	$l_{11}\theta_{11}$	θ_e	θ_{total}	ψ_{ev}
-1	0	$-4\pi/6$	0	0	$-4\pi/6$	$E_2(b)$
+1	0	$+4\pi/6$	0	0	$+4\pi/6$	$E_2(a)$
Excited State						
l_6	l_{11}	$l_6\theta_6$	$l_{11}\theta_{11}$	θ_e	θ_{total}	ψ_{ev}
0	0	0	0	π	π	B

$\Delta\theta = -4\pi/6$

3.2.2 Simulating Rovibronic Transitions

Equation 3.1 describes the selection rule for a rovibronic transition. The equation will be non-zero when the product of the symmetries of the rovibronic wavefunctions and μ_A contain the totally symmetric symmetry species $\Gamma^{(s)}$ [1],

$$\Gamma(\psi'_{evr}) \otimes \Gamma(\mu_A) \otimes \Gamma(\psi''_{evr}) \supset \Gamma^{(s)}. \quad \text{Equation 3.9}$$

In the D_{6h} point group, $\Gamma^{(s)}$ is the A_{1g} symmetry species. μ_A is always antisymmetric with respect to any inversion operation (i.e. it has a -1 character for any permutation-inversion operations and a +1 character for everything else) and so transforms as the antisymmetric representation, Γ^* [1]. In the D_{6h} molecular symmetry group the antisymmetric wavefunction, Γ^* , is of symmetry A_{1u} .

Thus for an allowed rovibronic transition in a D_{6h} molecule such as benzene,

$$\Gamma(\psi'_{evr}) \otimes \Gamma(\psi''_{evr}) \supset \Gamma^* \equiv A_{1u} . \quad \text{Equation 3.10}$$

This relationship produces the selection rules for rovibronic transitions that will define the shape of the rovibrational absorption contour.

The symmetry of a rovibronic wavefunction can simply be represented as the product of the symmetries of each individual component, i.e.:

$$\Gamma(\psi_{evr}) \supset \Gamma(\psi_e) \otimes \Gamma(\psi_v) \otimes \Gamma(\psi_r). \quad \text{Equation 3.11}$$

The symmetry of a rotational wavefunction however, is dependent upon the magnitude as well as the direction of the rotational motion relative to the laboratory fixed reference frame.

When discussing molecular motion the total angular momentum is represented by the quantum number, J [†]. k , the rotational angular momentum quantum number, is the projection of the total angular momentum vector onto the molecular z-axis (see Figure 3.3). There are $2(J + 1)$ possible values of k ranging from $-J \leq k \leq +J$. Wilson describes the rotational symmetries for a symmetric rotor for all possible values of k [3]. These rotational symmetries are presented in Table 3.4 along with the symmetries of the ψ_{evr} involved in the transitions relevant to this report. Once the rovibrational symmetry for a wavefunction has been established then Equation 3.10 must be satisfied when considering whether a transition between particular rovibronic states is possible.

However, satisfying Equation 3.10 is not the only requirement for an allowed transition. It is well known that for perpendicular rovibronic transitions, such as those considered here, the selection rules of $\Delta J = \pm 1$ or 0 (with $J = 0 \leftrightarrow 0$ forbidden) and $\Delta k = \pm 1$ also must hold [1,11].

When working with degenerate vibronic wavefunctions the selection rules must be extended to incorporate the different l_j values. Hougen introduced the quantum number, g , which incorporates l_j , to classify the rovibronic wavefunctions of a symmetric-top [12]. Selection

[†] The total angular momentum vector is the sum of the rotational, electronic orbital, spin and vibrational angular momenta (10) Bernath, P. F. *Spectra of Atoms and Molecules*, 2nd ed.; Oxford University Press: New York, 2005.

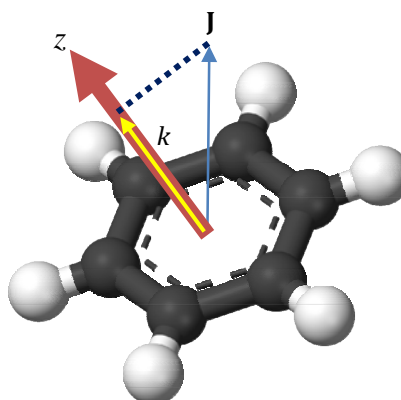


Figure 3.3: Assignment of rotational angular momentum quantum number, k .

Table 3.4: Rovibronic symmetries of states involved in the $6_0^1 16_1^1$ transition. (‡) Rotational symmetries, $\Gamma(\psi_r)$, are taken from Wilson [3]. Not all states are involved in each $\Delta k = \pm 1$ transition.

		$\Gamma(\psi_{ev})$			
		E_{2u}	E_{1g}	B_{1g}	B_{2g}
k level	$\Gamma(\psi_r)$ ‡	$\Gamma(\psi_{evr}) (= \Gamma(\psi_r) \otimes \Gamma(\psi_{ev}))$			
$k = 0,$ J even or 0	A_1	E_{2u}	E_{1g}	B_{1g}	B_{2g}
$k = 0,$ J odd	A_2	E_{2u}	E_{1g}	B_{2g}	B_{1g}
$k = 6p$	$A_1 + A_2$	$2E_{2u}$	$2E_{1g}$	$B_{1g} + B_{2g}$	$B_{1g} + B_{2g}$
$k = 6p \pm 1$	E_1	$B_{1u} + B_{2u} + E_{1u}$	$A_{1g} + A_{2g} + E_{2g}$	E_{2g}	E_{2g}
$k = 6p \pm 2$	E_2	$A_{1u} + A_{2u} + E_{2u}$	$B_{1g} + B_{2g} + E_{1g}$	E_{1g}	E_{1g}
$k = 6p \pm 3$	$B_1 + B_2$	$2E_{1u}$	$2E_{2g}$	$A_{1g} + A_{2g}$	$A_{1g} + A_{2g}$

rules are then dependent upon the associated g label of a rovibronic wavefunction. Hougen's rules highlight that both states of a degenerate wavefunction are not always involved in a rovibronic transition. Knowing the energetic degeneracy of a transition is important when trying to establish the strength of a transition, as this in turn influences the intensity of the observed spectral line. An outline of how Hougen's quantum number is assigned to a rovibrational wavefunction is given below.

Hougen defines the signed quantum number as:

$$g = g_{ev} - k, \quad \text{Equation 3.12}$$

where g_{ev} is the sum of the vibrational and electronic Hougen quantum numbers:

$$g_{ev} = g_e + g_v. \quad \text{Equation 3.13}$$

Analogous to Mills' assignment of the symmetry of vibronic wavefunctions (see Section 3.2.1), the value of g_e depends upon how ψ_e transforms under the operation C_n , where n is the order of the principle molecular rotation axis. For example, for a symmetric-top, g_e has a value of 0 for electronic states of symmetry A, $\frac{1}{2}n$ for B states. For E_s states (where $s = 1, 2, 3, \dots$), g_e is given the value of $\pm s$.

Hougen's vibrational quantum number is defined as:

$$g_v = \left(\frac{n}{2}\right) \sum_B \nu_B + \sum_j s_j l_j . \quad \text{Equation 3.14}$$

The first term in this equation is simply a summation of the number of vibrations of symmetry B multiplied by $n/2$. The second term incorporates the vibrational angular momentum label, l_j , for degenerate states of symmetry E_s .

Consider for example, the assignment of g values to rotational states in the $6^1 16^1$ vibrational combination state in the $^1B_{2u}$ excited electronic state of benzene. The electronic state is of symmetry B, thus $g_e = 3$. When calculating g_v we must realise that both ν_6 and ν_{16} are degenerate vibrations of symmetry e_{2g} and e_{2u} , respectively. Each degenerate vibration contributes a $+l$ and $-l$ component to the combination band, where $l = 1$. Benzene belongs to the D_{6h} point group so n in Equation 3.7 is equal to 6. Therefore, there are three unique values for g_v : 0 and ± 4 . The three unique g_{ev} values are thus: +3, a B state, and +7 and -1 for each component of the degenerate E_1 state. These results have been summarised in Table 3.5. The vibronic symmetries determined in Table 3.2 we are reproduced in Table 3.5 to demonstrate the symmetry associated with the Hougen quantum numbers.

The selection rule for an allowed rovibronic transition then becomes:

$$\Delta g = 0 \text{ mod } n . \quad \text{Equation 3.15}$$

Table 3.5: Determination of Hougen's quantum number for the 6^116^1 vibronic state in the ${}^1B_{2u}$ excited electronic state of benzene. (†) The symmetries were calculated in Table 3.2.

Vibrational angular momentum quantum number		Hougen's quantum numbers			$\Gamma(\psi_{ev})$ †
l_6	l_{16}	g_v	g_e	g_{ev}	
-1	-1	-4	+3	-1	$E_1(B)$
+1	+1	+4	+3	+7	$E_1(A)$
-1	+1	0	+3	+3	B
+1	-1	0	+3	+3	B

Analogous to the determination of vibronic symmetry in Equation 3.7, Hougen describes the rovibronic symmetry by determining how the wavefunction ψ_{evr} transforms under the symmetry operation C_n :

$$C_6\psi_{evr} = e^{-2\pi ig}\psi_{evr} . \quad \text{Equation 3.16}$$

This leads to the simple relationship where we can determine the rovibronic symmetry for a symmetric-top simply from the value of g . This is summarised in Table 3.6.

Table 3.6: Assignment of rovibronic symmetries using Hougen's quantum number, g .

$ g / \text{mod } n$	$\Gamma(\psi_{evr})$
0	A_1A_2
1	E_1
2	E_2
3	B_1B_2

The energetic degeneracy of the A and B rovibronic states can be split with the introduction of l -type resonances [13,14], however, the energetic shifts that they cause are not observable at the resolution with which these experiments were performed and so were not included in the simulations.

In summary, an allowed rovibronic transition is one which satisfies both the symmetry requirement of Equation 3.10, the ΔJ and Δk selection rules, as well as Hougen's selection rule presented in Equation 3.15. Figure 3 and Figure 3 illustrate the rovibronic transitions that are allowed between different vibronic states involved in the $6_0^1 16_1^1$ transition. The allowed rovibrational transitions are indicated by the blue arrows. Each rovibrational level has been labelled with the appropriate g and $\Gamma(\psi_{evr})$ value.

Another useful label for the different components of a degenerate rovibronic wavefunction is $\pm l$ [11,15]. These labels arguably simplify the transition selection rules and can be used to determine the positive or negative effect that Coriolis interaction will have on the energy of the state. A Coriolis effect is caused by the interaction of rotational and vibrational motion – an effect which is most pronounced when both components of a degenerate vibration are excited. It is a common misconception that it is the relative signs of k and l that determine the $\pm l$ label. While this is true for singly degenerate vibronic states, Mills showed that the sign of l is actually determined by the relative signs of k and g_{ev} as follows [16][‡]:

$$\text{sign} \left[k \sin \left(\frac{2\pi g_{ev}}{n} \right) \right]. \quad \text{Equation 3.17}$$

[‡] Note that in his paper Mills refers to g_v not g_{ev} since he is referring to rovibrational levels. In this report the equation has been modified to be relevant to rovibronic states.

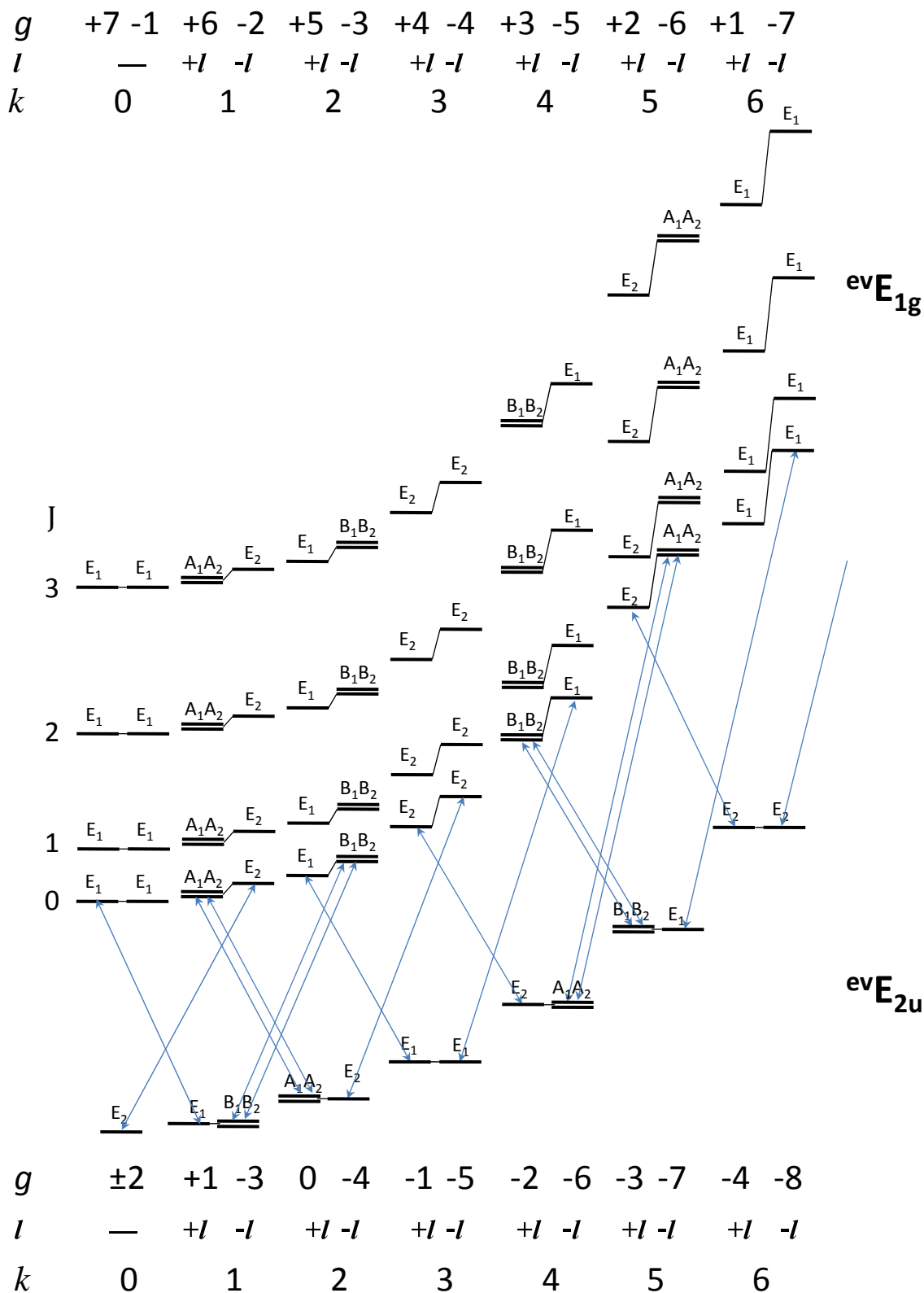


Figure 3.4

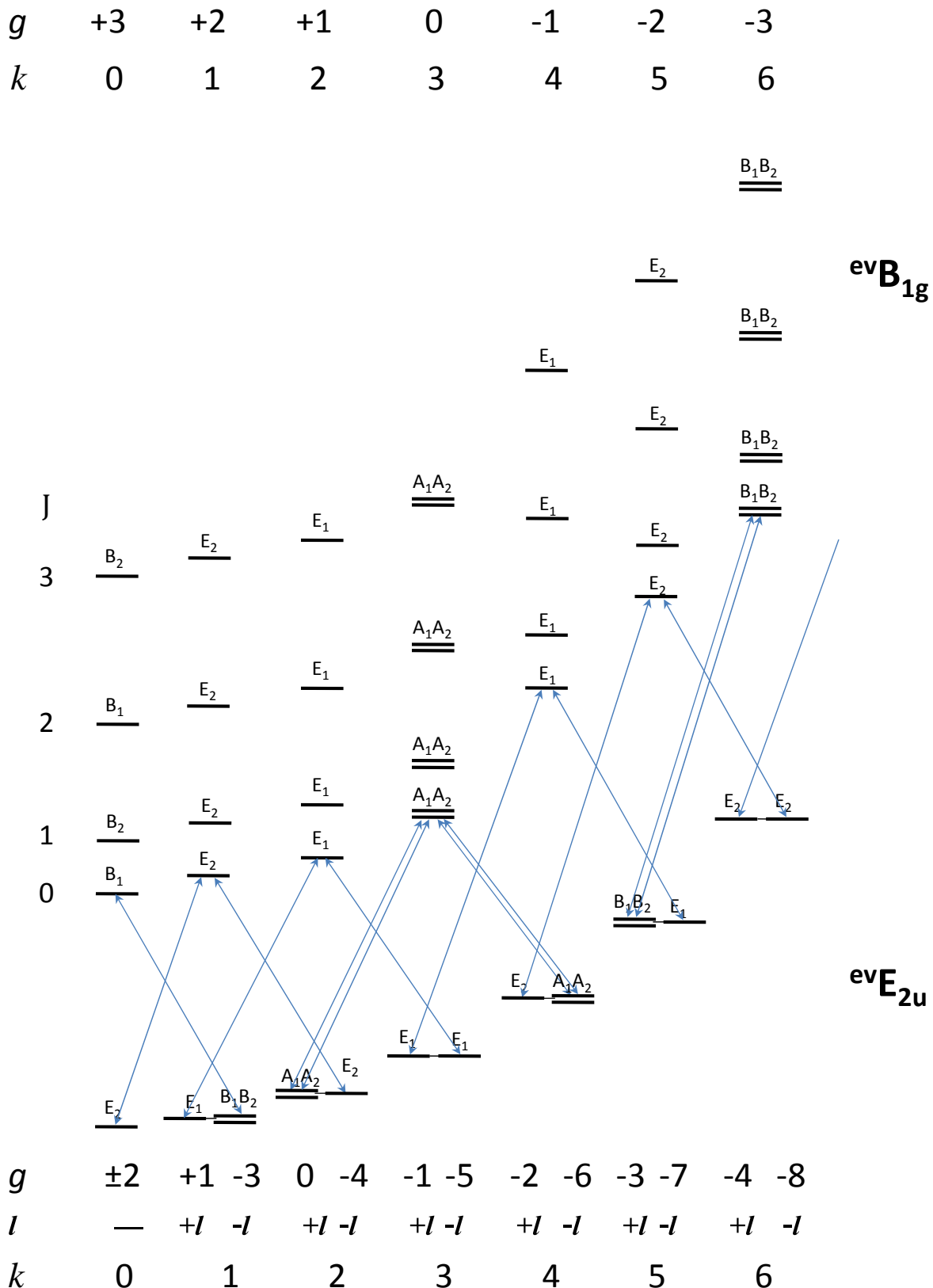


Figure 3.5

Figure 3.4: Allowed rovibrational transitions within the $6_0^1 16_1^1$, ${}^{ev}E_{1g} \leftarrow {}^{ev}E_{2u}$ vibronic transition. Rovibrational levels are labelled with Hougen's quantum number, g . Allowed transitions are those that involve $\Delta g = 0 \pmod n$. In degenerate vibronic states such as ${}^{ev}E_{1g}$, Coriolis effects destroy the energetic degeneracy of the rovibronic state. The lower rovibronic states in this case do not display Coriolis splitting since the vibronic state is made from ν_{16} which has $\zeta_{16} = 0$. The symmetry of each rovibronic state has been assigned according to Wilson's theory [6] and summarised in Table 3.4.

Figure 3.5: Allowed rovibrational transitions within the $6_0^1 16_1^1$, ${}^{ev}B_{1g} \leftarrow {}^{ev}E_{2u}$ vibronic transition. There are several important differences to note with Figure 3.4 - now that the transitions are between a degenerate and a non-degenerate vibronic state. Firstly the rovibrational levels in the non-degenerate excited electronic state are not split by Coriolis effects even though the vibronic state is the result of the product of two degenerate vibrations (ν_6 and ν_{16}). Also, note the alternating symmetries of the $k = 0$ states in ${}^{ev}B_{1g}$ as a consequence of the odd or even nature of J . Finally, symmetry restrictions prevent any transitions from the ground B_2 rovibronic state when $k = 1$, whilst allowing transitions out of the B_1 state. This is important to note when calculating the line strength of this transition.

Positive results are given the $+l$ label and negative results $-l$. Section 3.2.3 describes how the assignment of the label to one component of a degenerate rovibrational wavefunction is used in determining the energy of the wavefunction. From Figure 3.4 and 3.5 we can see that there is a general rule involving Δl for transitions between states. These rules are summarised in Table 3.7 for the vibronic transitions relevant to this study.

The only time when Equation 3.17 is undefined, i.e. $(k \sin(\frac{2\pi g_{ev}}{n}) = 0)$, is when $k = 0$ (and thus there is no Coriolis effect) or when $(\frac{2\pi g_{ev}}{n}) = 0$ or π because ψ_{ev} is non-degenerate. If the non-degenerate vibronic state is generated from the product of degenerate vibrations, for example:

$${}^e B_{2u} \otimes {}^v e_{2g} \otimes {}^v e_{2u} \supset {}^{ev} B_{1g} + {}^{ev} B_{2g} + {}^{ev} E_{1g} ,$$

Coriolis effects are still felt by the vibrating molecule despite the undefined l value and are shown to influence the rovibronic energy of the wavefunction.

Once the allowed transitions have been established the energies and relative intensities of the individual rovibrational transitions must be determined.

Table 3.7: $\pm l$ selection rules for rovibronic transitions

Vibronic Transition	$\Delta k = \pm 1$
${}^{ev} E_1 \leftarrow {}^{ev} E_2$	$\mp l \leftarrow \mp l$
${}^{ev} B_{1,2} \leftarrow {}^{ev} E_2$	$0 \leftarrow \pm l$
${}^{ev} E_1 \leftarrow {}^{ev} A_{1,2}$	$\pm l \leftarrow 0$

3.2.3 Energy of a Rovibronic State

For an oblate symmetric top the energy of a rovibronic state, E_0 , above the zero point energy is defined as [17]:

$$E_0(v_i, l, J, k) = T_e + G_0(v_i, l) + E_{rot}(J, k, l), \quad \text{Equation 3.18}$$

where T_e is the energy of the electronic state and G_0 and E_{rot} the vibrational and rotational contributions to the energy of the state, respectively.

The energy of individual vibrational levels are dependent upon the anharmonic constants ω_i , x_{ij} and g_{ij} - the latter two are an indication of the degree of coupling between the vibrational modes i and j [18]:

$$G_0(v_i, l) = \sum_i \omega_i v_i + \sum_i \sum_{j \geq i} x_{ij} v_i v_j + \sum_i \sum_{j \geq i} g_{ij} l_i l_j \quad \text{Equation 3.19}$$

where v_i is the quantum number of the vibrational mode, i , and l_i the signed vibrational angular momentum quantum number .

The energy of an individual rotational level is described by:

$$E_{rot}(J, k, l) = BJ(J + 1) + (C - B)k^2. \quad \text{Equation 3.20}$$

B and C are the rotational constants describing rotational motion about the B and C molecular axis, respectively. Higher order terms that deal with centrifugal distortion are not included in these simulations since the resolution of the experimental spectra was not great enough to warrant their inclusion.

When dealing with degenerate vibrations, perturbations caused by Coriolis effects must be considered. The effective Coriolis constant (ζ_{eff}) is a measure of the interaction that can occur between a molecule's rotational and vibrational angular momentum components. Coriolis interaction not only causes energetic splitting of symmetrically degenerate species but also affects the probability of transitioning out of the perturbed state. The absolute value of ζ_{eff} greatly influences the shape of the resultant rotational contour [2], as will be shown in the simulation results below. A degenerate vibration is capable of inducing a Coriolis effect if the nuclear motion has some component directed along the principle molecular rotation axis. In benzene this means that all of the in-plane e_{2g} and e_{1u} vibrations can potentially interact with the rotational motion about the C_6 axis [2]. In practice however, only ν_6 and ν_8 , both of symmetry e_{2g} , show a non-zero value for the Coriolis interaction [9].

The shape of a rovibrational contour is very sensitive to the values of ζ . Atkinson and Parmenter [9] built upon an expression developed by Callomon [2] that allows the prediction of the contour shape based on the value of χ .

$$\chi = -1 \mp \sum_i l'_i \zeta'_i \pm \sum_i l''_i \zeta''_i . \quad \text{Equation 3.21}$$

Here the superscripts '' indicate the value is of the ground electronic state, and ' of the excited electronic state. The contours are labelled as type I – IV depending upon the value of χ . The

contour types are illustrated in Figure 3.6. In general, a benzene band contour is always of type II unless the transition involves the Coriolis active ν_6 or ν_8 vibrations [9].

The Coriolis perturbation can be added to the relationship for rotational energy in the form:

$$E_{rot}(J, k, l) = BJ(J + 1) + (C - B)k^2 - 2Ck\zeta_{eff} , \quad \text{Equation 3.22}$$

where

$$\zeta_{eff} = \sum_j l_j \zeta_j .$$

For degenerate ψ_{ev} , an alternate definition of ζ_{eff} can be employed:

$$\zeta_{eff} = \text{sign} \left[\sin \left(\frac{2\pi g_{ev}}{n} \right) \right] \times \sum_j l_j \zeta_j .$$

This definition is convenient since we can replace the first term with the $\pm l$ labels that were introduced in Section 3.2.2. The Coriolis term in Equation 3.22 then becomes:

$$\mp 2C|k|\zeta_{eff} \quad \text{for } \pm l \text{ states.}$$

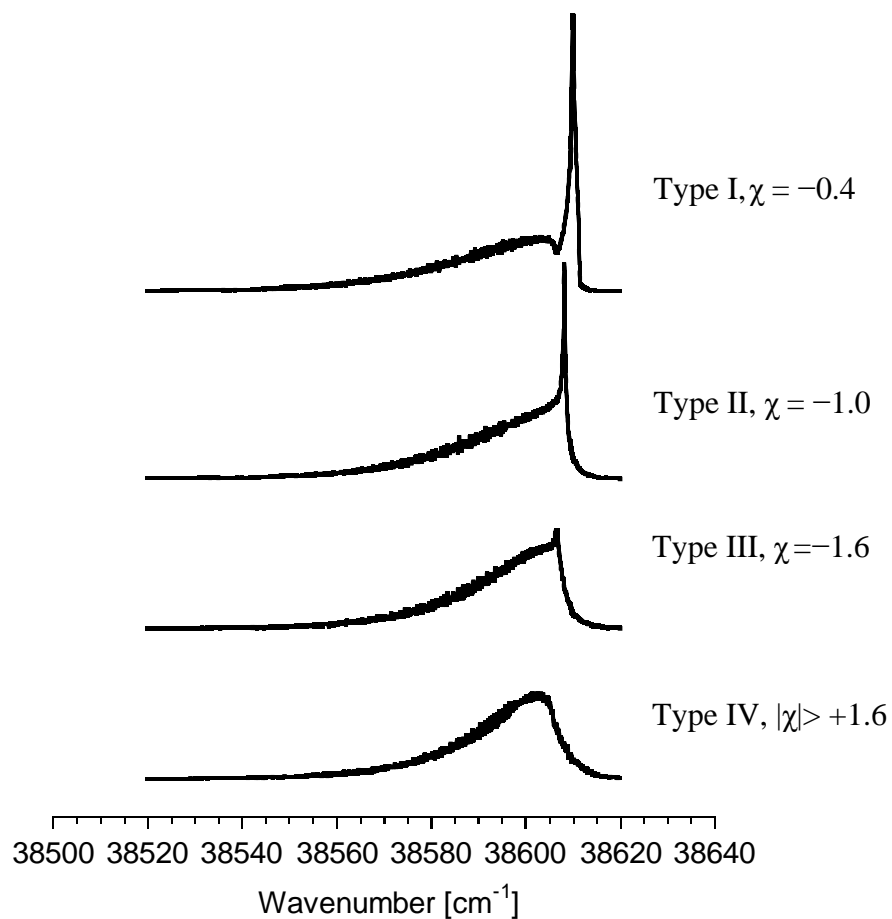


Figure 3.6: The effect of the magnitude of χ on the shape of a rovibrational contour. These examples have been calculated by changing the value of ζ'_{eff} for the 6_0^1 transition. Atkinson and Parmenter [10] established a general rule for contour shapes based on Equation 3.2.1.

3.2.4 Intensity of a Rovibronic Transition

The intensity of a rovibronic absorption transition, $I_{i \leftarrow j}$, is given as [19]:

$$I_{i \leftarrow j} = C A_{jk} (2J_j + 1) G_{jk} e^{-\frac{E}{k_B T_{rot}}} . \quad \text{Equation 3.23}$$

C , the Frank-Condon factor, is the same for all rotational transitions in a particular vibronic transition [19]. A_{jk} is the Hönl-London factor for the particular rovibronic transition. Hönl-London factors as designated by Herzberg, for perpendicular transitions are listed in Table 3.8. $(2J_i + 1)$ is the rotational degeneracy of the initial state, i , and G_{jk} is the statistical weight for the transition[§]. The statistical weight is dependent upon the nuclear spin degeneracy of the rovibronic state. Wilson has shown that the nuclear spin functions for benzene combine to form wavefunctions of symmetry $13A_1 + A_2 + 7B_1 + 3B_2 + 9E_1 + 11E_2$ [3]. Thus the statistical weight for a transition out of a rovibronic state of symmetry B_2 , for example, will have $G_{jk} = 3$.

Table 3.9 gives more examples of statistical weights relevant to the ${}^{ev}B_{1g} \leftarrow {}^{ev}E_{2u}$ transition discussed in Figure 3.5.

The last component in Equation 3.23, $e^{-E/k_B T_{rot}}$, is the Boltzmann factor for the initial state. This factor accounts for the population of molecules that are in that initial state at the time of photon absorption. E is the rovibronic energy of the state, k_B is Boltzmann's constant and T_{rot} the rotational temperature of the ensemble of absorbing molecules.

[§] Statistical weights are also known as nuclear spin statistics.

Table 3.8 : Hönl-London factors for a perpendicular transition [11]. $K = |k|$. J and K values are from the initial rotational states involved in the rotational transition. The upper signs are for $\Delta K = -1$ transitions, lower signs are for $\Delta K = +1$ transitions. (*) If $K=0$ and $\Delta K = +1$, then the factor must be multiplied by 2.

NOTE:

This table is included on page 59 of the print copy of the thesis held in the University of Adelaide Library.

Table 3.9: Examples of statistical weights calculated for some of the vibronic transitions allowed within the vibronic transition ${}^{\text{ev}}B_{1g} \leftarrow {}^{\text{ev}}E_{2u}$, and displayed in Figure 3.5. (‡) Note that although the total symmetry of ψ''_{evr} is $B_1 + B_2$ when $k = 1$, only the wavefunctions of symmetry B_1 can undergo the $\Delta k = -1$ transition due to symmetry restrictions. The statistical weight reflects only the degeneracy of states that are involved in the transition.

Transition	$\Gamma(\psi''_{\text{evr}})$	\mathcal{G}_{Jk}
$k(2 \leftarrow 1)$	E_{1u}	9
$k(0 \leftarrow 1)$	$B_{1u} + B_{2u}$	7^\ddagger
$k(3 \leftarrow 2)$	$A_{1u} + A_{2u}$	13+1
$k(1 \leftarrow 2)$	E_{2u}	11
$k(6 \leftarrow 5)$	$B_{1u} + B_{2u}$	7+3

When simulating fluorescence from state i which has been populated by the absorption of a photon from state j , this Boltzmann factor is replaced by the function:

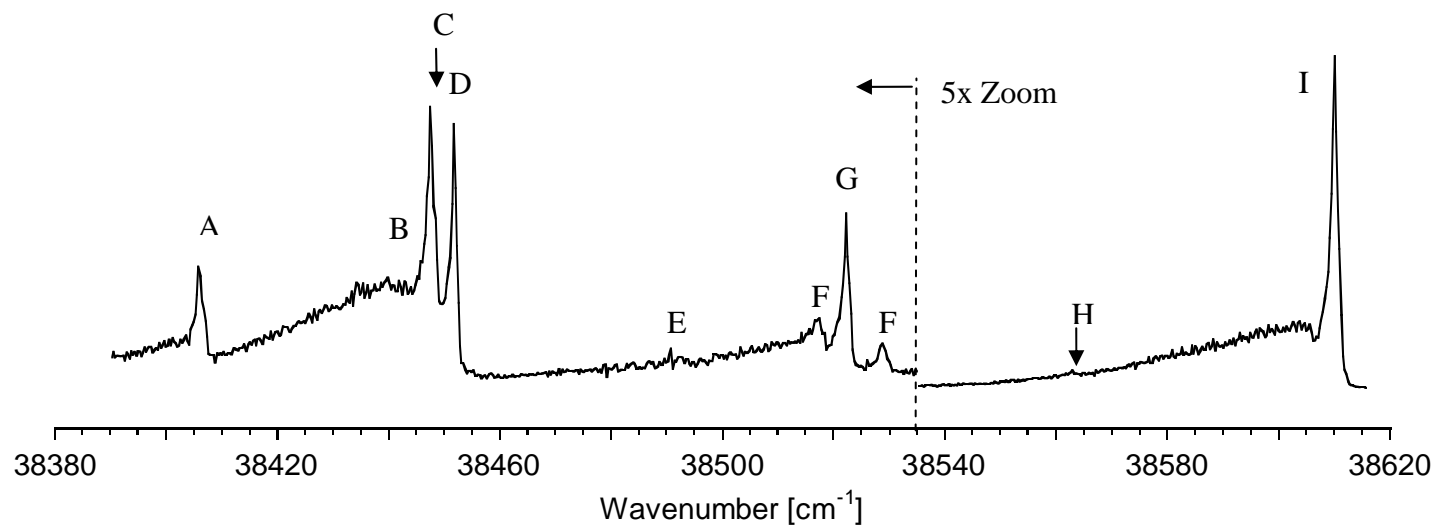
$$Pop_j = \sum_j (I_{i \leftarrow j} \times e^{-0.5[(\Delta E_{(i \leftarrow j)} - E_{\text{hv}})/\sigma_{\text{hv}}]^2}), \quad \text{Equation 3.24}$$

where the second factor in the function is a Gaussian of Full Width Half Maximum (FWHM) equivalent to the energy resolution of the absorbed photon (σ_{hv}) and centred at the frequency of the absorbed photon [20].

3.3 Simulation of the Vibronic Transitions within ${}^1B_{2u} \leftarrow {}^1A_{1g}$

Figure 3.7 shows a 1+1 REMPI spectrum of benzene generated in an equilibrated gas phase cell. The absorption bands and their components were assigned using the theory outlined in Section 3.2 and are in general agreement with Stephenson [7], Atkinson [5] and Fischer [21]. This region of the spectrum was chosen to study for several reasons. Firstly, it is easily accessible with modern laser systems and the strengths of the absorption features are great. Secondly, the region has both cold and hot bands which will give us information about different types of vibrationally excited species in addition to those undergoing vibrationless motion. All of the vibrations that are involved in these transitions are illustrated in Figure 3.8. The vibronically induced transitions considered in this work are displayed in Table 3.10. Here ψ'_{ev} refers to the wavefunction in the excited electronic state and ψ''_{ev} to the wavefunction in the ground electronic state.

The ${}^1B_{2u} \leftarrow {}^1A_{1g}$ region of the benzene UV absorption spectrum has been extensively studied. Callomon, Dunn and Mills [2] were the first to perform a detailed analysis of the rovibrational structure of absorption bands in this region and their work was then extended by the series of investigations performed by Atkinson and Parmenter [5,9,22]. The 6_0^1 absorption band has received the most attention due to its large absorption cross-section and it is the simplest example of the excitation of a degenerate vibration, with non-zero Coriolis effects. The high resolution analysis of the band by Okrusch, Muller and Hese has achieved arguably



(A)	$6_1^0 l_{\mp 1}^0 1_0^1 l_0^0$	(D)	$6_0^1 l_0^{\mp 1} 16_1^1 l_{\pm 1}^{\pm 1}$	(F)	$6_1^2 l_{\pm 1}^0 / 6_1^0 l_{\pm 1}^0 11_0^2 l_0^0$	(I)	$6_0^1 l_0^{\mp 1}$
(B)	$6_0^1 l_0^{\mp 1} 16_1^1 l_{\mp 1}^{\mp 1}$	and	$6_0^1 l_0^{\pm 1} 16_1^1 l_{\pm 1}^{\mp 1}$	(G)	$6_1^2 l_{\mp 1}^2$		
(C)	$6_0^1 l_0^{\mp 1} 11_1^1 l_0^0$	(E)	$6_0^1 l_0^{\mp 1} 18_1^1 l_{\mp 1}^{\pm 1}$	(H)	$16_0^2 l_0^{\mp 2}$		

Figure 3.7: 1+1 REMPI spectrum of benzene generated in a room temperature gas-phase static cell. Band assignments are in agreement with those of Stephenson [1], Atkinson [2] and Fischer [3].

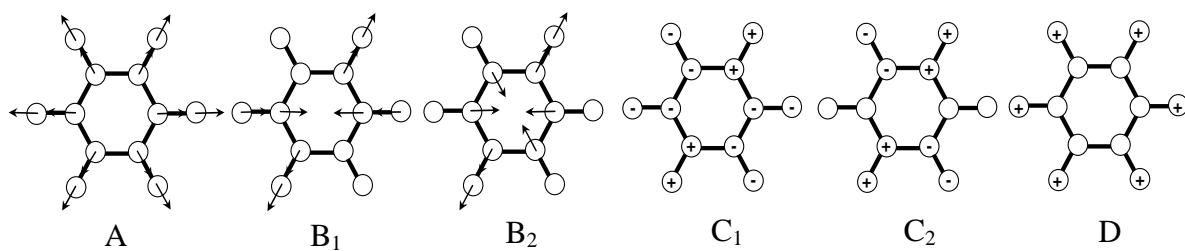


Figure 3.8: (A) ν_1 : In-plane ring stretch, (B) ν_6 : Degenerate in-Plane ring squash, (C) ν_{16} : Degenerate out-of-plane ring deformation, (D) ν_{11} : Out-of-plane C-H wagging.

Table 3.10: The vibronically induced transitions simulated in this study and their symmetry according to Mills' polar co-ordinate assignment. (*) These transitions were only used in the 2D simulated spectra discussed in Section 3.4.

Transition	Species		Transition	Species	
	ψ''_{ev}	ψ'_{ev}		ψ''_{ev}	ψ'_{ev}
$6_0^1 l_0^{-1}$	A	E ₁ (A)	$6_0^1 l_0^{-1} 16_1^1 l_{-1}^{-1}$	E ₂ (B)	E ₁ (B)
$6_0^1 l_0^{+1}$	A	E ₁ (B)	$6_0^1 l_0^{+1} 16_1^1 l_{+1}^{+1}$	E ₂ (A)	E ₁ (A)
$6_1^2 l_{-1}^{-2}$	E ₂ (B)	E ₁ (B)	$6_0^1 l_0^{-1} 16_1^1 l_{+1}^{+1}$	E ₂ (A)	B
$6_1^2 l_{+1}^{+2}$	E ₂ (A)	E ₁ (A)	$6_0^1 l_0^{+1} 16_1^1 l_{-1}^{-1}$	E ₂ (B)	B
$6_1^2 l_{+1}^0$	E ₂ (A)	B	$6_0^1 l_0^{+1} 16_1^1 l_{+1}^{-1}$	E ₂ (A)	B
$6_1^2 l_{-1}^0$	E ₂ (B)	B	$6_0^1 l_0^{-1} 16_1^1 l_{-1}^{+1}$	E ₂ (B)	B
$6_1^0 l_{+1}^0 11_0^2 l_0^0$	E ₂ (A)	B	$1_1^0 l_0^0 6_0^1 l_0^{-1} 16_1^1 l_{-1}^{-1} *$	E ₂ (B)	E ₁ (B)
$6_1^0 l_{-1}^0 11_0^2 l_0^0$	E ₂ (B)	B	$1_1^0 l_0^0 6_0^1 l_0^{+1} 16_1^1 l_{+1}^{+1} *$	E ₂ (A)	E ₁ (A)
$6_0^1 l_0^{-1} 11_1^1 l_0^0$	A	E ₁ (A)	$1_1^0 l_0^0 6_0^1 l_0^{-1} 16_1^1 l_{+1}^{+1} *$	E ₂ (A)	B
$6_0^1 l_0^{+1} 11_1^1 l_0^0$	A	E ₁ (B)	$1_1^0 l_0^0 6_0^1 l_0^{+1} 16_1^1 l_{-1}^{-1} *$	E ₂ (B)	B
$1_1^0 l_0^0 6_0^1 l_0^{-1} 11_1^1 l_0^0 *$	A	E ₁ (A)	$1_1^0 l_0^0 6_0^1 l_0^{+1} 16_1^1 l_{+1}^{-1} *$	E ₂ (A)	B
$1_1^0 l_0^0 6_0^1 l_0^{+1} 11_1^1 l_0^0 *$	A	E ₁ (B)	$1_1^0 l_0^0 6_0^1 l_0^{-1} 16_1^1 l_{-1}^{-1} *$	E ₂ (B)	B

the most accurate values for the ground and excited state rotational constants to date [23]. Whilst the rotational constants for many other vibrational states in $^1A_{1g}$ have been obtained from high resolution infrared studies [24,25], many of the rotational constants for vibrational states in $^1B_{2u}$ have yet to be reported. As a consequence, before trying to use the simulated contours to analyse the experimental data of Chapters 4 and 5, we must first find the values of any relevant unknown spectroscopic constants so that the spectra can be accurately simulated. To do this a simulated spectrum is fit to a standard spectrum produced in a thermally equilibrated environment and at ambient temperature. The spectroscopic constants are found when the best fit to the experimental spectrum is achieved.

Two different techniques were used to obtain the standard gas phase, room temperature spectrum. The first involved 1+1 REMPI of benzene vapour in a static cell. The cell was equipped with a pair of 1 cm^2 electrodes separated by a distance of 1 cm and biased with a potential difference of 90 V. The spectrum was recorded at a benzene pressure of 0.45 Torr by passing the resulting photocurrent from each electrode through a differential amplifier. Molecular equilibration is ensured in such a static system and so confidence can be placed in the fact that the temperature associated with the observed rotational envelopes is that of the room (295 K). Due to the mass insensitivity of this technique however, the static-cell benzene spectrum is contaminated with the spectrum of C-13 isotope substituted benzene ($^{13}\text{C}^{12}\text{C}_5\text{H}_6$). The presence of the isotope can be seen as a shoulder on the high energy side of the 6_0^1 band (marked with * in Figure 3.9). The relative intensity of the $^{13}\text{C}^{12}\text{CH}_6$ band is low since the relative abundance of the ^{13}C isotope is $\sim 1.1\%$ compared to ^{12}C isotope.

The inability to distinguish between the rotational contours of $^{12}\text{C}_6\text{H}_6$ and $^{13}\text{C}^{12}\text{C}_5\text{H}_6$ means the static cell spectrum is inadequate to use as a template with which to fit out spectral constants for the individual vibronic transitions. Mass selectivity was achieved by performing 1+1 REMPI on the background benzene vapour in the Source Chamber of the TOF-MS. We

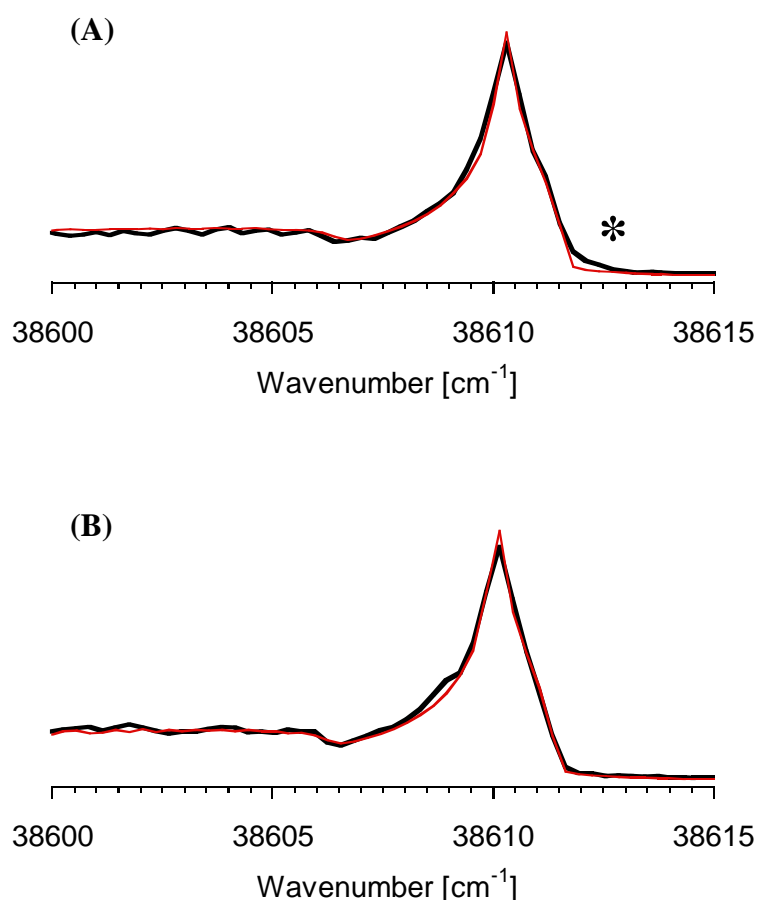


Figure 3.9: Zoom in of the P branch of the 6_0^1 absorption contour; experimental spectrum (black) and simulated spectrum (red). (A) The experimental absorption contour was generated by 1+1 REMPI of benzene vapour in a static cell. This technique is not mass selective so the absorption contour of $^{13}\text{C}^{12}\text{C}_5\text{H}_6$ is simultaneously generated, appearing blue shifted from the $^{12}\text{C}_6\text{H}_6$ contour; It appears as a small shoulder on the high energy side of the $^{12}\text{C}_6\text{H}_6$ 6_0^1 band. This is marked with an asterisk (*). The simulated contour is only the 6_0^1 band of $^{12}\text{C}_6\text{H}_6$, hence the poor fit between experimental and simulated contours at the (*) position. (B) The experimental spectrum generated from room temperature background signal in the TOF-MS. By performing 1+1 REMPI in the TOF-MS, mass selection of the ions allows the $^{12}\text{C}_6\text{H}_6$ molecules to be analysed independently of the $^{13}\text{C}^{12}\text{C}_5\text{H}_6$ isomer. Comparison with the simulated spectrum shows that the shoulder caused by the $^{13}\text{C}^{12}\text{C}_5\text{H}_6$ isomer is no longer present. The absorption contours generated after mass selection were used in the best temperature fit analyses.

are confident that we observed thermally equilibrated benzene inside the TOF-MS since the sum of the $^{12}\text{C}_6\text{H}_6$ and $^{12}\text{C}_5^{13}\text{CH}_6$ rotational contours produced in the TOF-MS are equivalent to the spectrum generated in the static cell.

All of the different absorption bands are first simulated and then fit to the experimental room temperature spectrum. An absorption spectrum is a 1D spectrum consisting of absorption cross-section as a function of photon energy. Fitting of a 1D spectrum is performed using a Levenberg-Marquardt non-linear least squares algorithm [26]. However, for the more complex absorption feature, the $6_0^1 16_1^1 / 6_0^1 11_1^1$ combination band, 2D (absorption/fluorescence), room temperature spectra were also generated in an effort to deconvolute the overlapping bands and increase the accuracy of the fitting results (see Section 3.4). Due to the increased number of variables required to fit a 2D spectrum, the more sophisticated Simplex algorithm was employed [26,27].

For all the simulations performed here, the initial ground state rotational constants are taken from high resolution infrared studies by Hollenstein *et al* [25] and Okrus *et al* [23]. For all the bands (except the 6_0^1), rotational constants in the $^1B_{2u}$ electronic state are estimated by varying the simulation parameters until a best-fit, that is, a minimum in χ^2 , is obtained. Each spectral line within the simulated contour is convoluted with a Gaussian of FWHM 0.3 cm^{-1} to account for the bandwidth of the laser as well as any Doppler broadening effects. Overlaying each of the simulated contour generated here with the absorption spectra reported by Atkinson [9] also shows good correlation.

Comparison with a rotationally cold benzene spectrum generated in a free-jet expansion shows the simulations accurately reproduce the change in shape of a rotational contour with temperature. 5 K benzene was produced by expanding benzene in a free-jet of Helium or Nitrogen (10 kPa benzene in 350 kPa of buffer gas). Micron sized capillary nozzles have proven to be capable of creating a free jet expansion [28,29] so the same orifice used to

produce the *in vacuo* liquid micro-jet is used to expand the benzene/buffer gas mix into the vacuum. It is known that the energy distribution of molecules cooled in this way can often be slightly non-Boltzmann since the gas phase collisions cool the molecules so efficiently that the rotational populations can be frozen before they are able to reach equilibrium [30]. For this reason the simulations – which assume a Boltzmann population distribution amongst rotational states, differ slightly in shape from the gas jet cooled benzene contours [31] - however the major features and band splitting are accurately reproduced.

3.3.1 Simulation of the 6_0^1 Absorption Feature

Simulation of the 6_0^1 contour was straightforward since all the rotational constants were taken from the high resolution studies by Okruss *et al* [23]. Table 3.11 and Table 3.12 show the vibrational angular momentum terms and spectroscopic constants that must be considered when simulating the 6_0^1 band. From Figure 3.6 it is clear that the 6_0^1 contour should be of type since Okruss reports the excited state Coriolis constant of $\sim +0.6$.

When fit to the gas phase room temperature spectrum the simulations give an accurate indication of the ground state rotational temperature of the benzene sample (see Figure 3.10). For temperature fitting of the room temperature 6_0^1 band the part of the P branch overlapping with the 16_0^2 band was not included. The 6_0^1 absorption spectrum generated in a free-jet expansion of nitrogen is shown in Figure 3.10(B). The best-fit simulated contour was found to have a rotational temperature of 5.2 ± 0.1 K, where the error is 1 standard deviation. As previously mentioned it is common for molecules to exhibit non-Boltzmann rotational distributions when expanded in a free-jet environment [30]. This is thought to be the cause of the small intensity mismatch between the simulated and cold experimental spectrum.

Table 3.11: Vibrational anharmonicity energy factors and effective Coriolis constant involved in the 6_0^1 transition.

State	l_6	$\sum_i \sum_{j \geq i} g_{ij} l_i l_j$	ζ_{eff}
$6^1 l^{-1}$	-1	$g'_{6,6}$	$-\zeta'_6$
$6^1 l^{+1}$	+1	$g'_{6,6}$	ζ'_6
6_0	0	0	0

Table 3.12 Spectroscopic constants used in the simulation of $6_0^1 l_0^{\mp 1}$. All rotational constants and the Coriolis constant were taken from Okrusz [23]. The anharmonic constants are taken from Atkinson [5].

Constant [cm^{-1}]	Vibronic State	
	$6_0 l_0$	$6^1 l^{\mp 1}$
B	0.18977	0.18179
C	0.09489	0.09087
ζ_{eff}	-	0.5785

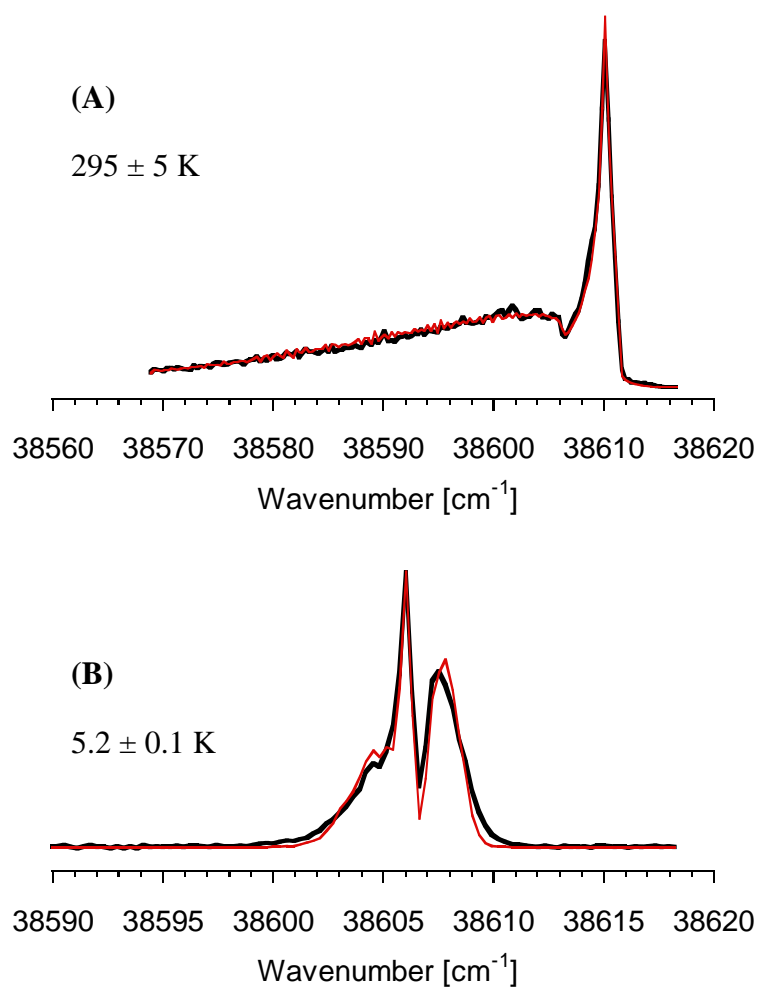


Figure 3.10: Simulation of 6_0^1 absorption feature. In Figure (A) the simulated contour (red) is fit to an experimental spectrum (black) generated by 1+1 REMPI in the Source of a TOF-MS. In Figure (B) the simulated contour is fit to an experimental spectrum generated in free-jet expansion of benzene and nitrogen. The best-fit temperatures were found by using the spectroscopic constants reported in Table 3.12. The reported errors are 1 standard deviation of the best-fit temperature.

3.3.2 Simulation of the 6_1^2 and $6_1^0 11_0^2$ Absorption Features

Like the 6_0^1 transition, both the 6_1^2 and $6_1^0 11_0^2$ transitions involve a single quanta change in the vibration ν_6 . The states and their vibrational angular momentum components are summarised in Table 3.13 and Table 3.14.

Table 3.13: Vibrational anharmonicity energy factors and effective Coriolis constant for states involved in the transition 6_1^2 .

State	l_6	$\sum_i \sum_{j \geq i} g_{ij} l_i l_j$	ζ_{eff}
$6^2 l^{-2}$	-2	$+4g'_{6,6}$	$-2\zeta'_6$
$6^2 l^{+2}$	+2	$+4g'_{6,6}$	$2\zeta'_6$
$6^2 l^0$	0	0	0
$6_1 l_{-1}$	-1	$g''_{6,6}$	$-\zeta''_6$
$6_1 l_{+1}$	+1	$g''_{6,6}$	ζ''_6

Table 3.14: Vibrational anharmonicity energy factors and effective Coriolis constant for states involved in the transition $6_1^0 11_0^2$.

State	l_6	l_{11}	$\sum_i \sum_{j \geq i} g_{ij} l_i l_j$	ζ_{eff}
$6^0 l^0 11^2 l^0$	0	0	0	0
$6_1 l_{+1}$	+1	-	$g''_{6,6}$	ζ''_6
$6_1 l_{-1}$	-1	-	$g''_{6,6}$	$-\zeta''_6$

Recall from Section 3.2.3 that it is the values of ζ_{eff} that primarily determines the shape of a rovibrational contour. Knowing that the value of ζ''_6 is $\sim +0.6$ [18], from the data in Table 3.13 and Table 3.14 it is clear both contours should be type I since $\chi \sim -0.4$. However, the 6_1^2 is split by the interaction of two quanta of the degenerate ν_6 vibration in the excited state. In Table 3.10 it is shown that there are 4 different allowed combinations of vibrational angular momenta, resulting in two independent transitions $6_1^2 l_{\mp 1}^{\mp 2}$ and $6_1^2 l_{\pm 1}^0$. From Equation 3.19 we

can see that the energy of each of the possible 6^2 states can differ due to the $\sum_i \sum_{j \geq i} g_{ij} l_i l_j$ factor (see Table 3.13). The vibrational interaction results in an energetic splitting of the bands of $4g'_{6,6}$. Page *et al* reported a $g'_{6,6}$ value of 1.7 cm^{-1} causing a splitting of the bands of $\sim 7 \text{ cm}^{-1}$ [6]. This value agrees with our simulation of the 6_1^2 band. However, the absorption contours are further complicated by the fact that the $6^2 l^0$ and 11^2 states are of the same vibronic symmetry and nearly energetically degenerate and so interact by fermi resonance. Mixing of the states causes a shift in frequency of each state as well as affecting the intensity of transitions into these states. As a result the vibrational origin of each component of this mixed band appears on either side on the $6_1^2 l_{\mp 1}^{\mp 2}$ vibrational origin. The assignment of these bands agrees with that suggested by Fischer [21] and supported by the fluorescence studies of Stephenson [7]. From the best-fits of the simulation to the experimental room temperature spectrum, the frequency shift caused by the fermi resonance was estimated to be 5.919 cm^{-1} . The fermi resonance and vibrational mixing effect seen in these bands are summarised in Figure 3.11.

At ambient temperatures in this area of the benzene absorption spectrum all of the rotational contours overlap and distort the shape of the adjacent bands. As a consequence of this, when trying to overlay a simulated contour with an experimental contour, a baseline consisting of the tail of the neighbouring contour has to be removed. Sitting on the tail of the 6_0^1 P branch Atkinson and Parmenter identified the 16_0^2 band [5]. This band was also simulated in this study so that it could be removed as a baseline running under the neighbouring $6_1^2/6_1^0 11_0^2$ combination band. The rotational constants for this band were taken from Weber and Neusser [32]. Table 3.15 outlines the vibrational angular momentum combinations of each state involved in the transition 16_0^2 . Reidle and Pliva's high resolution studies of benzene show that ν_{16} produces little Coriolis interaction ($\zeta_{16} = 0.0003$) so the 16_0^2 is classed as type II [33].

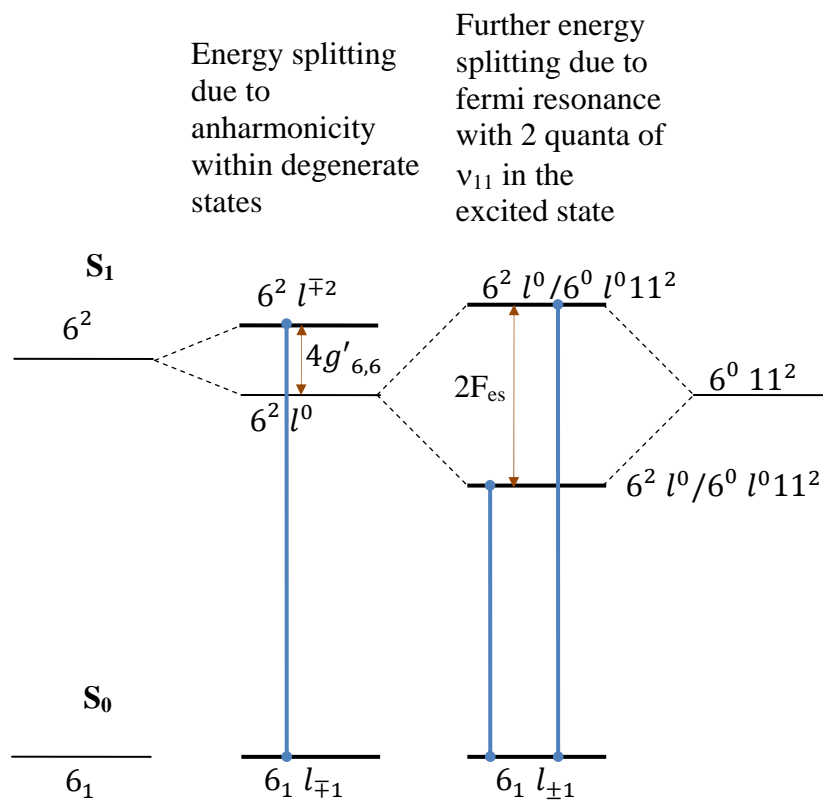


Figure 3.11: Illustration of the perturbation of vibronic state energies due to both anharmonic interaction and fermi resonances between vibronic states. The result is the distortion of predicted intensities of the rovibrational contours as well as displacement from their unperturbed origins. The levels in bold are those that are thought to be involved in the transitions.

Table 3.15: Vibrational anharmonicity energy factors and effective Coriolis constant from states involved in the 16_0^2 transition.

State	l_{16}	$\sum_i \sum_{j \geq i} g_{ij} l_i l_j$	ζ_{eff}
$16^2 l^{+2}$	+2	$4g'_{16,16}$	$2\zeta'_{16}$
$16^2 l^{-2}$	-2	$4g'_{16,16}$	$-2\zeta'_{16}$
16_0	0	0	0

ν_{16} does not show a Coriolis effect since the nuclear motion is out-of-plane, parallel to the molecular axis [2].

The overlay of simulated and experimental spectra is displayed in Figure 3.12. From the simulation results of the 6_0^1 absorption band the room temperature spectrum is found to have a rotational temperature of 295 K. Assuming the same rotational temperature for the room temperature $6_1^2/6_1^0 11_0^2$ band, the value of the excited state spectroscopic constants were varied until best-fit between the simulated and experimental spectrum was obtained. On the tail of the $6_1^2/6_1^0 11_0^2$ Lyman identified the $6_0^1 18_1^1$ band [34]. For spectral fitting this part of the $6_1^2/6_1^0 11_0^2$ band was not included. The ground-state constants were taken from the high-resolution infrared studies performed by Hollenstein *et al* [25]. The best-fit values for the excited state constants determined in this study are reported in Table 3.16. During the fitting it was assumed that $6_1 l_{\mp 1}$ and $6_1 l_{\pm 1}$ states are indistinguishable and so are described by the same spectroscopic constants.

The constants reported in Table 3.16 were used when temperature fitting the cold spectrum generated in the free-jet expansion. The results of simulating the cold benzene spectrum are displayed in Figure 3.12(B). The best-fit rotational temperature is determined to be 5.2 ± 0.1 K, where the quoted error is 1 standard deviation in the temperature (1σ). This rotational

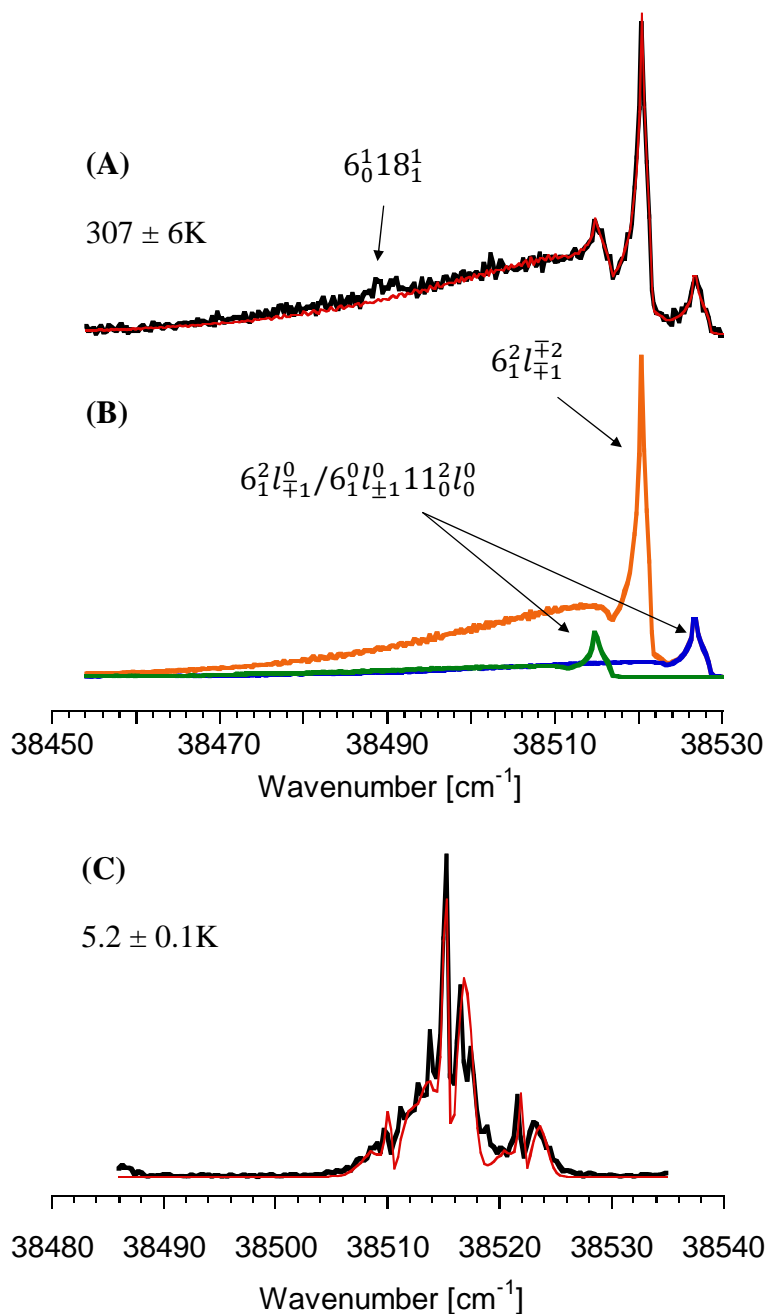


Figure 3.12: Figure (A) is an overlay of the simulated (red) contour with the experimentally obtained REMPI spectrum (black) of room temperature benzene vapour. The tail of the adjacent 16_0^2 and 6_0^1 bands were removed as a baseline from the experimental spectrum before fitting. The small bump on the tail on the contour has been assigned by Lyman as the $6_0^1 18_1^1$ band [33]. This band was not included in the simulations. Figure (B) identifies the three sub-bands that contribute to the overall contour. The blue and green bands are identical except that they are split by fermi resonance (see Figure 3.11). Figure (C) is an overlay of the simulated (red) contour with the experimental spectrum obtained from a free-jet expansion of benzene in nitrogen (black). The temperatures quoted are the best temperature fits to the experimental contours using the spectroscopic constants from Table 3.16.

Table 3.16: Spectroscopic constants used in the simulation of $6_1^2/6_1^0 11_0^2$. (*)Ground state rotational constants were taken from Hollenstein [25]. (†) The value for the ground state Coriolis constant was taken from Weber [18] The anharmonic constants are taken from Atkinson [5]. The excited state rotational constants were determined by fitting of the room temperature experimental spectrum with a simulated spectrum. The standard deviation is given in parenthesis in units of the last digit.

Constant [cm^{-1}]	Vibronic State		
	$6_1 l_{\mp 1}$	$6^2 l^{\mp 2}$	$6^2 l^0 / 6^0 l^0 11^2 l^0$
B	0.189635*	0.181982(3)	0.181309(9)
C	0.09482*	0.090803(3)	0.090961(7)
ζ_6	0.588†	0.1951(5)	0.1951(5)
$g_{6,6}$	0	1.7	1.7
$x_{6,6}$	1.05	0.7	0.7
$x_{6,11}$	-	-4.5	-4.5
Fermi splitting	-	-	5.919(6)

temperature is consistent with the rotational temperature of the vibrationless ground state determined when fitting the 6_0^1 cold spectrum. The close fit between the simulated and experimental cold spectra shows that the simulation procedure is able reproduce the benzene 1+1 REMPI spectrum over a very broad temperature range. This result is justification for using the technique to determine the rotational temperature of absorption spectra generated in environments of unknown temperature. The small intensity disparities are attributed to the departure of the rotational population from Boltzmann as was observed in the 6_0^1 band.

Both 6_1^2 and $6_1^0 11_0^2$ are hot bands which originate from a single quantum vibration of type ν_6 . Therefore, their relative intensities depend primarily upon the relative strengths of the Frank-Condon factor, C . The $6_1^0 11_0^2$ transition involves an unfavourable 3 quanta vibrational change which Fischer predicts results in the band being about $\frac{1}{30}$ the intensity of the 6_1^2 transition [21]. Fermi resonance, however, is thought to allow the $6_1^0 11_0^2$ transition to steal intensity from the $6_1^2 l_{\pm 1}^0$ transition making it stronger than predicted. The results of the spectral fitting in this

study show the relative intensities are 2.3: 1 for $6_1^2 l_{\mp 1}^{\mp 2} : (6_1^2 l_{\pm 1}^0 / 6_1^0 l_{\pm 1}^0 11_0^2)$ - consistent with Fischer's analysis of the same band.

The difference between the excited and ground state rotational constants determined from the spectral fitting are reasonable when rotational defects caused by electronic and vibrational excitation are considered. Consistent with the values for the rotational constants involved in the 6_0^1 transition, all the transitions here show a common decrease (of $\sim 4\%$) in the value of B with electronic excitation. A decrease in B indicates that the average ring diameter is larger when benzene is electronically excited. In general, all of the bands studied also showed a deviation from planar geometry in the excited electronic state i.e., $C' \neq B'/2$ [2,35]. The high resolution studies by Reidle *et al* have confirmed that electronic excitation of benzene distorts the planar geometry [36]. When vibrational excitation accompanies the electronic transition the planar ring can be distorted even further. The effect is described by the rotational defect (Δ_ν) which is defined as [33,35]:

$$\Delta_\nu = \frac{h}{8\pi^2 c} \left(\frac{1}{C_\nu} - \frac{2}{B_\nu} \right). \quad \text{Equation 3.25}$$

C_ν and B_ν are the rotational constants for state ν , h is Plank's constant and c , the speed of light. As expected, the different types of vibrations differ in their effect on the excited state rotational constants since they distort the molecular geometry in different ways. Figure 3.8 describes the nuclear motion for the vibrations of interest and Table 3.17 shows the rotational defect observed in the excited states studied here. Literature values of Δ_ν have also been included in the table for comparison. Consistently it is the out-of-plane vibrations (ν_{11} , ν_{16} , ν_{10}) that show the largest rotational defects. The in-plane ring stretches (ν_1 , ν_6 , ν_{14}) show little defect though their effect is understandably increased with an increased number of vibrational

quanta excited. Interestingly, separate analysis of the two sub states $6^2 l^{\mp 2}$ and $6^2 l^0$ shows that rotational defects for each state are of opposite sign. Reidle and Pliva made the same observation in their study of rotationally resolved sub-bands of both the $6_0^1 10_0^2$ and $6_0^1 16_0^2$ [33]. They attributed this result to an inability of the theory to adequately describe the result of mixing vibrational angular momenta.

Table 3.17: Comparison of rotational defects for molecules vibrating in the ${}^1B_{2u}$ electronic state of benzene. All rotational constants are the best-fit values from fitting of the room temperature absorption spectrum. Δ_v given in units of $\text{amu}\cdot\text{\AA}^2$. For comparison literature values of rotational constants and Δ_v are included in the bottom half of the table. These values were taken from the following sources: (*) Riedle [19], (¥) Weber [33], (†) Sieber [37].

Vibronic states	B'	C'	Δ_v	
$6^1 l^{\mp 1}$	0.18179	0.09087	0.051	
$6^2 l^{\mp 2}$	0.181982(3)	0.090803(3)	0.384	
$6^2 l^0 / 6^0 l^0 11^2 l^0$	0.181309(9)	0.090961(7)	-0.627	
$1^1 6^1 l^{\mp 1}$	0.181648	0.090855	-0.0633	*
$6^1 l^{\mp 1} 16^2 l^0$	0.181746	0.089941	1.92	¥
$6^1 l^{\pm 1} 16^2 l^{\mp 2}$	0.181722	0.092572	-3.43	¥
$6^1 l^{\mp 1} 10^2 l^0$	0.181941	0.090398	1.17	¥
$6^1 l^{\pm 1} 10^2 l^{\pm 2}$	0.181778	0.091541	-1.32	¥
14^1	0.1812836	0.0907110	-0.142	†
$10^2 l^{\mp 2}$	0.181741	0.090949	-0.1601	¥
$16^2 l^{\pm 2}$	0.181660	0.091189	-0.7313	¥

3.3.3 Simulation of the $6_0^1 16_1^1$ and $6_0^1 11_1^1$ Absorption Features

The feature that appears at $\sim 38450 \text{ cm}^{-1}$ was tentatively assigned by Fischer as the overlapping combination bands $6_0^1 16_1^1$ and $6_0^1 11_1^1$ [7,21]. Fluorescence studies by both Stephenson [7] and Atkinson and Parmenter [5] support this assignment. Assignment of the bands according to their vibrational anharmonic components is, however, not straightforward. Since both ν_6 and ν_{16} are degenerate vibrations, the $6_0^1 16_1^1$ transition comprises of 6 individual components that are distinguished by their combinations of angular momenta from each

vibration. The $6_0^1 l_0^{\mp 1} 16_1^1 l_{\pm 1}^{\pm 1}$ and $6_0^1 l_0^{\mp 1} 16_1^1 l_{\mp 1}^{\mp 1}$ components produce individual contours of type I. These bands are split by vibronic interaction on the order of $2g'_{6,16}$ (see Table 3.18). Garfold and Ingold estimate the split as $\sim 4 \text{ cm}^{-1}$ giving a unsigned $g'_{6,16}$ value of $\sim 2 \text{ cm}^{-1}$ [38], which is close to the -1.55 cm^{-1} estimated by Atkinson and Parmenter** [5]. The last two components of this band are $6_0^1 l_0^{\pm 1} 16_1^1 l_{\pm 1}^{\mp 1}$. The vibrational origin of these components sit under the $6_0^1 l_0^{\mp 1} 16_1^1 l_{\mp 1}^{\mp 1}$ components however they appear shifted to lower energies since they produce a type III band which is much more symmetrical than a type I band. Atkinson and Parmenter predict that this band would be difficult to identify in the spectrum since type III contours are broad and featureless, and in addition this component is a third-order transition ($|\Delta l_6|=1, |\Delta l_{16}|=2$) and the transition probability for such a transition would be low [9].

Table 3.18: Vibrational anharmonicity energy factors and effective Coriolis constant for states involved in the transition $6_0^1 16_1^1$.

State	l_6	l_{16}	$\sum_i \sum_{j \geq i} g_{ij} l_i l_j$	ζ_{eff}
$6^1 l^{-1} 16^1 l^{-1}$	-1	-1	$g'_{6,6} + g'_{16,16} + g'_{6,16}$	$-\zeta'_6 - \zeta'_{16}$
$6^1 l^{+1} 16^1 l^{+1}$	+1	+1	$g'_{6,6} + g'_{16,16} + g'_{6,16}$	$\zeta'_6 + \zeta'_{16}$
$6^1 l^{+1} 16^1 l^{-1}$	+1	-1	$g'_{6,6} + g'_{16,16} - g'_{6,16}$	$\zeta'_6 - \zeta'_{16}$
$6^1 l^{-1} 16^1 l^{+1}$	-1	+1	$g'_{6,6} + g'_{16,16} - g'_{6,16}$	$-\zeta'_6 + \zeta'_{16}$
$6_0 l_0 16_1 l_{+1}$	0	+1	$g''_{16,16}$	$+\zeta''_{16}$
$6_0 l_0 16_1 l_{-1}$	0	-1	$g''_{16,16}$	$-\zeta''_{16}$

Unlike ν_{16} , ν_{11} is not a degenerate vibration so it does not contribute to the vibrational angular momentum in the excited state. Consequently, $6_0^1 11_1^1$ is split into only two components, $6_0^1 l_0^{\mp 1} 11_1^1 l_0^0$ resulting in a single band of type I. Until this study, the exact position of the band under the $6_0^1 16_1^1$ had not been known precisely because the frequency of ν_{11} in the ${}^1B_{2u}$ electronic state was known only to an accuracy of a few wavenumbers ($515\text{-}518 \text{ cm}^{-1}$) [5,6]. Fischer and Jakobson noted that because the Frank-Condon factor for $6_0^1 11_1^1$ is similar to

** The sign of the anharmonic constants depends upon the arbitrary assignment of the signed l quantum numbers.

$6_0^1 16_1^1$ and the Boltzmann factor is half that of $6_0^1 16_1^1$, then the intensity of the underlying $6_0^1 11_1^1$ band should be comparable to a sub-band of the $6_0^1 16_1^1$ [21]. The anharmonic constants required to simulate the $6_0^1 11_1^1$ absorption band are shown in Table 3.19.

Table 3.19: Vibrational anharmonicity energy factors and effective Coriolis constant for states involved in the transition $6_0^1 11_1^1$.

State	l_6	l_{11}	$\sum_i \sum_{j \geq i} g_{ij} l_i l_j$	ζ_{eff}
$6^1 l^{-1} 11^1 l^0$	-1	0	$g'_{6,6}$	$-\zeta'_6$
$6^1 l^{+1} 11^1 l^0$	+1	0	$g'_{6,6}$	$+\zeta'_6$
$6_0 l_0 11_1 l_0$	0	0	0	0

The room temperature absorption spectrum of these bands was overlaid with the simulated contours and variables adjusted until a best-fit was achieved. The fitting variables consisted of the excited state rotational constants, Coriolis and anharmonic factors, the relative intensity of the third-order component, $6_0^1 l_0^{\pm 1} 16_1^1 l_{\pm 1}^{\mp 1}$, and the intensity and position of the $6_0^1 l_0^{\mp 1} 11_1^1 l_0^0$ relative to the first order $6_0^1 16_1^1$ components. The spectroscopic constants for this band are reported in Table 3.20 and Table 3.21. The best-fit simulation is displayed in Figure 3.13(A).

The value of $g_{6,16}$ in the excited electronic state was determined from the degree of splitting between the different components of the $6_0^1 16_1^1$. The value of -2.089 cm^{-1} is close to the value estimated by Atkinson of -1.55 cm^{-1} [5].

For simplicity it was assumed that states with different vibrational angular momentum components have the same value for the rotational constants^{††}. The tail of the adjacent $6_1^2 / 6_1^0 11_0^2$ band was removed as a baseline from the experimental spectrum before fitting. At

^{††} In the 2D simulations this assumption was not necessary as a more advanced fitting algorithm was used that can handle more fitting variables.

Table 3.20: Spectroscopic constants used in the simulation of the $6_0^1 16_1^1$ contour. (*) Ground state rotational constants were taken from Hollenstein [25]. The anharmonic constants are taken from Atkinson [5]. The excited state rotational constants were determined by fitting of the room temperature experimental spectrum with a simulated spectrum. It was assumed that the intensity of the third-order component (the $6_0^1 l_0^{\pm 1} 16_1^1 l_{\pm 1}^{\mp 1}$ transitions) was negligible during the fitting process. Allowing the rotational constants of the excited states to be different did not produced any improvements in the fit. The results reported here were generated assuming that the rotational constants in the excited state were equal. The standard deviation is given in parenthesis in units of the last digit for constants determined in this study.

Constant [cm^{-1}]	Vibronic State		
	$6_0 l_0 16_1 l_{\pm 1}$	$6^1 l^{\mp 1} 16^1 l^{\pm 1}$	$6^1 l^{\pm 1} 16^1 l^{\pm 1}$
B	0.189661	0.181280(6)	0.181280(6)
C	0.09483	0.090879(5)	0.090879(5)
Δ_v	-	-0.489	-0.489
ζ_{eff}	-	0.4795(9)	0.4795(9)
$g_{6,6}$	-	1.7	1.7
$g_{16,16}$	-0.52	0.88	0.88
$g_{6,16}$	-	-2.089(4)	-2.089(4)
$x_{6,6}$	-	0.7	0.7
$x_{16,16}$	-1.4	-1.22	-1.22
$x_{6,16}$	-	0.45	0.45

Table 3.21: Spectroscopic constants used in the simulation of the $6_0^1 11_1^1$ contour. (*) Ground state rotational constants were taken from Hollenstein [25]. The anharmonic constants are taken from Atkinson [5]. The excited state rotational constants were determined by fitting of the room temperature experimental spectrum with a simulated spectrum. The standard deviation is given in parenthesis in units of the last digit for constants determined in this study.

Constant [cm^{-1}]	Vibronic State	
	$6_0 l_0 11_1 l_0$	$6^1 l^{\mp 1} 11^1 l^0$
B	0.189638	0.18104(2)
C	0.09482	0.093018(7)
Δ_v	-	-5.00
ζ_{eff}	-	0.499(1)
$g_{6,6}$	-	1.7
$x_{6,6}$	-	0.7
$x_{6,11}$	-	-4.5

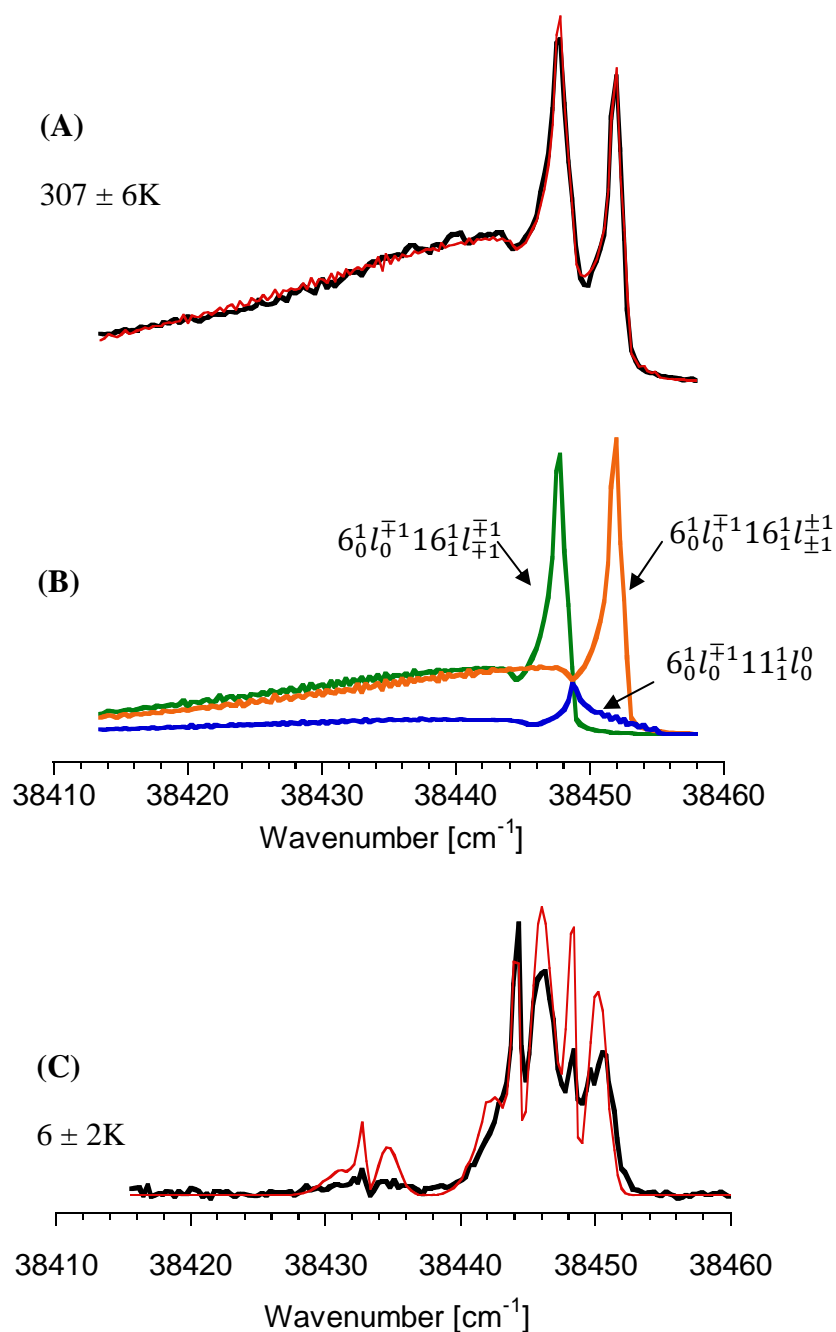


Figure 3.13: Figure (A) is an overlay of the simulated (red) contour with the experimentally obtained REMPI spectrum (black) of room temperature benzene vapour. The temperatures quoted are the best temperature fits to the experimental contours using the spectroscopic constants Table 3.20 and Table 3.21. Figure (B) identifies the sub-bands that contribute to the overall contour. Figure (C) is an overlay of the simulated (red) contour with the experimental spectrum (black) obtained from a free-jet expansion of benzene in nitrogen. The unidentified feature at $\sim 38434 \text{ cm}^{-1}$ was also simulated assuming it was also a type I band.

cold rotational temperatures this was not necessary as the rotational contours do not overlap. Cooling benzene down to 6 K in a free-jet expansion revealed the presence of another band with vibrational origin shifted $\sim 12.5 \text{ cm}^{-1}$ to the red of the $6_0^1 l_0^{\mp 1} 16_1^1 l_{\pm 1}^{\pm 1}$ component band origin. This unidentified band can also be seen in all of the fluorescence spectra of the sequence absorptions $6_0^1 16_1^1 1_0^n$ investigated by Atkinson and Parmenter [5]. This band is discussed further in Section 3.4.4. The unidentified band was added to the simulations of the cold spectrum in Figure 3.13(C) to demonstrate that it is likely a type I band in absorbance.

The best-fit results reported thus far are not deemed reasonable, though the residuals from the fits are small. To generate the best-fit simulated absorption spectrum shown here, the third-order transition $6_0^1 l_0^{\pm 1} 16_1^1 l_{\pm 1}^{\mp 1}$ had zero intensity, and the $6_0^1 l_0^{\mp 1} 11_1^1 l_0^0$ band shape is greatly distorted. Since ν_6 is the active vibration in this transition (ν_{11} is only active in the Frank-Condon factor) it is expected that the shape of the $6_0^1 16_1^1$ bands should be identical to the 6_0^1 band, differing only in any rotational defects caused by the out-of-plane vibrations. The shape of the simulated $6_0^1 11_1^1$ band shown in Figure 3.13 displays a rotational defect of -5.0, much larger than any other defects reported – even for states that involve multiple quanta of out-of-plane vibrations (see Table 3.17). The poor fit of the whole simulated spectrum to the free-jet spectrum is further evidence that the simulations are not accurately reproducing the $6_0^1 16_1^1 / 6_0^1 11_1^1$ feature. Although the temperature fitting produced a rotational temperature very close to the other rotational temperatures observed in the free-jet expansion, the intensities of the individual components are grossly distorted.

The main problem with fitting this eight component absorption band is that the band shows only two main features at room temperature. Consequently the multidimensional fitting surface is shallow and contains many local minima – making it difficult to locate the global fitting minimum. To overcome this problem, we developed a technique for producing a two-dimensional (2D) experimental spectrum, where fluorescence from a state could be monitored

as well as absorption into the state. Although this increases the number of variables that need to be fit, the addition of a second dimension means that the different components can be visually separated, minimising the area of the fitting surface that must be explored. A 2D absorption/fluorescence spectrum of the $6_0^1 16_1^1 / 6_0^1 11_1^1$ feature was produced using the Laser Induced Dispersed Fluorescence (LIDF) technique outlined below. When the 2D experimental spectrum is fit with a 2D simulated spectrum the values obtained for the spectroscopic constants are more accurate than those determined from fitting the equivalent 1D absorption spectrum. The details of this technique and the results of the simulation fitting are reported in Section 3.4.

3.4 Laser Induced Dispersed Fluorescence (LIDF)

The de-convolution of overlapping absorption bands in the benzene UV spectrum greatly enhances the accuracy with which the origin of the electronic transitions can be reported. In particular, the coincidental energies of the electronic transitions $6_0^1 16_1^1$ and $6_0^1 11_1^1$ in benzene have prevented an accurate measurement of the vibrational frequency of ν_{11} in the ${}^1B_{2u}$ excited electronic state. In turn this limits the accuracy with which the rotational contours can be simulated. Accurate simulations are required in this study as they are used to determine molecular rotational and vibrational temperatures of the data presented in Chapters 4 and 5.

The Laser Induced Dispersed Fluorescence (LIDF) technique developed in the Lawrance Laboratory at The Flinders University of South Australia^{‡‡} has the capability of separating out the overlapping bands whilst maintaining their identity by exploiting the different anharmonic coupling between vibrational states in the ground electronic state. At the time of publication it is believed that the LIDF spectra presented herein are the highest resolution 2D spectra of their type produced to date.

^{‡‡} Flinders University of South Australia, Bedford Park, South Australia

3.4.1 Experimental Technique

The LIDF technique involves collecting a dispersed fluorescence spectrum from all of the states excited from an absorption transition of a molecule. The result is a two-dimensional (2D) map of the photo-excitation/de-excitation process. If the final vibrational state for the fluorescence transition is chosen to be different to the initial state for the absorption transition then bands that overlap in the absorption dimension can be visually separated in the LIDF spectrum and thus analysed independently.

A schematic of the experimental setup is shown in Figure 3.14. A room temperature benzene LIDF spectrum is produced by first expanding the benzene into a chamber through a pulsed nozzle. To ensure the benzene is thermally equilibrated the expansion is scattered from a metal plate inside the chamber and no buffer gas is used in the expansion. The backing pressure behind the pulsed nozzle is the room temperature vapour pressure of benzene (11 Torr).

Benzene molecules that pass through the path of the UV laser may absorb the UV photons and then fluoresce. The fluorescence is collected and focused through a slit by a 100 mm focal length lens. The width of the slit is variable and ultimately determines the resolution at which the emission spectra can be observed. The fluorescence is introduced into a 4.2 m Czerny-Turner spectrometer which is operating in the fourth order at a dispersion of $5\text{cm}^{-1}.\text{mm}^{-1}$. The fluorescence is dispersed by the internal grating and then imaged upon a home built CCD Camera with a Kodak KAF-0402ME sensor. The incident photon's horizontal displacement on the camera array is a function of its frequency. If the slit has a width of 100 μm or less, then the fluorescence profile is Gaussian, at larger slit widths the profile tends toward a boxcar shape [20]. All the experiments conducted here used a 25-100 μm slit width. The

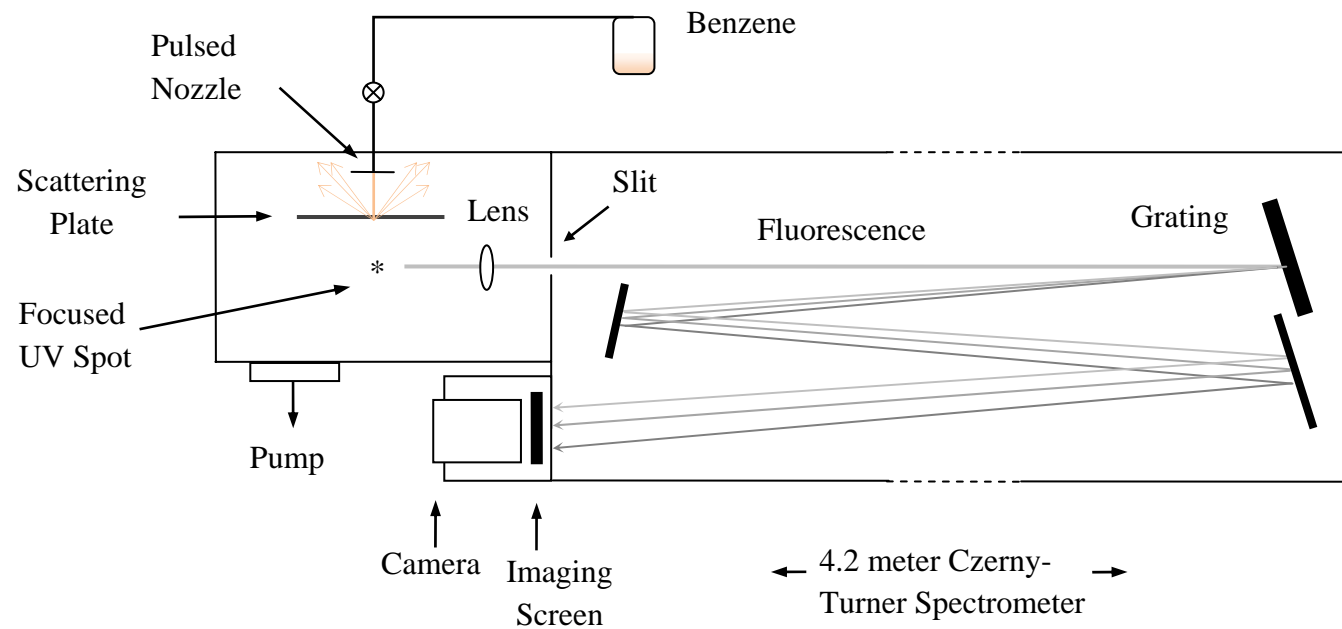


Figure 3.14: Experimental setup for recording the 2D - LIDF spectrum of room temperature benzene.

result is a dispersed fluorescence spectrum such as in Figure 3.15 which is typically generated by 5000 -10,000 laser shots. For a 10 Hz laser this equates to 8-16 minutes per image. At low temperatures a single rotational contour of dispersed fluorescence fits well within the 100 cm^{-1} frequency window of the camera.

It is important to keep the pressure in the chamber low to avoid re-absorption of the fluorescence as well as to prevent collisional relaxation of the electronically excited molecules. Whetton *et al.* have shown that collisional relaxation from rotational levels in the excited electronic states of benzene occurs at pressures greater than 60 mTorr [39]. Any collisional relaxation would distort the dispersed fluorescence spectrum obtained, so the Source Chamber is maintained at a stable base pressures of $\sim 10\text{-}20$ mTorr. At pressures higher than this fluorescence intensities decreased dramatically.

Rotationally cold spectra were also produced by replacing the room temperature expansion of benzene with a free-jet expansion of benzene in Helium. The chamber was evacuated to $\sim 10^{-6}$ Torr and the expansion mixture was typically 1% benzene in the buffer gas.

A schematic of the LIDF process is illustrated in Figure 3.16. A LIDF spectrum is produced by scanning the wavelength of the excitation laser and collecting the dispersed fluorescence at each wavelength. The integrated intensity of each dispersed fluorescence spectrum (which is proportional to the total undispersed fluorescence) as a function of excitation frequency generates an excitation (LIF) spectrum which when combined with the dispersed fluorescence spectra produces a 2D map of the photo excitation/de-excitation process. UV laser power was monitored with an Ophir pyrometer (Ophir PE9-SH) at the exit to the Source Chamber. The power was recorded as a function of time and then correlated with the integrated intensity of the images at each wavelength. A concern with measuring the power after the chamber was

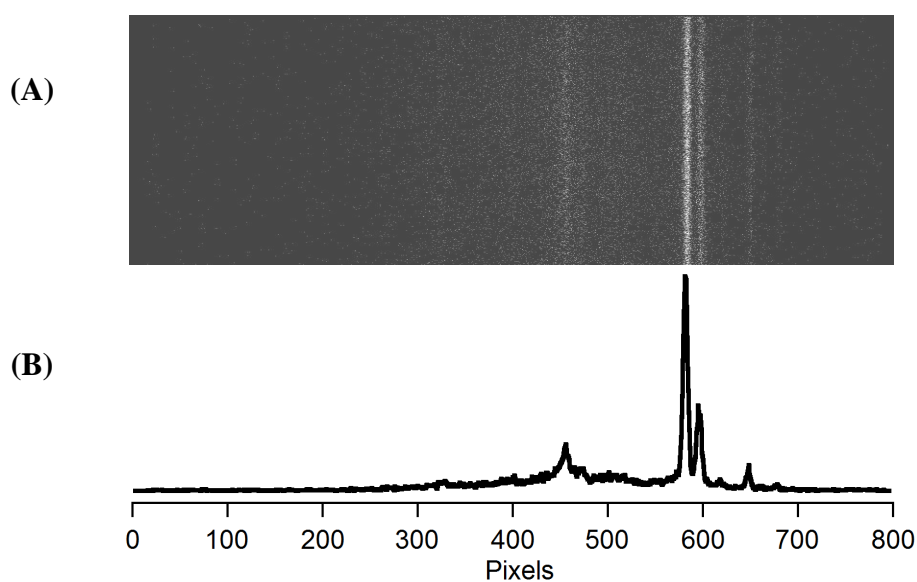
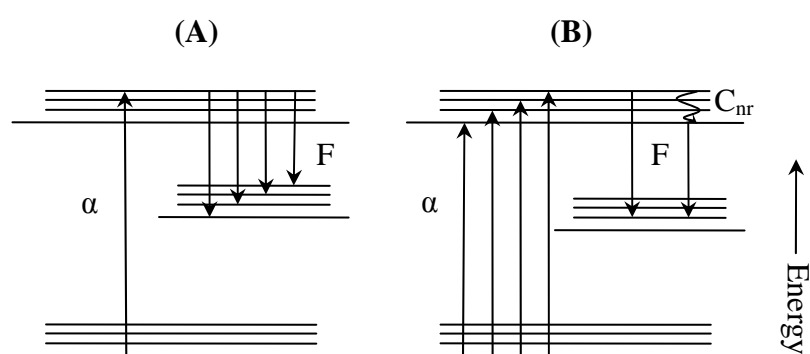


Figure 3.15: Typical dispersed fluorescence spectrum generated by the imaging spectrometer. This image was collected over 10,000 laser shots with a slit size of $100\ \mu\text{m}$, giving a resolution of $0.5\ \text{cm}^{-1}$. This image was generated by exciting warm benzene with light of energy $38447\ \text{cm}^{-1}$ which corresponds to the absorption transition $6_0^1 16_1^1 / 6_0^1 11_1^1$. The observed dispersed fluorescence is $1_1^0 6_0^1 16_1^1 / 1_1^0 6_0^1 11_1^1$.



(α) Absorption

(F) Fluorescence

(C_{nr}) Non-radiative relaxation
caused by molecular collisions

Figure 3.16: (A) Laser Induced Fluorescence. The energy of the excitation photon remains constant whilst the spectrum of emitted photons is collected. (B) Dispersed Fluorescence. The energy of the excitation laser is scanned whilst monitoring the intensity of the emitted photons. A single fluorescence energy can be monitored or the total summed fluorescence. The LIDF technique simultaneously records both the Laser Induced and Dispersed Fluorescence spectra.

that the frequency dependent absorption by the benzene molecules may distort the recorded power spectrum. However at these Source Chamber pressures the percentage of light absorbed by the molecules is smaller than the noise in the recorded power spectrum.

3.4.2 Interpretation of a LIDF image

Figure 3.17 and Figure 3.18 are examples of experimentally generated, room temperature LIDF spectra of vibronic bands of benzene. Figure 3.17 was generated by absorbance through the 6_0^1 vibronic transition and the subsequent collection of the dispersed fluorescence through the same transition, 6_0^1 . Figure 3.18 was generated by absorbance through the $6_1^2/6_1^0 11_0^2$ vibronic transition and the subsequent collection of the dispersed fluorescence through the same transition, $6_1^2/6_1^0 11_0^2$. Parallel to the main diagonal feature in both LIDF spectra run two additional diagonals of much lower intensity. These features are called Rowland ghosts and they are produced by periodic errors in the spectrometer grating groove locations [40].

An interesting feature of all of the experimentally obtained LIDF spectra is the striping or ‘feathering’ of the sub-bands. This feathering is rotational structure and is reproduced in the simulated images. The enhanced resolution of the LIDF spectrum compared with the 1D absorption spectrum, is due solely to the introduction of a second dimension of observation. Since the detail of rotational structure can now be seen, fitting of simulated spectra to the experimental spectra can be performed with a much higher accuracy.

To demonstrate the effect of the size of the Coriolis constant (ζ) on the shape of the LIDF spectra, the $6_0^1/6_0^1$ LIDF spectrum was simulated with varying values for the excited state effective Coriolis constant (ζ_6'). Examples of simulated LIDF spectra based on this $6_0^1/6_0^1$

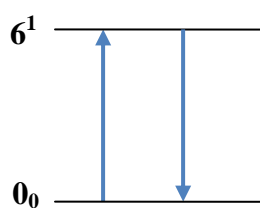
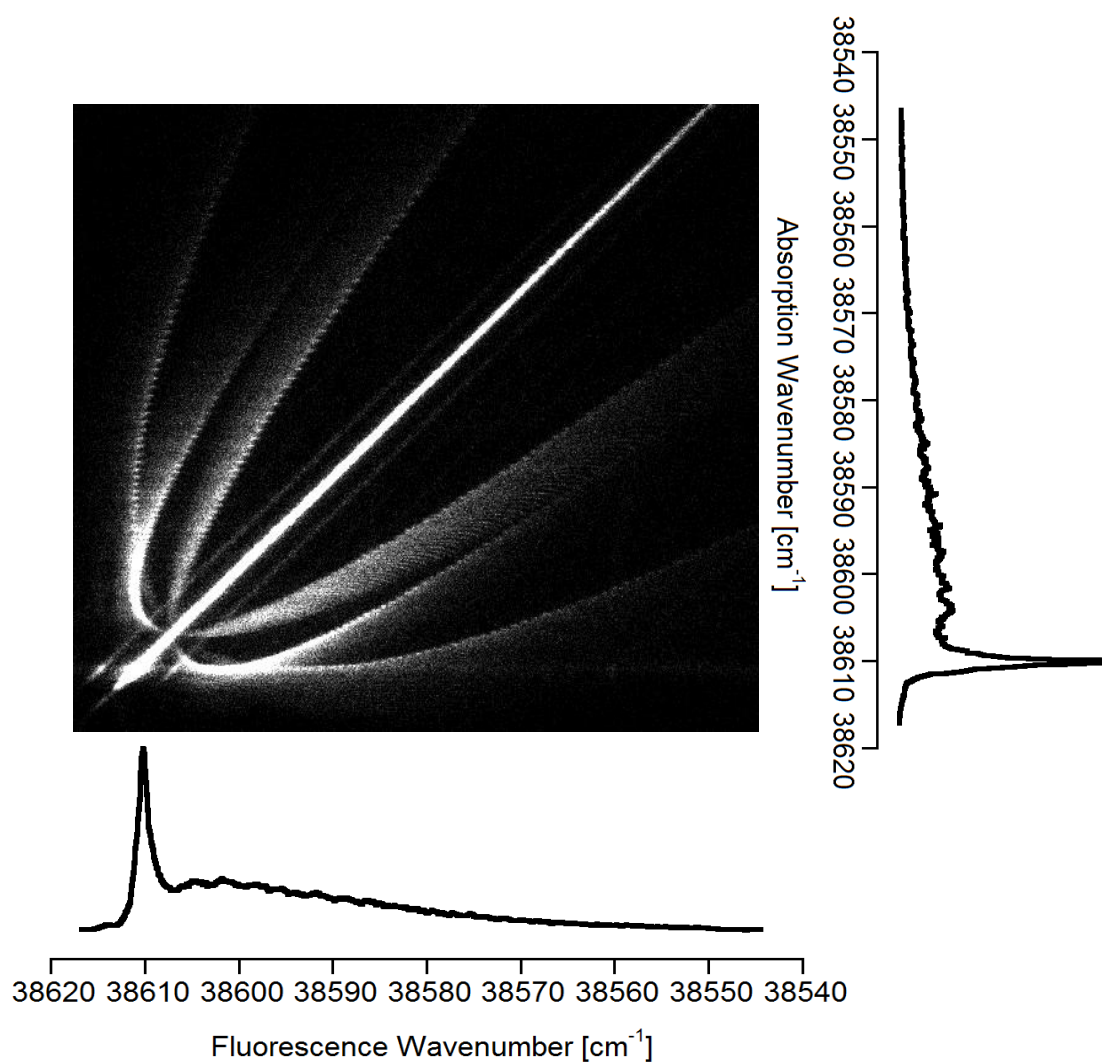


Figure 3.17: Experimental LIDF spectrum of the 6_0^1 absorbance / 6_0^1 fluorescence transition. Absorption step size 0.001 nm, Fluorescence energy/pixel 0.13 cm^{-1} (fluorescence slit width of $25 \text{ }\mu\text{m}$). This spectrum has not been normalised to laser power. The intensity fluctuations of the absorption contour are due to fluctuations in laser power.

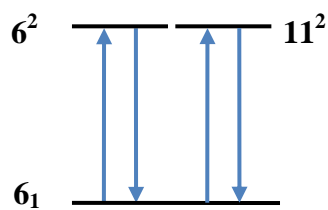
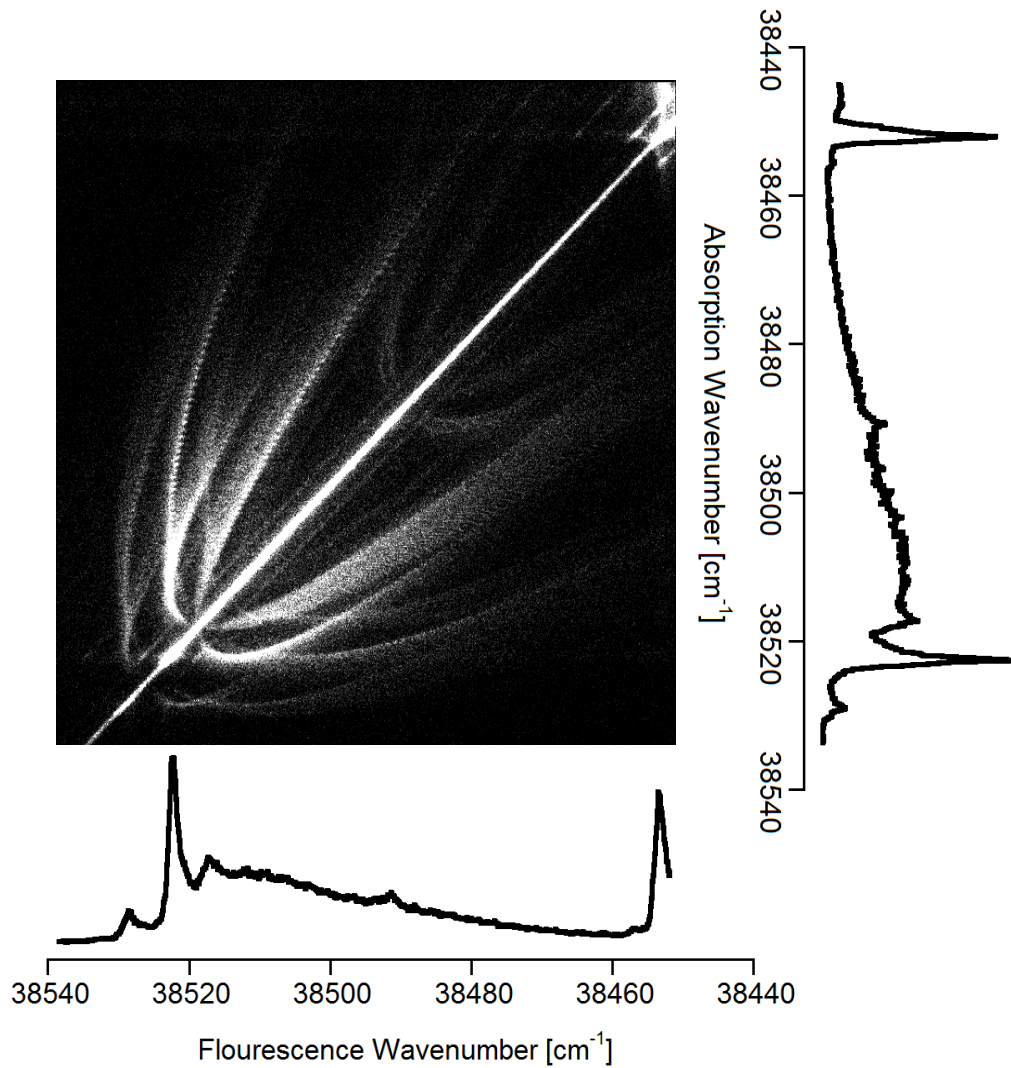


Figure 3.18: Experimental LIDF spectrum of the $6_1^2/6_1^0 11_1^2$ absorption/ $6_1^2/6_1^0 11_1^2$ fluorescence transition. The spectrum has not been normalised to laser power. Absorption step size 0.001 nm, Fluorescence energy/pixel 0.13 cm^{-1} (fluorescence slit width of $25 \mu\text{m}$). The presence of the $6_0^1 18_1^1$ can clearly be seen half-way along the main diagonal feature. A more detailed schematic of the transitions involved in the absorption step of this LIDF spectrum is shown in Figure 3.11.

process are illustrated in Figure 3.19 - Figure 3.22. The same ζ'_6 value is used in both the excitation and de-excitation processes so the contour types are the same in each dimension. These spectra can be correlated with the different contour types discussed in Section 3.2.4.

Integration of the images along each dimension show the contour shapes in the fluorescence and absorption dimensions. The LIDF images are labelled according to the shapes of the fluorescence and absorption contour that they produce. For example, a type III,I LIDF spectrum produces an absorption contour of type III in absorbance and type I in fluorescence. Figure 3.19 includes the assignment of the different rotational sub-bands to the different features of a type I,I LIDF spectrum. The rotational sub-bands have been labelled, where $\uparrow R \downarrow P$ refers to a R type ($J_{excited} - J_{ground} = +1$) transition in absorbance and a P type ($J_{excited} - J_{ground} = -1$) transition in fluorescence.

As discussed in Section 3.3.3 the $6_0^1 16_1^1$ transition involves six sub-transitions $6_0^1 l_0^{\mp 1} 16_1^1 l_{\pm 1}^{\mp 1}$, $6_0^1 l_0^{\mp 1} 16_1^1 l_{\pm 1}^{\pm 1}$ and $6_0^1 l_0^{\pm 1} 16_1^1 l_{\pm 1}^{\mp 1}$. The last two are predicted to be very weak in absorbance because they are third-order transitions, that is, they involve a three quanta change in vibrational angular momentum. In fluorescence, of the six allowed sub-transitions, the $1_1^0 6_0^1 l_0^{\pm 1} 16_1^1 l_{\pm 1}^{\mp 1}$ transitions are also less likely to occur because they are also third-order transitions. The possibility that there may be absorption through a first-order transition and fluorescence through the third-order transition (or vice versa) must also be considered. Figure 3.23 demonstrates how a LIDF spectrum would appear if only these transitions occurred. Importantly there are several distinct features which do not appear in any of the spectra which involve absorbance and fluorescence transitions of the same order. These features have been marked with ♣ in the figure. Also note that the LIDF spectrum generated from these series of transitions do not produce a diagonal feature.

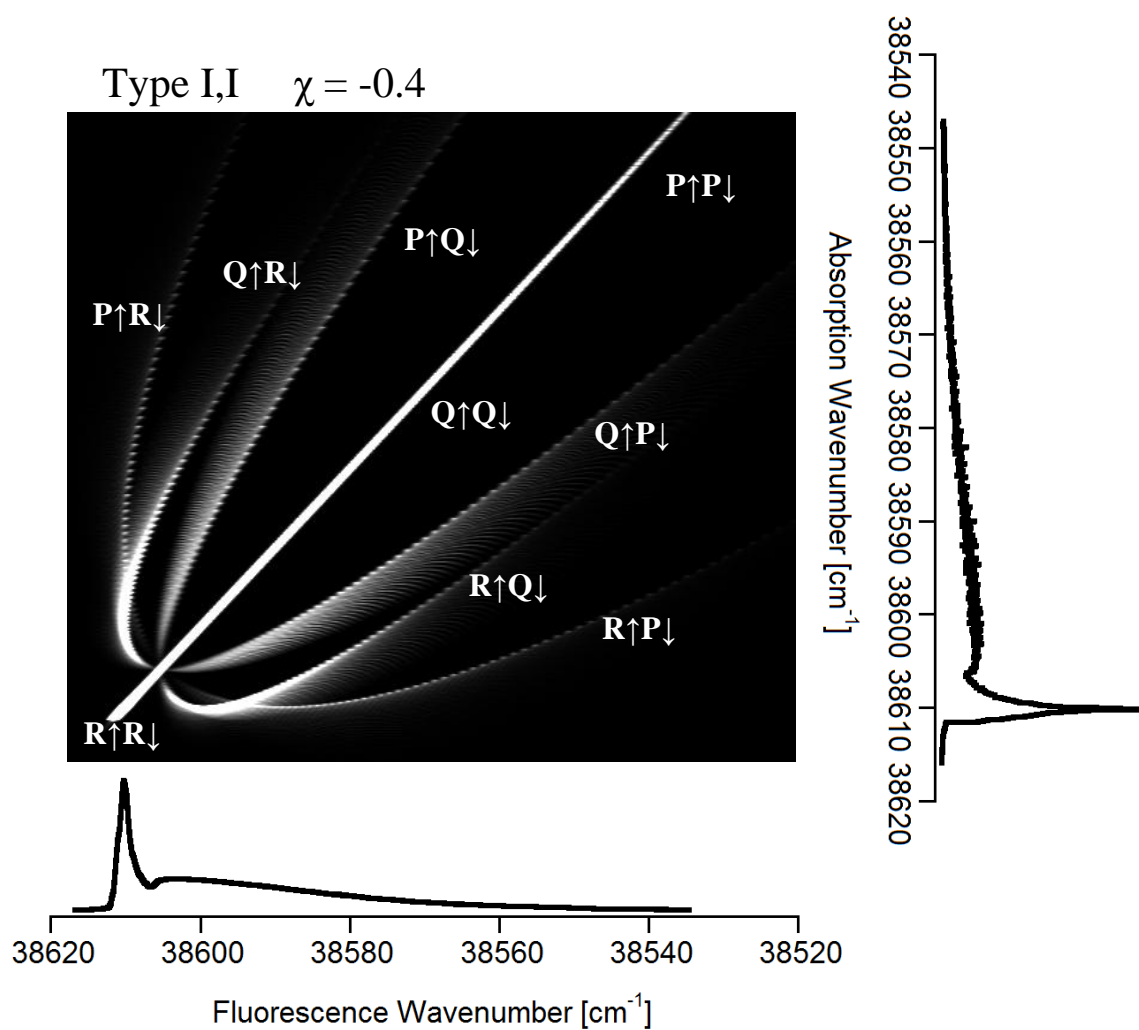


Figure 3.19: Simulated LIDF spectrum based on the 6_0^1 absorbance/ 6_0^1 fluorescence transition. The ζ_{eff} in the excited state has been set to +0.6, generating absorption and fluorescence spectra both with shape of type I. The absorption points are convoluted with a Gaussian of 0.001 nm FWHM. Whilst the fluorescence points are convoluted with a Gaussian of 0.004 nm FWHM.

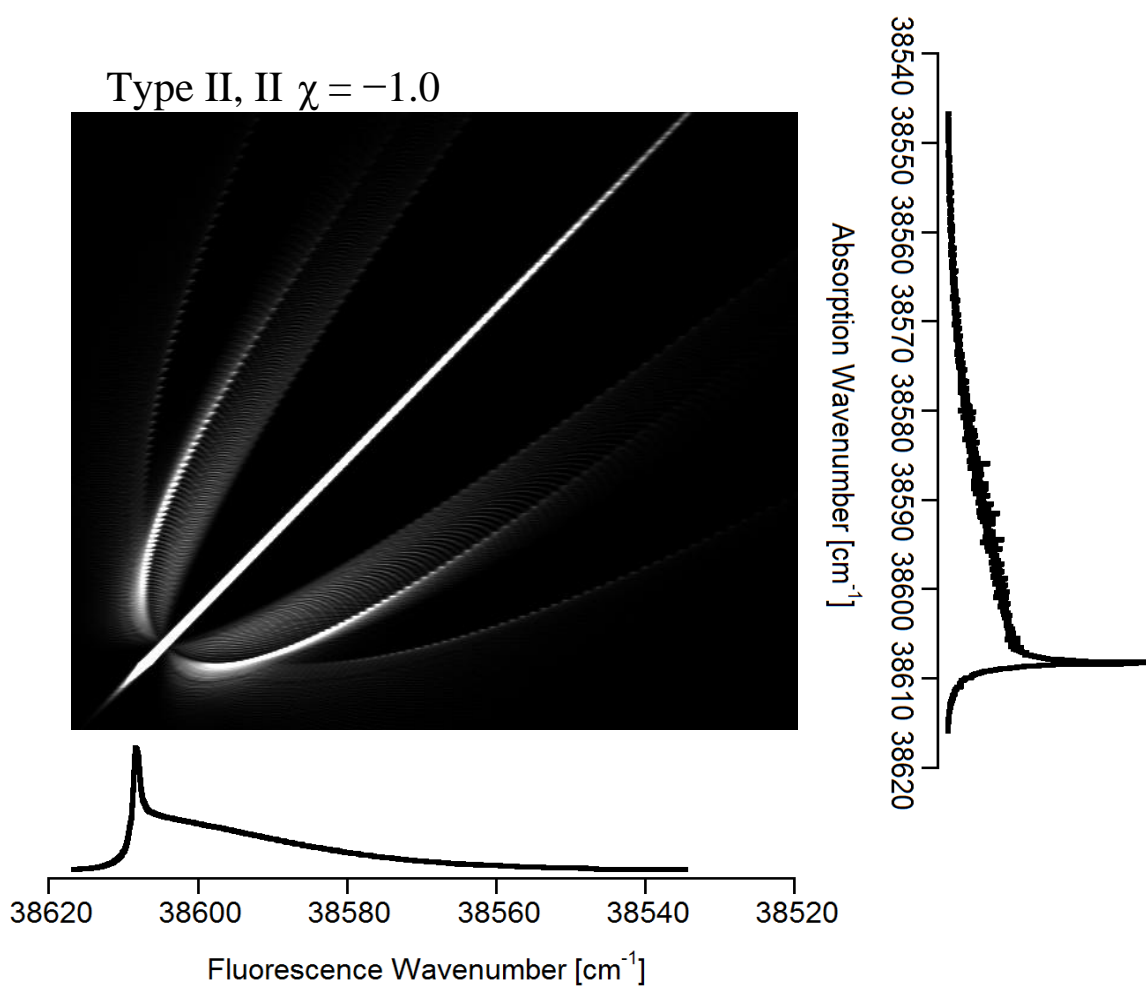


Figure 3.20: Simulated LIDF spectrum based on the 6_0^1 absorbance/ 6_0^1 fluorescence transition. The ζ_{eff} in the excited state has been set to 0, generating absorption and fluorescence spectra both with shape of type II.

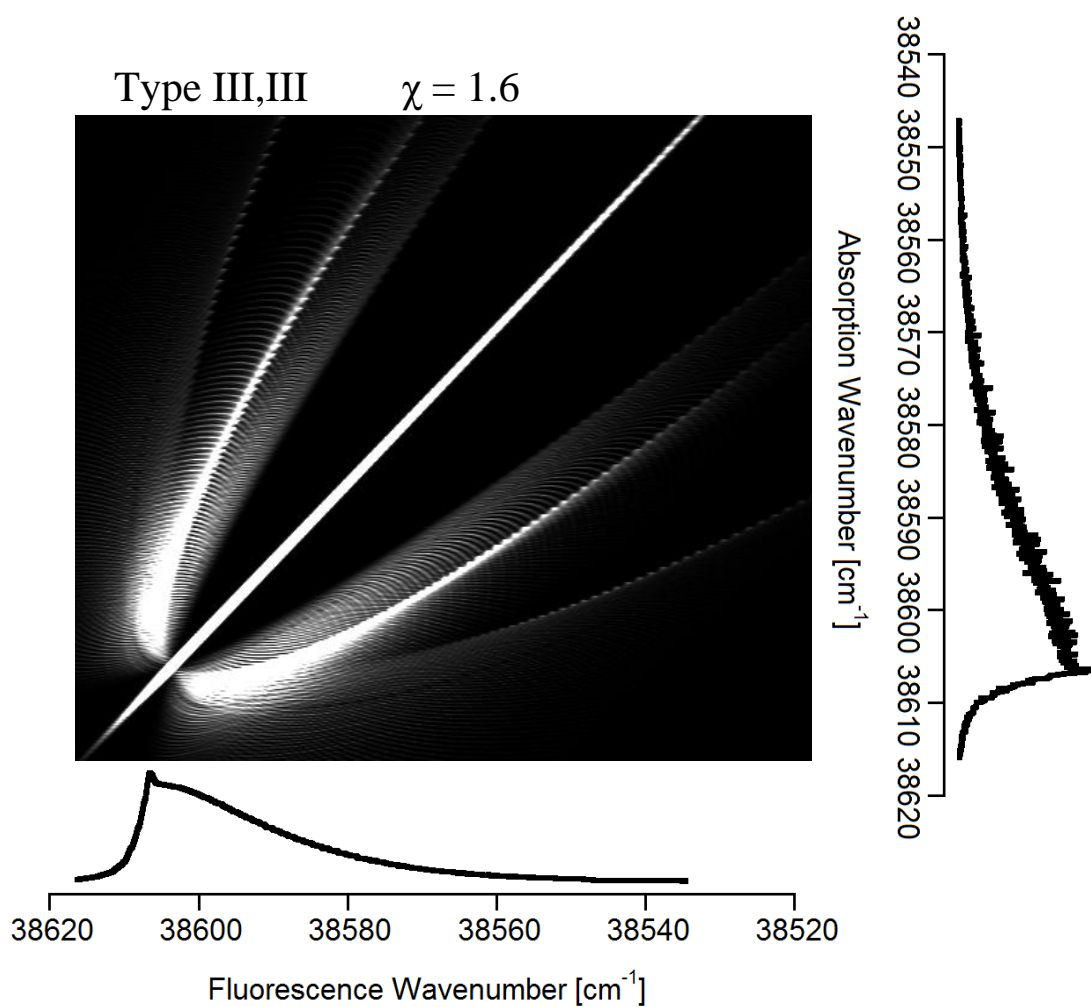


Figure 3.21: Simulated LIDF spectrum based on the 6_0^1 absorbance/ 6_0^1 fluorescence transition. The ζ_{eff} in the excited state has been set to -0.6 , generating absorption and fluorescence spectra both with shape of type III.

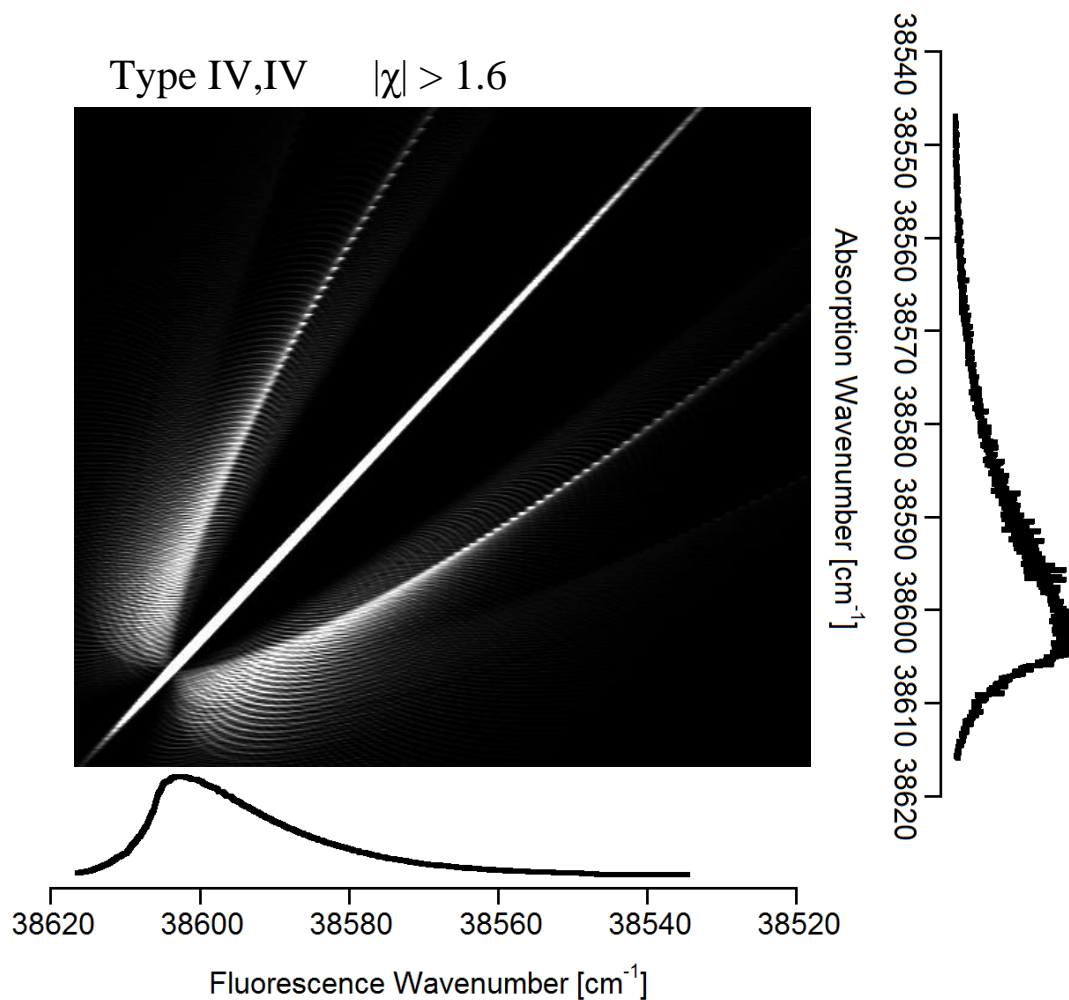


Figure 3.22: Simulated LIDF spectrum based on the 6_0^1 absorbance/ 6_0^1 fluorescence transition. The ζ_{eff} in the excited state has been set to -1.2 , generating absorption and fluorescence spectra both with shape of type IV.

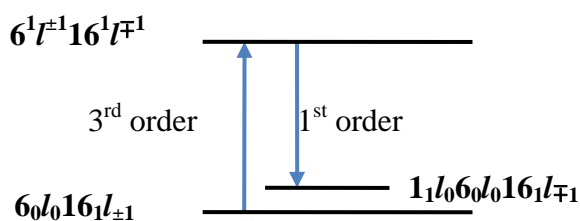
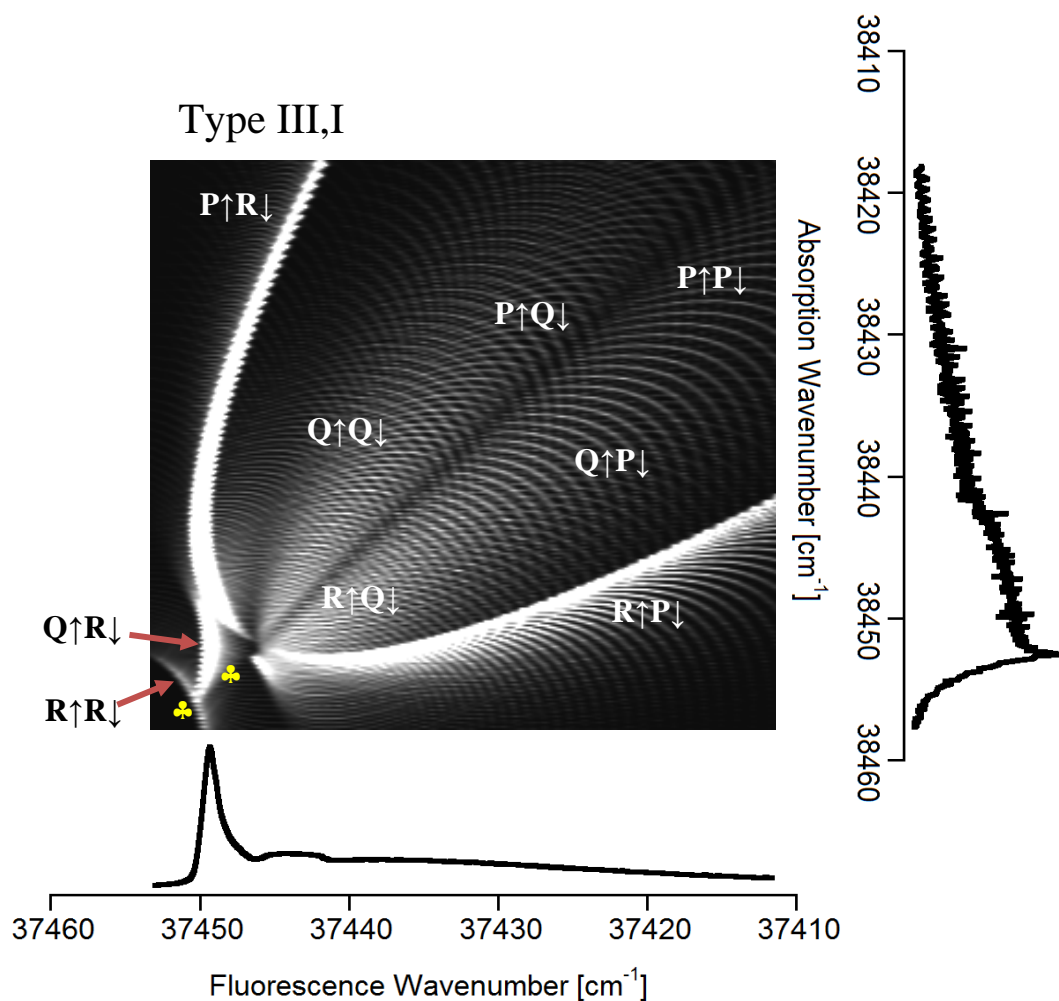


Figure 3.23: Simulated image based upon absorption through a third-order transition and fluorescence through a first-order transition. The features marked with ♣, are unique features to a LIDF spectrum that involves this type of transition pathway. The complimentary process, absorption through a first-order transition and fluorescence through a third-order transition, produces an identical LIDF spectrum except it is reflected about the main diagonal.

3.4.3 De-convolution of the $6_0^1 16_1^1 / 6_0^1 11_1^1$ Absorption Band

In Section 3.3.3 the difficulties of accurately obtaining spectroscopic constants from linear-least squares fitting of 1D absorption spectra were discussed. Due to the high number of fitting variables as well as the lack of features in the absorption spectrum the results of fitting the $6_0^1 16_1^1 / 6_0^1 11_1^1$ absorption band were far from convincing. However, application of the LIDF technique successfully de-convolutes the absorption band. In addition to this advancement on the analysis of the band, upgrading the fitting algorithm to the more sophisticated Simplex method [26,27] proved more successful in treating a system with a very large number of fitting variables.

The vibronic transition energies involved with the $6_0^1 16_1^1$ and $6_0^1 11_1^1$ transitions are almost identical and because of this, in an absorption spectrum the two bands are overlaid. However, excitation of another quanta of a different vibration can split this energetic degeneracy of the transitions and separate the two bands. Recall that the energy of a vibrational level is dependent upon the anharmonic constants x_{ij} and g_{ij} , where x_{ij} is a measure of the interaction between vibrations of type i and of type j and g_{ij} is a measure of the interaction between the vibrational angular momentum components of the same vibrations (see Section 3.2.3). If the lower vibrational state of each of these transitions were mixed with a non-degenerate vibration such as ν_1 then the difference in energy between the two transitions, $1_1^0 6_0^1 16_1^1$ and $1_1^0 6_0^1 11_1^1$ would be $x_{1,16} - x_{1,11}$. The difference in the strength of the interaction between ν_1 and ν_{16} or ν_{11} determines the energy displacement of the bands from each other. Miani *et al* calculated all of the x_{ij} values for benzene using density functional theory and from their results it is estimated that $x_{1,16} - x_{1,11}$ is $\sim 1.5 \text{ cm}^{-1}$ [41]. This small energetic splitting of the bands is not enough to totally separate the overlapping bands when observed in the absorption (or fluorescence) dimension alone. However, if the spectrum is

produced in two (or more) dimensions, then this small difference in anharmonic constants is enough to visually separate out the overlapped bands.

Figure 3.24 and Figure 3.25 both show the experimentally generated $6_0^1 16_1^1 / 1_1^0 6_0^1 16_1^1$ LIDF spectrum – they are exactly the same image, but they have been displayed with different brightness so that all the features of the spectrum can be seen. The LIDF spectrum was generated at room temperature at a cell pressure of 14 mTorr. The image was normalised to laser power by monitoring the laser power as function of time and correlating this to the wavelength of the absorption laser. The absorption wavelength was stepped at an interval of 0.001 nm. The width of the slit in front of the spectrometer was reduced to 100 μm ; which generates a dispersed fluorescence spectrum of resolution $0.5 \text{ cm}^{-1}/\text{camera pixel}$.

Figure 3.24 highlights all the rotational structure on the branches of the spectrum as well as the presence of many other absorption bands that are hidden in a 1D absorption spectrum. The features labelled in Figure 3.25 have been assigned with the aid of fluorescence studies performed by Nicholson [42]: All three features are a result of absorbance through $6_1^0 1_0^1$ and fluorescence into (1) $4_1^0 10_1^0 1_0^1$, (2) $8_1^0 1_0^1$ and (3) $6_1^0 1_1^1$. Figure 3.25 clearly demonstrates the splitting of the main diagonal feature. The less intense diagonal feature at higher fluorescence energies is the $6_0^1 11_1^1 / 1_1^0 6_0^1 11_1^1$ band.

A cold LIDF spectrum of the $6_0^1 16_1^1 / 1_1^0 6_0^1 16_1^1$ transition was also generated by expanding a 1% mix of benzene in helium into the evacuated Source Chamber. The cold LIDF spectrum is shown in Figure 3.26. The $6_0^1 11_1^1 / 1_1^0 6_0^1 11_1^1$ band is clearly seen shifted to the blue of the $6_0^1 16_1^1 / 1_1^0 6_0^1 16_1^1$ in the fluorescence dimension. If argon is used as a carrier gas then this feature is much less intense. This is due to the high collisional cooling efficiency of argon causing a depletion in the population of the 11_1 vibronic state.

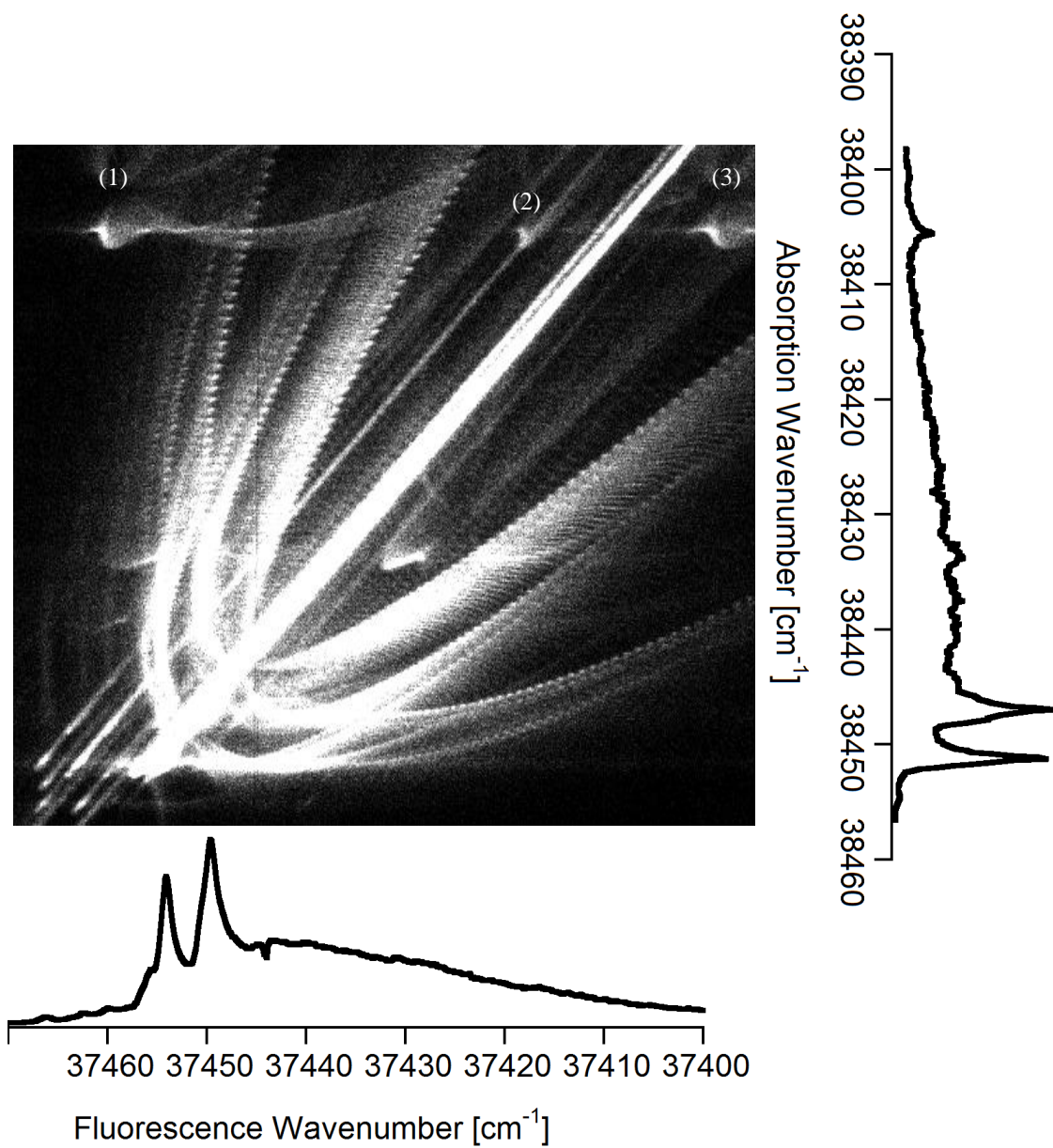


Figure 3.24: Experimental, room temperature LIDF spectrum of the $6_0^1 16_1^1 / 6_0^1 11_1^1$ absorption $1_1^0 6_0^1 16_1^1 / 1_1^0 6_0^1 11_1^1$ fluorescence transition.

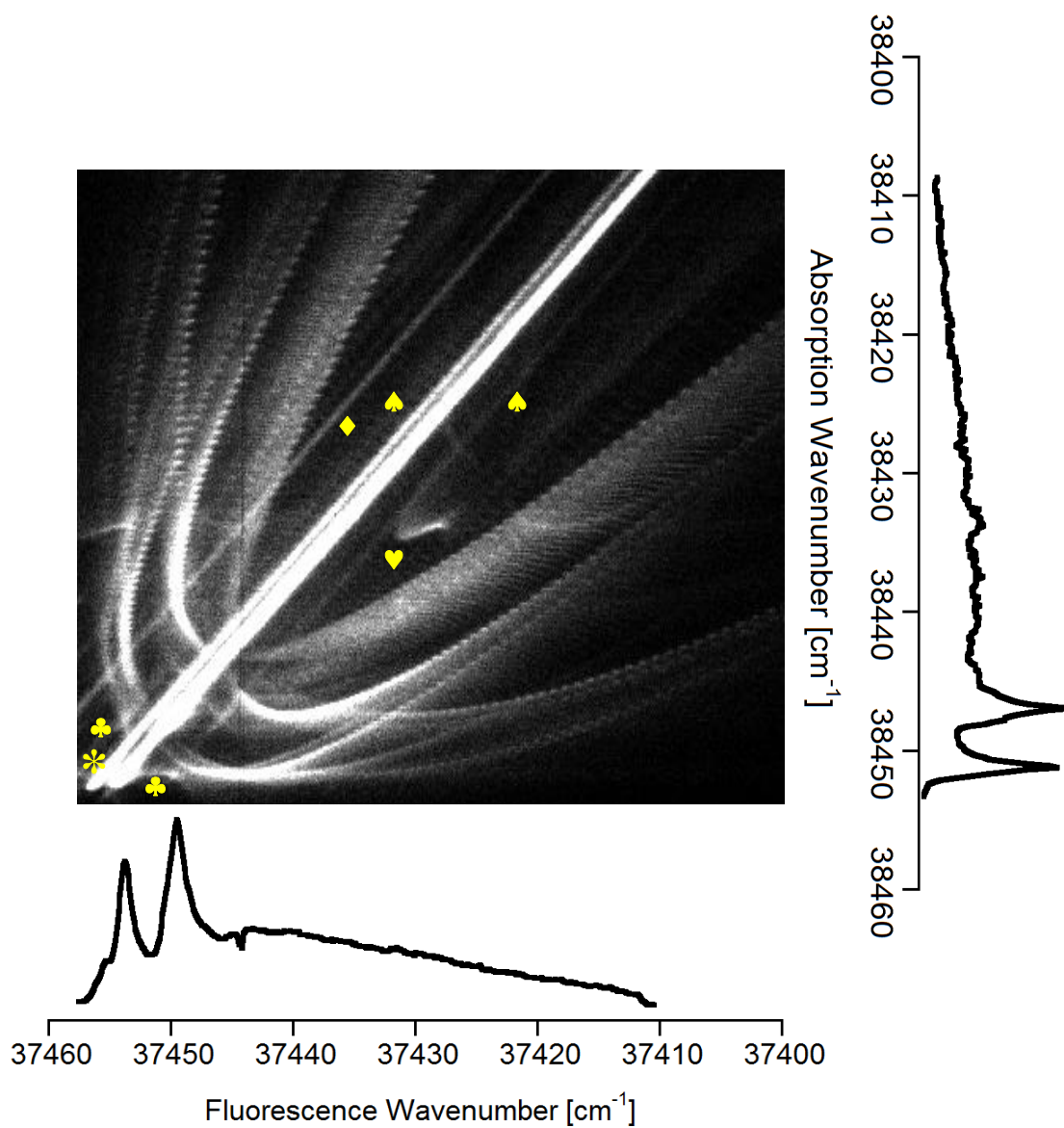


Figure 3.25: Experimental, room temperature LIDF spectrum of the $6_0^1 16_1^1 / 6_0^1 11_1^1$ absorption $1_1^0 6_0^1 16_1^1 / 1_1^0 6_0^1 11_1^1$ fluorescence transition. The sharp dip in signal seen in the fluorescence profile is due to a damaged pixel in the detector. See Section 3.4.4 for explanation of marker symbols.

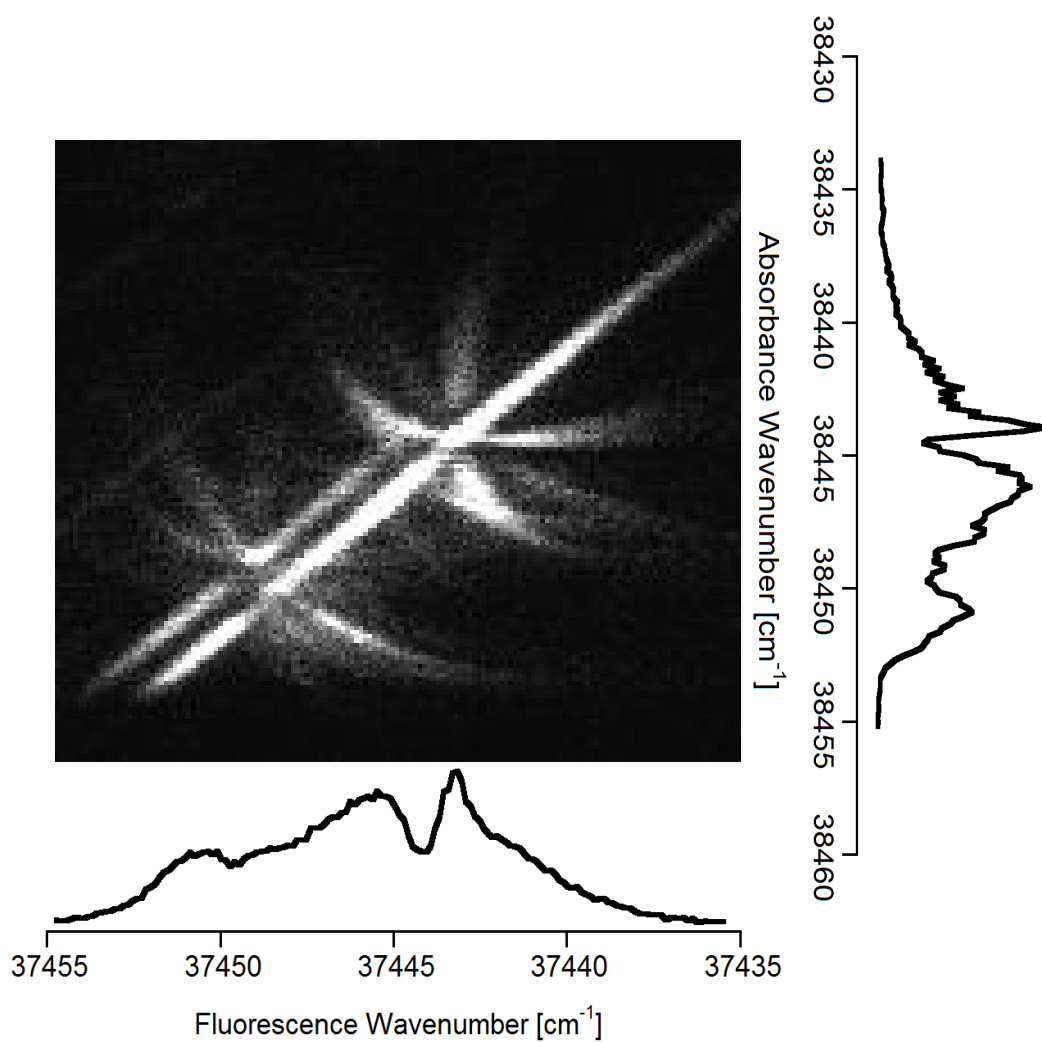


Figure 3.26: Experimental, cold LIDF spectrum of the $6_0^1 16_1^1 / 6_0^1 11_1^1$ absorption $1_1^0 6_0^1 16_1^1 / 1_1^0 6_0^1 11_1^1$ fluorescence transition generated in a free-jet expansion of benzene in helium.

Figure 3.27 shows the complex transition pathways that have been used to simulate the spectrum. The LIDF spectrum was simulated and then the spectroscopic constants varied to obtain a best-fit to the room temperature spectrum. The fitted variables and their best-fit values are reported in Table 3.22. The error in the values are given in brackets in units of the last digit.

The initial ground state B'' rotational constants have been taken from the high resolution infrared studies by Hollenstein *et al* [25]. The ground state C'' rotational constants are not taken as equal to $B / 2$, instead they are calculated using the values for the rotational defects determined by Jagod [35]. The effect of using a value of C'' greater than $B / 2$ makes no dramatic change to the observed spectrum if the C' value is also changed by the same amount. All other C rotational constants were varied independently of the B constants. The low relative intensities of the transitions involving $6_0^1 l_0^{\pm 1} 16_1^1 l_{\pm 1}^{\mp 1}$ and $6_0^1 l_0^{\mp 1} 11_1^1$ result in a lower accuracy in the determined rotational constants involved in these transitions.

The resultant simulated spectra are shown in Figure 3.28 and Figure 3.29. Also included are difference spectra which show the difference between the experimental and simulated spectra. If the image is white then this means that the experimental spectrum was more intense at that position, and conversely, if the image is black, then the simulated spectrum was more intense at that position.

For comparison with the results of fitting only in the absorption dimension (Figure 3.13) the values for the spectroscopic constants determined from fitting the LIDF spectrum have been used to reproduce the absorption spectrum of the band. This result is presented in Figure 3.30. The position and relative intensity of the $6_0^1 11_1^1$ band has been elucidated and the presence of the third-order transition band is a clear contributor to the shape of the $6_0^1 16_1^1 / 6_0^1 11_1^1$ band.

Table 3.22: Summary of spectroscopic constant values generated from best-fit to the LIDF spectrum in Figure 3.25. (*) Value taken from Hollenstein [25]. (†) Values calculated from the rotational defects reported by Jagod [35]. All other rotational constants are the result of best-fit simulations performed in this study. 1 standard deviation is given in parentheses in units of the last digit. Δ_v given in units of $\text{amu}\cdot\text{Å}^2$, all other constants have units cm^{-1} . (♣) When calculated from the shape of the third-order transition, $1_1^0 l_0^0 6_0^1 l_0^{\pm 1} 16_1^1 l_{\pm 1}^{\mp 1}$, the best-fit was a Δ_v value of -0.497 and $\zeta_{eff} = 0.484(3)$.

Vibronic State	B	C	Δ_v	ζ_{eff}
$6_0 l_0 16_1 l_{\pm 1}$	0.189661 *	0.094976 †	-0.272 †	0
$6^1 l^{\mp 1} 16^1 l^{\pm 1}$	0.181404(3)	0.091014(5)	-0.637	$-0.4794(9)$ *
$6^1 l^{\mp 1} 16^1 l^{\mp 1}$	0.181362(4)	0.090868(7)	-0.382	$-0.478(1)$
$6^1 l^{\pm 1} 16^1 l^{\mp 1}$	0.18143(2)	0.09096(3)	-0.492	0.484(3)
$1_1 6_0 l_0 16_1 l_{\pm 1}$	0.189521(4)	0.094907(5)	-0.275 *	0
$1_1 6_0 l_0 16_1 l_{\mp 1}$	0.189523(7)	0.094909(9)	-0.277	0
$6_0 l_0 11_1 l_0$	0.189640 *	0.094897 †	-0.144 †	0
$6^1 l^{\mp 1} 11^1 l^0$	0.181155(9)	0.09084(1)	-0.545	$-0.475(2)$
$1_1 6_0 l_0 11_1 l_0$	0.189508	0.09488(1)	-0.249	0

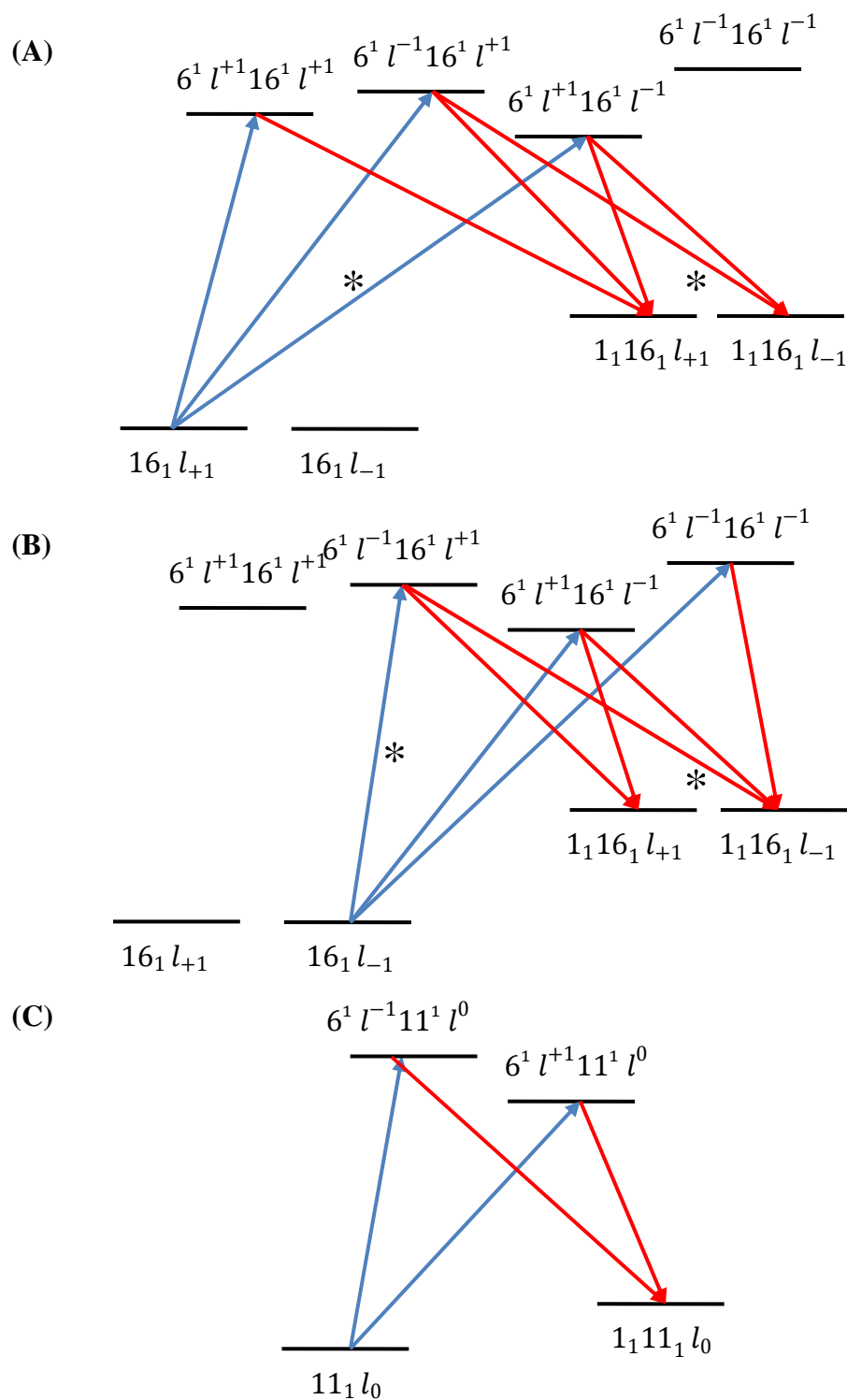


Figure 3.27: Schematic of the transition pathways that were used to create the simulated LIDF spectrum. Absorption transitions are in blue and fluorescence transitions are in red. (A) and (B) are all the allowed pathways within the $6_0^1 16_1^1$ absorption/ $1_1^0 6_0^1 16_1^1$ fluorescence process. The varying energy of the excited states is due to the magnitude of the Coriolis and vibrational coupling constants. The transitions marked with (*) are third-order transitions and have a much lower transition probability than the first-order transitions. (C) shows the allowed transitions for the $6_0^1 11_1^1$ absorption/ $1_1^0 6_0^1 11_1^1$ fluorescence process.

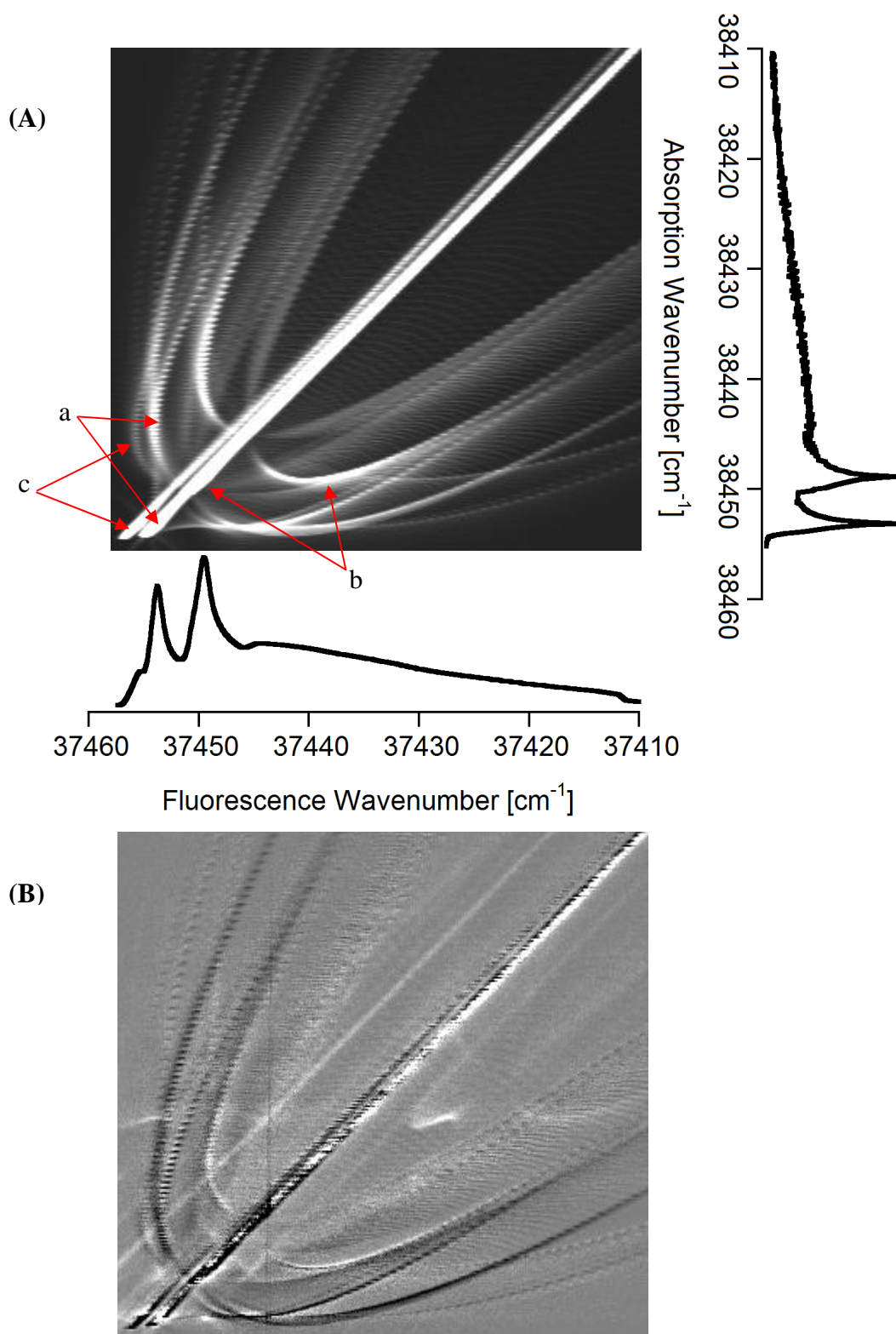


Figure 3.28: Best-fit simulation of the room temperature $6_0^1 16_1^1 / 6_0^1 11_1^1$ absorption, $1_1^0 6_0^1 16_1^1 / 1_1^0 6_0^1 11_1^1$ fluorescence LIDF spectrum. (A) Simulated LIDF spectrum using the spectroscopic constants from Table 3.22. The labelling of the bands is explained in Section 3.4.4. (B) Difference spectrum highlighting the discrepancies between the experimental and simulated spectra. The black areas indicate that the simulated spectrum is more intense, and the white areas indicate that the experimental spectrum is more intense.

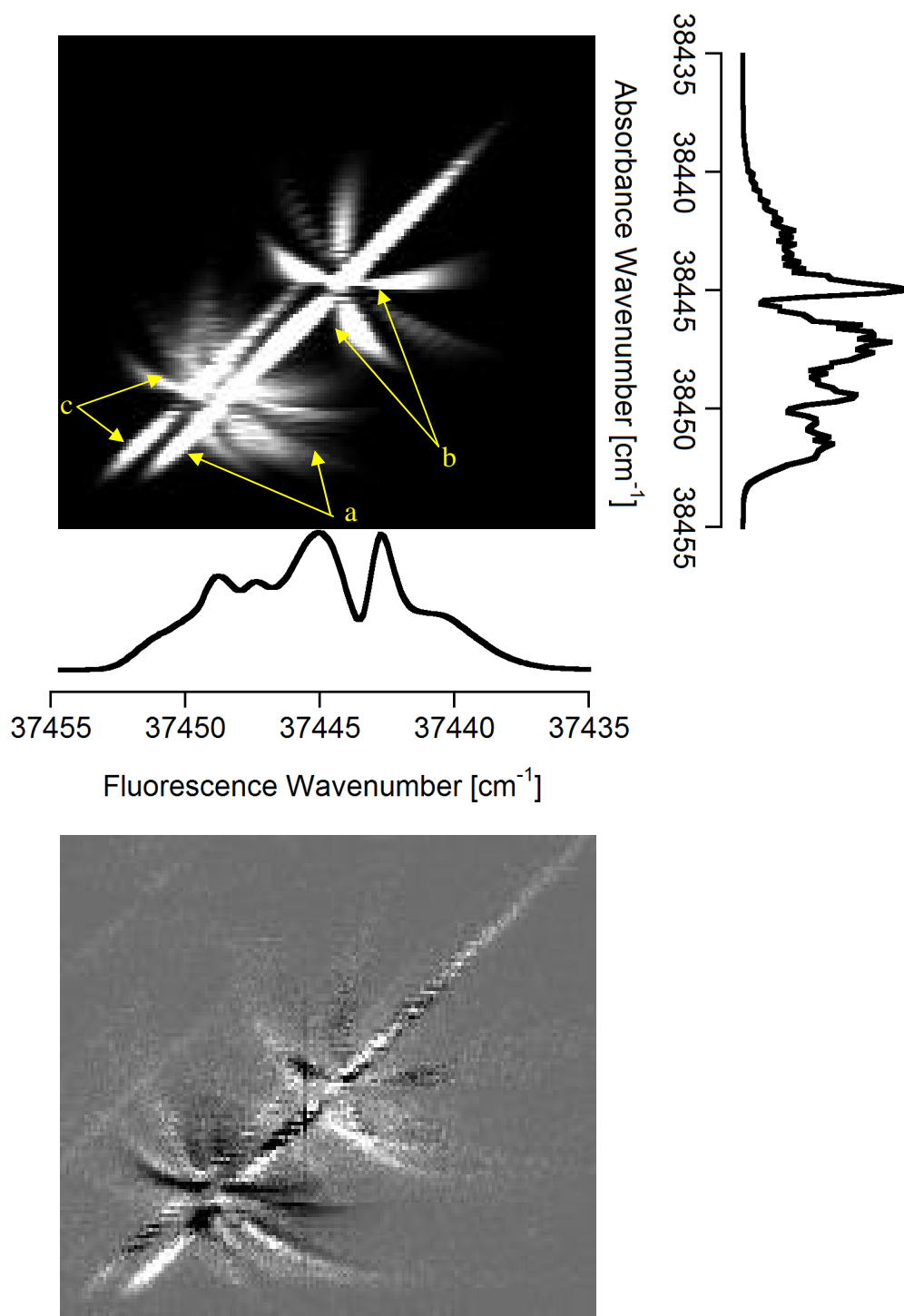


Figure 3.29: (A) Best-fit simulation of the rotationally cold $6_0^1 16_1^1 / 1_1^0 6_0^1 16_1^1$ LIDF spectrum shown in Figure 3.26. The rotational temperature of the spectrum was determined to be 8 ± 1 K. The labelling of the bands is explained in Section 3.4.4. (B) Difference spectrum highlighting the discrepancies between cold experimental and simulated spectra.

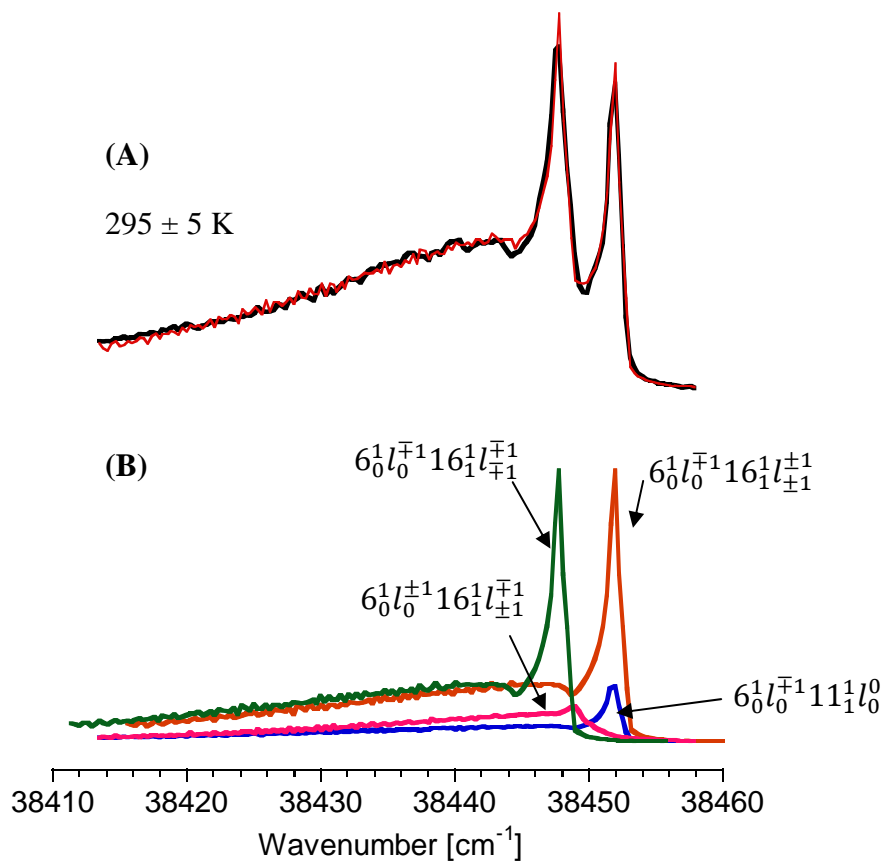


Figure 3.30: (A) An overlay of the simulated (red) absorption contour with the experimentally obtained REMPI spectrum (black) of room temperature benzene vapour. The spectroscopic constants used to generate the simulated contour are the result of best-fits to the LIDF spectrum presented in Table 3.22. (B) Identification of the sub-bands that contribute to the overall contour. In comparison with the results of Figure 3.13(B) the shape of the $6_0^1 l_0^{\mp 1} 11_1^1 l_0^0$ contour (blue) is now definitely of type I and sits directly under the $6_0^1 l_0^{\mp 1} 16_1^1 l_{\pm 1}^{\pm 1}$ sub-band (orange). The type III contour of the third-order transition, $6_0^1 l_0^{\pm 1} 16_1^1 l_{\pm 1}^{\mp 1}$ (pink), now appears centred between the two main absorption features.

3.4.4 Analysis of $6_0^1 16_1^1 / 6_0^1 11_1^1$ Absorption, $1_1^0 6_0^1 16_1^1 / 1_1^0 6_0^1 11_1^1$ Fluorescence LIDF Spectrum

The positions of the sub-bands have been identified and are labelled in Figure 3.28 and Figure 3.29.

$$(a): 6_0^1 l_0^{\pm 1} 16_1^1 l_{\pm 1}^{\mp 1} / 1_1^0 6_0^1 l_0^{\pm 1} 16_1^1 l_{\pm 1}^{\mp 1} \text{ and } 6_0^1 l_0^{\mp 1} 16_1^1 l_{\pm 1}^{\pm 1} / 1_1^0 6_0^1 l_0^{\mp 1} 16_1^1 l_{\pm 1}^{\pm 1}.$$

$$(b): 6_0^1 l_0^{\mp 1} 16_1^1 l_{\mp 1}^{\mp 1} / 1_1^0 6_0^1 l_0^{\mp 1} 16_1^1 l_{\mp 1}^{\mp 1}.$$

$$(c): 6_0^1 l_0^{\pm 1} 11_1^1 l_0^0 / 1_1^0 6_0^1 l_0^{\pm 1} 11_1^1 l_0^0.$$

Although the intensity of the third-order transition is predicted to be much weaker than the other transitions, its presence is not unimportant. In fact, it was the identification of the features of the third-order transitions which enabled unambiguous assignment of the positions of each band. Recall from Figure 3.23 that if a third-order absorption transition is followed by a first-order fluorescence transition (or vice versa) then unique band features appear in the LIDF spectrum at high energies. These features can be seen in the experimental image (Figure 3.25) at the head of the (a) bands and are marked with ♣. These third-order features do not appear around the head of the band at the (b) position. Since there are no third-order transitions allowed which involve the excited state $6^1 l^{\mp 1} 16^1 l^{\mp 1}$ (see Figure 3.27), it must be the first-order transition, $6_0^1 l_0^{\mp 1} 16_1^1 l_{\mp 1}^{\mp 1} / 1_1^0 6_0^1 l_0^{\mp 1} 16_1^1 l_{\mp 1}^{\mp 1}$ as well as the third-order transition at the (a) position.

Analysis of the intensities of the third-order transition features helps to determine the relative transition probability of the third and first order transitions. Fitting of the simulated LIDF spectrum to the room temperature experimental spectrum reveals that the intensity of the third-order transition $6_0^1 l_0^{\pm 1} 16_1^1 l_{\pm 1}^{\mp 1}$ is approximately one third the intensity of any of the first-order absorption transitions. Since all the absorption transitions start in the same ground

vibronic state this relative intensity is an indication of the relative Frank-Condon factors for the transitions.

When searching for the best-fit to the experimental spectrum, the excited states with different combinations of vibrational angular momentum quantum numbers were treated as unique, since they each describe a vibronic wavefunction of different symmetry. The spectroscopic constants for these states were varied independently along with the Frank-Condon factors for the transitions into and out of these states. The best-fit results showed slight variation in the rotational constants for the different states, whilst the first-order transitions displayed similar Frank Condon factors. The relative Frank Condon factors are 1.2 : 1 for the $6_0^1 l_0^{\pm 1} 16_1^1 l_{\pm 1}^{\mp 1}$: $6_0^1 l_0^{\mp 1} 16_1^1 l_{\mp 1}^{\mp 1}$ transitions.

The value of the rotational defect (Δ_v) as defined in Equation 3.25 is perhaps the best indication of the validity of the determined rotational constants. In Section 3.3.3 it was the Δ_v value for the $6^1 11^1$ state determined from the best fit to the 1D absorption spectra that best demonstrated that the values of the excited rotational constants was unlikely to be correct.

Table 3.22 shows that all Δ_v values calculated from fitting the LIDF spectrum fall between the range -1 to $+1$. Compared with the ground states, in the excited states the rotational defects are consistently larger, indicating that the vibronic excitation has distorted the planar geometry of the benzene ring dramatically. In contrast to the rotational defects that Reidle and Pilva [33] observed for different vibrational angular momentum combinations within the $6^1 16^2$, the rotational defects for the $6^1 16^1$ states remain the same in sign, though they differ in magnitude. Also, the addition of the totally symmetric, non-degenerate ν_1 vibration to the ground state does not appear to affect the Δ_v value dramatically, if at all.

Both bands at position (a) share the same vibrational origin and are displaced from the band at (b) due to the effects of vibrational coupling. From Table 3.18 it can be seen that the bands

will be split by the factor $2g'_{6,16}$. From the simulations the value for $g'_{6,16}$ is found to be $-2.086 \pm 4 \times 10^{-3} \text{ cm}^{-1}$.

Marked with (*) in Figure 3.25 is the band head of the $6_0^1 11_1^1 / 1_1^0 6_0^1 11_1^1$. It is clearly separated from the head of the $6_0^1 16_1^1 / 1_1^0 6_0^1 16_1^1$ along the fluorescence dimension. This separation is due to the difference in the anharmonic constants ($x_{1,11} - x_{1,16}$). From the results of the spectral fitting this value is found to be $1.164 \pm 5 \times 10^{-3} \text{ cm}^{-1}$. This value correlates with the density functional theory results of Miani *et al* who found that $x_{1,16} = 1.57 \text{ cm}^{-1}$ and $x_{1,11} < 0.5 \text{ cm}^{-1}$ [41].

Previously the exact position of the $6_0^1 11_1^1$ band underneath the $6_0^1 16_1^1$ band was not known because of the several wavenumbers uncertainty in the excited state frequency of ν_{11} . From Figure 3.25 it is clear that the head of the band sits directly under the head of the $6_0^1 l_0^{\mp 1} 16_1^1 l_{\pm 1}^{\pm 1}$ component in the absorption dimension. Since the transition energies of the $6_0^1 16_1^1$ sub-bands are accurately known the excited state fundamental frequency of ν_{11} from the best-fit simulation is calculated to be $517.193 \pm 6 \times 10^{-3} \text{ cm}^{-1}$. The clear separation of the bands also means that the relative intensity of the $6_0^1 11_1^1 / 1_1^0 6_0^1 11_1^1$ compared to the $6_0^1 16_1^1 / 1_1^0 6_0^1 16_1^1$ can be calculated, which in turn gives an indication of the relative Frank-Condon factors for each of the transitions. The $6_0^1 11_1^1$ absorption was 0.51 times the intensity of the first-order component, $6_0^1 l_0^{\mp 1} 16_1^1 l_{\pm 1}^{\pm 1}$, with an overall integrated intensity equal to 11.0% of the total $6_0^1 16_1^1$ signal. This translates into relative Frank-Condon factors of 1: 0.83 for $6_0^1 16_1^1 : 6_0^1 11_1^1$.

Figure 3.24 is an extended version of the LIDF spectrum. In this image there are many weak bands whose position in the absorption dimension is almost directly under the $6_0^1 16_1^1$ band head. The displacement of these bands in the fluorescence dimension is due to different $x_{1,j}$

values. The presence of these bands is probably the main source of the large errors in the spectroscopic constants that were obtained from fitting of the 1D absorption band.

The features marked by ♠ in Figure 3.25 are artefacts of diffraction of the fluorescence light as it enters the spectrometer. The feature designated with ♦ is not thought to be a result of diffraction since its displacement from the main diagonal is not equidistance with the other diffraction features. Thus it is thought to be a real band, but as yet remains unidentified. The feature designated with ♥ is part of the band head for the unidentified absorption feature at $\sim 38421 \text{ cm}^{-1}$. This feature was also observable in the absorption spectrum of the same band, recorded by Atkinson and Parmenter and is also identified in the absorption contour shown here in Figure 3.13 [5]. The band does not have the typical shape of type I,I contour, but recall from Section 3.3 the shape of the absorption band was of type I. This means that it is unlikely to be produced from a 6_0^1 transition in fluorescence. The band does not appear to be split in either the fluorescence or absorption dimensions, so it is unlikely to involve more than two quanta of a degenerate vibration in either the ground or excited electronic states. Also, we can deduce that the frequency of the ground state from which the absorption transition begins must be much higher in frequency than 16_1 for this band. This is evident since in the absorption dimension the relative intensity of the band grows relative to the $6_0^1 16_1^1$ when benzene is cooled in a free-jet expansion. As will be demonstrated in Chapters 4 and 5, in a free-jet expansion, the higher frequency vibrations are not cooled as efficiently as the lower frequency vibrations and so absorption bands generated from the higher frequency initial states increase in relative intensity in the free-jet spectrum [43-45]. Given all these clues it is still difficult to confidently assign this unusual feature. There are no obvious vibrational combination bands that would generate a fluorescence or absorption feature at these energies. Further investigation is needed to identify this feature.

The simulations reproduce the shapes of the bands within the experimental, room temperature spectrum quite well, though there are still several discrepancies with the relative intensities of the bands. These problems are exasperated in the simulations of the cold spectrum (compare Figure 3.26 and Figure 3.29). The shape of both the $6_0^1 l_0^{\mp 1} 16_1^1 l_{\mp 1}^{\mp 1} / 1_1^0 6_0^1 l_0^{\mp 1} 16_1^1 l_{\mp 1}^{\mp 1}$ band (labelled (b) in Figure 3.29) and the $6_0^1 l_0^{\pm 1} 11_1^1 l_0^0 / 1_1^0 6_0^1 l_0^{\pm 1} 11_1^1 l_0^0$ band (labelled (c) in Figure 3.29) appear to show only small intensity discrepancies with the experimental spectrum. However, the shape and position of the (a) bands appear to be a completely incorrect. Upon closer investigation, the shape of the experimental band more closely represents a band with an excited state effect Coriolis constant (ζ_{eff}) close to zero. If a zero ζ_{eff} value is used in the simulation of this band then the fit of simulated and experimental LIDF spectra at low temperatures is much closer. However, if those same spectroscopic constants are then used to generate a warm temperature spectrum, the fit to the room temperature experimental LIDF spectrum is no longer close. This result suggests that either there is another band sitting at the (a) position that is distorting the shape of the observed cold spectrum or that the spectroscopy used to describe the bands at this position is inadequate. Although possible, the likelihood that the spectral anomaly is due to the presence of another band (not related to the $6_0^1 16_1^1$) is small. This new band is not shifted from the main diagonal feature in the fluorescence dimension which means that it must interact with the ν_1 vibration to exactly the same degree as ν_{16} . Also, the presence of another band is not evident in the room temperature spectrum at the (a) position. In the free-jet expansion, if this band was generated by transitioning from an initial state of frequency other than that of ν_{16} then the intensity of the band should be variable depending upon the identity of the carrier gas. As previously mentioned, when the free-jet expansion used argon as a carrier gas, the $6_0^1 11_1^1 / 1_1^0 6_0^1 11_1^1$ band was much less intense than when helium was used. This phenomenon is due to the different vibrational cooling efficiencies of the carrier gases. Changing carrier gas did not change any relative intensities of

the bands at the (a) position, which further dismisses the possibility that the distortion at (a) is due to the presence of another band.

The inability to accurately reproduce the bands at the (a) position is likely to be due to the limitations of the spectroscopic theory presented in Section 3.2. In their high resolution studies of the vibrational angular momentum sub-states of $6^1 10^2$ and $6^1 16^2$ at low rotational temperatures, Riedle and Pliva found that the rotational constants that described each state were different, as was the effective Coriolis for each state [33]. They attributed the large distortion in rotational structure and the mixing of the sub-states to *l*-type resonances. Consideration of *l*-type resonance in the $6^1 16^1$ vibronic state may well improve the accuracy of the simulations presented here but is beyond the scope of this research.

The simulated spectra presented here are used in the rotational temperature analysis of benzene molecules that are liberated from an *in vacuo* liquid surface. As will be discussed in Chapters 4 and 5, all the rotational temperatures measured were greater than 100 K. The results displayed in Figure 3.30 demonstrate that the LIDF simulations have enabled us to now reproduce warm $6_0^1 16_1^1$ absorption spectra quite accurately, which means they are an appropriate tool for rotational temperature measurements of warm benzene. At low rotational temperatures the simulations fail to reproduce the experimental spectra with sufficient accuracy. However, the sensitivity of the rotational temperature to the detail of the rovibrational spectrum is not great. The rotational temperature of benzene in the free-jet expansion as determined from fitting the $6_0^1 16_1^1 / 1_1^0 6_0^1 16_1^1$ spectrum was shown to be 8 ± 1 K. Within error this result is the same as the rotational temperatures determined from fitting the absorption spectra of the 6_0^1 and $6_1^2 / 6_1^0 11_0^2$ in Sections 3.3.1 and 3.3.2. This demonstrates the simulations can be used as a temperature probe at these low temperatures, but their uncertainty is increased by several Kelvin.

3.5 Conclusion

Several rovibrational bands in the ${}^1B_{2u} \leftarrow {}^1A_{1g}$ absorption spectrum of gaseous benzene were simulated. The accuracy with which the shapes and positions of the absorption bands can be reproduced depends not only upon the application of the correct selection rules for allowed transitions between states but also on the definition of the energy of the state. The accuracy with which the energy of a state is reproduced depends upon the values of the spectroscopic constants used. The spectroscopic constants that were not able to be obtained from the literature were determined in this study by searching for the values of the constants that produced a simulated spectrum which best-fit an experimentally generated spectrum of known temperature. In this way values for several rotational constants in the excited states of benzene were obtained. For the more complex features of the absorption spectrum – those that involved several overlapping absorption bands – a new visualisation technique was developed to de-convolute the features. The Laser Induced Fluorescence technique generates a 2D spectrum showing the intensity of both absorption into and fluorescence out of an excited electronic state. Simulation of the LIDF spectra allows us to obtain accurate values for the spectroscopic constants involved in the $6_0^1 16_1^1$ and $6_0^1 11_1^1$ transitions. In particular a value for the long sort after excited state frequency of the ν_{11} vibration was obtained. Since the shapes of the absorption bands can now be confidently reproduced at varying temperatures, the simulated spectra can be used as a tool to determine the internal temperatures of benzene molecules under different experimental conditions.

3.6 References

- (1) Bunker, P. R.; Jensen, P. *Fundamentals of Molecular Symmetry*; Institute of Physics Publishing: London, 2005.
- (2) Callomon, J. H.; Dunn, T. M.; Mills, I. M. *Philos. Trans. R. Soc. London Ser. A* 1966, 259, 499.
- (3) Wilson Jr., E. B. *Journal of Chemical Physics* 1935, 3, 276.
- (4) Muller, G.; Fan, J. Y.; Lyman, J. L.; Schmid, W. E.; Kompa, K. L. *Journal of Chemical Physics* 1989, 90, 3490.
- (5) Atkinson, G. H.; Parmenter, C. S. *Journal of Molecular Spectroscopy* 1978, 73, 52.
- (6) Page, R. H.; Shen, Y. R.; Lee, Y. T. *Journal of Chemical Physics* 1988, 88, 5362.
- (7) Stephenson, T. A.; Radloff, P. L.; Rice, S. A. *Journal of Chemical Physics* 1984, 81, 1060.
- (8) Mills, I. M. *Molecular Physics* 1964, 7, 549.
- (9) Atkinson, G. H.; Parmenter, C. S. *Journal of Molecular Spectroscopy* 1978, 73, 31.
- (10) Bernath, P. F. *Spectra of Atoms and Molecules*, 2nd ed.; Oxford University Press: New York, 2005.
- (11) Herzberg, G. *Molecular Spectra and Molecular Structure. II. Infrared and Raman Spectra of Polyatomic Molecules*; Van Nostrand: New York, 1945.
- (12) Hougen, J. T. *Journal of Chemical Physics* 1962, 37, 1433.
- (13) Oka, T. *Journal of Chemical Physics* 1967, 47, 5410.
- (14) Cartwright, G. J.; Mills, I. M. *Journal of Molecular Spectroscopy* 1970, 34, 415.

-
- (15) Herzberg, G. *Molecular Spectra and Molecular Structure. III. Electronic spectra and electronic structure of polyatomic molecules*; Van Nostrand: New York, 1966.
- (16) Mills, I. M.; Hoy, A. R. *Journal of Molecular Spectroscopy* 1973, 46, 333.
- (17) Banwell, C. N.; McCash, E. M. *Fundamentals of molecular spectroscopy*, Fourth ed.; Tata McGraw-Hill Publishing Company Ltd: New Dehli, 1994.
- (18) Weber, T.; Riedle, E.; Neusser, H. J. *Journal of the Optical Society of America B: Optical Physics* 1990, 7, 1875.
- (19) Riedle, E.; Knittel, T.; Weber, T.; Neusser, H. J. *Journal of Chemical Physics* 1989, 91, 4555.
- (20) Gascooke, J. R., Personal Communication.
- (21) Fischer, G.; Jakobson, S. *Molecular Physics* 1979, 38, 299.
- (22) Atkinson, G. H.; Parmenter, C. S. *Journal of Molecular Spectroscopy* 1978, 73, 20.
- (23) Okruss, M.; Müller, R.; Hese, A. J. *Mol. Spec.* 1999, 193, 293.
- (24) Snels, M.; Hollenstein, H.; Quack, M.; Cane, E.; Miani, A.; Trombetti, A. *Molecular Physics* 2002, 100, 981.
- (25) Hollenstein, H.; Piccirillo, S.; Quack, M.; Snels, M. *Molecular Physics* 1990, 71, 759.
- (26) Press, W. H.; Flannery, B. P.; Teukolsky, S. A.; Vetterling, W. T. *Numerical Recipes: The Art of Scientific Computing*; Cambridge University Press: New York, 1986.
- (27) Fajer, P. G.; Bennett, R. L. H.; Polnaszek, C. F.; Fajer, E. A.; Thomas, D. D. *Journal of Magnetic Resonance (1969)* 1990, 88, 111.
- (28) Grams, M. P.; Cook, A. M.; Turner, J. H.; Doak, R. B. *Journal of Physics D: Applied Physics* 2006, 39, 930.

-
- (29) Braun, J.; Day, P. K.; Toennies, J. P.; Witte, G.; Neher, E. *Review of Scientific Instruments* 1997, 68, 3001.
- (30) Demtroder, W. *Atomic and Molecular Beam Methods*; Oxford University Press: New York, 1992; Vol. 2.
- (31) Parkin, J. E.; Morlet-Savary, F.; Dimicoli, I. *Chemical Physics* 1990, 142, 213.
- (32) Weber, T.; Neusser, H. J. *Journal of Chemical Physics* 1991, 94, 7689.
- (33) Riedle, E.; Pliva, J. *Chemical Physics* 1991, 152, 375.
- (34) Lyman, J. L.; Müller, G.; Houston, P. L.; Piltch, M.; Schmid, W. E.; Kompa, K. L. *The Journal of Chemical Physics* 1984, 82, 810.
- (35) Jagod, M.-F.; Oka, T. *Journal of Molecular Spectroscopy* 1990, 139, 313.
- (36) Riedle, E.; Neusser, H. J.; Schlag, E. W. *Journal of Chemical Physics* 1981, 75, 4231.
- (37) Sieber, H.; Riedle, E.; Neusser, H. J. *Journal of Chemical Physics* 1988, 89, 4620.
- (38) Garforth, F. M.; Ingold, C. K. *Journal of the Chemical Society* 1948, 417.
- (39) Whetton, N. T.; Lawrance, W. D. *Journal of Physical Chemistry* 1992, 96, 3717.
- (40) Palmer, C. *Diffraction Grating Handbook*; Newport Corporation, 2005; Vol. 6th Edn.
- (41) Miani, A.; Cane, E.; Palmieri, P.; Trombetti, A. *Journal of Chemical Physics* 2000, 112, 248.
- (42) Nicholson, J. A.; Lawrence, W. D.; Fischer, G. *Chemical Physics* 1995, 196, 327.
- (43) Bernshtein, V.; Oref, I. *Journal of Physical Chemistry B* 2005, 109, 8310.
- (44) Clary, D. C.; Gilbert, R. G.; Bernshtein, V.; Oref, I. *Faraday Discussions* 1995, 102, 423.

- (45) Murakami, J.; Kaya, K.; Ito, M. *Journal of Chemical Physics* 1980, 72, 3263.

Chapter 4. Molecular Evaporation

The Dynamics of Evaporation from a Liquid Surface

4.1 Introduction

While the thermodynamics of evaporation have been understood for over a century [1,2], the molecular-level dynamics of the evaporation process remain inadequately defined. Developing a comprehensive molecular-level understanding of evaporative mass and energy transfer has a wide-ranging practical importance in, for example, better understanding atmospheric [4] and industrial [5] processes.

Inferences about the dynamical processes of surface desorption have been made using various techniques [6] including molecular scattering [7-10] and thermal desorption [11-15]. However, the great variety in the results implies that the nascent distribution of molecular energy is greatly dependent upon the nature of the surface from which the molecules are escaping. Some of the earliest studies involved looking at evaporation from solid surfaces. Since the number of evaporating molecules is extremely low, the nascent distributions observed can be assumed to be a result of spontaneous evaporation. Spontaneous evaporation occurs only when molecules are liberated from the condensed phase in the absence of external forces; all the energy to leave the surface is supplied either from the bulk phase beneath the evaporating molecule or by the molecule's own internal energy [16]. Though the number of studies is few, the results from observations of spontaneous evaporation from a solid surface of the same material show some striking similarities. As early as 1962, Klemperer's studies on the sublimation of Iodine [17] revealed that vibrational temperatures of subliming I_2 were consistent with the temperature of the bulk. Nesbit [18] found that CO_2 subliming from a thin film of solid CO_2 displayed Boltzmann distributions amongst the rotational and vibrational modes of nascent molecules and the rotational and vibrational temperatures were the same as

that measured in the bulk. When the temperature of the film was raised, increasing the likelihood of gas-phase collisions, they observed rotational cooling down to temperatures 0.8 times the measured surface temperature. Similarly, studies of the sublimation of NO from its bulk showed rotational distributions that described the surface temperature of 50 K [19]. Sadtchenko *et al* [20] observed that the D₂O molecules evaporating from an *in vacuo* ice filament display a translational energy distribution that describes a temperature the same as that of the bulk. The common results of the studies suggest that spontaneous evaporation of molecules from their solid phase produces internal motions which are thermally equilibrated with the bulk.

In contrast, many experiments of heterogeneous systems, where the thermally desorbed molecule is different to the material of the surface, show results that conflict with the aforementioned studies. Both theoretical and experimental studies show significant rotational cooling of molecules desorbed from solid surfaces [8,21,22]. For example, both Muhlhausen [8] and Cavanagh [12] observed cooler than surface temperature rotations for NO molecules desorbing from Ag(111) and Ru(001). In their review of the chemical dynamics of the gas-surface interface, Rettner *et al* point out that gas molecules that are trapped and then desorbed by the surface typically display a rotational energy distribution that is Boltzmann with a temperature that is less than the surface [23]. Theoretical calculations by Muhlhausen confirm that the effect is due to the strong rotation to translation coupling along the desorption coordinate. The driving force for the rotation to translational energy transfer above solid surfaces, is the presence of an energy barrier along the desorption co-ordinate, where internal energy must be partitioned into the translational co-ordinate if the molecule is to escape the surface. The desorption co-ordinate is typically assigned along the direction normal to the surface since it has been repeatedly shown that the flux of molecules evaporating from a surface, be it liquid or solid, is maximised along the surface normal [6,24-26].

While the energy distribution within internal degrees of freedom show discrepancies between experiments, the distribution of translational energies are repeatedly demonstrated as being in non-equilibrium with the surface. Theorists modelling collision-free molecular evaporation from the condensed phase typically describe the translational velocity distribution of escaping molecules as a half-range or modified Maxwellian distribution. Backward scattered molecules are not found in the vapour phase [27-29] since the surface escape requirement is to have a velocity along the surface normal. The presence of molecular collisions above the surface distort the nascent distribution toward a floating Maxwellian with a translational temperature cooler than the surface and with a net translational velocity away from the surface [26,30-35]. References to the great body of research performed on the translational velocities of real desorption systems can be found in reviews such as those by Comsa [6] and Rettner [23].

In general, the difficulty in studying the immediate properties of molecules liberated from an equilibrated liquid surface arises from the presence of a jacket of vapour molecules that sits above it. This jacket of emerging vapour molecules blurs the boundary between the isotropic liquid and vapour phases. This region of space is called the interface. The properties of energy transfer through the interface have been studied extensively by Molecular Dynamics (MD) and other theoretical methods [16,29,36-55]. In a recent review of simulations describing this interface, Garrett and co-workers [4] highlight the general conclusions that *(i)* the density transition from bulk liquid to water vapour occurs over a laterally-averaged distance of 0.3 – 0.6 nm, that is, over molecular length scales, and *(ii)* the interface is rough over these molecular length scales. Garrett's simulations suggest that localised regions of the liquid-vapour interface are molecularly sharp, but as a whole, the interface appears as a rough outer layer consisting of molecules in direct contact with one another penetrating into the vacuum. X-ray scattering studies have measured liquid water surface roughness values that are in good agreement with the predictions from MD simulations [56]. In general, the high vapour pressure of liquids enhances surface roughness and widens interface thickness - adding

complexity to the evaporation processes. The low volatility of liquid sodium presented a unique situation which allowed for the study of spontaneous emission of Na_2 from its bulk liquid surface [24,25]. As with the solid surfaces it was found both the rotational and vibrational temperatures were the same as that of the bulk phase.

Traditionally, collisional energy transfer that occurs between the evaporating molecule and the vapour phase prevents us from learning about the spontaneous mass transfer process since molecular collisions redistribute the molecule's nascent internal energy. The presence of vapour phase collisions can tend to focus the molecular flux along the surface normal [6,11,24-26,28,31,32], remove molecular anisotropy [18,29], equilibrate the internal molecular degrees of freedom [31,35] as well as reducing the net evaporation flux by forcing some molecules to return back to the surface [16]. Temperature constraints on the bulk system can be used to control the number of vapour phase collisions a molecule experiences as it escapes from a liquid surface. Placing geometric constraints on the surface itself allows for the study of spontaneous emission from more volatile liquids. An *in vacuo* cylindrical filament of water, for example, is able to satisfy the Knudsen condition for obtaining collision-free molecular flow from the liquid surface if the diameter of the filament is less than the estimated mean free path of the evaporating molecules [57-59].

Faubel *et al* were able to use *in vacuo* $\text{L}\mu\text{Js}$ to determine translational velocity distributions of nascent, volatile liquids such as water [60] and carboxylic acids [61]. For pure water $\text{L}\mu\text{Js}$ of 5 μm micron diameter they found that translational velocities could be fitted with a floating Maxwellian distribution. Here the net bulk velocity was thought to be a result of only a few gas-phase collisions converting the internal energy of the evaporating molecules into translational energy away from the bulk. For $\text{L}\mu\text{Js}$ of 25 μm radius or greater the distribution observed was significantly narrower, which they concluded was due to significant cooling from collisions within the interface [61]. Saykally and co-workers have undertaken a more

extensive investigation of the number of the gas-phase collisions as a function of both liquid filament thickness and temperature [62].

Recently, Molecular Dynamics (MD) simulations of evaporation have begun to provide insight into the mass and energy transfer across the liquid–vapour interface in unprecedented detail. Most commonly, simulations of monatomic liquids have made predictions about the translational energy content of the evaporate after it has passed through the interfacial region [16,63,64]. However, MD simulations have rapidly evolved to the stage that they are able to describe polyatomic liquid interfaces and have, within a rigid rotor approximation, included predictions of the rotational energy content of the evaporate [29,30]. Further extensions that explore the vibrational energy content of evaporating molecules have yet to be reported, although predictions of bulk thermodynamic properties from simulations that explicitly incorporate intramolecular flexibility are emerging [65].

This study aims to build upon the small body of experimental research by quantifying the intramolecular energy distribution of molecules spontaneously evaporating from an *in vacuo* L μ J. Specifically the energy distribution within benzene molecules which have evaporated from the surface of a 15 μ m diameter aqueous L μ J. Benzene was chosen as the candidate with which to determine the internal energy distribution of molecules liberated from a L μ J because its spectroscopy is well characterised [66-69]. The shape and intensity of a molecule's rovibrational absorption contour is indicative of the temperature of the molecule's rotational and vibrational motion, respectively. Temperature itself is essentially a description of the distribution of molecular energy within a particular degree of freedom. In this study we report the vibrational temperatures of several vibrational modes of benzene as well as the associated rotational temperatures. Results of complimentary gas phase studies and the modelling of collision numbers therein, show that benzene displays ground electronic state collision-induced energy transfer dynamics that are sensitive to widely different collision number

regimes. The observed temperatures of evaporating benzene can thus be correlated with the number of collisions the molecule experiences as it passes from the liquid into the vacuum. Based upon Saykally's findings, molecules evaporating from such a L μ J are predicted to experience no more than ~ 7 collisions in the interface above the liquid surface. The results of the experiments presented here suggest the collision number is actually an order of magnitude greater than this prediction.

4.2 Experimental Method

A schematic illustration of the apparatus used to perform the experiments reported here is shown in Figure 4.1. For evaporation experiments a collimated UV laser with a Full-width Half Maximum (FWHM) diameter of 150 μm ($\sim 0.9 \times 10^7 \text{ W.cm}^{-2}$) runs perpendicular to both the Time-of-Flight (TOF) and L μ J axes. The UV light is produced by pumping a dye laser (Sirah, CSTR-LG-24) with the third harmonic of a Nd:YAG (Continuum SL-10-III, 355nm) and then frequency doubling the output. An arrangement of 4 pellin brocca prisms after the frequency doubling unit isolates the doubled light as well as compensates for any changes in the pointing of the laser light that can occur when the wavelength is changed. Benzene is ionised by 1+1 Resonance Enhanced Multiphoton Ionisation (REMPI) via the ${}^1B_{2u} \leftarrow {}^1A_{1g}$ transition for the first absorption step. The UV light is reproducibly positioned along the length of the L μ J as well as at distances from the L μ J using an XYZ translation stage. The distance from the capillary exit along the L μ J axis is determined by setting the zero position as the point at which the UV light cannot exit the chamber because it is being blocked by the injection system. The UV laser beam is positioned at reproducible distances away from the L μ J by setting the zero position when the beam irradiates the L μ J and produces a diffraction pattern. The UV beam is then translated away from the L μ J using a micrometer translation stage.

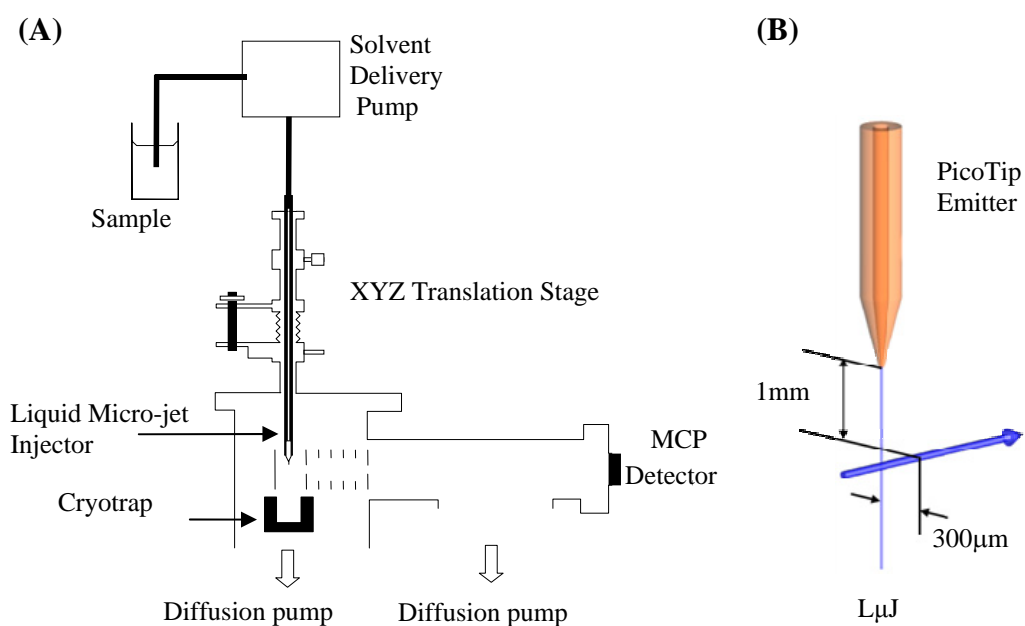


Figure 4.1: (A) Schematic of the TOF-MS with L μ J source. (B) Illustration of the relative laser position for evaporation experiments. The blue arrow represents the collimated UV laser. The laser is positioned perpendicular to both the L μ J and TOF axes and between the L μ J and detector. Only those evaporating molecules that have an initial velocity component along the TOF axis will reach the laser ionisation volume, be ionised and then detected.

The L μ J is formed by forcing the a solution at high pressure through a tapered silica capillary (New Objective PicoTip emitter, uncoated SilicaTip). The L μ Js used here are of 15 μ m diameter and comprise of a solution of 1×10^{-3} M benzene (BDH 99.7%) in a 25% v.v. ethanol (Ajax Finechem, 99.5%) deionised water mix. The use of a solvent mix does add potential complexity to interpreting experimental results. As noted by Klein and co-workers, segregation of water and ethanol leads to an enhanced ethanol concentration at the liquid surface and possibly exacerbates the surface roughness [70-72]. More recent water-alcohol simulations support these conclusions [73,74]. To explore the influence of the ethanol concentration on the measured energy distributions experiments were performed with a 10% v.v. EtOH-H₂O solvent mix as well. Within error, there was no observed difference in the rotational temperatures observed for benzene molecules evaporating from the 25% or 10% solvent mixes. Similarly, Zhang found that adding small amounts of alcohol to a glycerol/water matrix had no effect on the observed vibrational temperatures of laser desorbed benzimidazole [75]. For this reason, only the properties of evaporation from the 25% ethanol L μ J were explored in detail.

The quality of the L μ J in the vacuum is monitored through a viewing window mounted on the side of the Source Chamber. The residence time for the liquid surface in the vacuum before interrogation is determined by the flow rate of the solution (typically 0.25 mL/min) and the position of the UV beam downstream from the nozzle. Any benzene molecules which evaporate from the liquid surface and pass through the ionisation volume can be ionised and detected in the Time-of Flight Mass Spectrometer (TOF-MS). The UV wavelength of the laser is varied as the benzene mass peak is monitored and in this way an absorption spectrum is generated. Mass spectra were collected over 50 laser shots at each UV laser wavelength. Several consecutive wavelength scans were averaged to generate the wavelength spectra reported herein.

The rotational temperature of each of the bands is determined by varying the temperature of a simulated contour until the best-fit to the experimental spectrum is obtained. The fitting algorithm used is a Levenberg-Marquardt non-linear least squares algorithm [76] assuming a Boltzmann distribution amongst the rotational energy levels. Vibrational temperatures are determined by the difference in relative intensities of the cold and hot vibrational absorption bands compared with a room-temperature, equilibrated gas phase spectrum* [77]. This is discussed further in Section 4.3.2.

The bulk liquid temperature just before entering the vacuum was estimated by attaching a thermocouple to the stainless tube which holds the L μ J capillary. When placed under vacuum and with liquid flowing through the injection system, the thermocouple registered a temperature of ~ 283 K; 10 K less than the temperature of the liquid reservoir housed outside the Source Chamber. 283 K is thus assumed to be the temperature of the bulk liquid just prior to exiting the tip and the ensuing surface evaporative cooling process.

4.3 Results and Discussion

4.3.1 Rotational Temperatures

Examples of typical spectra recorded of benzene evaporating from the surface of an *in vacuo* L μ J are displayed in Figure 4.2. The 6_0^1 , $6_1^2/6_1^0/11_0^2$ and $6_0^1/6_1^1/6_0^1/11_1^1$ vibronic transitions were chosen for analysis from the UV absorption spectra since each group has a different initial state and thus a unique initial population. Studying the 6_0^1 band gives us information about molecules in the vibrationless ground state (0_0) whilst the vibrationally excited states

* The method used to generate the room-temperature gas-phase spectra is described in Chapter 3.

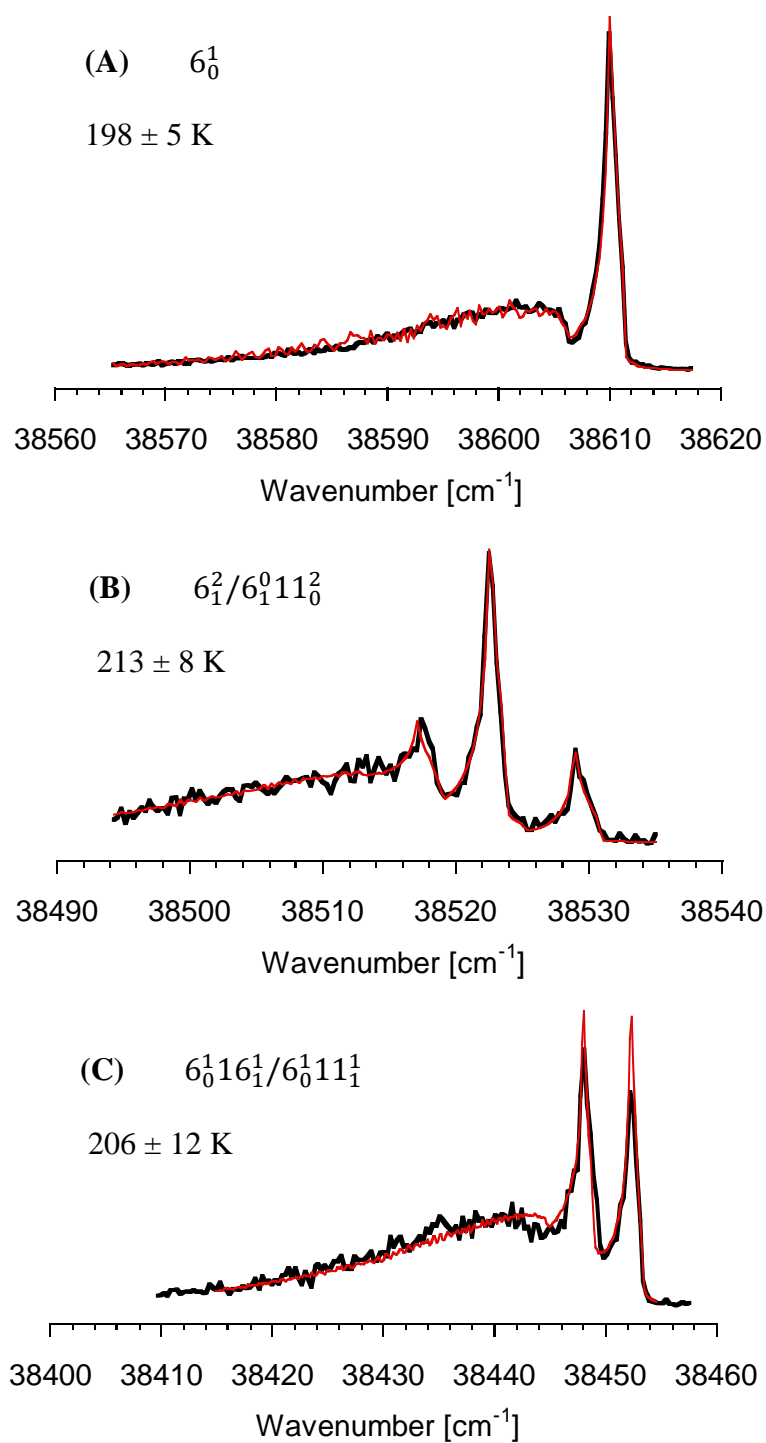


Figure 4.2: Example of best temperature fits to the 3 rovibrational contours of interest. Each experimental spectrum (black) is the convolution of at least 4 consecutive wavelength scans and overlaid with the best-fit simulated spectrum (red). Temperatures of simulated spectra are displayed with error bars indicating 1 standard deviation from the mean. When fitting spectrum (C) it was assumed that 16_1 and 11_1 vibrational levels were at the same rotational temperature. The justification for this assumption is provided later in this chapter.

6_1 , 16_1 and 11_1 are accessed through the $6_1^2/6_1^0 11_0^2$ and $6_0^1 16_1^1/6_0^1 11_1^1$ bands, respectively. The experimental spectra displayed in Figure 4.2 were all measured at a distance of 1 mm down from the L μ J nozzle orifice and 300 μ m from the surface of the L μ J. All experimental spectra analysed are the convolution of at least 4 consecutively taken spectra. The purpose of summing together many faster scans is to ensure that the shape of the contour is reproducible over time. Fluctuations in the position of the L μ J filament or in background pressure can change the intensity of the ion signal and thus distort the shape of the spectrum. Any spectrum which was not reproducible over at least 4 consecutive runs was discarded.

Overlaid on each experimental spectrum is the best temperature-fit simulated spectrum. The technique used to generate the simulated spectra is discussed in Chapter 3. The simulated spectra, displayed as the red lines in Figure 4.2, are convoluted with a Gaussian of 0.3 cm^{-1} (FWHM) to account for the laser bandwidth. At 295 K the rotational contours are large enough that most of them extend into the region of the neighbouring absorption feature. Overlapping of bands distorts their shape making it difficult to fit each band with a simulated spectrum. This quandary was overcome by simulating the neighbouring bands and subtracting them as a baseline from the rotational contour of interest. For example, at 295 K the $6_0^1 16_1^1/6_0^1 11_1^1$ rotational contour overlaps with the tail of the $6_1^2/6_1^0 11_0^2$ rotational contour. The $6_1^2/6_1^0 11_0^2$ rotational contour was simulated at 295 K and used as a baseline running under the experimentally observed $6_0^1 16_1^1/6_0^1 11_1^1$ experimental spectrum. This baseline was subtracted from the $6_0^1 16_1^1/6_0^1 11_1^1$ before being temperature fit. Temperature fitting was performed on truncated versions of the $6_1^2/6_1^0 11_0^2$ and $6_0^1 16_1^1/6_0^1 11_1^1$ bands so that the small absorption features which appear on the tails of the absorption bands do not affect the quality of the fits. The results of the temperature fits are displayed with error bars indicating 1 standard deviation from the mean (1σ).

Studies of desorption from solid surfaces have shown that rotations can be a sensitive probe of the dynamics of the desorption process. For example, Zare *et al* observed rotational anisotropy of NO desorbing from Pt(1,1,1) and concluded that the NO must leave the surface in a helicopter motion [15]. Indeed MD simulations of benzene on the surface of water show that although the benzene is free to rotate it preferentially orientates itself parallel to the liquid surface [78,79]. The surface of a liquid is rough, thermal motion creating gaps and protrusions which the evaporating molecule will encounter during its journey toward the vacuum. The small energy defect of a molecule's rotational levels means that any slight interaction with its surroundings is likely to redistribute rotational energy into an equilibrated distribution. Therefore it is expected that molecular collisions within the interface will remove any evidence of non-equilibration amongst the rotational states before the benzene escapes. The results of Figure 4.2 demonstrate that the rotational motion of evaporating molecules is at thermal equilibrium. The simulated spectra were created with a Boltzmann population of rotational states so the good correlation between the shapes of the simulated and experimental contours demonstrates that the rotational states of the evaporating molecules are also equilibrated.

Figure 4.3 summarises the results of measuring the rotational temperatures at different positions relative to the liquid surface. Each data point is the average of fitting at least nine spectra equivalent to those presented in Figure 4.2. The error associated with each data point represents three times the weighted error of the mean (3σ). In Figure 4.3(A) the rotational temperatures were determined at several distances from the nozzle orifice but at a set distance of 300 μm from the liquid surface. Increasing distance from the nozzle orifice can be equated to an increased residence time of the liquid surface in the vacuum. Within error, the rotational temperatures appear unchanging for the range of surface residence times interrogated as well as being independent of the degree of vibrational excitation. All rotational temperatures observed fall within the range of 200-230 K.

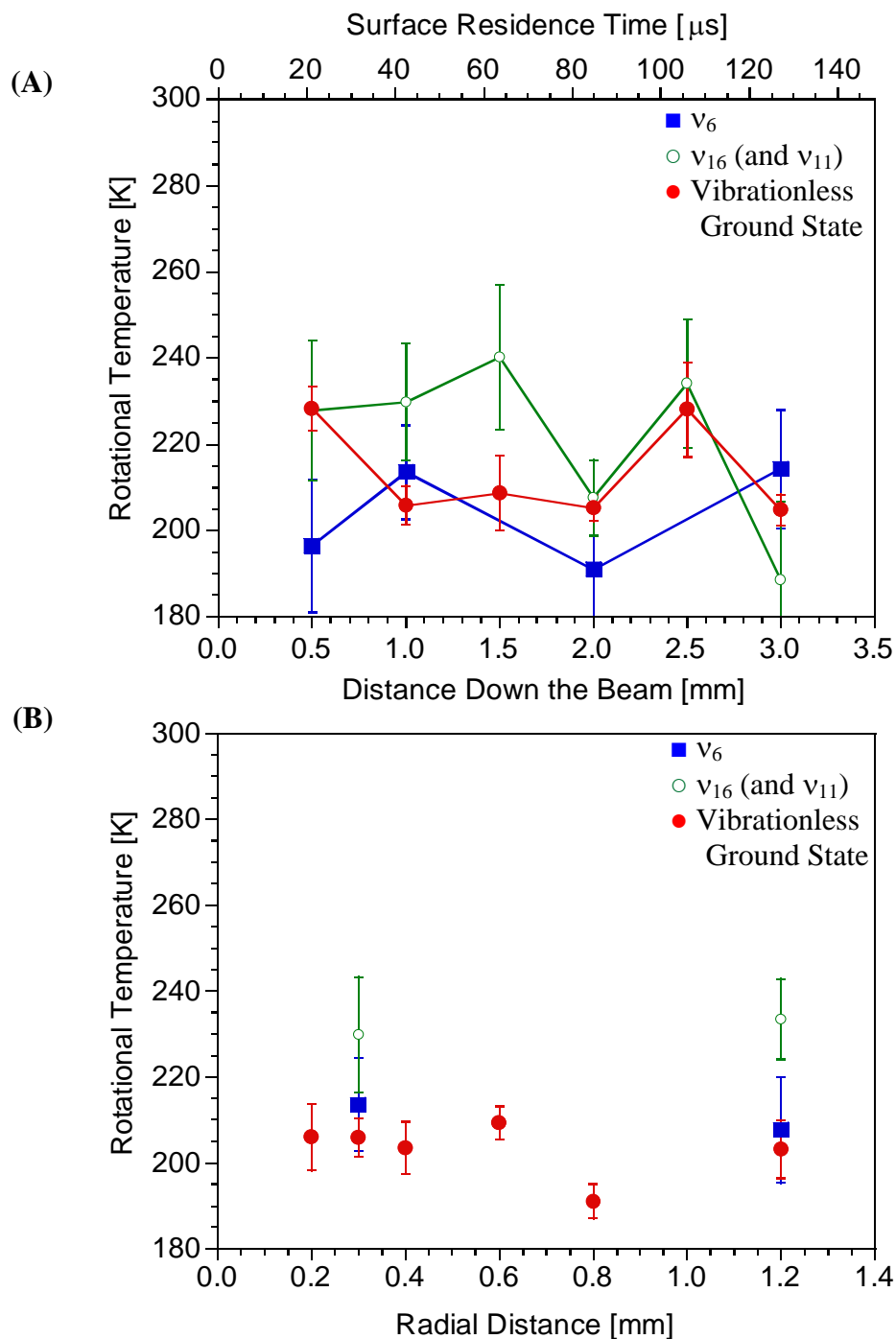


Figure 4.3: (A) Rotational temperatures of different vibrational modes of benzene as a function of surface residence time in the vacuum. Residence time is determined by the vertical distance of the ionising laser from the $L\mu\text{J}$ nozzle and the flow rate of the $L\mu\text{J}$. (B) Rotational temperatures of different vibrational modes of benzene as a function of radial distance from the liquid surface. Vibrationless rotational temperatures are represented by the solid circles (\bullet), whilst rotational temperatures for ν_6 , ν_{16} (and ν_{11}) are represented by the solid squares (\blacksquare) and open circles (\circ), respectively. The error bars represent 3 times the weighted error of the mean, 3σ .

If evaporation under these conditions is totally spontaneous, the results of the aforementioned collision-free evaporation/thermal desorption studies would suggest that the rotational temperatures are representative of the surface temperature. Indeed Faubel believed that the ~200 K translational temperature that he observed for water molecules evaporating from an *in vacuo* L μ J to be evidence of a supercooled liquid surface [60]. However, a kinetic study of the Faubel's experiment performed by Sibold and Urbassek [32] revealed that cooling of the translational motion is due to collisional energy transfer within the expanding vapour. They predicted that the surface temperature needed to generate such a translational distribution would actually be closer to 300 K - some 100 K higher than that predicted by Faubel. If internal degrees of freedom are considered in the study, then Faubel predicts that the surface temperature will be lowered by ~5%. This adjustment would then drop Sibold's predicted surface temperature to 285 K.

Saykally and co-workers have used Raman thermometry to investigate evaporative cooling rates of water and methanol from various sized L μ Js into the vacuum [80,81]. In each case they observed that the liquid surface temperatures decrease non-linearly with surface residence time, and the more volatile methanol cools much more rapidly than water. They also observed that decreasing the diameter of the L μ J enhanced the amount of surfaced cooling achieved. Extrapolation of Saykally's results to our own experimental conditions was performed to obtain an estimate of the surface temperature of the L μ Js produced for these studies. The 15 μ m diameter aqueous L μ Js used here comprise of only 25% ethanol. Although ethanol and water are totally miscible, MD simulations have shown that in a binary solution of ethanol and water hydrophobic effects cause a slight increase in the concentration of ethanol at the solution surface [70-72,82]. Thus, it is expected that the surface of the L μ Js used here will cool slightly faster than the 21 μ m water L μ Js used by Saykally, but slower than the same diameter methanol L μ Js since ethanol has only half the vapour pressure of

methanol at 295 K[†]. This corresponds to a surface temperature range of 270-260 K over the 1-3 mm downstream distance (20-130 μ s residence time) from the L μ J nozzle. Recall that in this study the temperature of the bulk solution just prior to entering the vacuum was found to be \sim 283 K. This bulk temperature correlates well with Saykally's earliest residence time measurements. Also, the minor cooling of \sim 10 K that they observed over this distance is consistent with the insensitivity of our rotational temperatures to liquid filament residence time. However, the rotational temperatures observed here are consistently \sim 50 K cooler than the predicted surface temperature; an effect that we contribute to collisional cooling within the interface.

Once the evaporating molecule has surmounted any escape barrier it must travel through the interface. It is well established by studies of purely gas phase expansions [3,85] and supported by numerical investigations of evaporation [30] that gas phase collisions cause the rotational temperature to rapidly converge toward the translational temperature. The efficient energy transfer is primarily due to the small energy defect of rotational levels. When molecules evaporate from the surface of an *in vacuo* cylindrical liquid surface they experience a molecular density profile in the vapour phase that is inversely proportional to the distance from the liquid filament [32,33]. As a result of the high molecular density within the interface, there are many low velocity, multi-body collisions which are efficient in transferring energy between rotations and translation. Frezzotti's numerical simulations of evaporation of a rigid rotor into the gas phase show that rotations and translations rapidly converge over as few as 20 mean free paths [30].

The rotational temperatures that we observe for evaporating benzene are significantly colder than the bulk liquid. This is attributed to the partitioning of rotational energy into translational motion along the desorption co-ordinate. Simulations of the free energy change as benzene

[†] At 298 K the relevant vapour pressures are : water (23.54 Torr), methanol (126.092 Torr) and ethanol (58.525 Torr) (83) Bridgeman, O. C.; Aldrich, E. W. *J. Heat Transfer* **1964**, 86, 279, (84) Ambrose, D.; Sprake, C. H. S.; Townsend, R. *J. Chem. Thermodyn.* **1975**, 7, 185.

molecules move across the liquid water/vacuum interface show that there is a deep free energy minimum at the surface from which the benzene must escape before it can evaporate [4,79,86]. In essence this is the same as the barrier to desorption experienced by molecules adsorbed onto solid surfaces, so it is reasonable to assume that benzene must have a significant translational component directed along the surface normal if it is to escape. Bowans' model of a weakly bound rigid rotor leaving a planar surface predicts that there would be significant rotational cooling observed upon desorption [22].

It is important to ascertain whether the measured temperatures represent the final values, i.e., whether collisional cooling is complete prior to laser ionisation of the benzene evaporate. In Figure 4.3(B), the spectrum of benzene was recorded at several distances away from the $L\mu J$, but always at a distance of 1 mm downstream from the nozzle orifice. Within the 3σ experimental error, there is no significant change in the rotational temperatures of either the vibrationless or vibrationally excited species as a function of distance from the liquid filament. This result indicates that collisional energy transfer is complete at a distance of 200 μm from the liquid surface since continued collisions away from the surface would have further reduced the rotational temperatures at larger distances. In other words, all measurements have been made in the collision-free molecular flow regime and our experiment probes the quantum state distributions of benzene after collisional energy transfer is complete.

The absence of a room-temperature background signal in the recorded spectra is evident from the data displayed in Figure 4.3, since even at very large distances from the liquid surface the temperatures of the different molecular degrees of freedom show no evidence of warming. Theoretically, even at infinite distances from the surface the collision probability is non-zero, due to the planar geometry along the length of the $L\mu J$ [33]. However, in the evaporation results presented here the number of collisions at distances greater than 200 μm does not appear to be significant as the temperature does not change with distance.

Within experimental error, Figure 4.3 shows that the rotational temperature of the evaporating molecules appears to be uninfluenced by vibrational excitation, remaining between 210-230 K. To obtain the rotational temperatures of molecules excited in the 16_1 and 11_1 vibrational states, it was assumed that both the contours $6_0^1 16_1^1$ and $6_0^1 11_1^1$ possess the same rotational temperature. This was a necessary assumption since the absorption bands are completely overlapped and cannot be de-convoluted in the single dimension of absorption. The validity of this assumption is supported by the observation that the vibrationless ground state and the vibrationally excited 6_1 state - which are separated by an energy defect of 608.3 cm^{-1} - display the same rotational temperature. It is understandable then, that both the 11_1 (defect of 674 cm^{-1}) and 16_1 (defect of 398.8 cm^{-1}) rotational temperatures are also unchanging and equivalent to the 0_0 temperature at all distances from the liquid surface.

However, the excitation of ν_{16}/ν_{11} does consistently appear to produce rotational temperatures at the upper end of the temperature range. This result could be an artefact of the aforementioned assumption that 11_1 and 16_1 have the same rotational temperature or it could be an indication of dynamics of the evaporation process. It is possible that warming of rotations in molecules that are excited with the out-of-plane (OOP) vibrations (such as ν_{16} and ν_{11}) is due to the interaction of the vibrating molecule with the 'surface'. MD simulations of benzene lying on an aqueous surface show that the molecule preferentially lays flat at the liquid surface [78,79]. As the benzene reaches the outer limits of the interface on its way to liberation, the OOP vibrations can kick benzene into rotating slightly faster by pushing off the adjacent surface. As the number of gas phase collisions after the interface is negligible under these conditions, the benzene will retain its 'hot' distribution of rotations for molecules excited by the OOP vibration. Support for this theory would come in the observation of an enhanced rotational warming of molecules excited with multiple quanta of the OOP vibrations. This should be the subject of further investigation.

4.3.2 Vibrational Temperatures

In Figure 4.4 we present absorption spectra spanning all of the absorption features discussed in this study. The spectra were all generated via 1+1 REMPI but under different experimental conditions. In Figure 4.4(A) the spectrum was produced in the room-temperature gas phase static cell introduced in Chapter 3. Figure 4.4(B) is the absorption spectrum for benzene molecules evaporating from the surface of an *in vacuo* L μ J. For comparison, the spectrum of benzene molecules that are entrained in a free-jet expansion of nitrogen is included in Figure 4.4(C). This spectrum is discussed further in Section 4.4.2. Each vibronic band in each spectrum is generated by an electronic transition out of a different vibrational state. The 6_0^1 band originates in the vibrationless electronic ground state, 6_1^2 and $6_1^0 11_0^1$ are hot bands which both start with one quanta of the in-plane (IP) ring squashing vibration, ν_6 , and $6_0^1 16_1^1$ and $6_0^1 11_1^1$ are hot bands with one quanta of the OOP vibrations ν_{16} and ν_{11} , respectively.

As the temperature of the vibration changes, the relative intensity of the absorption feature involving that vibration also changes due to changes in population of the initial excited state. By monitoring the changes in intensities of the hot bands relative to the cold band (6_0^1) we can follow how the population within the vibrational states is being redistributed with the change in conditions [77]. The room temperature spectrum is used as a reference since we can be confident the system is at equilibrium; which means that all the different vibrations will be at the same temperature - 295 K. The relative intensity of each band in this spectrum is thus due to the different Frank Condon (FC) factors for each of the transitions. The temperature, T_j , of the vibration, ν_i , in the system can thus be determined by the relationship:

$$\frac{I_{\nu_i, T_j} / I_{\nu_0, T_j}}{I_{\nu_i, T_{295}} / I_{\nu_0, T_{295}}} = e^{\left[\frac{E}{R} \left(\frac{1}{T_k} - \frac{1}{T_j} \right) \right]}, \quad \text{Equation 4.1}$$

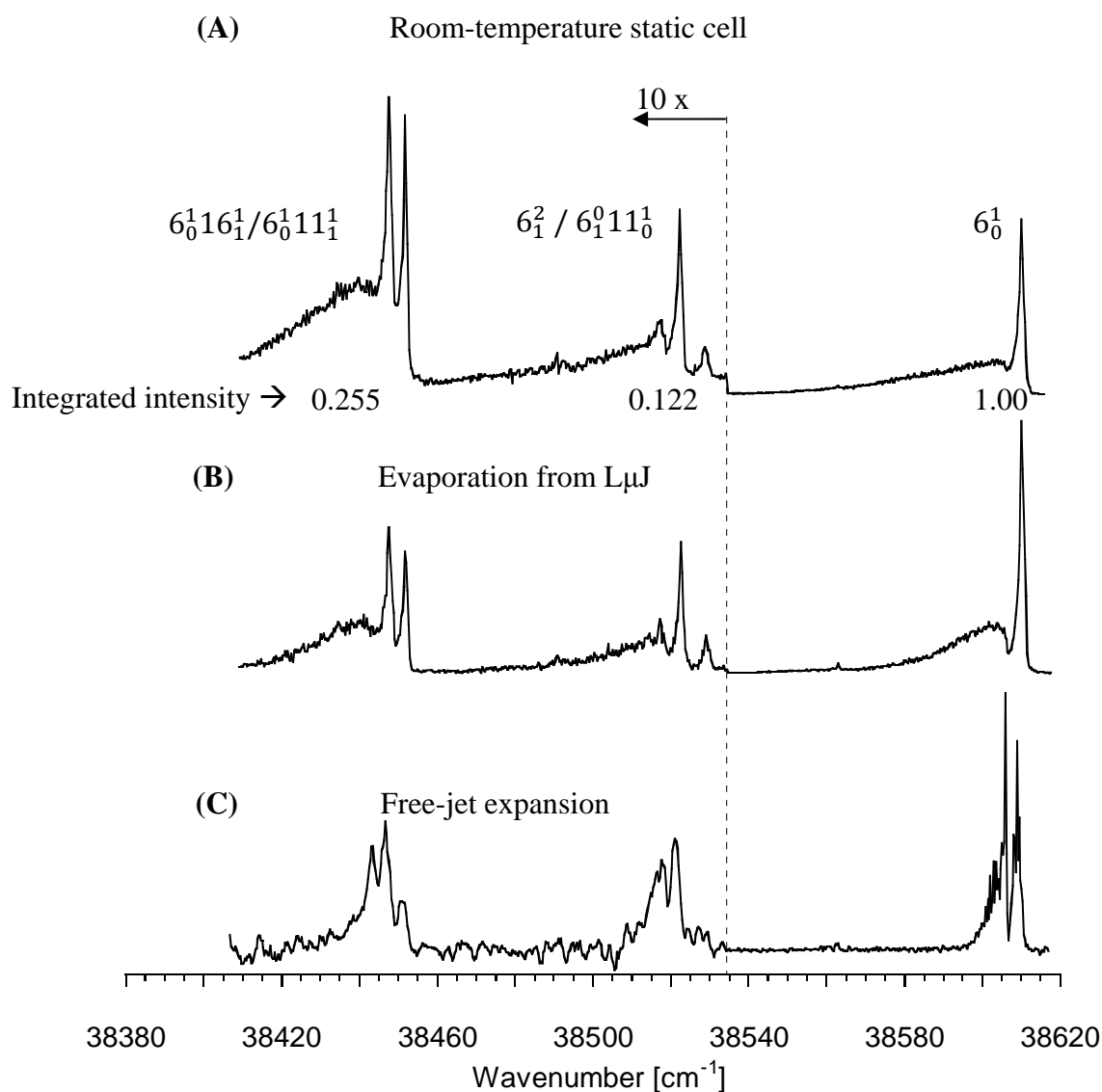


Figure 4.4: Benzene 1+1 REMPI absorption spectrum produced under various experimental conditions. (A) In a room temperature static cell. The integrated intensities of the hot bands relative the 6₀¹ are indicated under each band. (B) Evaporation of benzene from an *in vacuo* L_μJ. The ionising laser was positioned 1 mm from the nozzle and 300 μm from the jet surface. (C) Benzene seeded into a free-jet expansion of nitrogen. The expansion conditions are reported in Section 4.4.2. The intensity of all spectra at energies less than 38535 cm⁻¹ have been enhanced ten-fold for display purposes.

where ν_0 represents the vibrationless ground state. $I_{\nu_i, T_{295}}$ is the integrated intensity of the band which is generated from a transition out of a state involving ν_i at room temperature (295 K). The integrated intensities of the hot bands relative to the 6_0^1 at 295 K are given in Figure 4.4(A). Analysis of simulated spectra confirm that the integrated intensities of the absorption bands are essentially uninfluenced by a change in rotational temperature which means that the rotational temperature of a vibration has no effect on the measurement of vibrational temperatures determined via this method.

Although the absorption band with the origin at 38520 cm^{-1} is due to the energetic overlap of the two transitions, 6_1^2 and $6_1^0 11_0^1$, the initial vibrational level prior to laser excitation includes 6_1 in each case, so the application of Equation 4.1 to the overlapping absorption bands allows us to determine the degree of evaporative cooling for the ν_6 vibrational mode. Such analysis yields a ν_6 evaporative vibrational temperature of $256 \pm 11\text{ K}$. The uncertainty represents 3 times the weighted error of the mean, 3σ .

To lower transition energy, the series of peaks around $38,440\text{ cm}^{-1}$ are assigned to the $6_0^1 16_1^1$ and $6_0^1 11_1^1$ vibronic transitions. Analysis of these overlapping bands to determine vibrational temperatures is less straightforward because the transitions arise from molecules which are initially excited with either ν_{11} or ν_{16} in the ground electronic state. However, the spectral analysis of this band performed in Chapter 3 revealed the shape, position and relative FC factor for the underlying $6_0^1 11_1^1$ band. This information is thus used to perform a non-linear least squares fit of the intensity of this band under the $6_0^1 16_1^1$. This subsequently allows the determination of the vibrational temperature of the ν_{11} and ν_{16} independently. Using the ratio of FC factors for $6_0^1 16_1^1$: $6_0^1 11_1^1$ as 1: 0.83, an analysis of the evaporation spectrum reveals vibrational temperature of $230 \pm 13\text{ K}$ for ν_{16} and $251 \pm 15\text{ K}$ for ν_{11} . Again, the uncertainty represents the 3 times the weighted error of the mean.

Table 4.1: Temperatures of the different internal degrees of freedoms of benzene molecules evaporating from an *in vacuo* aqueous surface.

Benzene Internal Energy Mode	Temperature (K)
Rotation	210-230
ν_{16}	230
ν_{11}	251
ν_6	256

Just as with the rotational temperatures, Figure 4.5 shows that within experimental error, all of the vibrational temperatures are unchanging as a function of both surface residence time and probing distance from the liquid surface. In the lower energy levels of a ground electronic state the density of vibrational states is low and so the intramolecular vibrational energy redistribution process is dominated by collision induced processes [87]. The vibrational cooling observed of benzene molecules evaporating from the $L\mu\text{J}$ surface is a result of collisional cooling as the molecules traverses the liquid-vacuum interface. Each molecule excited with a different vibration type cools to a different extent since the absolute rate of deactivation of a vibrational level is dependent upon the nature of the collisional interaction [88-90] as well as the amount of energy transferred during the collision [90-94]. Computational studies by Bernshtein and Oref *et al* [95,96] have shown that only the 3 vibrational modes of benzene that have the smallest frequency, namely ν_{16} , ν_6 and ν_{11} , have an appreciable vibrational relaxation cross-section. Of these three, ν_{16} has a relaxation cross-section an order of magnitude greater than the other two. This enhanced cross-section is attributed not only to the mode's lower frequency but also because it's motion is out-of-plane (OOP). This efficiency of collisional energy transfer out of level 16_1 is evident in the evaporation results presented here since benzene excited with one quanta of ν_{16} are observed at much lower vibrational temperatures than either ν_6 or ν_{11} .

However, the dynamical effect of the vibrational motion on the efficiency of collisional cooling is perhaps most evident in the comparison of the ν_6 and ν_{11} temperatures. If the

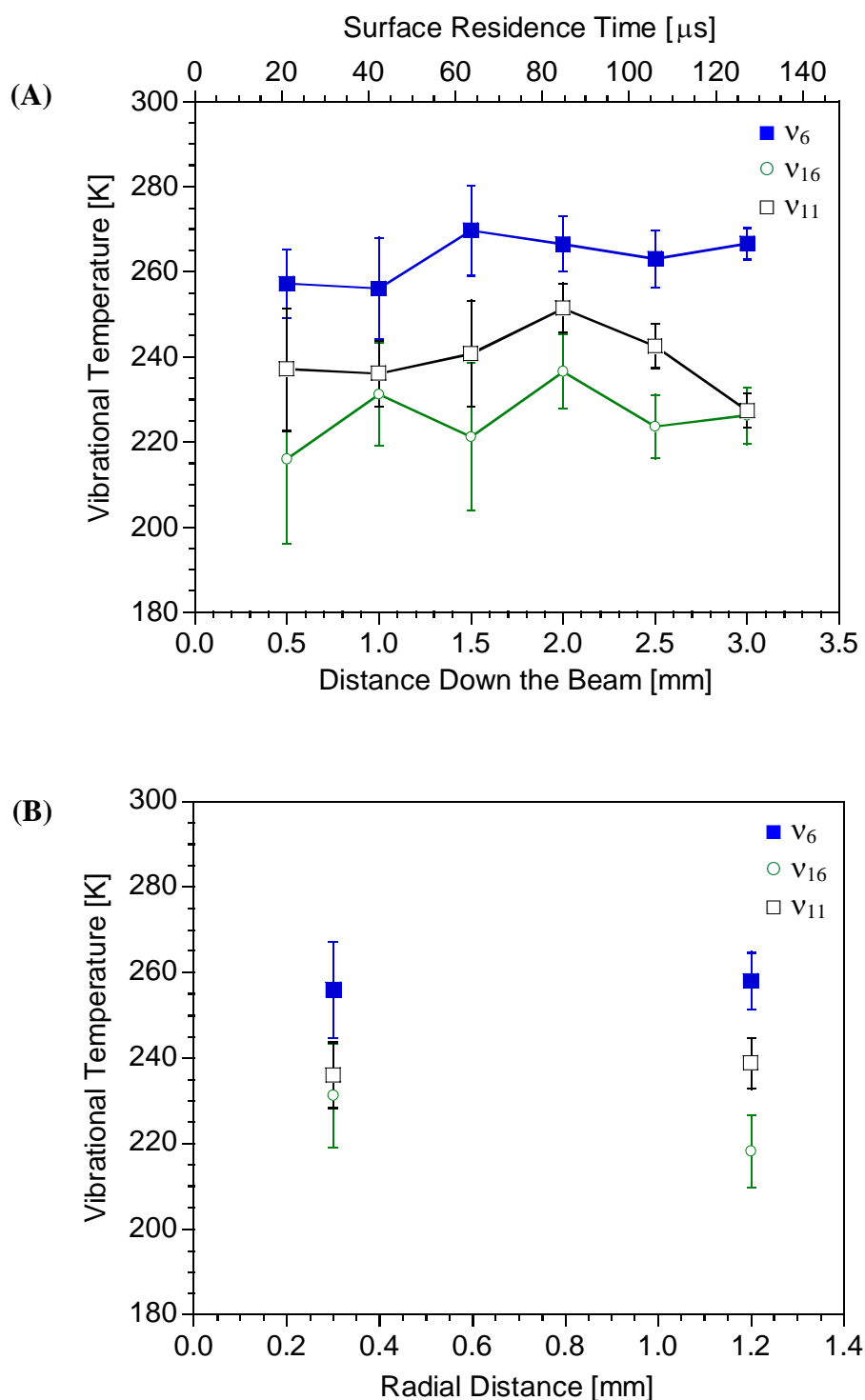


Figure 4.5: (A) Vibrational temperatures of benzene as a function of residence time in the vacuum. (B) Vibrational temperatures of the different vibrational modes as a function of distance from the liquid surface. The vibrational temperatures for ν_6 , ν_{16} and ν_{11} are represented by the solid squares (\blacksquare), open circles (\circ) and open squares (\square), respectively. The error bars represent 3 times the weighted error of the mean, 3σ .

relative collisional cooling efficiencies were solely dependent upon the relative frequencies of the vibrations, then it would be expected that ν_{11} (674 cm^{-1} in ${}^1A_{1g}$) would appear vibrationally warmer than ν_6 (608.3 cm^{-1} in ${}^1A_{1g}$). However, quantum calculations by Clary *et al* [95] predict that the OOP nature of the vibration increases the collisional cross-section of benzene molecules excited with ν_{11} so it is effectively only slightly smaller than those excited with ν_6 . The results shown here support Clary's findings as the evaporating benzene molecules which were excited with ν_{11} were seen to cool (within error) by the same amount as those excited with ν_6 .

The important results to emerge from this study are that (i) the rotational and vibrational temperatures of the benzene evaporate are different, and (ii) the vibrational temperatures of ν_6 , ν_{11} and ν_{16} are different. This is only possible if there have been insufficient collisions to establish equilibrium between the rotational and various vibrational degrees of freedom as benzene passes from the liquid into the collision-free region of the gas phase. As we have noted earlier, for sufficiently thin L μ Js, gas phase collisions above the liquid surface are largely, but not completely, eliminated [32,60,61]. For example, the sharp boundary interface model used by Faubel and others to analyse evaporative translational energy distributions predicts that, at a liquid surface temperature of 295 K, water molecules evaporating from a 7.5 mm radius L μ J – as used in the experiments reported here – will undergo no more than ~ 7 hard sphere gas phase collisions. As we demonstrate below, this small collision number is insufficient, by more than an order of magnitude, to cool ν_{16} to the extent observed.

4.4 Determination of Collision Numbers upon Evaporation from an *In Vacuo* Liquid Surface

The aim of this study is to qualify the number of collisions a molecule experiences as it travels from a room temperature surface into the vacuum. This is determined by first calculating the probability of collisional energy transfer out of a particular vibrational level in the ground electronic state of benzene through observation of the extent of vibrational cooling that occurs when benzene is seeded in a free-jet expansion. This probability can then be correlated with the vibrational cooling observed in the evaporation experiments and thus be used to quantify the number of collisions the molecule undergoes as it has traverses the liquid interface.

4.4.1 Collisional Energy Transfer

Collisional energy transfer is a radiationless energy transfer process whereby collisions between the “bath” and the molecule of interest can cause energy to be redistributed amongst the different degrees of freedom. Determination of the rate of relaxation of a particular freedom tells us the efficiency of hard-sphere collisions to transfer population out of the excited energy state into the surrounding levels. The average transition probability, P_{ij} , is the probability that a collision will result in a change of state from wavefunction ψ_i to ψ_j and is directly related to the Effective Collision Frequency, Z_{ij} , for the process in question.

$$P_{ij} = \frac{Z_{ij}}{Z_{HS}}, \quad \text{Equation 4.2}$$

where Z_{HS} is the gas-kinetic, hard-sphere collision frequency [97]:

$$Z_{HS} = \sigma \left(\frac{8kT}{\pi\mu} \right)^{1/2} \mathcal{N}. \quad \text{Equation 4.3}$$

Here σ is the hard-sphere collision cross-section, k is the Boltzmann constant, T is the temperature of the system, μ the reduced mass of the system and \mathcal{N} the number density.

The efficiency of a collision at transferring population from state ψ_i to state ψ_j is dependent upon the energy defect of the states, i.e. $E_i - E_j$. The smaller the defect, the more likely that the collision will be able to induce the population transfer by transferring energy between collision partners [98-100]. This means that transitions that require more energy than the average kinetic energy of the bath gas (kT – where T is the translational temperature) will have a low probability of occurring [87,94]. Typically, rotational and translational transition probabilities are faster than gas-kinetic, meaning there is a rapid collision induced equilibration within the rotational manifold of the molecule as well as between rotational and translational temperatures. For the same reason vibration \rightarrow vibration transitions are favoured over vibration \rightarrow rotation/translation transitions; the latter only occurring through the lowest energy vibrational modes [94]. As a result a collision induced equilibration process may result in a non-equilibrated steady state situation, where the different degrees of freedom each can be described by a unique temperature [94].

Generally, collisional relaxation process in the ground state have been studied with techniques such as infrared Laser Induced Fluorescence techniques [101,102] for the lower lying vibrational states of small molecules or Stimulated Emission Pumping [41] and high resolution Diode Laser Spectroscopy [103] to observe the highly vibrationally excited, electronic ground states. An in-depth review of earlier studies of relaxation in the ground state was performed by Weitz and Flynn [104] and more recently by Nesbitt and Field [105]. Indeed, collisional relaxation of electronically excited [90,98-100,103,106-110] and highly vibrationally excited [103,111,112] benzene has been studied in some detail. However studies performed in the low energy levels of the electronic ground state of benzene are scarce [113].

In his review of energy redistribution processes, Bondybey [87] concluded that, in general, collisional relaxation in an electronic ground state is much slower than in an electronic excited state - a phenomenon likely due to the increased polarisability of the excited state strengthening intermolecular interactions. Using Information Theory in combination with LIF Lyman predicted ground state vibrational relaxation rates for benzene are less than 1% of the gas-kinetic rate [113]. In comparison, the vibrational relaxation rates in the $^1B_{2u}$ state of benzene have been shown to be on the order of 10^6 effective collisions per second [108]. In contrast, Lawrance's seminal study of *p*-difluorobenzene showed there was little difference between deactivation rates in the electronically excited state and vibrationally excited ground state of this aromatic [114]. Since the vibrational relaxation rates for the low-lying energy levels of benzene are not well established here we attempt to make our own estimate of rates of energy redistribution out of selected vibrational states in benzene's electronic ground state.

4.4.2 Modelling Collisional Energy Transfer Rates

Initial experiments attempted to simulate the conditions of the L μ J-based evaporation experiments by expanding a room temperature benzene/water/ethanol vapour mix (5 kPa benzene, 2 kPa H₂O, 0.5 kPa EtOH) into the vacuum. Micron-sized capillary nozzles have proven to be capable of creating free-jet expansions [115,116] so the 15 μ m L μ J nozzle was the orifice through which the gas was expanded into vacuum. Expansion using the room-temperature vapour pressures of water and ethanol was found to be insufficient to observe any collisional cooling in the benzene and so N₂ (15 kPa) was added as a carrier gas. Alternate experiments were performed with the water and ethanol vapour present and absent in the expansions. Within experimental error, no differences in the benzene spectral profiles were observed, indicating that water and ethanol do not have unusually large collisional relaxation efficiencies with benzene and, for illustrative purposes, can therefore be considered to be comparable in efficiency to N₂. In this study we use the collisional relaxation efficiencies of

nitrogen, determined as described below, to represent a lower limit to the efficiencies expected for a water-ethanol system.

The relaxation efficiencies for N_2 were determined following measurement of the 1+1 REMPI spectrum of benzene vapour cooled in a nitrogen (10 kPa benzene in 350 kPa N_2) free-jet expansion. The resultant spectrum is shown in Figure 4.4(C). Consistent with previously reported trends [68,117-119], the temperatures 1 mm downstream from the nozzle orifice were determined to be 290:270:208:20 K for $T_{\text{vib}(v_6)}:T_{\text{vib}(v_{11})}:T_{\text{vib}(v_{16})}:T_{\text{rot}}$ using the temperature-fitting techniques described in Section 4.3.1 and 4.3.2. The rotational temperature quoted here is that of the ground, vibrationless state (measured from the shape of the 6_0^1 rovibrational contour). The measured rotational temperatures of the hot bands displayed in Figure 4.4(C) were found to all possess essentially the same rotational temperature as the ground state. Using established methods for characterizing the physical properties of 3D free-jet expansions as a function of distance downstream from the nozzle orifice [3], we can quantify properties such as the total collision number and translational temperature under the experimental conditions reported here. The results of modelling the translational temperature inside the free-jet expansion are illustrated in Figure 4.6. Such modelling predicts that at a distance of 1 mm from the nozzle orifice ~ 360 binary hard-sphere collisions have occurred, producing a translational temperature of $\sim 4 \text{ K}^\ddagger$. Relating this to our evaporation results, means that even after 360 gas-phase collisions v_6 has undergone essentially no cooling from the temperature of the bulk. On the other hand, v_{11} and v_{16} show increasing amounts of vibrational cooling and the rotations are substantially cooled, almost attaining the expected translational temperature of the expansion [3,120].

[‡] The parameters used in the 3D jet simulation were taken from Ref (85) Miller, D. R. *Atomic and Molecular Beam Methods*; Oxford University Press: New York, 1991; Vol. 1. N_2 Hard-sphere cross-section (σ) 3.85 Å, heat Capacity ratio (γ) = 1.4.

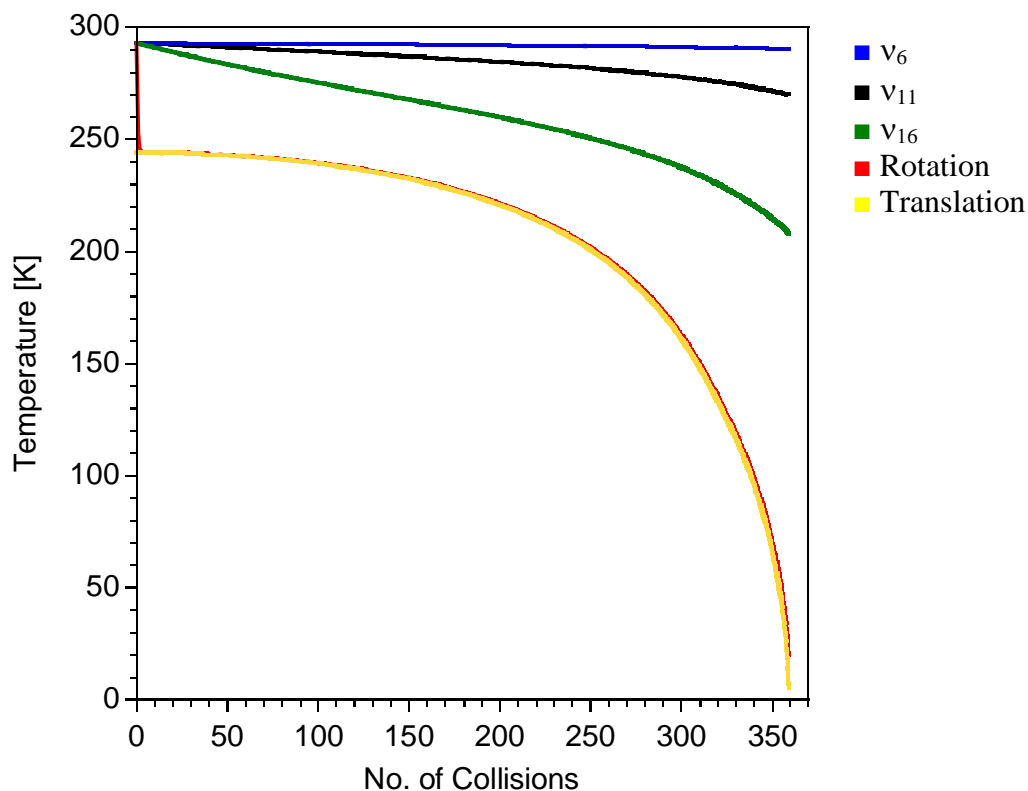


Figure 4.6: Illustration of the collisional cooling experienced in the nitrogen free-jet expansion as a function of binary collision number. The translational temperature of benzene is determined by the expansion properties of the 3D jet, including the orifice diameter and the heat capacity of the carrier gas [85]. Under the experimental conditions reported here the translational temperature asymptotes to a maximum of 360 binary collisions. The collisional cooling efficiencies of the other modes were varied until their temperature at 360 collisions was equal to that observed experimentally. The collisional cooling efficiencies required to achieve these temperatures are given in Table 4.2.

4.4.3 Temperature Gap Model of Collisional Relaxation Rates

Two different kinetic models were used to describe the collisional relaxation efficiencies observed in the above mentioned experiment. The first is the very simple yet surprisingly accurate model that has been used by several groups [3,117,121,122] to model rotational and vibrational collisional energy transfer. The model predicts that the rate of collisional energy transfer is linearly proportional to the extent that the particular mode deviates from its equilibrium value. Adopting a similar approach, but expressing the energy transfer rate in terms of hard-sphere collision number ($Coll.$) rather than time, a simple ‘temperature gap’ (TG) model can be expressed as:

$$\frac{dT_i(Z)}{dColl.} = k_{i\infty}[T_{trans}(Coll.) - T_i(Coll.)] , \quad \text{Equation 4.4}$$

where $k_{i\infty}$ represents the collisional energy transfer efficiency of the particular mode, i , into the surrounding levels, $T_i(Coll.)$ is the temperature of the rotation or vibrational mode under investigation and $T_{trans}(Coll.)$ is the translational temperature of the colliding gas (as determined from the free-jet expansion modelling). The latter two parameters are expressed as a function of collision number. The mode-specific collisional energy transfer efficiencies (*i.e.*, $k_{i\infty}$) of benzene in nitrogen determined here are reported in Table 4.2. An illustration of how the internal temperatures change as a function of binary collision number was illustrated in Figure 4.6. Rotational relaxation is found to be occurring at almost the hard-sphere collision rate; it is ~200 times more efficient than relaxation of ν_{16} , ~1000 times more efficient than ν_{11} and 10,000 times more efficient than relaxation of ν_6 . ν_{16} relaxation is ~50 times more efficient than relaxation of ν_6 and ~5 times more efficient than ν_{11} .

Table 4.2: Mode-specific collisional energy transfer efficiencies ($k_{i\infty}$) of benzene in nitrogen.

Benzene Internal Energy Mode	$k_{i\infty}$ (collision ⁻¹)
Rotation	0.9
ν_{16}	4.3×10^{-3}
ν_6	9.0×10^{-5}
ν_{11}	8.1×10^{-4}

4.4.4 Master Equation Model of Collisional Relaxation Rates

The second, more complex kinetic model, called here the ‘Master Equation’ (ME) model involves a series of linearly coupled differential equations to describe the flow of population amongst the selected vibrational states upon molecular collision. Assuming a first order decay of population, the general rate equation which describes the exchange of population between lower and upper states ψ_i and ψ_j , respectively, as a function of collision number can be described as[§]:

$$\frac{d[N_i]}{d \text{ Coll.}} = k_{ij}g_i[N_j] - k_{ij}g_j[N_i]e^{-\Delta E_{ij}/kT}, \quad \text{Equation 4.5}$$

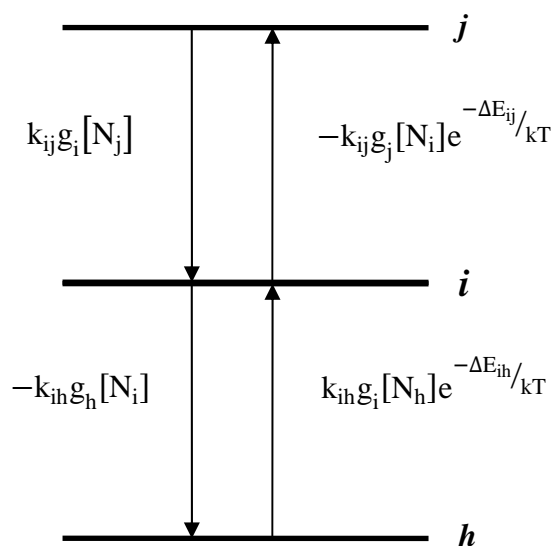
where, again, *Coll.* is the number of hard-sphere collisions, N_i is the population and g_i the degeneracy of the state i , k_{ij} is the rate constant describing the rate of population transfer between the states. The first term in Equation 4.5 represents a gain in population for state ψ_i by relaxation of the higher ψ_j state. The second term represents a loss in population for ψ_i as its population is promoted to the ψ_j state. For the endoergic (up) transitions an extra exponential factor was added in accordance with Parmenter’s observations for energy transfer rates in the electronically excited state [99].

[§] Rate equations developed in communication with Prof. Warren Lawrance, The Flinders University of South Australia.

In actuality modelling population transfer can become quite complex since we must consider the possibility that a state may exchange its population with all neighbouring states. This is illustrated in Figure 4.7. In the S_0 state of benzene there are several low lying vibrational levels between which energy can be exchanged upon molecular collision. The probability of energy exchange has been shown to depend upon several factors. As mentioned earlier, the exchange of energy greater than the thermal energy of the bath gas is unlikely, so energy exchange between closely energetic states (V-V exchange) is often more likely than total vibrational relaxation to the ground state since this would require all vibrational energy to be exchanged for rotational and translational energy [87,96]. Consequently a model needed for monitoring energy/population transfer out of a single vibronic level must include all the surrounding energetically and dynamically accessible vibrational states. Flynn notes that the number of kinetic rate constants needed to describe a system of n levels scales as $n(n - 1)/2$ [94]. In the S_0 electronic state of benzene there are 8 vibrational states as well as the vibrationless ground state with energies under 1300 cm^{-1} ; giving a total of 36 rate constants needed to describe the collisional energy rearrangement in the low levels of S_0 benzene. Stephenson and Rice showed that in actuality only a small subset of the energetically accessible levels are involved in the redistribution, though this varies with the vibrational level excited [123]. In order to limit the number of rate constants needed to be generated for this model several simplifications were enforced according to the observed propensities for collisional energy transfer [87,93,98,99].

The number of rate constants were limited by applying the following simplifications:

1. Allowed transitions involve no more than a two quanta change in vibration.



$$\frac{d[N_i]}{d \text{ Coll.}} = k_{ij}g_i[N_j] - k_{ij}g_j[N_i]e^{-\Delta E_{ij}/kT} - k_{ih}g_h[N_i] + k_{ih}g_i[N_h]e^{-\Delta E_{ih}/kT}$$

Figure 4.7: General description of rates of population transfer into and out of state i .

2. The difference between energy levels involved in a transition (energy defect) is on the order of the thermal energy of the bath ($\sim 200 \text{ cm}^{-1}$) or smaller.
3. Only transitions that have a starting level of appreciable population at room temperature are included.
4. Transitions that involve the same quanta change of a particular vibration are described by the same rate constant. For example, the rate constants, $k_{(6,16)16}$ and k_{60} , are assumed to be equal since they both describe a single quantum change in ν_6 , i.e. the rate of $[6_1 16_1 \rightarrow 16_1] \equiv [6_1 \rightarrow 0_0]$

All the states included in this model of collision energy transfer out of the vibrational states 6_1 , 16_1 and 11_1 in S_0 benzene are shown in Table 4.3. All the possible population transfer pathways are illustrated in Figure 4.8. It was necessary to include states of higher energy than 6_1 in the ME model since their exclusion would overestimate the rate of population loss from 6_1 . Transfer of population from the higher states into 6_1 was necessary to produce the overall effect of a minimal collision induced population change in 6_1 – i.e. minimal collisional cooling. Application of the limitations outlined above mean that only 17 transitions were included in the model. Several of these transitions involve a change in the same number of quanta of a particular vibration. These transitions were assigned the same rate constants. This means that only 11 independent rate constants were needed to describe the collision induced population transfer for the low lying vibrational levels of ground state benzene (see Table 4.3).

By monitoring the change in state population with collision number we are able to determine the k_{ij} values needed to obtain the observed vibrational temperatures inside the free-jet expansion. The temperature of a vibrational mode was determined using the well known relationship:

Table 4.3: Summary of possible levels to be included in the ME model of relaxation rates in S_0 benzene. (\ddagger) Degeneracies correlate with those quoted in Parmenter [98]. (*) Populations are relative to the vibrationless ground state at 295 K. Highlighted rows are the transitions that were included in the model. Of the 36 possible transitions only 17 are included in this model; the other transitions were discarded upon enforcement of the simplifications as stated in the text. Δ , Ω , ∞ : these transitions were given equivalent rate constants, (k_{ij}), as they involve the same number of quanta change of a particular vibration. This leaves 11 independent rate constants to be calculated using the series of differential equations.

Initial				Final			Transition Energy Defect	Quanta Change Δv
State	Frequency cm^{-1}	g_i \ddagger	Relative Population *	State	Frequency cm^{-1}	g_i		
16 ₁	399	2	0.29	0 ₀	0	1	399	1 Δ
6 ₁	608	2	0.11	0 ₀	0	1	608	1 ∞
11 ₁	674	1	0.04	0 ₀	0	1	674	1 Ω
4 ₁	707	1	0.03	0 ₀	0	1	707	1
16 ₂	798	3	0.07	0 ₀	0	1	798	2
6 ₁ 16 ₁	1007	3	0.02	0 ₀	0	1	1007	2
6 ₂	1216	3	0.01	0 ₀	0	1	1216	2
6 ₁ 11 ₁	1282	2	0.00	0 ₀	0	1	1282	2
6 ₁	608	2		16 ₁	399	2	209	2
11 ₁	674	1		16 ₁	399	2	275	2
4 ₁	707	1		16 ₁	399	2	308	2
16 ₂	798	3		16 ₁	399	2	399	1 Δ
6 ₁ 16 ₁	1007	3		16 ₁	399	2	608	1 ∞
6 ₂	1216	3		16 ₁	399	2	817	3
6 ₁ 11 ₁	1282	2		16 ₁	399	2	883	3
11 ₁	674	1		6 ₁	608	2	66	2
4 ₁	707	1		6 ₁	608	2	99	2
16 ₂	798	3		6 ₁	608	2	190	3
6 ₁ 16 ₁	1007	3		6 ₁	608	2	399	1 Δ
6 ₂	1216	3		6 ₁	608	2	608	1 ∞
6 ₁ 11 ₁	1282	2		6 ₁	608	2	674	1 Ω
4 ₁	707	1		11 ₁	674	1	33	2
16 ₂	798	3		11 ₁	674	1	124	3
6 ₁ 16 ₁	1007	3		11 ₁	674	1	33	3
6 ₂	1216	3		11 ₁	674	1	542	3
6 ₁ 11 ₁	1282	2		11 ₁	674	1	608	1 ∞
16 ₂	798	3		4 ₁	707	1	91	3
6 ₁ 16 ₁	1007	3		4 ₁	707	1	300	3
6 ₂	1216	3		4 ₁	707	1	509	
6 ₁ 11 ₁	1282	2		4 ₁	707	1	575	3
6 ₁ 16 ₁	1007	3		16 ₂	798	3	209	2
6 ₂	1216	3		16 ₂	798	3	418	4
6 ₁ 11 ₁	1282	2		16 ₂	798	3	484	4
6 ₂	1216	3		6 ₁ 16 ₁	1007	3	209	2
6 ₁ 11 ₁	1282	2		6 ₁ 16 ₁	1007	3	575	2
6 ₁ 11 ₁	1282	2		6 ₂	1216	3	66	2

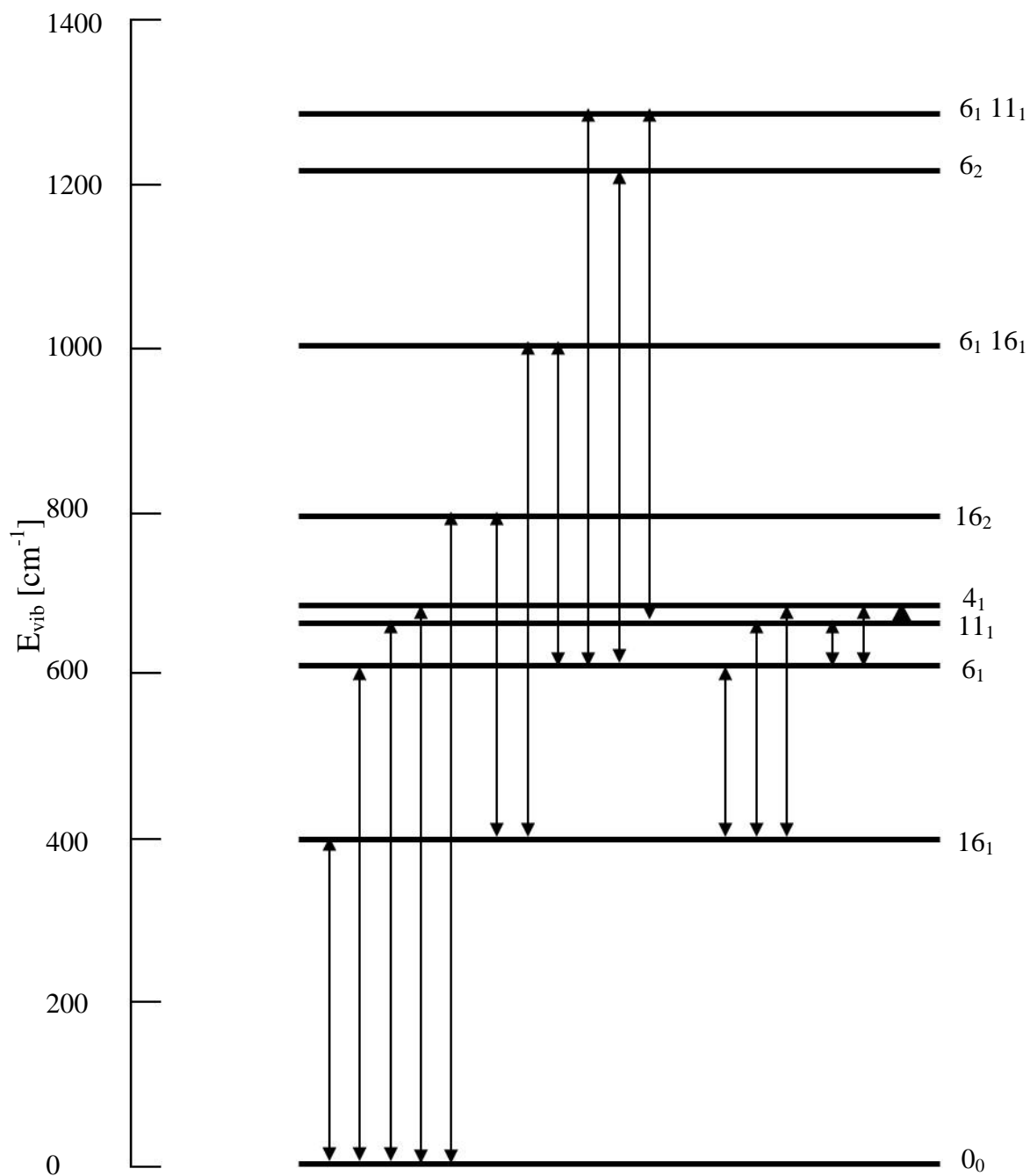


Figure 4.8: The 17 transitions included in the Master Equation (ME) kinetic model.

$$k_B T = -h\nu_i / \ln \left(\frac{N_i g_0}{N_0 g_i} \right) \quad \text{Equation 4.6}$$

Where k_B is Boltzmann's constant, ν_i and g_i is the frequency and degeneracy of mode i , and N_0 the population of the vibrationless ground state. An initial Boltzmann distribution of population was assumed at time zero.

4.4.5 Results of Master Equation Modelling

All rates were calculated relative to the $6_1 \leftrightarrow 0_0$ collisional energy transfer efficiency. First attempts at solving for the rate constants employed Lyman's value for $6_1 \rightarrow 0_0$ relaxation via benzene-Argon collisions [113]. In his study, Lyman monitored the population changes within ν_{18} via LIF and was able to estimate the deactivation rate for $6_1 \rightarrow 0_0$ as $4.5 \times 10^{-7} \text{ cm}^3 \text{ molecule}^{-1} \text{ s}^{-1}$ (which is equivalent to $1.55 \times 10^{-7} \text{ collision}^{-1}$ at 300 K). The use of this base value to calculate the other rate constants in our model yields collisional efficiencies for many of the transitions that are 3 orders of magnitude greater than that of $6_1 \rightarrow 0_0$. In comparison, when the $6_1 \rightarrow 0_0$ rate calculated from the TG model (Equation 4.4) is employed ($9.0 \times 10^{-5} \text{ collision}^{-1}$) the resulting k_{ij} values are more realistic, approaching the relative values observed by Parmenter [98] in the S_1 state for benzene colliding with nitrogen. The discrepancies between Lyman's result and ours is unlikely to be due to the choice of collision partner, since as Rainbird shows in the S_1 state of benzene - d_6 both nitrogen and Argon have comparable collisional relaxation cross-sections.

The results of the ME model are presented in Table 4.4. The results show that the redistribution of population upon molecular collision is dominated by transitions that involve the smallest energy defect. As seen in S_1 benzene [98], normally unfavourable inter-mode transitions such as $11_1 \leftrightarrow 6_1$ have an unusually large rate due to their very small energy defect. Flynn noted that the stretching modes of SO_2 are quick to equilibrate with each other but slow

to equilibrate with the SO₂ bend [104]. This is also observed here, where the exchange of energy between the two IP, ring deformation modes ν_4 and ν_6 (i.e. $4_1 \leftrightarrow 6_1$) is favoured over the $11_1 \leftrightarrow 6_1$ transition which has a smaller energy defect but involves a switch between an OOP and IP vibration. As discussed in the Section 4.3.2, cooling of ν_{16} and ν_{11} is fast because the dynamics of molecular collisions means that OOP vibrations are more likely lose energy upon molecular collision than IP vibrations like ν_4 and ν_6 [96,124,125].

The results of the ME model demonstrate that the rate of an individual transition may have little bearing upon the overall transfer of energy out of the particular state (as described by the TG model). For example, the transition $4_1 \leftrightarrow 6_1$ has a k_{ij} larger than the overall transfer rate out of ν_6 (Table 4.2) however, because the two states are close to isoenergetic, energy is taken out of the state as quickly as it is put in, meaning the transition has no effective influence upon the rate at which ν_6 is seen to collisionally cool.

Table 4.4: k_{ij} values obtained using the Master Equation model.

Transition	Energy Defect (cm ⁻¹)	Multiple of $6_1 \leftrightarrow 0_0$ rate	k_{ij} (Collision ⁻¹)
$16_1 \leftrightarrow 0_0$, $16_2 \leftrightarrow 16_1$, $6_1 16_1 \leftrightarrow 6_1$	399	61	6×10^{-3}
$6_1 \leftrightarrow 0_0$, $6_1 16_1 \leftrightarrow 16_1$, $6_1 11_1 \leftrightarrow 11_1$, $6_2 \leftrightarrow 6_1$	608	1	9×10^{-5}
$11_1 \leftrightarrow 0_0$, $6_1 11_1 \leftrightarrow 6_1$	674	2.2	2×10^{-4}
$4_1 \leftrightarrow 0_0$	707	2×10^{-5}	2×10^{-9}
$16_2 \leftrightarrow 0_0$	798	13	1×10^{-3}
$6_1 \leftrightarrow 16_1$	209	2×10^{-5}	2×10^{-9}
$11_1 \leftrightarrow 16_1$	275	1×10^{-6}	9×10^{-11}
$4_1 \leftrightarrow 16_1$	308	1×10^{-5}	9×10^{-10}
$11_1 \leftrightarrow 6_1$	66	17.4	2×10^{-3}
$4_1 \leftrightarrow 6_1$	99	25.6	2×10^{-3}
$4_1 \leftrightarrow 11_1$	33	2.5	2×10^{-4}

4.4.6 Estimate of Collisional Numbers upon Evaporation

The collisional relaxation efficiencies given in Table 4.4 can now be used to model the collisional energy transfer of benzene following evaporation from a water-ethanol L μ J and thus estimate the number of collisions that benzene undergoes as it crosses the liquid-vacuum interface. Two constraints are imposed on this analysis. Recall that in Section 4.4.2 we found that ~ 360 hard-sphere collisions result in negligible cooling of the ν_6 vibrational mode of benzene in the free-jet ($\Delta T \sim 5$ K). This vibrational mode is thus considered to be insensitive to collision number. Indeed, due to this insensitivity the experimentally-determined evaporative ν_6 vibrational temperature of 256 K provides an approximate measure of the liquid filament surface temperature. Cooling of the liquid surface by ~ 40 K from ambient is consistent with previous reports of the extent of cooling of water-based liquid beams observed by Saykally and discussed in Section 4.3.1.

The second constraint is that because the free-jet expansion results demonstrate that the rotational temperature of benzene closely follows the translational temperature (due to efficient collisional energy transfer), the experimentally-determined evaporative rotational temperature of 206 K provides an approximate measure of the translational temperature of the benzene evaporate. This conclusion is consistent with predictions arising from recent MD simulations which indicate that the translational and rotational temperatures of the evaporate rapidly converge [30]. In particular, MD simulations of the evaporation of water clusters into vacuum demonstrate that the temperature of the evaporate tends toward ~ 215 - 220 K, independent of the starting temperature [126]. Attempts were made to directly measure the translational velocity distribution of benzene evaporating from the L μ J using the delayed ion extraction technique commonly employed for MALDI systems [127,128]. However, the experiments did not yield sensible results; the observed distributions indicated a bulk velocity travelling toward the liquid surface. This strange result is likely to be a consequence of distortion of the TOF ion arrival times by stray electric fields in the TOF-MS. It is unlikely to

be due to interaction of the accelerated ions with the plume of continuously evaporating molecules since our results show there are essentially no active molecular collisions at distances greater than 200 μm from the liquid surface. The translational temperature is therefore fixed at 206 K, equal to the rotational temperature, in our subsequent modelling of evaporative energy transfer.

The constraints above leave both ν_{16} and ν_{11} as the internal modes of benzene whose temperatures are most sensitive to the number of collisions involved in evaporation. Using the collisional energy transfer efficiencies reported in Table 4.4, together with the constraints given above (*i.e.*, a liquid surface temperature of 260 K and a fixed translational temperature of 206 K), the mode-specific temperatures as a function of collision number are presented in Figure 4.9. The translational temperature is fixed in recognition that this degree of freedom reaches an asymptotic limit almost instantaneously during the evaporative phase transition. For comparison the results of both the ‘Temperature Gap’ (TG) model and the ‘Master Equation’ (ME) model are included in the figure. The results of the two models are slightly different as the TG model is influenced by the assignment of the translational temperature, whereas the ME model determines vibrational temperatures solely on the rate of population change per collision determined from the free-jet analysis. From Figure 4.9 we see that both models show that the temperature of ν_6 is almost independent of collision number dropping by only a few degrees. The TG model shows that the rotational temperature rapidly equilibrates to the translational temperature within just a few collisions. Both models indicate that the vibrational temperatures will continue to fall, attempting to equilibrate with the translational and rotational temperatures, if gas phase collisions continue to occur. The results of the evaporation experiments showed that the vibrational temperatures are frozen as a function of distance from the surface – meaning that collisions have essentially stopped by 200 μm from the surface. Using the vibrational temperatures of ν_{16} and ν_{11} from the plot we can calculate the lower and upper limits to the number of collisions that must have occurred.

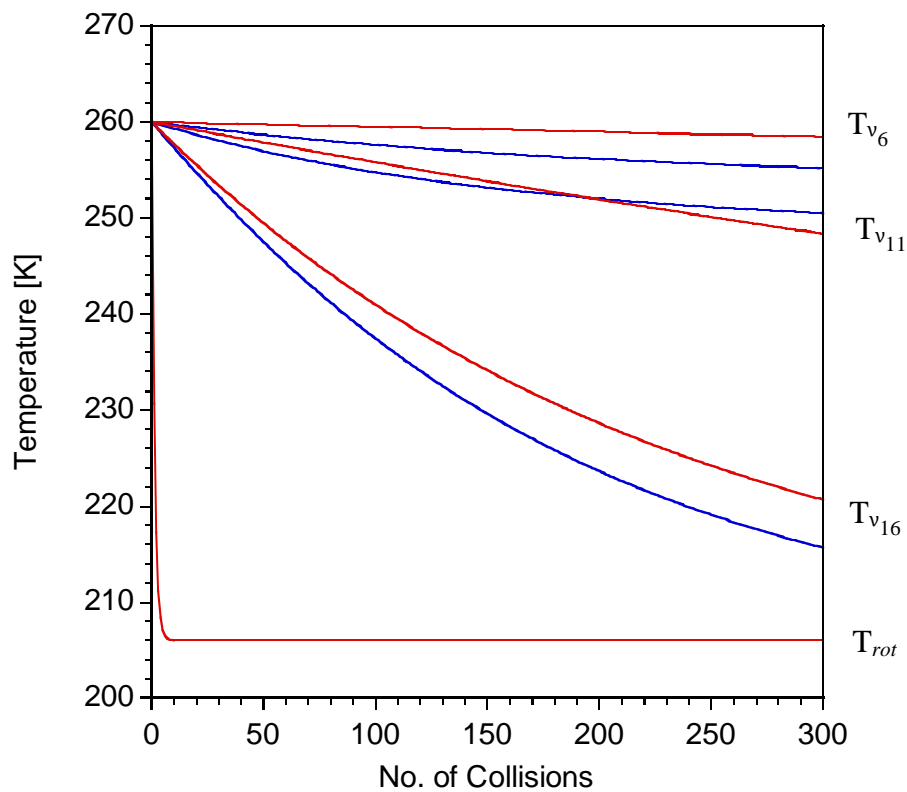


Figure 4.9: Modelling the change in temperature of the different degrees of freedom of benzene as a function of binary, hard-sphere collision number. The results of the TG model are indicated using the red lines whilst the ME results are indicated with the blue lines.

From the TG model it is evident that the ν_{16} and ν_{11} vibrations reach their observed temperatures by 185 and 220 binary, hard-sphere collisions, respectively. Similarly the ME model predicts the evaporation temperatures should be reached by 150 and 260 collisions, respectively. In other words, this simple analysis suggests that molecules undergoing the transition from liquid to vacuum are subjected to several hundred collisions. This estimated collision number is sufficient to result in some cooling of the evaporate as it leaves the liquid surface, but is insufficient to equilibrate the various molecular degrees of freedom.

4.5 Conclusion

Having estimated the liquid surface temperature as ~ 260 K, our experiments indicate that the benzene rotational temperature is cooled by ~ 55 K during evaporation. Rotational cooling of water and methanol has been predicted in recent MD simulations of the evaporation process [29,30]. The extent of cooling predicted by these simulations is not as extensive as observed in the experimental studies reported here [29]. Rotational cooling is efficient for these polyatomics [3] and so the difference between our observations and the simulations are not likely to be a consequence of our use of benzene as a spy for behaviour at the water-ethanol liquid surface. This suggests that current MD simulations underestimate the extent of rotational cooling following evaporation. There are no simulation data yet available to compare to the observed vibrational cooling of ~ 30 K and ~ 10 K for the ν_{16} and ν_{11} vibrational modes of benzene.

There were several simplifications and extrapolations that were made in order to produce the collisional energy transfer rates report herein. Collisional energy transfer rates were calculated based upon the observed internal temperatures of benzene molecules seeded in a free-jet expansion. Collision numbers calculated were based on hard-sphere binary collisions. The collisional energy transfer rates in such an environment may differ from those experienced

within the liquid-vapour. For example, through molecular simulation of vapour-liquid equilibrium, Wang [129] shows that, although binary interactions are dominant, three-bodied interactions must be considered especially when modeling fluid mixtures. In comparison with the purely gas phase experiments, in the liquid-vapour interface the molecular velocities are much slower and the molecular density higher which will result in an increase in the number of multi-body collisions. Both of these factors have been shown to significantly enhance the efficiency of collisional energy transfer [90,96,108,123,130]. The extent to which the inclusion of these factors would change the measured collisional energy transfer rates is difficult to judge and will hopefully be the subject of further investigations.

4.6 References

- (1) Sadtler, P. B. *Journal of the Franklin Institute* **1909**, 166, 291.
- (2) Sadtler, P. B. *Journal of Industrial and Engineering Chemistry (Washington, D. C.)* **1910**, 1, 644.
- (3) Miller, D. R. Free Jet Sources. In *Atomic and Molecular Beam Methods*; Scoles, G., Ed.; Oxford University Press: New York, 1988; Vol. 1; pp 35.
- (4) Garrett, B. C.; Schenter, G. K.; Morita, A. *Chemical Reviews* **2006**, 106, 1355.
- (5) Innocenzi, P.; Malfatti, L.; Costacurta, S.; Kidchob, T.; Piccinini, M.; Marcelli, A. *Journal of Physical Chemistry A* **2008**, 112, 6512.
- (6) Comsa, G.; David, R. *Surface Science Reports* **1985**, 5, 145.
- (7) Sibener, S. J.; Lee, Y. T. *Journal of Chemical Physics* **1994**, 101, 1693.
- (8) Muhlhausen, C. W.; Williams, L. R.; Tully, J. C. *Journal of Chemical Physics* **1985**, 83, 2594.
- (9) Barker, J. A.; Auerbach, D. J. *Surface Science Reports* **1985**, 4, 1.
- (10) Quintella, C. M.; McCaffery, A. J.; Mohammed, D. Z. *Chemical Physics Letters* **1993**, 214, 563.
- (11) Cowin, J. P.; Auerbach, D. J.; Becker, C.; Wharton, L. *Surface Science* **1978**, 78, 545.
- (12) Cavanagh, R. R.; King, D. S. *Physical Review Letters* **1981**, 47, 1829.
- (13) King, D. S.; Cavanagh, R. R. *Journal of Chemical Physics* **1982**, 76, 5634.
- (14) Comsa, G.; David, R. *Surface Science* **1982**, 117, 77.
- (15) Jacobs, D. C.; Kolasinski, K. W.; Madix, R. J.; Zare, R. N. *Journal of Chemical Physics* **1987**, 87, 5038.
- (16) Matsumoto, M. *Fluid Phase Equilibria* **1998**, 144, 307.
- (17) Brown, R. L.; Brewer, R. G.; Klemperer, W. *Journal of Chemical Physics* **1962**, 36, 1827.

-
- (18) Weida, M. J.; Sperhac, J. M.; Nesbitt, D. J. *Journal of Chemical Physics* **1996**, *105*, 749.
- (19) Padowitz, D. F.; Sibener, S. J. *Surface Science* **1989**, *217*, 233.
- (20) Sadtchenko, V.; Brindza, M.; Chonde, M.; Palmore, B.; Eom, R. *Journal of Chemical Physics* **2004**, *121*, 11980.
- (21) Krempl, S. *Surface Science* **1991**, *259*, 183.
- (22) Bowman, J. M.; Gossage, J. L. *Chemical Physics Letters* **1983**, *96*, 481.
- (23) Rettner, C. T.; Auerbach, D. J.; Tully, J. C.; Kleyn, A. W. *Journal of Physical Chemistry* **1996**, *100*, 13021.
- (24) Becker, C. H. *Surface Science* **1985**, *149*, 67.
- (25) Miksch, G.; Weber, H. G. *Chemical Physics Letters* **1982**, *87*, 544.
- (26) Knox, C. J. H.; Phillips, L. F. *Journal of Physical Chemistry B* **1998**, *102*, 10515.
- (27) Frezzotti, A.; Gibelli, L.; Lorenzani, S. *Physics of Fluids* **2005**, *17*.
- (28) Sibold, D.; Urbassek, H. M. *Physics of Fluids a-Fluid Dynamics* **1993**, *5*, 243.
- (29) Ishiyama, T.; Yano, T.; Fujikawa, S. *Physics of Fluids* **2004**, *16*, 4713.
- (30) Frezzotti, A. *European Journal of Mechanics B-Fluids* **2007**, *26*, 93.
- (31) Meland, R.; Frezzotti, A.; Ytrehus, T.; Hafskjold, B. *Physics of Fluids* **2004**, *16*, 223.
- (32) Sibold, D.; Urbassek, H. M. *Physics of Fluids A - Fluid Dynamics* **1991**, *3*, 870.
- (33) Sone, Y.; Sugimoto, H. *Phys. Fluids* **1995**, *7*, 2072.
- (34) Sone, Y.; Sugimoto, H. *Physics of Fluids A* **1993**, *5*, 1491.
- (35) Knight, C. J. *Journal of Fluid Mechanics* **1976**, *75*, 469.
- (36) Matsumoto, M. *Fluid Phase Equilibria* **1996**, *125*, 195.
- (37) Matsumoto, M. *Molecular Simulation* **1996**, *16*, 209.

- (38) Matsumoto, M.; Kataoka, Y. *Physical Review Letters* **1992**, *69*, 3782.
- (39) Matsumoto, M.; Kataoka, Y. *Molecular Simulation* **1994**, *12*, 211.
- (40) Matsumoto, M.; Mizukuchi, H.; Kataoka, Y. *Journal of Chemical Physics* **1993**, *98*, 1473.
- (41) Matsumoto, M.; Mizukuchi, H.; Kataoka, Y. *Journal of Chemical Physics* **1993**, *98*, 1473.
- (42) Matsumoto, M.; Takaoka, Y.; Kataoka, Y. *Journal of Chemical Physics* **1993**, *98*, 1464.
- (43) Matsumoto, M.; Takaoka, Y.; Kataoka, Y. *Journal of Chemical Physics* **1993**, *98*, 1464.
- (44) Matsumoto, M.; Yasuoka, K.; Kataoka, Y. *Journal of Chemical Physics* **1994**, *101*, 7912.
- (45) Matsumoto, M.; Yasuoka, K.; Kataoka, Y. *Theochem-Journal of Molecular Structure* **1994**, *116*, 161.
- (46) Matsumoto, M.; Yasuoka, K.; Kataoka, Y. *Fluid Phase Equilibria* **1995**, *104*, 431.
- (47) Matsumoto, M.; Yasuoka, K.; Kataoka, Y. *Proceedings of the ASME-JSME Thermal Engineering Joint Conference, 4th, Lahaina, Hawaii, Mar. 19-24, 1995* **1995**, *2*, 465.
- (48) Matsumoto, M.; Yasuoka, K.; Kataoka, Y. *Thermal Science and Engineering* **1995**, *3*, 27.
- (49) Nathanson, G. M.; Davidovits, P.; Worsnop, D. R.; Kolb, C. E. *Journal of Physical Chemistry* **1996**, *100*, 13007.
- (50) Tsuruta, T.; Nagayama, G. *Microscale Thermophysical Engineering* **2002**, *6*, 267.
- (51) Tsuruta, T.; Nagayama, G. *Journal of Physical Chemistry B* **2004**, *108*, 1736.

- (52) Yasuoka, K.; Matsumoto, M.; Kataoka, Y. *Journal of Molecular Liquids* **1995**, 65/66, 329.
- (53) Yasuoka, K.; Matsumoto, M.; Kataoka, Y. *Proceedings of the ASME-JSME Thermal Engineering Joint Conference, 4th, Lahaina, Hawaii, Mar. 19-24, 1995* **1995**, 2, 459.
- (54) Garret, B. C.; Schenter, G. K. *Chemical Review* **2006**, 106, 1355.
- (55) Ishiyama, T.; Yano, T.; Fujikawa, S. *Physics of Fluids* **2004**, 16, 2899.
- (56) Penfold, J. *Reports on Progress in Physics* **2001**, 64, 777.
- (57) Charvat, A.; Bögehold, A.; Abel, B. *Aust. J. Chem.* **2006**, 59, 81.
- (58) Kondow, T.; Mafuné, F. *Annu. Rev. Phys. Chem.* **2000**, 51, 731.
- (59) Faubel, M.; Steiner, B.; Toennies, J. P. *Mol. Phys.* **1996**, 90, 327.
- (60) Faubel, M.; Schlemmer, S.; Toennies, J. P. *Zeitschrift Fur Physik D-Atoms Molecules and Clusters* **1988**, 10, 269.
- (61) Faubel, M.; Kisters, T. *Nature* **1989**, 339, 527.
- (62) Cappa, C. D.; Drisdell, W. S.; Smith, J. D.; Saykally, R. J.; Cohen, R. C. *J. Phys. Chem. B* **2005**, 109, 24391.
- (63) Frezzotti, A.; Gibelli, L.; Lorenzani, S. *Physics of Fluids* **2005**, 17, 012102.
- (64) Meland, R.; Frezzotti, A.; Ytrehus, T.; Hafskjold, B. *Physics of Fluids A - Fluid Dynamics* **2004**, 16, 223.
- (65) Raabe, G.; Sadus, R. J. *Journal of Chemical Physics* **2007**, 126, 7.
- (66) Callomon, J. H.; Dunn, T. M.; Mills, I. M. *Philos. Trans. R. Soc. London Ser. A* **1966**, 259, 499.
- (67) Okruss, M.; Muller, R.; Hese, A. *Journal of Molecular Spectroscopy* **1999**, 193, 293.
- (68) Murakami, J.; Kaya, K.; Ito, M. *J. Chem. Phys.* **1980**, 72, 3263.
- (69) Stephenson, T. A.; Radloff, P. L.; Rice, S. A. *J. Chem. Phys.* **1984**, 81, 1060.

- (70) Tarek, M.; Tobias, D. J.; Klein, M. L. *Journal of the Chemical Society-Faraday Transactions* **1996**, *92*, 559.
- (71) Tarek, M.; Tobias, D. J.; Klein, M. L. *Physica A* **1996**, *231*, 117.
- (72) Tarek, M.; Klein, M. L. *Journal of Physical Chemistry A* **1997**, *101*, 8639.
- (73) Chen, B.; Siepmann, J. I.; Klein, M. L. *Journal of the American Chemical Society* **2003**, *125*, 3113.
- (74) Chen, B.; Siepmann, J. I.; Klein, M. L. *Journal of the American Chemical Society* **2002**, *124*, 12232.
- (75) Zhang, J. Y.; Nagra, D. S.; Li, L. *Analytical Chemistry* **1993**, *65*, 2812.
- (76) Press, W. H.; Flannery, B. P.; Teukolsky, S. A.; Vetterling, W. T. *Numerical Recipes: The Art of Scientific Computing*; Cambridge University Press: New York, 1986.
- (77) Demtröder, W. Visible and Ultraviolet Spectroscopy: Physical Aspects. In *Atomic and Molecular Beam Methods*; Scoles, G., Ed.; Oxford University Press: New York, 1992; Vol. 2; pp 231.
- (78) Kereszuri, A.; Jedlovszky, P. *Journal of Physical Chemistry B* **2005**, *109*, 16782.
- (79) Dang, L. X.; Feller, D. *Journal of Physical Chemistry B* **2000**, *104*, 4403.
- (80) Wilson, K. R.; Rude, B. S.; Smith, J.; Cappa, C.; Co, D. T.; Schaller, R. D.; Larsson, M.; Catalano, T.; Saykally, R. J. *Review of Scientific Instruments* **2004**, *75*, 725.
- (81) Cappa, C. D.; Drisdell, W. S.; Smith, J. D.; Saykally, R. J.; Cohen, R. C. *Journal of Physical Chemistry B* **2005**, *109*, 24391.
- (82) Frediani, L.; Pomelli, C.; Jacopo, T. *Phys. Chem. Chem. Phys.* **2000**, *2*, 4876.
- (83) Bridgeman, O. C.; Aldrich, E. W. *J. Heat Transfer* **1964**, *86*, 279.

- (84) Ambrose, D.; Sprake, C. H. S.; Townsend, R. J. *Chem. Thermodyn.* **1975**, *7*, 185.
- (85) Miller, D. R. *Atomic and Molecular Beam Methods*; Oxford University Press: New York, 1991; Vol. 1.
- (86) Vacha, R.; Jungwirth, P.; Chen, J.; Valsaraj, K. *Physical Chemistry Chemical Physics* **2006**, *8*, 4461.
- (87) Bondybey, V. E. *Annual Review of Physical Chemistry* **1984**, *35*, 591.
- (88) Waclawik, E. R.; Lawrance, W. D. *Journal of Chemical Physics* **1998**, *109*, 5921.
- (89) Whetton, N. T.; Lawrance, W. D. *Journal of Physical Chemistry* **1992**, *96*, 3717.
- (90) Rainbird, M. W.; Webb, B. S.; Knight, A. E. W. *Journal of Chemical Physics* **1988**, *88*, 2416.
- (91) Seiser, N.; Kavita, K.; Flynn, G. W. *Journal of Physical Chemistry A* **2003**, *107*, 8191.
- (92) Sevy, E. T.; Rubin, S. M.; Lin, Z.; Flynn, G. W. *Journal of Chemical Physics* **2000**, *113*, 4912.
- (93) Flynn, G. W.; Parmenter, C. S.; Wodtke, A. M. *Journal of Physical Chemistry* **1996**, *100*, 12817.
- (94) Flynn, G. W. *Accounts of Chemical Research* **1981**, *14*, 334.
- (95) Clary, D. C.; Gilbert, R. G.; Bernshtein, V.; Oref, I. *Faraday Discussions* **1995**, *102*, 423.
- (96) Bernshtein, V.; Oref, I. *Journal of Physical Chemistry B* **2005**, *109*, 8310.
- (97) Atkins, P. W. *Physical Chemistry*, 6th ed.; Oxford University Press: Oxford, 1998.
- (98) Parmenter, C. S.; Tang, K. Y. *Chemical Physics* **1978**, *27*, 127.

- (99) Parmenter, C. S. *Journal of Physical Chemistry* **1982**, *86*, 1735.
- (100) McCaffery, A. J.; Osborne, M. A.; Marsh, R. J.; Lawrance, W. D.; Waclawik, E. R. *Journal of Chemical Physics* **2004**, *121*, 169.
- (101) Moore, C. B. *Annual Review of Physical Chemistry* **1971**, *22*, 387.
- (102) Moore, C. B. *Annual Review of Physical Chemistry* **2007**, *58*, 1.
- (103) Sedlacek, A. J.; Weston, R. E. J.; Flynn, G. W. *Journal of Chemical Physics* **1991**, *94*, 6483.
- (104) Weitz, E.; Flynn, G. W. *Annual Review of Physical Chemistry* **1974**, *252*, 275.
- (105) Nesbitt, D. J.; Field, R. W. *Journal of Physical Chemistry* **1996**, *100*, 12735.
- (106) Waclawik, E. R.; Lawrance, W. D.; Borg, R. A. J. *Journal of Physical Chemistry* **1993**, *97*, 5798.
- (107) Coveleskie, R. A.; Parmenter, C. S. *Journal of Chemical Physics* **1978**, *69*, 1044.
- (108) Stephenson, T. A.; Rice, S. A. *Journal of Chemical Physics* **1984**, *81*, 1073.
- (109) Waclawik, E. R.; Lawrance, W. D. *Journal of Chemical Physics* **1994**, *102*, 2780.
- (110) Logan, L. M. *Journal of Chemical Physics* **1980**, *72*, 5667.
- (111) Nicholson, J. A.; Lawrance, W. D. *Chemical Physics Letters* **1995**, *236*, 336.
- (112) Schranz, H. W. *Journal of Molecular Structure (Theochem)* **1996**, *368*, 119.
- (113) Lyman, J. L.; Muller, G.; Houston, P. L.; Piltch, M.; Schmid, W. E.; Kompa, K. L. *Journal of Chemical Physics* **1985**, *82*, 810.
- (114) Muller, D. J.; Lawrance, W. D.; Knight, A. E. W. *Journal of Physical Chemistry* **1983**, *87*, 4952.
- (115) Grams, M. P.; Cook, A. M.; Turner, J. H.; Doak, R. B. *Journal of Physics D: Applied Physics* **2006**, *39*, 930.

- (116) Braun, J.; Day, P. K.; Toennies, J. P.; Witte, G.; Neher, E. *Review of Scientific Instruments* **1997**, *68*, 3001.
- (117) Sulkes, M. *Chemical Physics Letters* **1985**, *119*, 426.
- (118) Langridge-Smith, P. R. R.; Drumbaugh, D.; Hayman, C.; Levy, D. H. *Journal of Physical Chemistry* **1981**, *85*, 3742.
- (119) Snavely, D. L.; Walters, V. A.; Colson, S. D.; Wiberg, K. B. *Chemical Physics Letters* **1984**, *103*, 423.
- (120) Smalley, R. E.; Blazy, J. A.; Fitch, P. S. H.; Kim, M. S.; Wharton, L.; Levy, D. H. *Optics Communications* **1976**, *18*, 59.
- (121) Luk'yanov, G. A. *Journal of Applied Mechanics and Technical Physics* **1972**, *13*, 413.
- (122) Vincenti, W. G.; C. H. Kruger, J. *Introduction to Physical Gas Dynamics*; Wiley: New York, 1965.
- (123) Stephenson, T. A.; Rice, S. A. *Journal of Chemical Physics* **1984**, *81*, 1083.
- (124) Bernshtein, V.; Oref, I. *Journal of Physical Chemistry A* **2006**, *110*, 1541.
- (125) Bernshtein, V.; Oref, I. *Journal of Physical Chemistry A* **2006**, *110*, 8477.
- (126) Caleman, C.; Spoel, D. *Journal of Chemical Physics* **2006**, *125*, 154508.
- (127) Berkenkamp, S.; Menzel, C.; Hillenkamp, F.; Dreisewerd, K. *American Society for Mass Spectrometry* **2002**, *13*, 209.
- (128) Gluckmann, M.; Karas, M. *Journal of Mass Spectrometry* **1999**, *34*, 467.
- (129) Wang, L.; Sadus, R. J. *Journal of Chemical Physics* **2006**, *125*, 0744503.
- (130) Bernshtein, V.; Oref, I. *Journal of Physical Chemistry A* **2001**, *105*, 3454.

Chapter 5. Infrared Desorption

Partitioning of Internal Energy within Benzene Molecules Thermally Desorbed from a Liquid Surface

5.1 Introduction

The introduction of molecules into the vacuum for spectrometric analysis is routinely performed via laser desorption techniques such as Matrix Assisted Laser Desorption (MALD) [1-3]. However, the desorption process, and in particular how the molecular energy is partitioned throughout the desorption plume is not well understood. The amount of internal energy a molecule possesses affects things such as the amount of fragmentation it undergoes or its role in ion-molecule reactions within the desorption plume [4]. This study focuses on quantifying the distribution of internal energy within a molecule that is desorbed from the surface of an *in vacuo* aqueous surface by pulsed infrared radiation.

In an in-depth review, Saalfrank classes the photo-desorption process into two types; direct or indirect [5]. Direct photo-desorption from a solid substrate involves matching the wavelength of the desorption laser to the frequency of some adsorption co-ordinate of the analyte - excitation of motion along the co-ordinate allowing the analyte to escape. The indirect desorption method involves excitation of the substrate to which the analyte is attached or excitation of the matrix in which it is embedded. In this method the thermal energy resulting from heating of the substrate is transferred into the analyte, giving it enough kinetic energy to escape the surface potential. When a matrix is used, the analyte is liberated into the vacuum where it becomes entrained in the plume of desorbing matrix molecules. The indirect desorption involved in the MALD process is reviewed in detail by Dreiseward [6].

One of the draw backs of using a solid matrix in the MALD experiments is that the crystalline structure can disrupt non-covalent interactions of the analyte preventing the analysis of entities such as hydration structures or macromolecular quaternary structures. In addition, if the analyte is thermally labile then it is unlikely to survive the high temperatures of the desorption process. As such, there has been a move toward desorption from liquid matrices, where the energy required for vaporisation of the matrix is substantially lower. The dynamics of UV desorption/ionisation from *in vacuo* aqueous jets has been explored by groups including Mafuné [7-12], Tsuchiya [13] and Holstein [14,15]. Here the desorption laser ionises components in the liquid matrix and the subsequent columbic explosion releases the analyte and its clusters into the vacuum [8,12]. A softer desorption process involves pulsed IR lasers focused onto the surface of the liquid. Brutschy *et al* were the first to use this method to isolate charged biomolecular complexes from an *in vacuo* liquid filament [16-21] and later a liquid droplet [22-24]. Termed LILBID (laser induced Liquid beam (bead) ionisation/desorption) it first employed a broadband CO₂ laser but later advanced into using IR photons that were resonant with a strong vibrational absorption band of the solvent. Abel and Faubel have established a similar technique termed IR-FL-MALDI (Infrared Free Liquid Matrix Assisted Laser Dispersion of Ions) [25]. They have also reported numerous applications of this technique to biologically relevant supramolecular species and their non-covalently bound aggregates [26,27] as well as to the study of fast, high temperature water chemistry [28]. Mafuné and Kondow have also extended their desorption studies to involve the IR desorption of small organic salts and their solvated clusters [12,29,30].

Detailed analysis of the dynamics of Infrared Matrix Assisted Laser Desorption (IR-MALD) has shown that little fragmentation of the desorbed molecules occurs because the rapid absorption of IR photons and subsequent heating process is faster than the rate of dissociation [6,31-33]. Consequently, the number of neutral molecules liberated into the gas-phase during IR-MALDI is much greater than the number of ions. Study of the liberated neutral species is

possible in a Time-of Flight Mass Spectrometer (TOF-MS) by coupling the resonant IR desorption with post-desorption ionisation. The two-laser technique has been used successfully in the past by performing Resonance Enhanced Multiphoton Ionisation (REMPI) on molecules laser desorbed from the surface of solid substrates [34-36]. Several groups have begun applying this two laser desorption/probe technique to study small neutral organic molecules desorbed from both from liquid micro-jets [4,31,37-40] and liquid aerosol particles [4,41,42]. This two-laser technique has been shown to have several advantages over the single laser UV desorption/ionisation. For example, Miller found that by separating the desorption and ionisation processes the resultant ion signal was increased by more than 2 orders of magnitude – a result they attribute to the higher collection efficiency of ions in the gas phase compared with the liquid phase [42]. Also, since the fluence and wavelengths of the desorption and ionisation laser are now independent, they can be tuned to reduce the amount of molecular fragmentation that occurs (if so desired) as well as allow for selective ionisation of the liberated molecules.

Insight into the dynamics of the desorption process has been obtained through both experimental and theoretical techniques. Imaging of the desorption plume shows the formation and propagation of shock waves that proceed the desorption plume and the distribution of nano and micron sized droplets that form as the surface disintegrates [25,28,43-46]. It is thought that evaporation of molecules from these superheated droplets cools the remaining liquid and this is what prevents thermal dissociation of the analyte [31]. It is for this reason that the IR desorption/UV ionisation technique therefore lends itself to the study of thermally labile, non-volatile compounds.

The behaviour of the desorption plume is found to depend upon the wavelength of desorption [28,30,47] and the penetration depth of the laser [28], the laser fluence [4,41] as well as the properties and preparation techniques of the matrix [47-49]. Monte Carlo simulations of the

temporal evolution of the desorption plume by groups such as Lucchese and Noorbach [50,51] and Sibold and Urbassek [52] have provided insight into the global flow features such as energy distributions and collision numbers. The simulations reveal that it is the number of post-desorption, gas phase collisions which determine whether the expansion can be described as thermal or explosive [51,52]. A thermal expansion is one where the temperatures of the desorbed molecules retain that of the bulk from which they were liberated. An explosive expansion is one where the internal energies are redistributed into conditions reminiscent of a gas-jet expansion. Both groups emphasise the importance of understanding the role of gas-phase collisions in distributing the energy within the expansion.

An important property of a desorption plume is the distribution of molecular energies amongst the translational, vibrational and rotational degrees of freedom. This property changes as the plume evolves and can give us an indication of the dynamical processes driving the expansion. Whilst several studies exist that quantify vibrational and/or rotational temperatures of molecules that are desorbed from solid surfaces [53-56], to our knowledge there have been no studies performed on the internal temperatures of molecules leaving a liquid surface using molecular spectroscopy. The study reported here attempts to elucidate the partitioning of energy within neutral benzene molecules that are liberated from an *in vacuo* liquid surface and entrained in a desorbed plume of the liquid matrix. Variation in the time between desorption and ionisation laser allows for the generation of translational velocity and temperature profiles. Spectroscopic analysis of the absorption spectra of the desorbing molecules allows us to determine rotational and vibrational temperatures at different positions within the desorption plume. By monitoring the internal temperatures of out-of-plane and in-plane vibrations of different frequencies, we are able to build of a more global picture of the transient properties of the flow including collision frequency and molecular density.

5.2 Experimental Method

The experimental setup is illustrated in Figure 5.1. The *in vacuo* liquid micro-jet (L μ J) is created by forcing the solution at high pressure through a tapered silica capillary (New Objective PicoTip emitter, uncoated SilicaTip) using a HPLC pump (Dionex P680) at pressures of typically (200-500 psi). For the solutions used here, these pressures achieve a flow rate of 0.25 ml.min⁻¹. The L μ J is 15 μ m in diameter and comprised of a solution of 1x10⁻³ M benzene (BDH 99.7%) in a 25% v.v. ethanol, (Ajax Finechem, 99.5%), deionised water mix. A collimated UV laser with a FWHM of 150 μ m ($\sim 0.9 \times 10^7$ W.cm⁻²) runs perpendicular to both the TOF and L μ J axes and acts as the ionisation probe for neutrals leaving the liquid surface. The UV light is produced by pumping a dye laser (Sirah, CSTR-LG-24) with the third harmonic of a Nd:YAG (Continuum SL-10-III, 355nm) and then frequency doubling the output. An arrangement of four pellin brocca prisms is placed after the frequency doubling unit to isolate the doubled light. This setup compensates for any changes in the pointing of the laser light that can occur when the wavelength is changed. The UV beam is reproducibly positioned at distances from the L μ J by setting the zero position when the UV beam shines onto the L μ J to produce a diffraction pattern. The UV is then translated away from the L μ J using a micrometer translation stage. For all the results presented here the centre of the UV laser beam is positioned 300 μ m from the centre of the L μ J. Any neutral benzene molecules that enter the ionisation volume of the UV beam can be state-selectively ionised by one colour REMPI. The first absorption step was via the 6_0^1 , $6_1^2/6_1^0/6_1^1/6_1^2$, or $6_0^1/6_1^1/6_0^1/6_1^1$ transitions depending upon the experiments being performed. Any ions formed are extracted into the TOF-MS by application of a 400 V.m⁻¹ potential gradient. The delay between ionisation and application of the extraction voltage is controlled by a digital delay generator (Griffith University, TARDIS II). The volatility of benzene means there is a continuous ion signal observable from benzene molecules that are naturally evaporating from the L μ J surface.

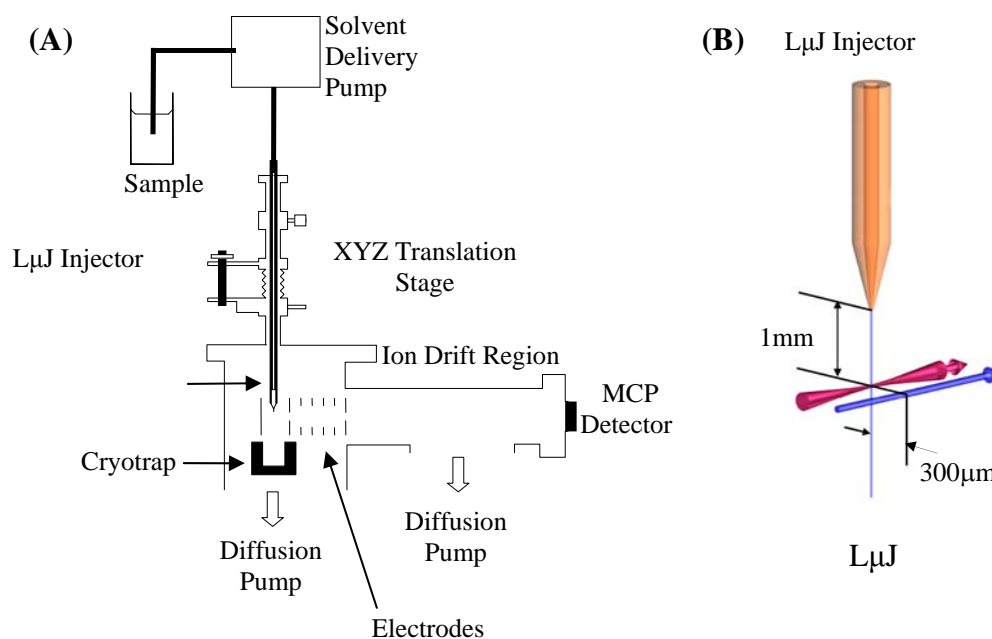


Figure 5.1: (A) Schematic of the TOF-MS with L μ J Source Chamber. (B) Illustration of the relative laser positions for desorption experiments. The blue arrow represents the collimated UV laser and the red arrow the focused IR laser. Both lasers are positioned perpendicular to both the L μ J and TOF axes. The IR laser is focused onto the surface of the L μ J, whilst the UV laser is positioned 300 μ m from the liquid surface between the L μ J and ion detector. Only those desorbed (or evaporating) molecules which leave the liquid surface with a velocity component along the TOF axis will reach the ionisation volume, be ionised and then detected.

The IR desorption light is generated using a manually tuneable OPO (Continuum SL OPO plus IR) that is pumped by the fundamental of a Nd:YAG (Continuum SLII-10). The IR light is guided to the TOF-MS using silver coated mirrors and enters the Source Chamber through a sapphire laser input window. The IR beam is aligned anti-parallel to the UV beam and is gently focused with a 750 mm CaF₂ lens onto the L μ J. The estimated spot size is ~600 μ m and fluence is 0.9 J.cm⁻². As with the UV laser beam, the position of the IR beam can be manipulated with the aid of a translation stage. When the IR laser alone is incident on the L μ J very little ion signal is observed. This makes the positioning of the IR beam onto the L μ J difficult, so an indirect alignment technique was developed. The IR beam alignment procedure involved first aligning the UV beam onto the L μ J (looking for the diffraction pattern) and then overlaying the counter propagating IR beam with the aid of heat sensitive paper*. Once the IR beam is in position, the UV beam is translated away from the L μ J the required distance. The timing between firing of the lasers is controlled by the same digital delay generator that controls the electrodes. Variation of the delay between the lasers enables ionisation of different parts of the desorption plume.

5.3 Features of the Desorption Mass Spectrum

Figure 5.2 demonstrates the effect of using the two-laser technique to enhance the flux of neutral molecules liberated from the liquid surface and thus detected in the TOF-MS. When only the desorption laser is incident upon the L μ J (IR only) there is no ion signal. Since the detection mechanism is only sensitive to positive ions, this demonstrates that the IR laser is not desorbing any positive ions from the solution nor is it causing any ionisation of molecules in the liquid. The wavelength of the UV laser is set to 38611 cm⁻¹. At this wavelength benzene is resonantly ionised by absorption through 6₀¹ vibronic transition. When the UV

* The UV light appears as visible fluorescence on the thermal paper – at the UV fluences used here the UV light does not evoke a thermal response from the paper.

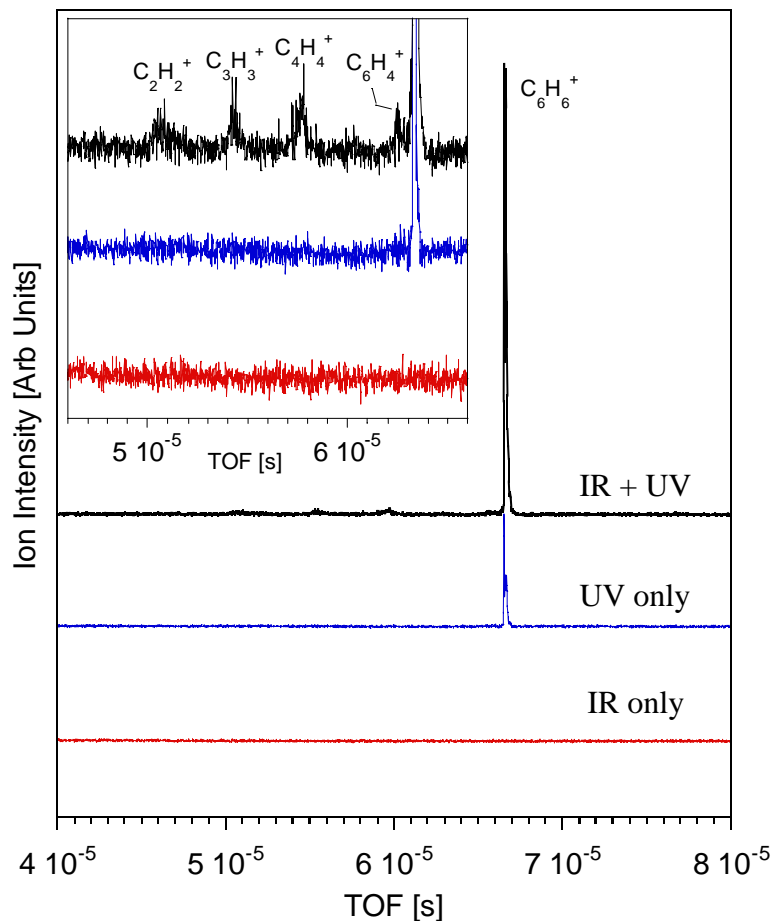


Figure 5.2: Comparison between mass spectra generated under different experimental conditions. IR only: Only the IR laser is incident upon the $L\mu\text{J}$. $\lambda_{\text{IR}} = 2.85 \mu\text{m}$. UV only: The UV laser is position $300 \mu\text{m}$ from the liquid surface, UV photon energy is 38611 cm^{-1} . The only ion signal observed is from benzene monomer that has evaporated from the liquid surface. IR + UV: The IR laser is fired and then the UV laser is fired. In this example spectrum the IR-UV delay is $10 \mu\text{s}$. Inset: zoom in on the baseline of the mass spectra show that the two-laser technique has greatly increased the number of C_6H_6^+ and fragment ions to be produced.

laser is placed 300 μm from the liquid surface a single ion signal appears. This ion signal has mass 78 and is assigned to the benzene monomer. Since the UV laser is only probing gas phase benzene molecules, the ion signal must be due to benzene that has evaporated from the liquid surface. This was confirmed by monitoring the signal intensity as a function of UV wavelength. The absorption spectrum that was subsequently generated was that of benzene. The properties of evaporating benzene were discussed in detail in Chapter 4. When the two lasers are fired sequentially the intensity of the benzene ion signal increases dramatically. In the example spectrum shown in Figure 5.2, the UV laser is fired 10 μs after the IR laser. At this IR-UV delay the benzene signal is ~ 5 times greater than the evaporation signal (UV only). This demonstrates that the IR laser is increasing the number of neutral benzene molecules into the gas phase which can then be resonantly ionised by the UV laser and detected.

Due to the large increase in gas phase benzene caused by the two laser setup, the signal-to-noise ratio of masses smaller than 78 amu are now intense enough to be seen above the noise of the baseline. Although these small ions are not baseline resolved, they have been assigned to benzene fragments with the aid of the photo-ionisation studies of Holland *et al* [57]. Confirmation that the fragment ions originate from the desorbed benzene is provided by the analysis of the wavelength dependence of the fragments. As Figure 5.3 illustrates, each fragment portrays the 6_0^1 vibronic spectrum of the benzene monomer. Since a rovibronic spectrum is a unique fingerprint for the entity being ionised this result shows that the fragmentation of the benzene occurs post ionisation. The shapes of the fragment spectra are slightly distorted however, when compared with the monomer spectrum. The differences are apparent at $\sim 38610 \text{ cm}^{-1}$ (on the R-branch) where the fragment spectra appear to be much thinner and at $\sim 38607 \text{ cm}^{-1}$ where the dip in the spectra is less pronounced. The distortions of the spectra are an indication that the rotational population of the fragmenting benzene molecules is non-Boltzmann. Therefore, the spectra cannot be described by a rotational

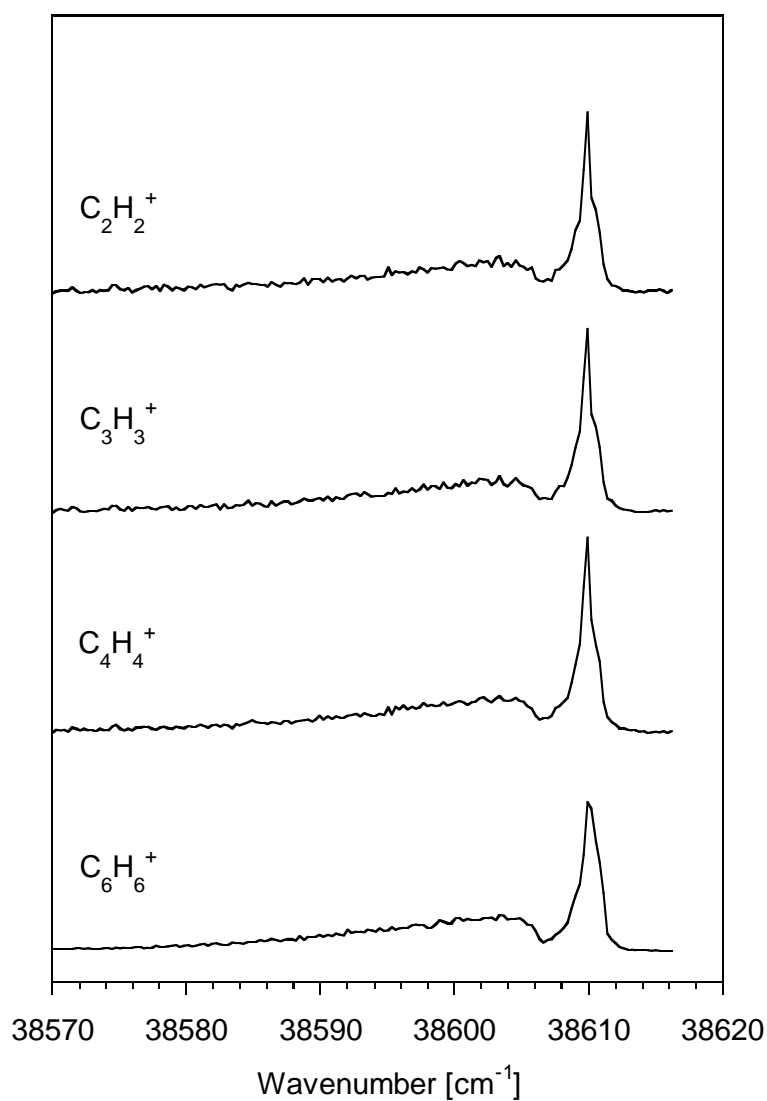


Figure 5.3: 1+1 REMPI spectra of the fragments identified in Figure 5.2. These spectra were generated with an IR-UV delay of 1.3 μs . Each fragment shows the same wavelength dependence - they all portray the 6_0^1 rovibronic spectrum of the benzene monomer.

temperature. This result is an interesting insight in the possible rotational quantum state preferences for fragmenting benzene but is not explored any further in this study.

As mentioned above, both the wavelength and fluence of the desorption laser affect the desorption dynamics. In the studies discussed here, the desorption laser was tuned to the fundamental, symmetric stretch absorption band of water. Kohno *et al* showed that the maximum amount of pre-formed ions IR-desorbed from an aqueous salt solution was achieved at desorption wavelengths on the high energy side of the solvent absorption band [30]. Their optimum wavelength (2.82 μm) was slightly shorter than the optimum wavelength used here of 2.85 μm . This discrepancy may be a result of the higher ejection energies needed to overcome electrostatic attraction between the pre-formed ions in solution compared with neutral benzene in water. This notion is supported by the observed dependence of the benzene desorption signal on the IR laser fluence as shown in Figure 5.4. The dependence of desorption yield (Y) on the laser fluence (ϕ) is described by the power relationship [5,30]:

$$Y = A\phi^n, \quad \text{Equation 5.1}$$

where n can be equated to the number of photons needed to liberate the molecule. n values reported by Kohno range from 1-5.3 depending upon the solution from which the ions were being desorbed [30]. Best fits of Equation 5.1 to the results presented here reveal that the desorption of the neutral benzene monomer is essentially a 1 photon process ($n = 0.8 \pm 0.1$). Mowry *et al* found that the desorption of neutral dipentylamine from various matrices showed a similar dependence on the desorption laser fluence ($n = 1-3$) and in contrast the intensity of desorbed, preformed ions reported higher n values of 2-4 [58]. The plateau of the monomer ion signal seen at the smaller laser fluences is due to the constant evaporation signal overwhelming any effect from the desorption laser. Thus, any threshold to desorption is masked by the constant evaporation signal.

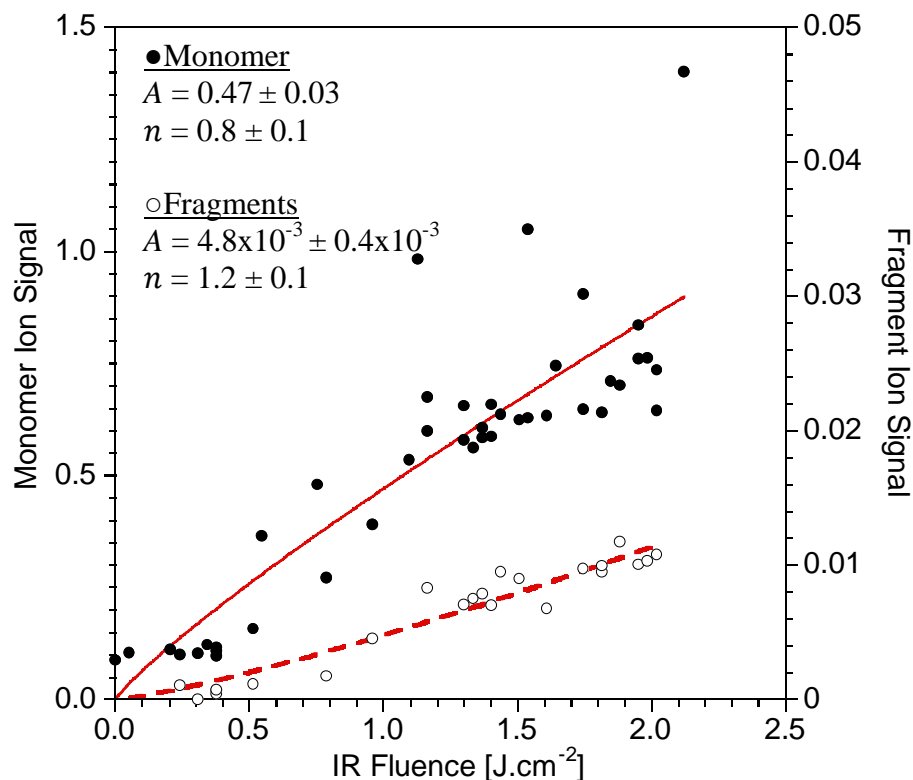


Figure 5.4: Dependence of ion signal on IR laser fluence. (●) Integrated intensity of benzene monomer ion signal (78 amu). (○) Integrated intensity of all benzene fragment ion signals. The UV laser is positioned 300 μm from the liquid surface. UV photon energy is 38611 cm^{-1} , where the first absorption step is via the 6_0^1 absorption band. λ_{IR} is 2.85 μm . The IR-UV delay is 10 μs . The fragment intensities show an IR fluence dependence similar to that of the monomer. When the data are fitted with Equation 5.1 the monomer ion signal shows an n value of 0.8 ± 0.1 , and the fragment ion signal an n value of 1.2 ± 0.1 .

From Figure 5.4 we can see that the amount of fragmentation observed in the mass spectrum displays a near linear dependence on the IR laser fluence: ($n = 1.2 \pm 0.1$) at a wavelength of 2.85 μm . It is reasonable that both the monomer and fragment ion intensity show similar laser fluence dependence since both are dependent upon the amount of desorbed material and that is influenced by the laser fluence. As more monomer is desorbed, there is more that can fragment. The two order of magnitude difference between the A scalar values from the fits is due to the relative intensities of the monomer and fragment ion signal in the gas phase. The units of the intensity scale are the same for both the fragments and the monomer, which demonstrates that the monomer intensity is 100 times that of the fragment signal. This intensity ratio illustrates that only $\sim 1\%$ of the benzene monomer undergoes fragmentation.

The features that appear in the mass spectrum of Figure 5.5 give an indication of the expansion environment. When the IR laser is incident upon the $\text{L}\mu\text{J}$ (in the absence of the UV laser and at the fluences reported in Figure 5.4) there is no noticeable ion signal at all. This means that any molecules that are IR laser desorbed from the liquid must retain their neutral state since our experimental setup only allows for the detection of positive ions. When the UV ionisation laser is introduced after the IR desorption (Figure 5.5(B)), the monomer intensity is much greater than when only the UV laser is employed (Figure 5.5(B)). Also, the two laser setup is now shown to produce a significant number of heavier ions (Figure 5.5(B)). This large change in mass spectrum compared with that of Figure 5.2(A) is due to the decrease in the IR-UV delay time from 10 to 0.5 μs .

The masses greater than 78 amu which appear in Figure 5.5 have all been assigned to clusters of a benzene ion and a solvent molecule or its neutral fragment. The heaviest clusters observed incorporate 6 water molecules which suggest this is the most stable configuration for small $\text{C}_6\text{H}_6^+ \cdot (\text{H}_2\text{O})_n$ clusters. This find is consistent with the results of step-wise hydration studies performed by Ibrahim *et al* on the benzene cation [59]. Interestingly the intensity of

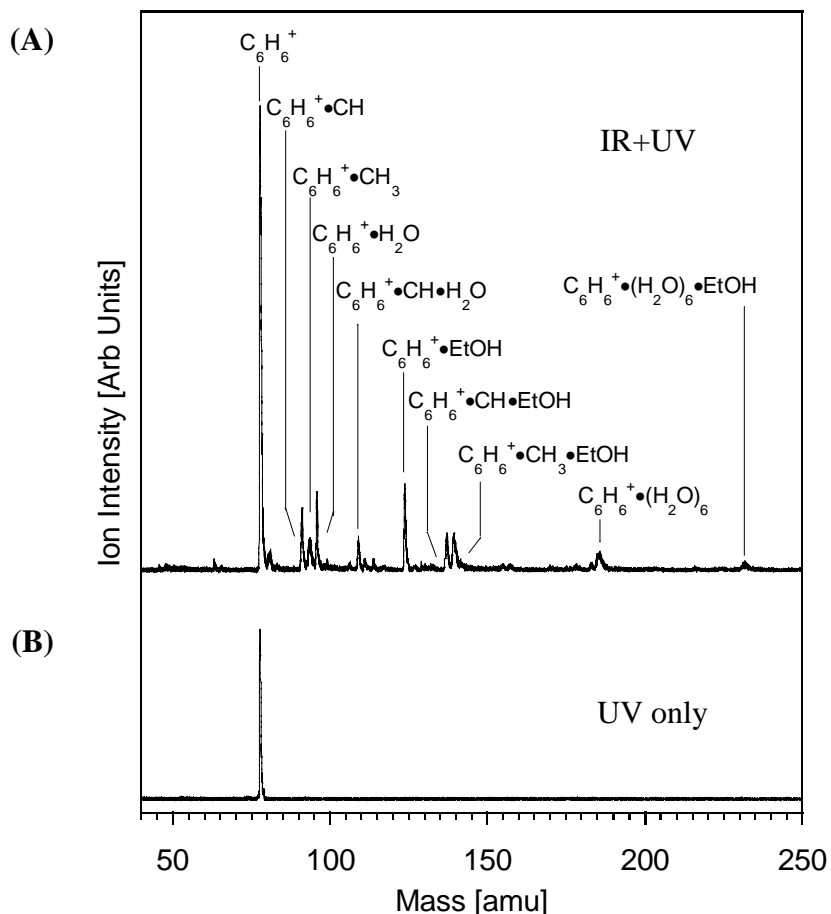


Figure 5.5: Mass spectrum of benzene (78 amu) desorbed from a 25% ethanol/water $L\mu J$. UV photon energy is 38611 cm^{-1} and UV fluence is $0.014\text{ J}\cdot\text{cm}^{-2}$. IR wavelength is $2.85\text{ }\mu\text{m}$ and IR fluence is $0.9\text{ J}\cdot\text{cm}^{-2}$. IR-UV delay is $0.5\text{ }\mu\text{s}$. Under these conditions the monomer ion signal has been enhanced by a factor of 4.3 by the introduction of the IR laser. The maximum enhancement of the monomer ion signal is seen at $\sim 3\text{ }\mu\text{s}$ delay, where the two-laser setup has enhanced the pure evaporation signal sixfold. There is no signal from the IR laser alone so it is not included in the figure. The observed clusters consist only of benzene ions clustered to solvent molecules or their fragments. Ethanol molecules are abbreviated as EtOH. No benzene dimer is seen.

the cluster signal increases with an increase in the delay between ionisation and ion extraction (time-lag). This effect is demonstrated in the mass spectra of Figure 5.6 where mass spectra produced with time-lag delays of from 0.39-1.1 are displayed. More clusters are apparent at the longer time-lag delays. This result suggests that cluster formation is active post ionisation since increasing the association time of the benzene ions in the desorption plume seems to increase the probability of clusters forming before they are extracted into the TOF.

The ion signal intensity of the clusters identified in Figure 5.5 were monitored as a function of ionisation wavelength. The wavelength region scanned was over the 6_0^1 absorption band of the benzene monomer and the results are displayed in Figure 5.7. If the observed clusters formed pre-ionisation then their absorption spectrum would reflect the structure of the cluster, appearing at a different energy to that of the benzene monomer. For example, multiphoton ionisation studies performed by Zweir *et al* showed that the 6_0^1 absorption feature for ($C_6H_6 \bullet H_2O$) is shifted $\sim 4 \text{ cm}^{-1}$ to the blue of the corresponding C_6H_6 transition. The absorption spectrum for each cluster observed here was found to be identical to that of the benzene monomer. This means that the entity that was ionised is the benzene monomer and that the resultant clusters that are observed in the mass spectrum must have formed post-ionisation.

The benzene dimer does not appear in the mass spectrum of Figure 5.5, and scanning of the UV laser wavelength to the expected absorption region of the benzene dimer ($\sim 30 \text{ cm}^{-1}$ to the red of monomer [60]) does not produce an ion signal in the dimer mass channel. This suggests that the dimer is not present at any time in the expansion. The observed wavelength dependence of the clusters and the absence of the benzene dimer suggests that the desorption plume is too hot to support Van der Waals clusters but cool enough to support clusters that are held together by ion-dipole interactions. Analysis of the shape of the rovibrational absorption contour of each cluster observed gives us an indication of the internal temperatures of the

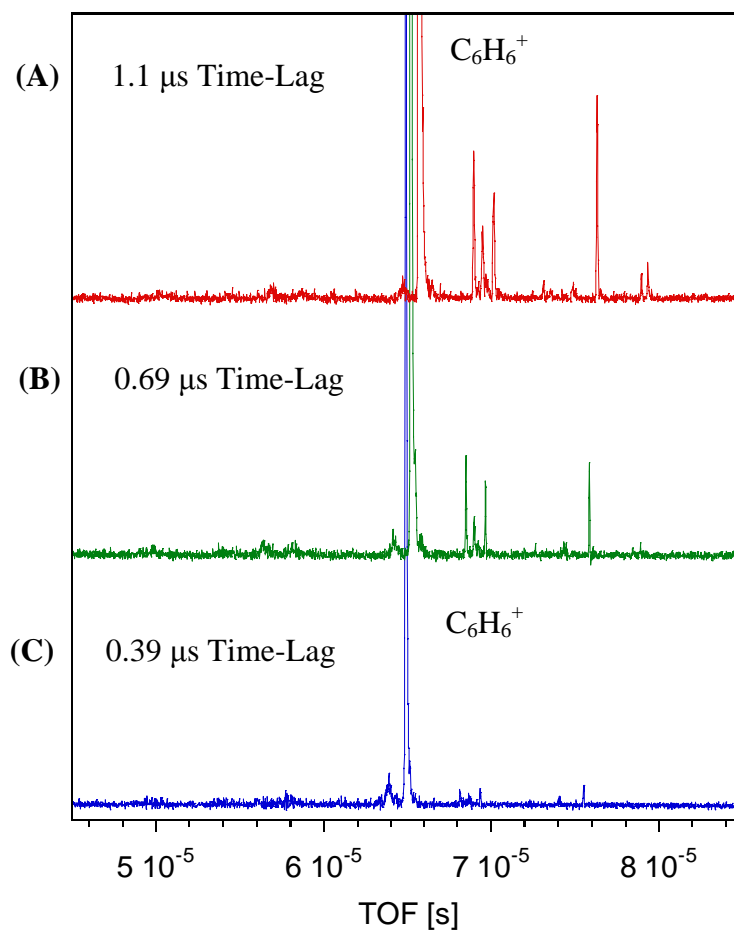


Figure 5.6: Changes in the observed TOF mass spectrum with time-lag delay. UV photon energy is 38611 cm^{-1} . IR wavelength is $2.85 \text{ }\mu\text{m}$. IR fluence is $0.9 \text{ J}\cdot\text{cm}^{-2}$. IR-UV delay is $2.5 \text{ }\mu\text{s}$. The time-lag delay between ionisation and ion extraction is 1.1, 0.69 and $0.39 \text{ }\mu\text{s}$ for spectrum (A),(B) and (C), respectively. Each spectrum is shifted to shorter flight times as the extraction delay time is decreased. The increase in cluster signal with time-lag delay is evidence that the clustering process is occurring post-ionisation of the benzene. At even longer time-lag delays, distortion of the mass peak shape occurs for all masses due to spatial limitations of the electrode assembly (see Chapter 2).

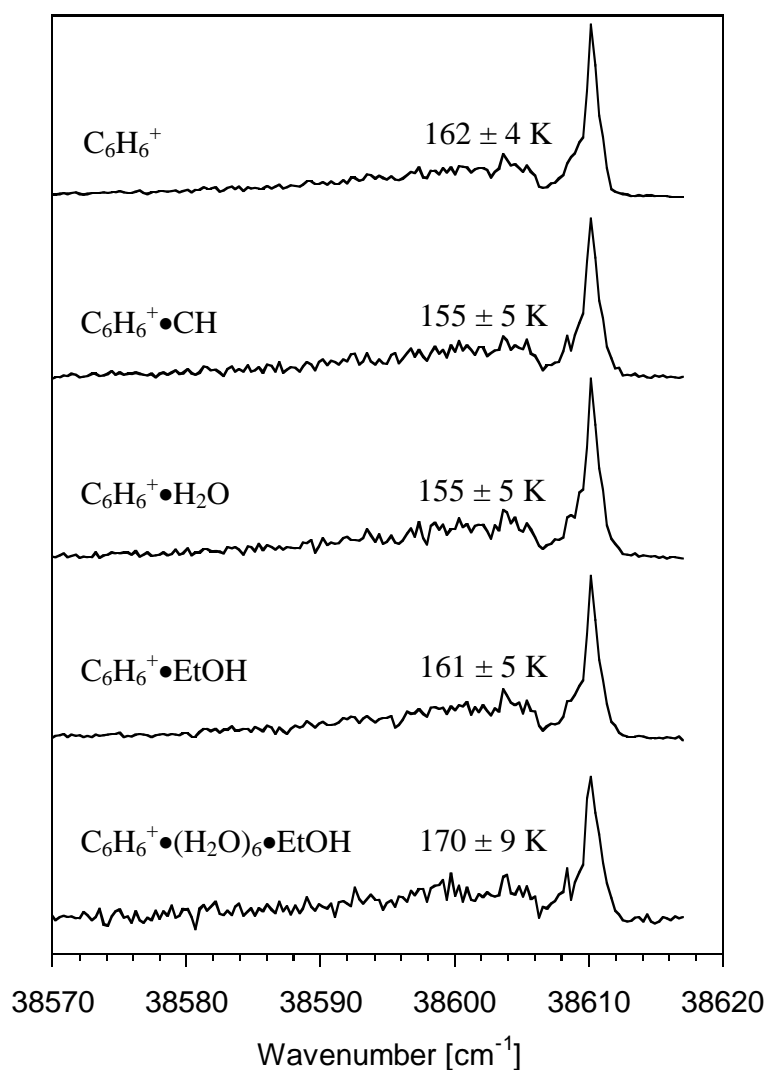


Figure 5.7: 1+1 REMPI spectra of selected clusters seen in the mass spectra with an IR-UV delay of 0.5 μ s. Each cluster shows the same wavelength dependence - they all portray the 6_0^1 vibronic spectrum of the benzene monomer. The best-fit ground state rotational temperatures of each contour are indicated with 1 standard deviation error (1σ). Within error, all of the clusters show the same rotational temperature as the monomer.

benzene ions before they are bound into a cluster. The technique used to determine the rotational temperature of each contour was described in Chapters 3 and 4. Briefly, the rotational temperature of a band is determined by varying the temperature of a simulated contour until the best fit to the experimental spectrum is obtained. The fit is achieved using a Levenberg-Marquardt non-linear least squares algorithm [61] and a Boltzmann distribution is assumed amongst the rotational energy levels. A decrease in rotational temperature is seen as a contraction of the rovibrational contour toward the vibronic origin as the population falls to the lowest rotational states.

Within error all of the rotational temperatures of the clusters were the same as that of the monomer, ~ 160 K at $0.5 \mu\text{s}$ IR-UV delay. Clusters are routinely formed in free-jet expansions but the rotational temperatures of molecules entrained in these purely gas phase expansions are routinely as low as 5 K. With rotational temperatures of ~ 160 K in the desorption plume it is surprising that we observe any clusters at all. Understandably, the ions that are observed are those that are held together by stronger ion-dipole interactions, not just the neutral-neutral, Van der Waals forces. For example, the binding energy of the $(\text{C}_6\text{H}_6^+\bullet\text{H}_2\text{O})$ dimer is almost 5 times stronger than that of the neutral [62] so they are more likely to form through association reactions and survive in the desorption plume than a neutral cluster. Kiemeier has shown that the dissociation energies of the dimer cation is almost 10 times greater than the neutral benzene dimer [60], yet it still does not appear in the desorption mass spectrum. This is therefore likely a result of the low concentration of benzene in the desorbed liquid solution.

The post-ionisation formation of the clusters also explains the effect of increased time-lag delay on the intensity of clusters shown in Figure 5.6. An increase in the time-lag delay means that there is more time for the association reactions to occur which increases the probability of ion-dipole clusters forming before they are extracted out of the interaction region.

Experimental conditions inside the TOF-MS source often produce a two-component mass peak for the $C_6H_6^+$ ion. Figure 5.8 is a zoom in on the monomer TOF peak displaying the two different components. The faster, sharper component is observable when only the UV laser is used so it is attributed to ionisation of benzene molecules that have freely evaporated from the liquid surface. When the IR laser is fired just prior to the UV laser, the slower, broader peak appears and this is attributed to benzene molecules that have been IR-desorbed from the liquid surface and then ionised. The relative intensities of each component can be manipulated with ion optics as well as with IR-UV delay time. At short delay times the evaporation signal dominates since the desorption plume has yet to reach the laser ionisation volume. However, by 1.5 μs the evaporation component is almost totally overwhelmed by the desorption component.

The mass peaks of Figure 5.8 fit well to a summation of two Gaussian distributions. The best-fit functions are shown by the overlaid red line in each figure. The fitting allowed for the determination of the intensity of each component[†]. The identity of each component of the mass peak is confirmed by monitoring the integrated intensity of each component independently as a function of UV wavelength. The shape of the absorption spectrum for each component was again identified as the 6_0^1 rotational contour of the benzene monomer (see Figure 5.8(B)). However, the subtle differences in the shapes of the spectra reveal that they have very different rotational temperatures. The spectrum generated from the fast component (green) was fit to a rotational temperature of 206 ± 7 K which unambiguously identifies it as the evaporation signal. In contrast, the spectrum generated from monitoring the slow component of the mass signal fits to a significantly cooler rotational temperature of 142 ± 4 K. This identifies the slow, broad component as being the desorption signal.

[†] The intensity of the evaporation component was obtained by subtracting the Gaussian that fit to the desorption component from the total mass peak.

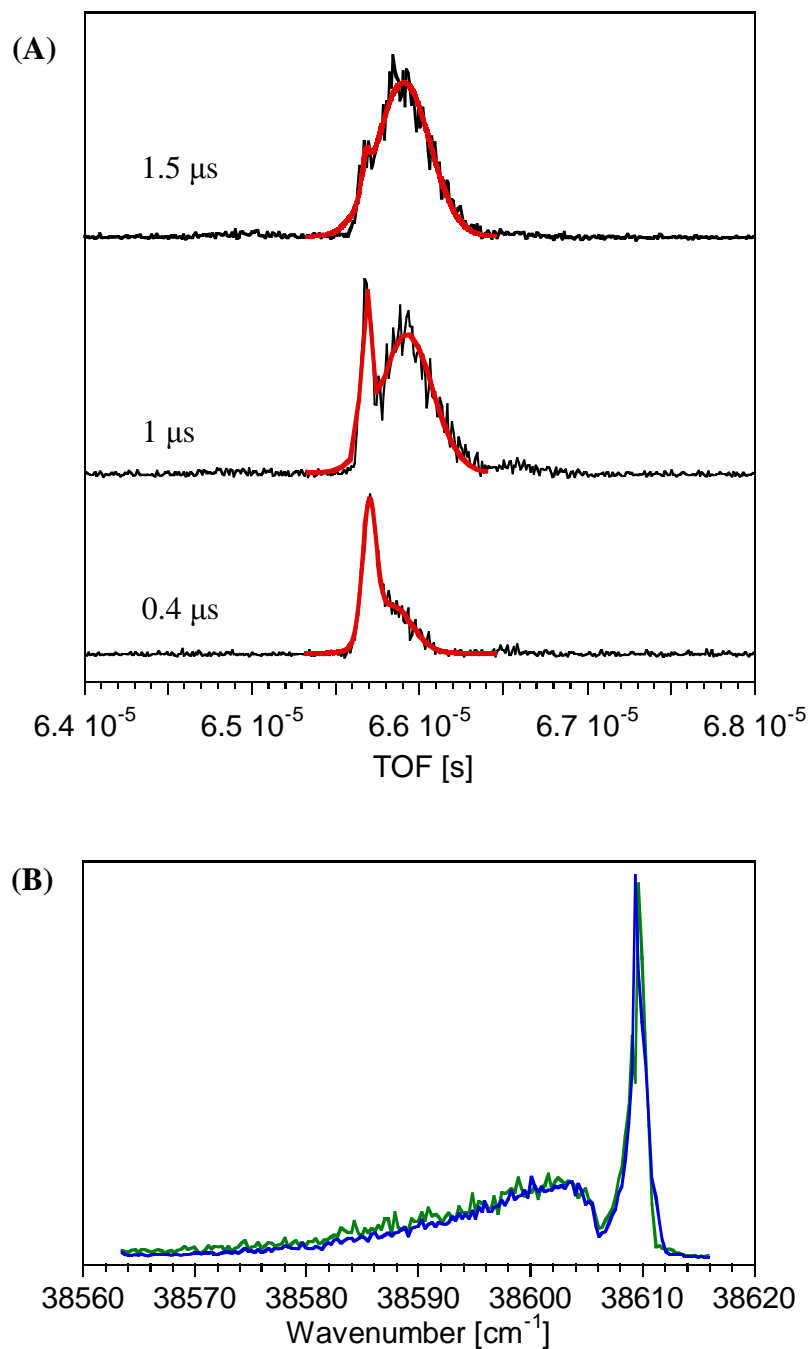


Figure 5.8: (A) The effect of changing IR-UV delay on the monomer TOF ion signal. The TOF peak displayed here belongs to the $C_6H_6^+$ ion. Each peak has been fitted to the sum of two Gaussians. The relative intensities of each component changes with IR-UV delay time. The identity of each component is confirmed by determining the rotational temperature of each component. (B) 6_0^1 vibronic spectrum of the benzene monomer generated with IR-UV delay of 1 μs . The green spectrum was generated by monitoring the intensity of the fast component of the mass peak. The blue spectrum was generated by monitoring the slow component.

Figure 5.9 shows the intensity of the monomer desorption signal as a function of IR-UV delay. The intensity of the monomer desorption signal is at a maximum when the IR-UV delay is ~ 3 μs . Since the position of both lasers is fixed, changing the delay between the desorption and ionisation lasers essentially allows for snapshots of the desorption plume as it passes through the ionisation volume of the UV laser. The intensity of the monomer signal observed is directly related to the density of the desorption plume, so Figure 5.9 gives us a rough indication of the temporal density profile of the plume along the TOF axis. The sharp rise in monomer signal indicates a fast moving, high density front of the plume followed by a slow decrease in density until pre-desorption gas phase molecular densities are re-established. Figure 5.9 also shows that cluster formation only occurs at short IR-UV delays, achieving a maximum at ~ 1 μs for two component, or 'binary' clusters ($\text{C}_6\text{H}_6^+\bullet\text{X}$, where X is the fragments CH, CH_3 , and solvent molecules H_2O and $\text{CH}_3\text{CH}_2\text{OH}$). The tertiary cluster distribution is a summation of the intensities of the $\text{C}_6\text{H}_6^+\bullet\text{X}\bullet\text{Y}$ masses ($\text{C}_6\text{H}_6^+\bullet\text{CH}\bullet\text{H}_2\text{O}$, $\text{C}_6\text{H}_6^+\bullet\text{CH}\bullet\text{CH}_3\text{CH}_2\text{OH}$ and $\text{C}_6\text{H}_6^+\bullet\text{CH}_3\bullet\text{CH}_3\text{CH}_2\text{OH}$). These higher order clusters are found to show an intensity maximum at increasingly shorter IR-UV delay times (see Figure 5.9(B)).

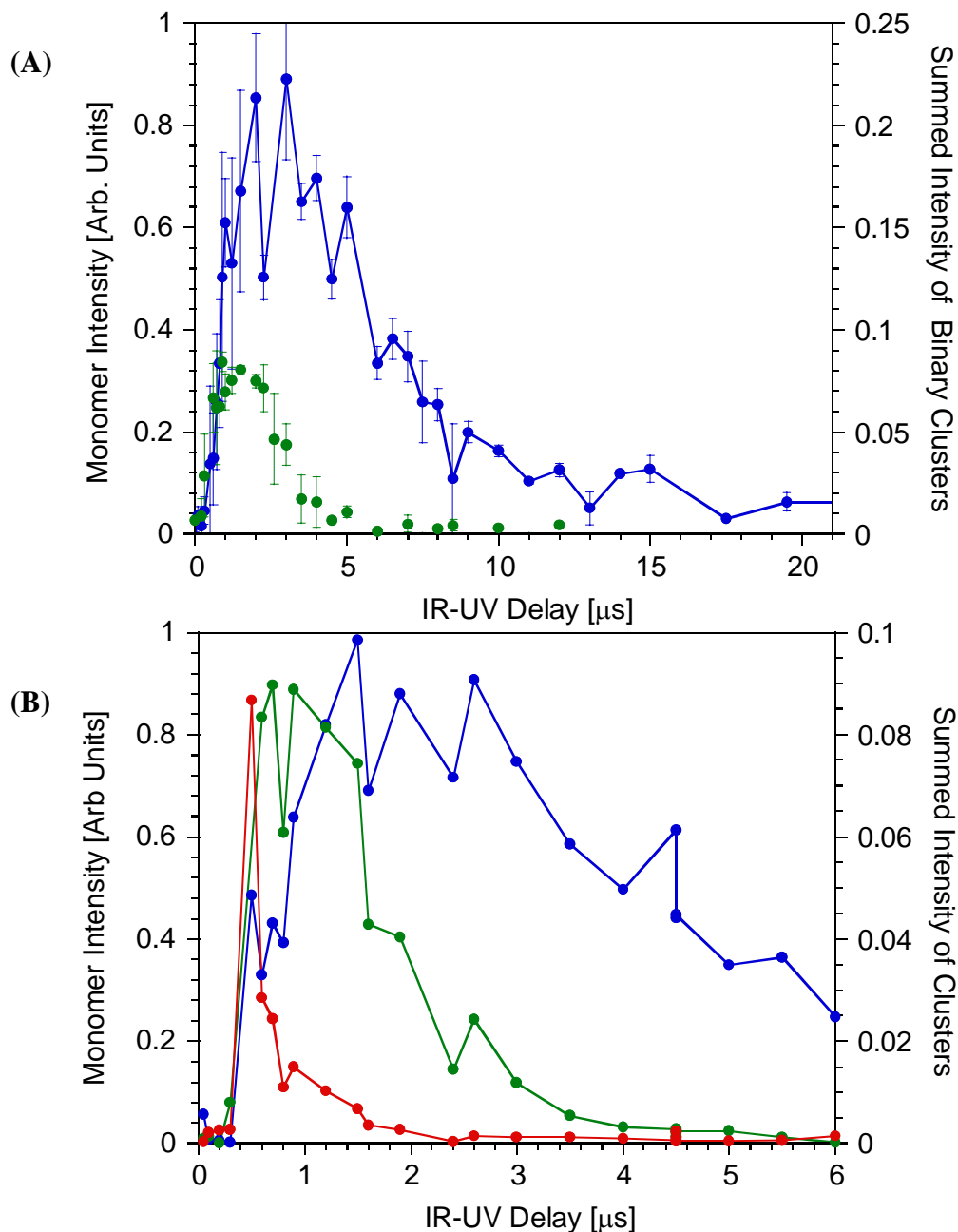


Figure 5.9: Monomer and cluster intensity as a function of IR-UV delay. (●) Benzene monomer, C_6H_6^+ , (●) two component (binary) clusters, $\text{C}_6\text{H}_6^+\bullet\text{X}$, (●) three component (tertiary) clusters, $\text{C}_6\text{H}_6^+\bullet\text{X}\bullet\text{Y}$. (A) The monomer achieves maximum desorption signal at an IR-UV delay of $\sim 3 \mu\text{s}$, whilst the binary cluster signal is maximised at a delay of $\sim 1 \mu\text{s}$. Data points in (A) are the average of the results from several mass spectra. Error bars represent 1σ error. (B) Zoom in on the overlay of monomer and cluster temporal profiles generated from a single mass spectrum. The tertiary clusters are now included. The plot demonstrates that stable cluster formation occurs early in the desorption plume (at short IR-UV delay). The maximum intensity of the tertiary clusters is seen at an IR-UV delay of $\sim 0.5 \mu\text{s}$.

5.4 Translational Velocity Distributions within the Desorption Plume

The translational velocity distribution of the desorbing species that are travelling toward the detector can be determined from an analysis of the data displayed in Figure 5.9. The distance between IR and UV lasers was kept constant ($d = 300 \mu\text{m}$), so we can use the following Jacobian for converting from time, (t), to velocity (v) to change the signal intensity as a function of IR-UV delay to a function of molecular velocity:

$$dv = \frac{-d}{t^2} dt . \quad \text{Equation 5.2}$$

The resultant velocity distributions for the benzene monomer and the binary clusters are illustrated in Figure 5.10. Note that the velocities were determined by observing the time it takes for the molecules to travel a distance of $300 \mu\text{m}$ - from the liquid surface to the centre of the ionisation volume. The width of the ionisation volume has not been considered in these velocity calculations.

Assuming an equilibrated distribution of velocities for benzene molecules entrained in the desorption plume, the translational temperature perpendicular to the L μ J axis and along the TOF axis (T_{\perp}), can be found by fitting the velocity distributions with a modified Maxwell-Boltzmann function. The exact form of the function commonly employed by groups varies slightly (primarily in the form of the pre-exponential factor) [4,6,32,37,53,63,64]. The differences between the different form of the function were investigated in detail by Knox [65]. In general, the function includes a scaling factor (A) and for unidirectional flows, a drift or “bulk” velocity (u_{\perp}) is added:

$$f(v_{\perp}) dv_{\perp} \propto A v_{\perp}^2 \exp\left(\frac{-m(v_{\perp} - u_{\perp})^2}{2RT_{\perp}}\right) dv_{\perp} , \quad \text{Equation 5.3}$$

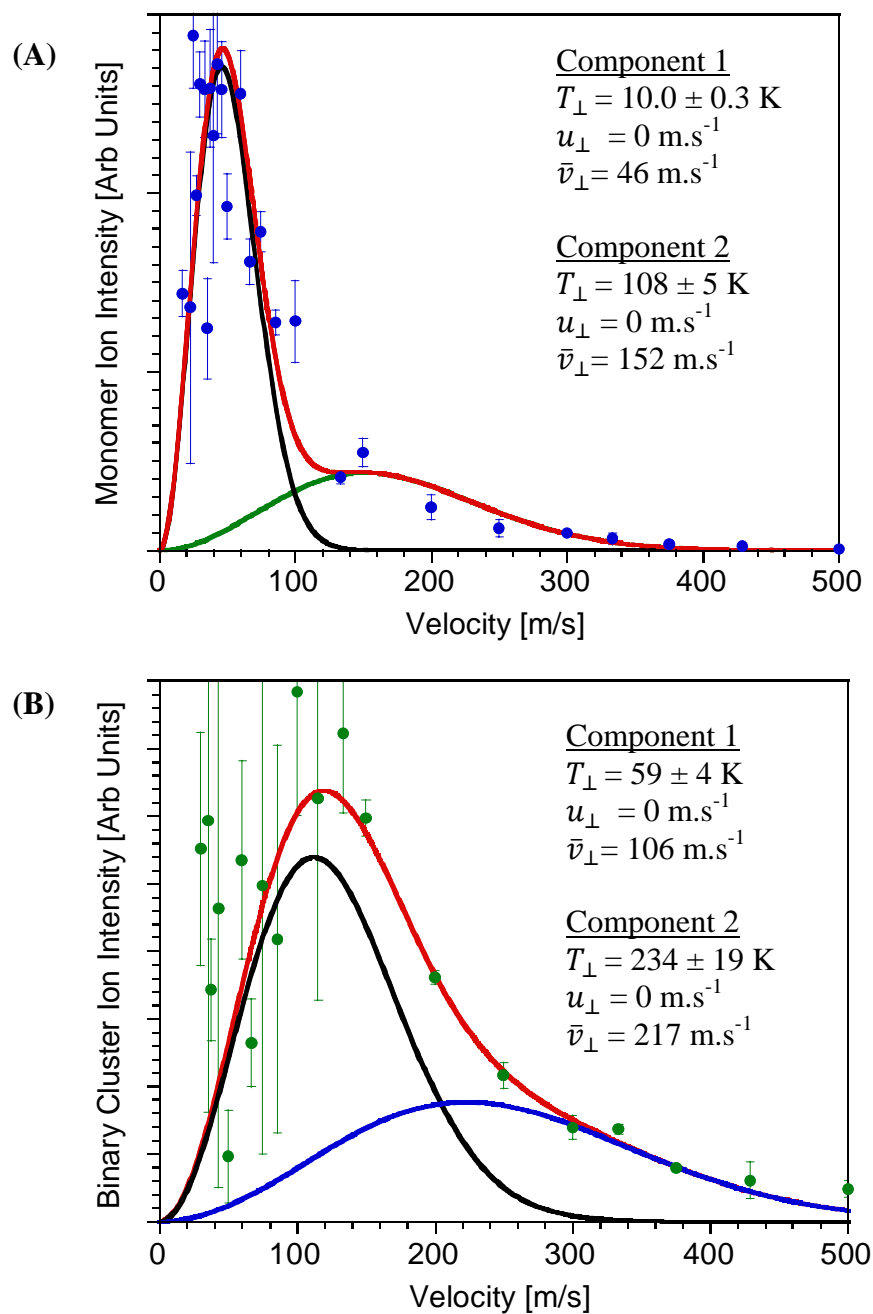


Figure 5.10: Fit of two Maxwell-Boltzmann distributions to (A) the benzene monomer ion signal (\bullet) and (B) the binary cluster ion signal (\bullet). Plots were produced by transforming the data of Figure 5.9(A) using Equation 5.2. The fits have been weighted by the displayed error in the data points. Both best-fits describe a velocity distribution that has zero drift velocity perpendicular to the jet axis (u_{\perp}). All distributions use a mass of 78 amu (benzene monomer). In both plots the red curve is the summation of both of the underlying components. The ionising laser energy is 38611 cm⁻¹ corresponding to the maximum in the 6_0^1 absorption band of the monomer.

where m is the mass of the benzene monomer (78 amu), v_{\perp} the molecular velocity along the TOF axis, toward the detector and R is the gas constant. We employ this form of the function so that we can compare our results to those of other desorption studies reported in the literature. A more accurate description of the velocity distribution would describe it as a function of desorption angle as well as treat the perpendicular and parallel temperature independently [52,65]. However, those parameters could not be resolved under our experimental conditions.

Initial fit results of a single velocity function were not significantly insightful as they did not reproduce the high intensity tail of the distribution and the best fits required a negative drift velocity. Since a negative drift velocity is a nonsensical result, the drift velocities were forced to be greater than or equal to zero during the fitting. Negative drift velocities are a common artefact of fitting to desorption distributions because of the significant signal intensity at long IR-UV delay times [32]. Under the experimental conditions employed here however, it was found that the application of any positive drift velocity actually worsened the fit of a single velocity distribution to the data. Adding a second Maxwell-Boltzmann distribution significantly enhances the quality of the fit, reproducing the high intensity fast component and the long tail of the distribution. The results of the best fits of two modified Maxwell-Boltzmann distributions to the observed velocity distribution of both the monomer and binary cluster ion signal are presented in Figure 5.10. The best-fit required that the function be weighted by the errors in the data points.

The translational temperatures of each component of the monomer velocity distribution are determined to be 10.0 ± 0.3 K and 108 ± 5 K with average velocities (\bar{v}_{\perp}) of 46 and 152 $\text{m}\cdot\text{s}^{-1}$, respectively. The translational temperatures of each component of the binary cluster velocity distribution are determined to be 59 ± 4 K and 234 ± 19 K with average velocities (\bar{v}_{\perp}) of 106 and 217 $\text{m}\cdot\text{s}^{-1}$.

Recall that the observed clusters are actually formed post-ionisation so the displayed cluster velocity distribution is in fact the velocity distribution of monomers which will eventually form clusters. If the probability of cluster formation was the same at all points inside the desorption plume then the cluster and monomer distributions of Figure 5.10 would be the same. However, as Figure 5.9 shows, the clusters are only formed at the front of the desorption plume – at the shortest IR-UV delay times. Thus the observed cluster velocity distribution is shifted to higher molecular velocities because the clusters are more likely to form in the fastest part of the desorption plume.

Cluster formation is favoured in an environment that provides three bodied collisions between internally cooled molecules that posses enough kinetic energy to surmount the activation energy for molecular association [66,67]. Analogous to the conditions of a free-jet gas expansion, the fast translational velocities are obtained by drawing energy from internal molecular degrees of freedom [66,68]. The result is a cooling of rotational and vibrational motion at this point in the expansion. This will be discussed further in Section 5.5. Focusing of translational velocity along the TOF axis is, in essence, a decrease in the random translational motion perpendicular to the TOF axis. This means that the fastest travelling molecules are also likely to be the most translationally cold – where the translational temperature here describes an ensemble of molecules distributed in a plane perpendicular to the TOF axis. The final requirement of a three bodied collision for clustering to occur suggests that the molecular density is highest at the IR-UV delay time which corresponds to the maximum in the cluster ion yield. Since the maximum production of tertiary clusters occurs at an even shorter IR-UV delay time (0.5 μs) than the binary clusters (1 μs), this suggests the maximum in molecular density actually occurs closer to 0.5 μs . This is much earlier than was suggested by the maximum in the monomer ion intensity distribution.

Many groups suggest that there are several elements to the desorption process which results in a multi-component velocity distribution [32,53,69-71]. In general, laser desorption is thought to involve some sort of explosive ejection of molecules (be it due to hydrodynamic [16,32,41,42], shock wave [72] or columbic [8,10,12,73] forces) followed by a thermalised, evaporation process [74]. It is the thermal process over a long period of time which causes the tail of the IR-UV delay distribution seen in Figure 5.9, and the explosive process which creates the tail of the velocity distribution seen in Figure 5.10. An excellent example of a bimodal velocity distribution of desorbing molecules was observed by Horimoto *et al* [40]. They observed two distinct IR-UV delay distributions when desorbing resorcinol from an aqueous $\text{L}\mu\text{J}$. The laser powers used in their studies were comparable to those used here, however, they used $1.9\ \mu\text{m}$ desorption light as opposed to the $2.85\ \mu\text{m}$ used in these studies. The maximum of their first component appeared at $0.3\ \mu\text{s}$ IR-UV delay (equivalent to $1000\ \text{m}\cdot\text{s}^{-1}$ in this study) and the maximum of the second, broad component appeared at $10\ \mu\text{s}$ (equivalent to $40\ \text{m}\cdot\text{s}^{-1}$ in this study). In comparison, the velocities of each component observed here are much slower, and also more similar in magnitude.

The validity of assigning a temperature to the observed velocity distribution is not clear since assignment of a temperature assumes that the translational motion has reached thermal equilibrium. By definition, an expansion process involves the concerted movement of gas away from the expansion origin which requires the translational motion to be in non-equilibrium. However, the modified Maxwell-Boltzmann distribution described by Equation 5.3 relaxes this definition, allowing for the description of a thermalised translational velocity distribution that is moving with a concerted bulk velocity away from the expansion source. Fitting of this modified function to the velocity distribution of Figure 5.10 showed the desorbed monomers have a drift velocity of $0\ \text{m}\cdot\text{s}^{-1}$. This result does not sit well with the concept of an expanding desorption plume. However, forcing a translational temperature and drift velocity description onto desorption data does offer an opportunity for comparing

experimental data sets. Kleinekofort *et al*'s analysis of the velocity distribution of Lysozyme and gramicidin D molecules IR desorbed from alcohol micro-jets also displayed negligible drift velocities, though their translational temperatures were significant higher at ~ 615 K [16]. In comparison, Charvat observed biomolecules IR desorbed from aqueous micro-jets with drift velocities of $2000\text{--}3000\text{ m.s}^{-1}$. Reanalysis of the velocity distributions observed for hydroquinone molecules IR desorbed from aqueous micro-jets revealed translational temperatures of 650 K sitting on a drift velocity of $\sim 400\text{ m.s}^{-1}$ ‡[38]. The disparity between results arises because of the many different experimental conditions that can influence the flow properties of the desorption plume as well as the different observation and analysis techniques. Several studies of desorption from both solid and liquid surfaces reveal that the observed velocity distribution is dependent upon laser fluence [4,43,75], the area of the origin of the desorption plume [32] as well as the identity and preparation technique of the matrix [54,76,77]. Each of these factors influences the number and energetics of gas phase collisions within the desorption plume – in essence it is the nature of the collisions which distort the gas-phase velocity distribution from the equilibrated distributions observed in the bulk liquid [51,52,78].

One of the assumptions made when converting the IR-UV delay distributions of Figure 5.9 into the velocity distributions of Figure 5.10 was that the size of the ionisation volume is negligible, that is, the ionisation volume was in fact a single point. This assumption effectively averages the spread of velocities that have arrived within the ionisation volume by a certain IR-UV delay. Recall that the ionisation volume has a diameter of $150\text{ }\mu\text{m}$ and the centre of that volume sits $300\text{ }\mu\text{m}$ from the centre of the $L\mu\text{J}$. This means that, for example, molecules travelling along the TOF axis with velocities between 22 and 36 m.s^{-1} will all reach the ionisation volume by given a $10\text{ }\mu\text{s}$ IR-UV delay and contribute to the ion signal. However, if the ionisation volume is treated as a point, as Equation 5.2 requires, then the total ion signal

‡ The hydroquinone data was reanalysed after performing the conversion Jacobian introduced at the start of this section.

is attributed only to molecules with velocity of 29 m.s^{-1} . At shorter IR-UV delays an even greater range of velocities will be averaged together by this assumption of point ionisation, which further distorts our interpretation of the translational velocity. The effect of the ionisation volume on the shape of the IR-UV delay distribution becomes increasingly important when the distance between the desorption and ionisation positions become comparable to the size of the ionisation volume. This is the case with the experiments performed here. In an effort to be able to incorporate the effects of ionisation volume into the analysis of the IR-UV delay distribution a simple, 3D Monte Carlo simulation of the desorption process was performed.

The Monte-Carlo simulation assumes that benzene monomers (78 amu) are released at random angles away from a cylindrical surface with a radius equivalent to that of the L μ J (7.5 μm). The probability of creating a monomer with a particular speed is described by the Gaussian function of the same form as the exponential of Equation 5.3. Thus the velocity distribution can be ascribed a translational temperature as well as a drift velocity. The benzene molecules are allowed to travel (collision-free) until a set time (t) at which their position will be recorded. If at t the molecules lie within an area designated as the ionisation volume of the UV laser then the molecules are said to be ionised and are included as detected ions. A schematic of the simulation conditions is displayed in Figure 5.11.

Figure 5.12 demonstrates the effect of changing the diameter of the ionisation region on the shape of the simulated IR-UV delay distribution. The distance from the centre of the ionisation volume to the centre of the L μ J was kept at 300 μm whilst the diameter of the UV, cylindrical volume was reduced from 150 μm to 1.5 μm . There is a dramatic difference in the observed distribution, when the UV volume is changed. As predicted, increasing the UV ionisation volume distorts the distribution to shorter IR-UV delay times due to the effects of velocity averaging. Even though the initial velocity distribution of the molecules in the

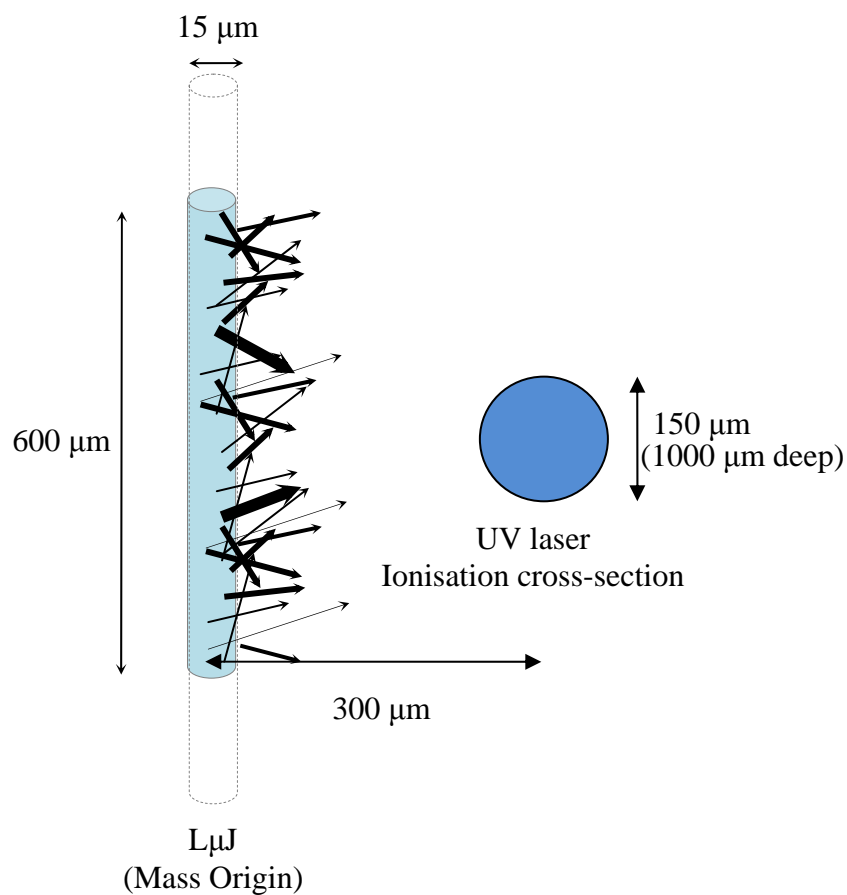


Figure 5.11: Schematic of the conditions of the 3D Monte Carlo simulation. Different length arrows represent molecules released from the liquid surface with different initial velocities. The volume of the ionisation region runs into the page, perpendicular to the L μJ axis. The different width arrows represent different initial masses emerging from the L μJ - this is used in the mass-independent velocity distribution simulations.

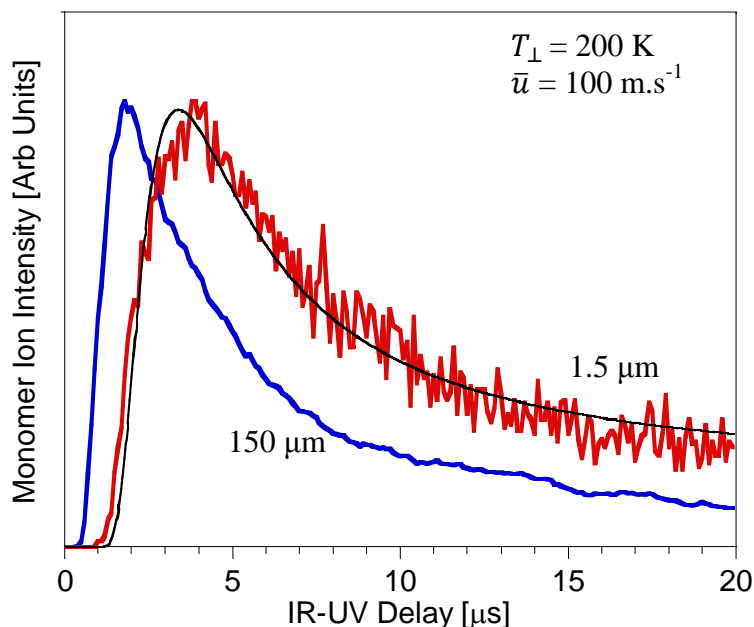


Figure 5.12: Demonstration of the effects of the diameter of the ionisation volume on the shape of the IR-UV delay distribution created by the 3D Monte Carlo simulations. The translational temperature and bulk velocity used in the simulations were 200 K and 100 m.s^{-1} , respectively. The diameter of the UV volume is $150 \mu\text{m}$ (blue line), diameter of the UV volume is $1.5 \mu\text{m}$ (red line). The signal/noise is worse when the UV volume is smaller since fewer molecules find themselves within the region at the time of ionisation. Larger ionisation volumes distort the maximum in the distribution to shorter delay times since molecules with a larger range of molecular velocities can reach the ionisation volume at the shorter delays. The distribution created with $1.5 \mu\text{m}$ diameter has been fitted with a function of the form of Equation 5.4 but without the pre-exponential factor, C/t^4 (black line). The best fit predicted a \bar{u} of $88 \pm 1 \text{ m.s}^{-1}$ and a T_{\perp} of $19 \pm 1 \text{ K}$.

simulation were identical in each case ($T_{\perp} = 200$ K and $u_{\perp} = 100$ m.s⁻¹), it is obvious that any attempt to extract the velocity distribution from an analysis of the IR-UV delay distribution using Equation 5.3 would yield very different results. To prove this, the simulated IR-UV delay distribution created with a 1.5 μm UV diameter was fit with a single Maxwell-Boltzmann distribution of the same form as Equation 5.3 but converted into the time domain [32,79].

$$f(t) dt \propto \frac{C}{t^4} \exp\left(\frac{-m\left(\frac{d}{t} - u_{\perp}\right)^2}{2RT_{\perp}}\right) dt, \quad \text{Equation 5.4}$$

Where C is a scaling factor, t is the IR-UV delay time and d is the distance between the IR and UV lasers along the TOF axis (300 μm in this case). In this form, the function did not fit well to the simulated distribution, in particular, failing to match the broad tail of the distribution. It was found that the best fit to the simulated data was obtained when the pre-exponential, C/t^4 , was removed leaving a function of the same form as the velocity distribution with which the simulated ions were created. The best fit is shown as the black line in Figure 5.12. The best fit to the simulated distribution required a bulk velocity (\bar{u}) of 88 ± 1 m.s⁻¹ and a translational temperature (T_{\perp}) of 19 ± 1 K. Whilst the best fit value for \bar{u} is close to that which was used to create the simulated distribution, the best fit T_{\perp} value is inaccurate by an order of magnitude. The results of the simulations emphasises the importance of considering the ionisation volume when determining the velocity distribution of the species being probed. They also question the validity of forcing distributions of the form of Equations 5.3 and 5.4 onto the experimental data in an effort to extract translational temperatures and bulk velocities of the molecules within the desorption plume.

Figure 5.13 shows the results of changing the drift velocity and temperature on the simulated IR-UV delay distribution. The major effects caused by increasing the temperature of the

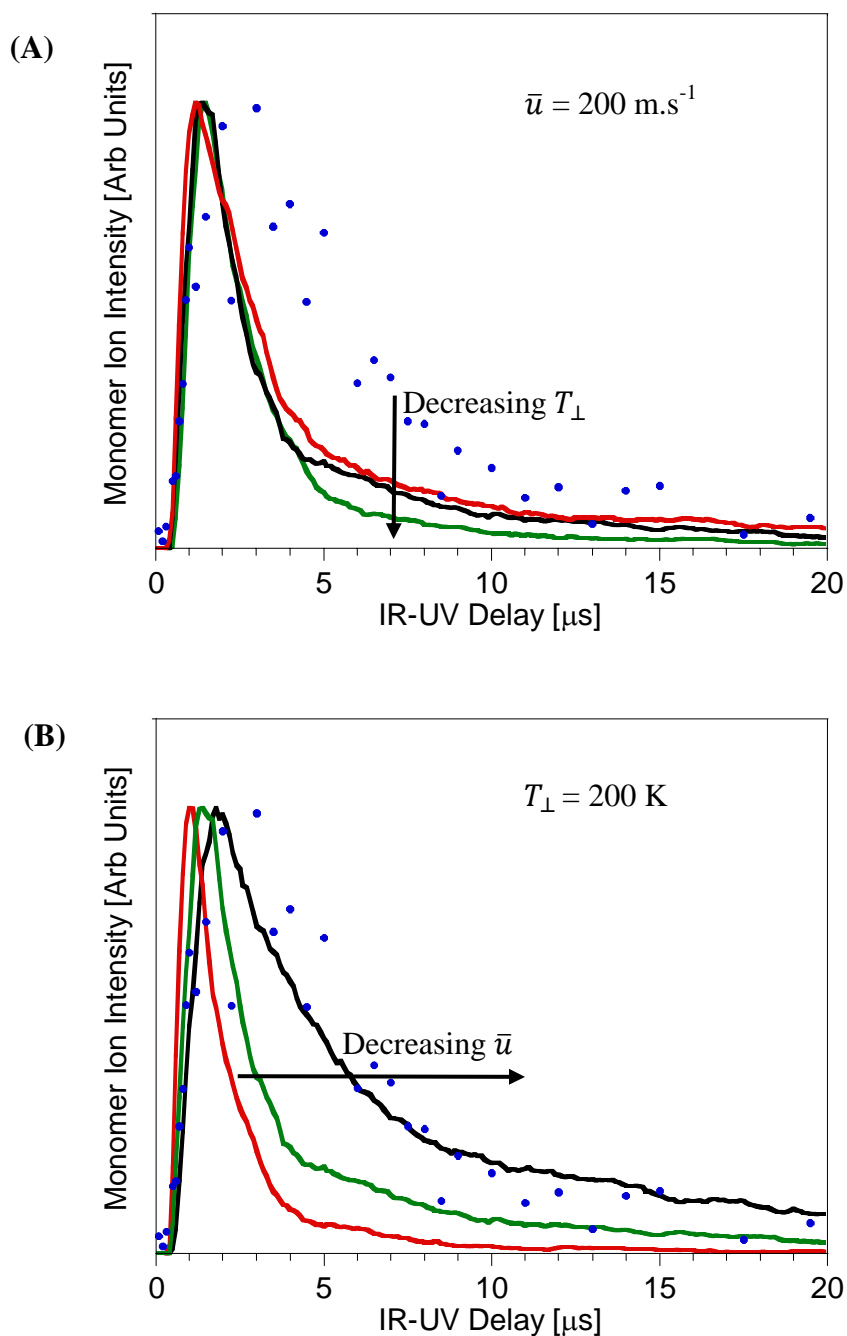


Figure 5.13: Simulated IR-UV delay distributions overlaid with the experimentally observed benzene monomer ion signal (\bullet) distribution. All the simulations in (A) have a bulk velocity of 200 m.s^{-1} but vary in translational temperature: (red line) 300 K, (black line) 200 K, (green line) 100 K. (B) shows the effects of changing the drift velocity in the simulations with a temperature of 200 K. (red line) 300 m.s^{-1} , (green line) 200 m.s^{-1} , (black line) 100 m.s^{-1} .

benzene monomers in the simulation is to increase the intensity of the distribution's tail at large IR-UV delays and to decrease the rate at which the maximum is reached at short IR-UV delays. Increasing the drift velocity shifts the sharp initial rise in intensity to shorter IR-UV delays and broadens the tail of the distribution. The experimentally observed IR-UV delay distribution of the monomer is reproduced in Figure 5.13 as the blue dots. Manual adjustment of these two parameters shows the best correlation between the simulated and experimental data occurs with a drift velocity of $\sim 100 \text{ m}\cdot\text{s}^{-1}$ and a translational temperature of $\sim 200 \text{ K}$. This result is displayed as the black line in Figure 5.13(B). Though the simulation is a very simple one, these results are very promising. As mentioned above, studies of laser desorption routinely describe the expansion as being fast moving and translationally hot. The results of these simulations show that the initial velocity of the desorbed molecules is predicted to have a temperature of a few hundred Kelvin with a large, positive drift velocity. However, the simulations do routinely produce sharper maxima in IR-UV delay distribution than is observed experimentally. Possible causes of the broadening of the maximum are discussed below.

Kinsel *et al* have performed an in-depth study of the dynamics of the MALDI process including velocity profiles of the desorbed ions [71]. They concluded that for heterogeneous systems such as an analyte entrained within a plume of matrix molecules, the observed velocity distributions can be interpreted as being independent of mass. Huth-Fehre and Becker were able to independently derive the velocity distributions of matrix and analyte molecules when Gramicidin S is laser desorbed from a Ferulic Acid Matrix [77]. They showed that both components displayed essentially the same velocity distribution, demonstrating that the analyte was entrained in the matrix expansion and that molecular velocity was independent of mass. The same interpretation of observed velocity distributions is also reserved for an analyte entrained in a purely gas phase supersonic expansion of carrier gas [66,68].

An earlier study by Kinsel *et al* [70] of laser desorbed Bovine Insulin clusters found that the desorption plume encompassed two distinct components. They interpreted the slower component to be the mass independent entrainment of the analyte molecules, but the fast, narrow component they found was best described by an ensemble of molecules travelling with the same translational energy.

In an effort to judge the applicability of Kinsel's concept that all of the desorbed masses travel with the same amount of translational energy, larger masses were introduced into the Monte Carlo simulation. The masses considered here were various sized clusters of benzene and water. For simplicity, in the simulation all masses are released simultaneously and with equal probability. The probability of each mass receiving a particular translational energy is described by a set translational temperature, thus on average, the heavier masses have smaller velocities and the smaller masses, larger velocities. In the simulation, once in the gas phase the water molecules evaporate from the hydrated clusters leaving behind a bare benzene monomer. The isolated benzene molecule subsequently travels with the velocity determined by the kinetic energy of the initial, heavier cluster of which it was a part.

Figure 5.14 shows the effects of adding heavier masses on the resultant IR-UV delay distribution. The example masses considered here are $C_6H_6 \bullet (H_2O)_n$, where n is 2 or 4. Figure (A) shows the shape of the distributions for the individual masses. Larger masses produce broader, maxima and are more intense in the tail of the distribution. The distribution of the larger masses is also shifted to longer delay times compared to the smaller masses since they cannot obtain as high velocities as the smaller masses for the same amount of initial translational energy. Figure (B) demonstrates the shape of the distribution that would result if equal amounts of each mass were added to the simulations. The effect of assuming a mass independent velocity distribution of the desorbed molecules manifests as a broadening and

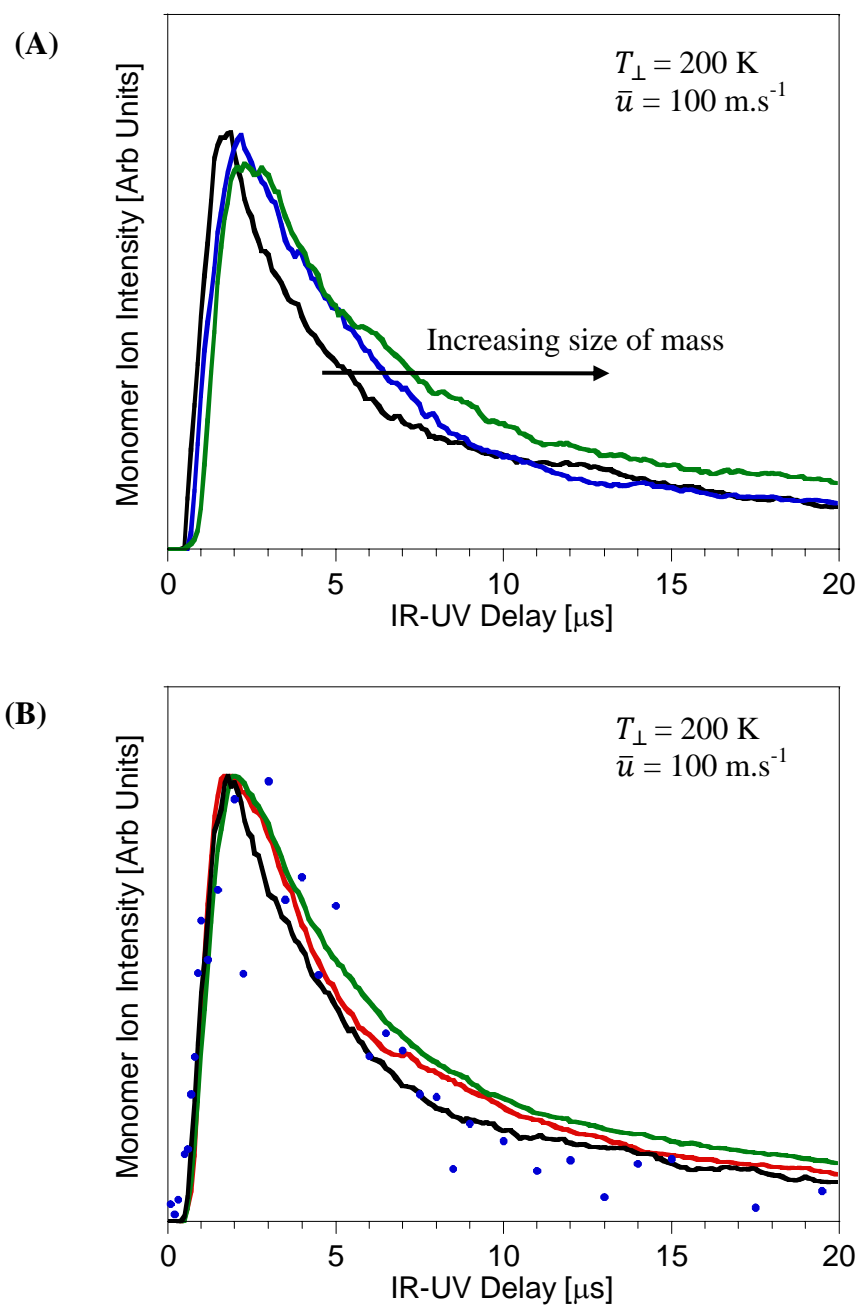


Figure 5.14: Simulated IR-UV delay distributions of different masses included in the 3D Monte Carlo simulation. (A) C_6H_6 , 78 amu (black line), $\text{C}_6\text{H}_6 \bullet 2\text{H}_2\text{O}$, 114 amu (blue line), $\text{C}_6\text{H}_6 \bullet 4\text{H}_2\text{O}$, 150 amu (green line). (B) When the distributions from each mass are summed together the resultant IR-UV delay is broader at the maximum which more closely resembles the shape of the experimentally observed distribution maximum. Only C_6H_6 (black line), C_6H_6 and $\text{C}_6\text{H}_6 \bullet 2\text{H}_2\text{O}$ (red line), C_6H_6 , $\text{C}_6\text{H}_6 \bullet 2\text{H}_2\text{O}$ and $\text{C}_6\text{H}_6 \bullet 4\text{H}_2\text{O}$ (green line). Experimental data (\bullet).

rounding of the peak in the IR-UV distribution as well as intensifying the tail of the distribution. The incorporation of masses larger than the benzene monomer into the simulations may help to explain why the experimentally observed IR-UV delay is much broader at the maximum than is expected for a single mass distribution.

An important advancement in the simulations would be the inclusion of gas phase collisions as these would tend to change the angular dependence of the desorbed molecules and thus the observed velocity distributions [78]. Also, in the results shown in Figure 5.14, it was assumed that masses of all sizes had an equal probability of being desorbed. This is an unlikely scenario since the mass spectra of many desorption experiments have demonstrated that clusters display size dependant intensity distributions [10,19,73]. Thus advancements of the simulation should include the investigation of the dependence of the simulation results on the probability of desorbing the different masses.

5.5 Distribution of Internal Energy by the Desorption Process

The internal energy content of a molecule entrained in a desorption plume influences the chemical reactivity as well as the degree of fragmentation that it will undergo. Determination of internal energies are thus important when trying to optimise the desorption technique for a desired degree of fragmentation. The limited number of studies of the internal energy of laser-desorbed neutral analyte molecules tend to show cooling of the analyte as it leaves the matrix. Cousins *et al* found that when NO molecules are UV desorbed from multilayer NO films, they undergo significant rotational cooling [53]. Elokhin observed vibrational cooling in aniline molecules IR desorbed from a solid CO₂ matrix [54]. Similarly, Zhang *et al* observed benzimidazole molecules are vibrationally cooled to temperatures as low as 46 K when IR-desorbed from near room temperature glycerol/water mixtures [56]. In comparison, Mowry's

studies of the internal energies of alkylamines laser-desorbed from larger molecule matrices showed the internal energy of the ejected analyte is comparable to the sublimation temperature of the matrix (440-520 K) [55]. Mowry suggests that the contradiction between these results and the results of the aforementioned experiments is likely due to the inefficiency of large polyatomic matrix molecules to efficiently collisionally cool the analyte. This is supported by the observations of Zhang where increasing the concentration of glycerol in the glycerol/water matrix was seen to decrease the amount of vibrational cooling observed [56].

In the experiments reported here, the rotational and vibrational temperatures of laser-desorbed neutral benzene molecules are monitored during the temporal evolution of the desorption plume. The absorption spectra of laser-desorbed benzene molecules are recorded by monitoring the integrated intensity of the parent mass peak (78 amu) whilst scanning the wavelength of the ionising laser. Example fits to the three absorption bands of interest are illustrated in Figure 5.15. The experimental spectra in Figure 5.15 were generated with an IR-UV delay of 3.9 μs . The fit temperature of the cold band, 6_0^1 , illustrates the rotational temperature of the vibrationless ground state whilst the fit temperature of the $6_1^2/6_1^0 11_0^2$ hot band illustrates the rotational temperature of the vibrationally excited 6_1 state. The third absorption feature is the overlapping rovibrational contours $6_0^1 16_1^1$ and $6_0^1 11_1^1$. The results of the simulation studies conducted in Chapter 3 demonstrated that the $6_0^1 11_1^1$ contour sits underneath the peak at $\sim 38452 \text{ cm}^{-1}$. The quoted rotational temperature of the hotband here assumes that the rotational temperature of the vibrational states 16_1 and 11_1 are the same. The justification for this assumption was discussed in Section 4.7.1.

In general, the shapes of the simulated contours of Figure 5.15 closely match the experimental data. This indicates that the distribution of energies within the rotational manifold of desorbed

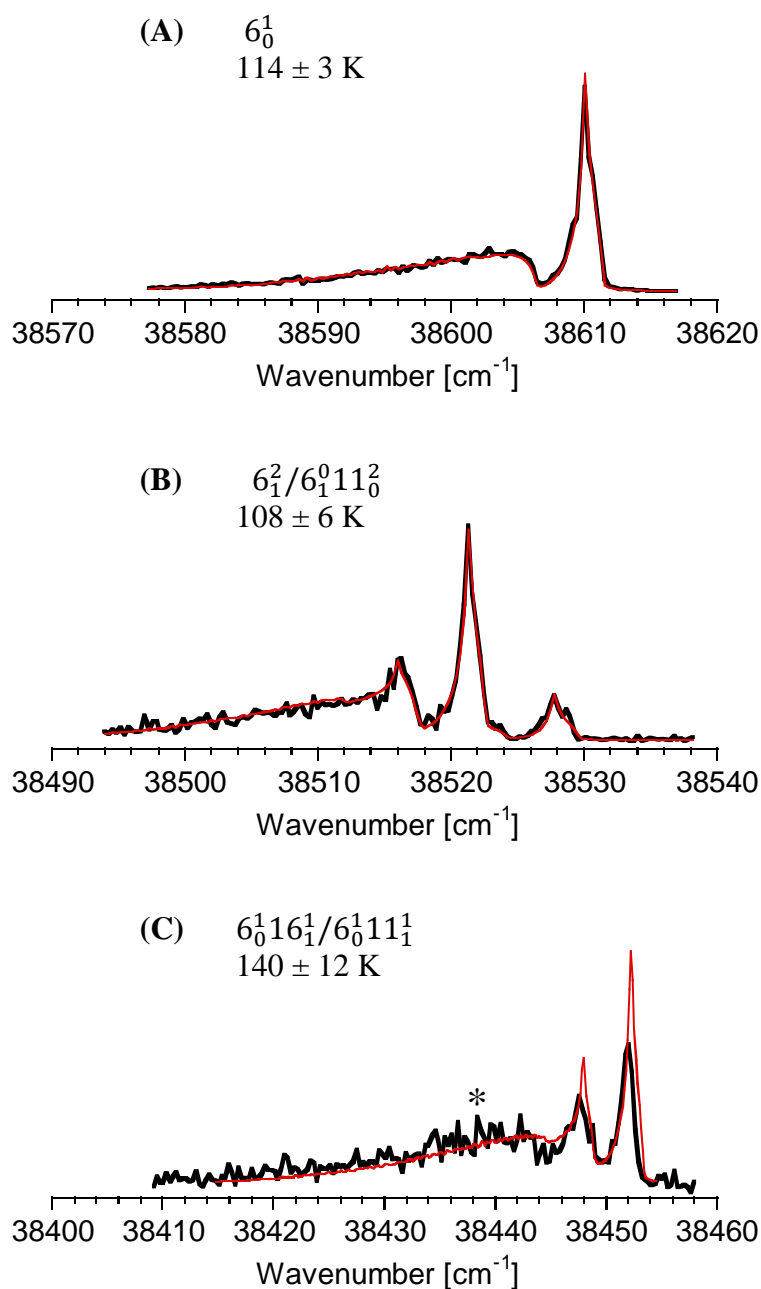


Figure 5.15: Rovibrational contours of benzene molecules IR desorbed from the $L\mu\text{J}$. These spectra were produced with an IR-UV delay time of $3.9 \mu\text{s}$. Temperature fits are displayed with error indicating 1 standard deviation from the mean. The lower signal/noise and larger fitting error of (C) is due to the dramatic decrease in the intensity of the band under desorption conditions. (*) See text for a discussion of this feature.

benzene is Boltzmann; i.e. there is equilibration of the rotational motion which is independent of vibrational excitation. Comparison of individual absorption spectra show that, within fitting error, the highest frequency vibration, ν_6 , displays the same rotational temperature as the vibrationless ground state. Cousins *et al* also observed that rotational temperatures of NO laser-desorbed from multilayer NO films was essentially independent of vibrational excitation, achieving temperatures of 105 and 130 K for ground and $\nu = 1$ states, respectively [53].

As discussed in Section 3.1.8, simulation of the $6_0^1 16_1^1 / 6_0^1 11_1^1$ band at low temperatures (~ 5 K) shows some intensity discrepancies with the experimental data at ~ 38440 cm^{-1} . This phenomenon was also often apparent in many of the $6_0^1 16_1^1 / 6_0^1 11_1^1$ desorption spectra appearing as an enhancement of the head of the P branch (marked with * in Figure 5.15(C)). It seems that the distortion of the rovibrational contour at this position is enhanced at lower rotational temperatures. The cause of this effect is unclear, but the appearance of extra absorption features in the room temperature Laser Induced Dispersed Fluorescence (LIDF) spectrum (Section 3.3.4) of the same band suggest that perhaps it is due to an underlying, unidentified absorption feature that has a greater relative intensity at the lower temperatures. This slight distortion does not appear to dramatically affect the rotational temperatures obtained since the fits are more heavily influenced by the shapes of the intense, high energy, R branch features.

Figure 5.16 shows a comparison between gas-phase benzene REMPI spectra (38380 – 38620 cm^{-1}) generated under 4 different conditions[§]: (A) benzene equilibrated in a room-temperature static cell, (B) benzene entrained in a free-jet expansion of nitrogen, (C) benzene that has evaporated from the surface of the *in vacuo* L μ J and (D) benzene IR desorbed from the

[§] The methods used to generate the conditions of A, B and C are described in Chapter 3 and 4.

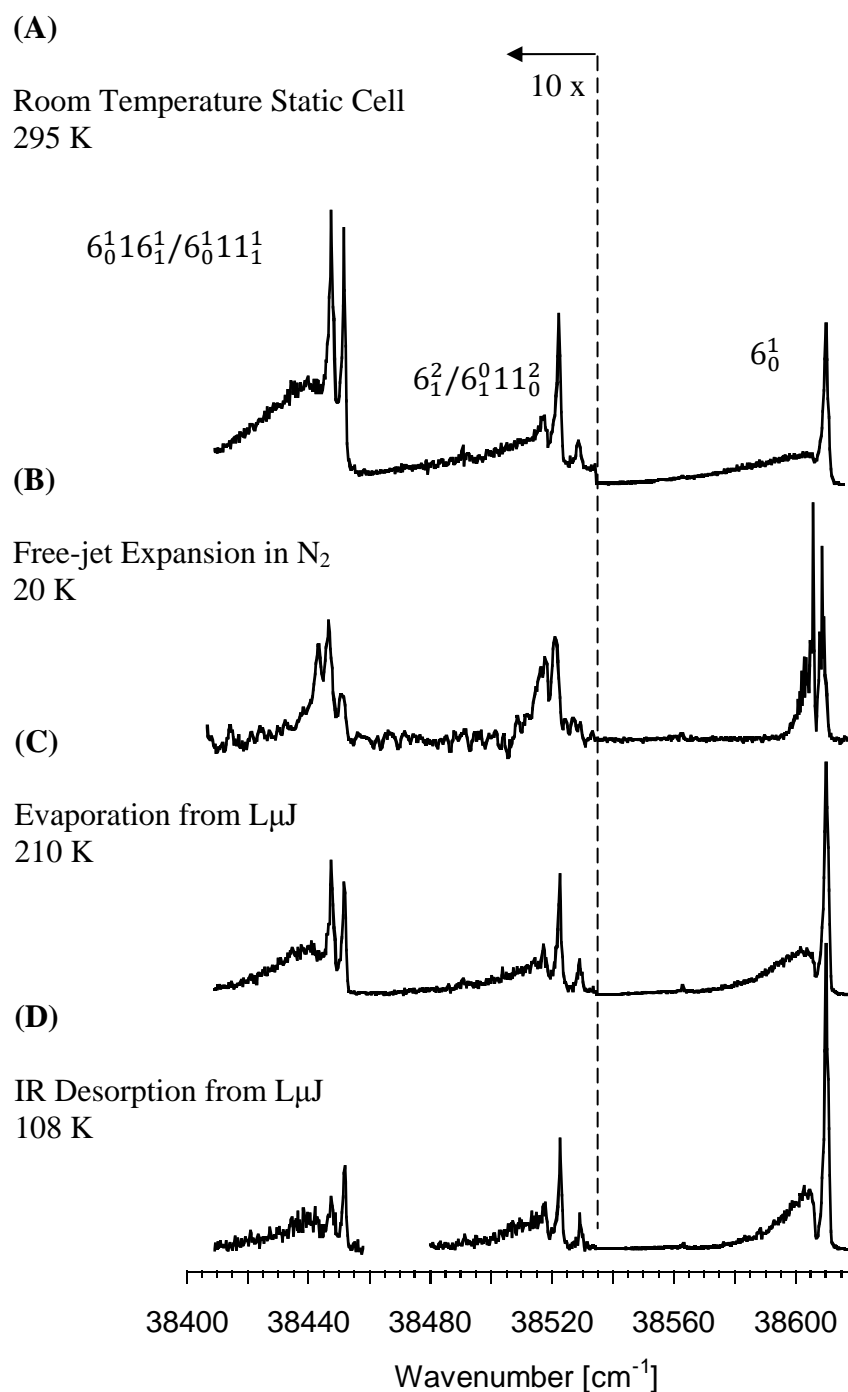


Figure 5.16: Comparison of the benzene absorption spectrum generated under different experimental conditions. See text for details. The rotational temperatures of benzene molecules are also quoted for each experimental environment. The IR-UV delay used to generate the desorption spectrum shown here was 4 μ s. The intensity of all spectra has been magnified ten-fold at energies less than 38535 cm^{-1} .

surface of the same $L\mu\text{J}$. The change in rotational temperature with each technique can be easily seen by comparing the shapes of each rovibrational band with those in the room temperature spectrum (Figure 5.16(A)). From Figure 5.16 it is evident that the rotational temperature of laser desorbed benzene is cooler than both the room temperature (295 K) and evaporation spectra (210 K), but warmer than the temperatures achieved in the free-jet expansion (20 K in this example). In this example, the rotational temperature of the desorbed molecules was 108 K.

Vibrational temperatures are determined by monitoring the change in relative intensities of the cold and hot rovibrational absorption bands compared with those in the room temperature, equilibrated gas phase spectrum [80]. Figure 5.16 shows that there is a dramatic difference in the relative integrated intensities of the $6_0^1 16_1^1 / 6_0^1 11_1^1$ and 6_0^1 bands between the room temperature and desorption spectra. In the room temperature spectrum all the vibrations are at equilibrium; i.e. at the same temperature. In the desorption spectrum the relative intensity of the $6_0^1 16_1^1 / 6_0^1 11_1^1$ has decreased dramatically, which illustrates that the desorption process has pulled population rapidly out of the 16_1 vibrational state, thus giving ν_{16} in benzene a lower vibrational temperature. Recall that the $6_0^1 11_1^1$ contour sits underneath the peak at $\sim 38452\text{ cm}^{-1}$. The increased intensity of this peak relative to its lower energy neighbour is evidence that the 11_1 state has a higher vibrational temperature than the 16_1 at this point in the desorption plume. The change in intensity of the whole $6_0^1 16_1^1 / 6_0^1 11_1^1$ band is not as dramatic with the $6_1^2 / 6_1^0 11_0^2$ band which means that the desorption process has not cooled the ν_6 vibration as efficiently as ν_{16} and ν_{11} . Collisional energy transfer efficiencies calculated in Chapter 4 revealed that ν_6 in the ground electronic state cooled ~ 50 times slower than ν_{16} and 9 times slower than ν_{11} . The amount of vibrational cooling observed in the desorption plume is thus dependent upon the identity of the vibration due to their different propensities for cooling through collisions.

The partitioning of internal energy at different points in the desorption plume is illustrated by recording the rotational and vibrational temperatures as a function of IR-UV delay. These results are illustrated in Figure 5.17. Each data point is the weighted mean of fitting at least 3 spectra equivalent to those presented in Figure 5.15. The error bars represent 3 times the weighted error of the mean (3σ). Recall that the ionisation volume of the probe laser lies perpendicular to the TOF axis, so the temperatures quoted here describe how the internal energy is distributed perpendicular to the TOF axis at different point in the desorption plume, in contrast to the translational temperatures quoted in Section 5.4. There are several interesting features of these distributions. Firstly, at the shortest delay times the measured rotational and vibrational temperatures are the same as that those which were observed in the results of Chapter 4 for benzene molecules that evaporate from the liquid surface. The trend of the temperatures recorded at the longest delay times indicate that the temperatures return to these initial values when the packet of desorbed material has passed the ionisation laser after some 20 μs . Figure 5.17 shows the internal temperatures of the molecules entrained in the desorption plume fall below that of the liquid surface, with both the vibrations and rotations experiencing a minima in temperature at $\sim 4 \mu\text{s}$. All the rotational motion is cooled by 60-100 K irrespective of vibrational excitation.

The relative amounts of vibrational cooling seen in the different vibration modes follows the same trends seen in purely gas phase expansions, with ν_{16} cooling the most, followed by ν_{11} and ν_6 (Figure 5.17(B)). Even though ν_{11} is slightly higher in frequency than ν_6 , Bernshtein and Oref have shown that the out-of-plane vibrational motion of ν_{11} increases the probability of collisional energy transfer, causing it to cool at a faster rate than the in-plane, ν_6 vibration [81-83].

The rotational and vibrational cooling observed is due to the adiabatic expansion of the desorption plume as it travels away from the liquid surface. It is expected that the amount of

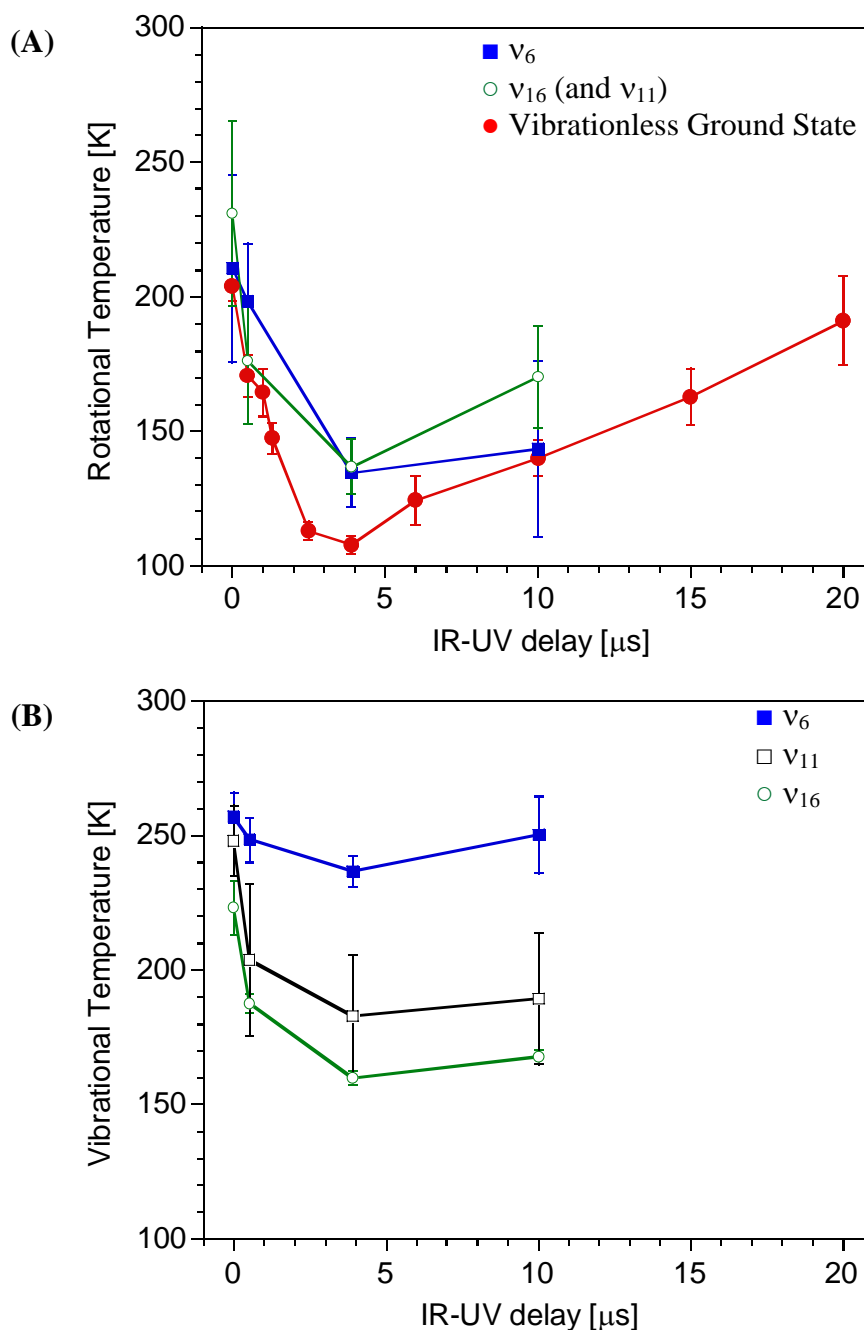


Figure 5.17: Temporal evolution of the internal temperatures of neutral benzene molecules laser desorbed from the surface of the L μ J. (A) Rotational temperatures as a function of IR-UV delay. It is assumed that the rotational temperatures of molecules excited with vibration ν_{16} and ν_{11} are equal. Vibrationless rotational temperatures are represented by the solid circles (\bullet), whilst rotational temperatures for ν_6 , ν_{16} (and ν_{11}) are represented by the solid squares (\blacksquare) and open circles (\circ), respectively. (B) Vibrational temperatures as a function of IR-UV delay. Vibrational temperatures for ν_6 , ν_{16} and ν_{11} are represented by the solid squares (\blacksquare), open circles (\circ), and open squares (\square), respectively. The error bars on all points represent 3 times the weighted error of the mean (3σ). The temperatures at 0 IR-UV delay are the temperatures of benzene molecules that are naturally evaporating into the vacuum from the L μ J.

cooling observed will increase with the probe distance from the surface since placing the ionisation laser further from the surface would mean a longer time for collisional energy transfer before the molecules are probed.

Vertes and co-workers' modelling of the velocity, temperature and density evolution within a desorption plume shows that the cooling of internal temperature of an entrained molecule depends on the probability of energy transfer out of the internal degrees of freedom as well as the time available for energy exchange [84]. The fact that the vibrational temperatures observed here do not raise above the pre-desorption liquid surface temperature shows that any vibrational excitation of the matrix (water) caused by the absorption of the IR laser photons is not transferred into the benzene molecules. This effect is due to what is known as an "energy bottleneck"[85] - where there is a vibrational frequency mismatch between the analyte and the matrix which slows vibration-vibration (V-V) transfer between the two components. In the experiments reported here, the desorption process is initiated by the water 'matrix' being vibrationally excited by the 2.85 μm desorption laser. From Figure 5.17 it is clear that the vibrational excitation of water is not transferred into the benzene analyte molecules; suggesting that the probability of V-V energy transfer is not great for a benzene-water collision. Indeed, the probability of V-V transfer is highest when the energy defect between excited vibrational states of colliding molecules is smallest [86-88]; and only the highest frequency vibrations of benzene come close to the 2.85 μm water vibrational frequency**.

The IR-UV delay which achieves the minimum in internal temperature matches closely to the delay of the monomer ion intensity maximum of Figure 5.9. However, the rate at which the internal temperatures return to the evaporation temperature is not as fast as the change in the monomer ion intensity as a function of IR-UV delay. Figure 5.18 is an overlay of the ground state rotational temperatures of Figure 5.17 and the monomer intensity distribution of

** The vibrational frequencies of benzene are given in Chapter 3.

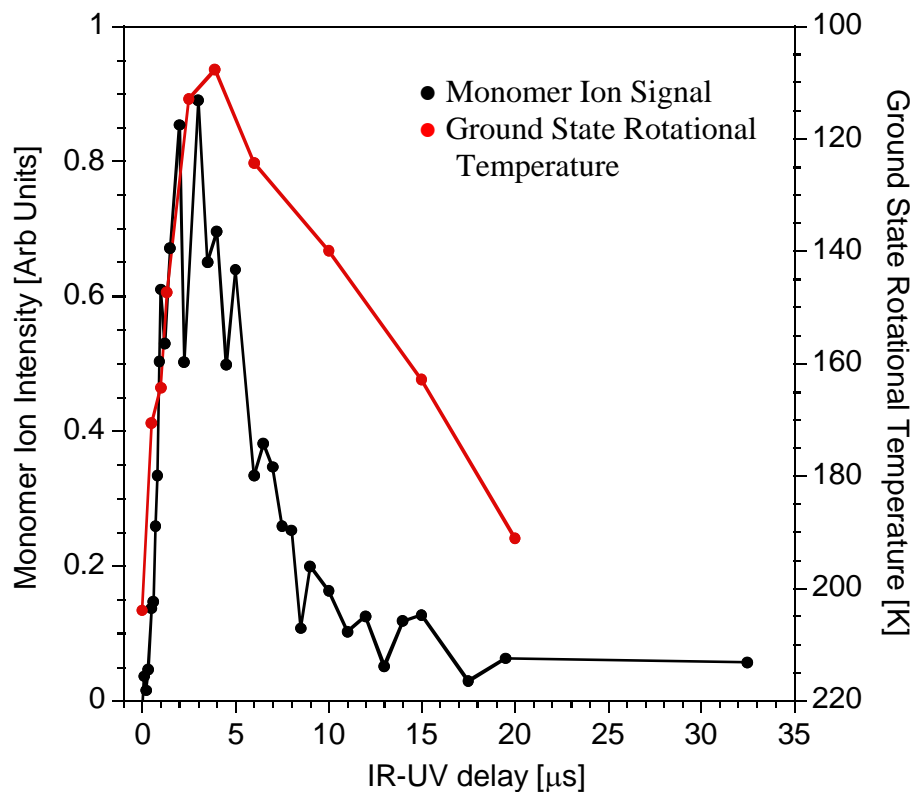


Figure 5.18: Comparison between the rates of change of ground state rotational temperatures (\bullet) and the observed intensity of the benzene monomer ion signal (\bullet) as a function of IR–UV delay. The temperature scale has been reversed to aid in the overlay. The data at 0 IR-UV delay are from benzene molecules that are naturally evaporating into the vacuum from the $L\mu\text{J}$.

Figure 5.9. The temperature scale has been inverted to aid in a visual comparison of the two distributions. It is evident that the monomer intensity tracks the rotational temperature very closely until the maximum is reached at $\sim 4 \mu\text{s}$. After the maximum, both the monomer ion intensity and the rotational temperature return to the pre-desorption conditions, but at different rates. The monomer ion intensity drops rapidly which is an indication of a rapid decrease in molecular density. However, the rotational temperature returns to the pre-desorption conditions at a much slower rate. The degree of rotational cooling is dependent upon the molecular density so it is expected that the monomer ion intensity and rotational temperature should track each other at all IR-UV delays. Together with the observation that clusters form at IR-UV delays earlier than the monomer ion intensity maximum this disparity between the distributions suggests that the monomer ion intensity distribution is being distorted in some way – and is not a true indication of molecular density.

Recall that the ion intensity distributions were generated by ionising through the $6^1 \leftarrow 0_0$ vibronic transition. The intensity of the ion signal produced is therefore dependent upon the number of neutral molecules that are in the 0_0 ground state. The observed ion signal intensity is thus affected not only by the temporal evolution of molecular density but also the change in vibrational temperature since, by definition, vibrational cooling is an increase in the relative population of the 0_0 state. This means that at $\sim 4 \mu\text{s}$, where the vibrationally coolest part of the desorption plume is probed, the molecular ion signal would be greater than in a vibrationally warmer part of the plume of the same molecular density. The cooling of vibrational motion will tend to distort the ion intensity distribution so the maximum ion intensity aligns with the minimum in internal cooling. As suggested in Section 5.3, the formation of clusters at the earlier IR-UV delay times suggests that the delay corresponding to the highest molecular density is likely to be closer to $0.5 \mu\text{s}$. The maximum in the monomer ion intensity may be being distorted to later delay times by this vibrational cooling effect. This phenomenon may

also be one of the causes of the observed distortion of the translational velocity distribution (Figure 5.9 and Figure 5.10) away from Maxwell-Boltzmann.

This distortion of the velocity distribution was also observed by Zhang in the aforementioned benzimidazole desorption experiments [56]. They found that the shape of the observed velocity distribution was dependent upon the wavelength of the ionising laser. When ionising through the hotband transition the distribution was slightly broader and closer to Maxwell-Boltzmann than when ionising from the ground state. Further experiments need to be performed to confirm that this effect is indeed present in our experiments. One such experiment should involve generating a monomer ion velocity distribution where the molecules are ionised through a transition which starts in, for example, the high frequency ν_6 state. Since ν_6 is seen to undergo limited vibrational cooling in the desorption plume its change in population should have a minimal effect on the ion yield.

5.6 Conclusion

This study involved an in-depth analysis of the dynamics of laser desorption of benzene from an *in vacuo* liquid surface. The use of separate desorption and ionisation lasers allows for mass selective spectroscopic analysis of the desorbed neutrals. The wavelength of the desorption laser was tuned to the fundamental vibrational absorption band of the solvent (water). At low desorption laser fluences the amount of laser induced fragmentation observed is minimal whilst still achieving up to a six-fold increase in the amount of monomer in the gas-phase. Spectroscopic analysis of the clusters observed in the mass spectra showed that they are formed post-ionisation of the monomer and their formation is favoured in the head of the desorption plume where the translational velocities are fastest and the molecular density at its highest.

Monte Carlo simulations of the IR-UV delay distribution of the monomer ion intensity show that the desorbed molecules can be described with a translational temperature of ~ 200 K and a drift velocity of ~ 100 m.s⁻¹. It was suggested that the broadening of the maximum of the experimentally observed distribution could be an indication of a mass independence of the velocity of the desorbed material.

The internal temperature of monomers that were not encompassed into clusters was measured as a function of IR-UV delay time. When the ionisation laser was positioned 300 μm from the liquid surface both the rotational and vibrational temperatures reached a minimum at ~ 4 μs . Overall the amount of internal cooling observed is significant, though not as dramatic as in a purely gas-phase expansion, supporting the description of the laser desorption process as a mild supersonic expansion [56,77,89].

The formation of clusters at the shortest IR-UV delay times suggests that the maximum in the velocity distribution should appear at a much faster velocity than is actually observed. It is possible that the observed velocity distributions are distorted by the change in internal temperature throughout the plume. To avoid the distortion by vibrational cooling, it is suggested that the velocity distributions are created by ionising through a transition whose initial state is not significantly cooled by the adiabatic expansion of the desorbed material.

5.7 References

- (1) Karas, M.; Bachmann, D.; Bahr, U.; Hillenkamp, F. *International Journal of Mass Spectrometry and Ion Processes* **1987**, *78*, 53.
- (2) Karas, M.; Bachmann, D.; Hillenkamp, F. *Analytical Chemistry* **1985**, *57*, 2935.
- (3) Karas, M.; Hillenkamp, F. *Analytical Chemistry* **1988**, *60*, 2299.
- (4) Woods, E.; Miller, R. E.; Baer, T. *Journal of Physical Chemistry A* **2003**, *107*, 2119.
- (5) Saalfrank, P. *Chemical Reviews* **2006**, *106*, 4116.
- (6) Dreisewerd, K. *Chemical Reviews* **2003**, *103*, 395.
- (7) Mafune, F.; Kohno, J.; Kondow, T. *Journal of Physical Chemistry* **1996**, *100*, 10041.
- (8) Mafuné, F.; Kohno, J.-y.; Nagata, T.; Kondow, T. *Chemical Physics Letters* **1994**, *218*, 7.
- (9) Mafune, F.; Takeda, Y.; Nagata, T.; Kondow, T. *Chemical Physics Letters* **1994**, *218*, 234.
- (10) Mafuné, F.; Takeda, Y.; Nagata, T.; Kondow, T. *Chemical Physics Letters* **1992**, *199*, 615.
- (11) Matsumura, H.; Mafune, F.; Kondow, T. *Journal of Physical Chemistry* **1995**, *99*, 5861.
- (12) Kondow, T.; Mafuné, F. *Annual Review of Physical Chemistry* **2000**, *51*, 731.
- (13) Tsuchiya, M.; Shida, Y.; Kobayashi, K.; Taniguchi, O.; Okouchi, S. *International Journal of Mass Spectrometry* **2004**, *235*, 229.
- (14) Holstein, W. L.; Dobeck, L. M.; Otten, D. E.; Metha, G. F.; Buntine, M. A. *Australian Journal of Chemistry* **2003**, *56*, 481.

-
- (15) Holstein, W. L.; Hammer, M. R.; Metha, G. F.; Buntine, M. A. *International Journal of Mass Spectrometry* **2001**, *207*, 1.
- (16) Kleinekofort, W.; Avdiev, J.; Brutschy, B. *International Journal of Mass Spectrometry and Ion Processes* **1996**, *152*, 135.
- (17) Kleinekofort, W.; Pfenninger, A.; Plomer, T.; Griesinger, C.; Brutschy, B. *International Journal of Mass Spectrometry and Ion Processes* **1996**, *156*, 195.
- (18) Wattenberg, A.; Sobott, F.; Brutschy, B. *Rapid Communications in Mass Spectrometry* **2000**, *14*, 859.
- (19) Sobott, F.; Wattenberg, A.; Kleinekofort, W.; Pfenninger, A.; Brutschy, B. *Fresenius J Anal Chem* **1998**, *360*, 745.
- (20) Sobott, F.; Kleinekofort, W.; Brutschy, B. *Anal. Chem.* **1997**, *69*, 3587.
- (21) Wattenberg, A.; Sobott, F.; Barth, H. D.; Brutschy, B. *International Journal of Mass Spectrometry* **2000**, *203*, 49.
- (22) Morgner, N.; Barth, H. D.; Brutschy, B. *Australian Journal of Chemistry* **2006**, *59*, 109.
- (23) Morgner, N.; Barth, H. D.; Schmidt, T. L.; Heckel, A.; Scheffer, U.; Gobel, M.; Brutschy, B. *Z. Phys. Chem.* **2007**, *221*, 689.
- (24) Morgner, N.; Kleinschroth, T.; Barth, H. D.; Ludwig, B.; Brutschy, B. *J Am Soc Mass Spectrom* **2007**, *18*, 1429.
- (25) Charvat, A.; Abel, B. *Physical Chemistry Chemical Physics* **2007**, *9*, 3335.
- (26) Charvat, A.; Lugovoj, E.; Faubel, M.; Abel, B. *European Physical Journal D* **2002**, *20*, 573.
- (27) Charvat, A.; Lugovoj, E.; Faubel, M.; Abel, B. *Review of Scientific Instruments* **2004**, *75*, 1209.
- (28) Charvat, A.; Stasicki, B.; Abel, B. *Journal of Physical Chemistry A* **2006**, *110*, 3297.

- (29) Kohno, J.; Mafune, F.; Kondow, T. *European Physical Journal D* **2002**, *20*, 339.
- (30) Kohno, J.; Toyama, N.; Buntine, M. A.; Mafune, F.; Kondow, T. *Chemical Physics Letters* **2006**, *420*, 18.
- (31) Lustig, D. A.; Lubman, D. M. *Review of Scientific Instruments* **1991**, *62*, 957.
- (32) Voumard, P.; Zenobi, R.; Zhan, Q. *Surface Science* **1994**, *307-309*, 360.
- (33) David, M. L. *Mass Spectrometry Reviews* **1988**, *7*, 559.
- (34) Tembreull, R.; Lubman, D. M. *Analytical Chemistry* **1987**, *59*, 1082.
- (35) Jürgen, G.; Ulrich, B.; Klaus, W.; Edward, W. S. *Organic Mass Spectrometry* **1986**, *21*, 645.
- (36) Boesl, U.; Grotemeyer, J.; Walter, K.; Schlag, E. W. *Instrumentation Science & Technology* **1987**, *16*, 151
- (37) Kohno, J.; Mafune, F.; Kondow, T. *Journal of Physical Chemistry A* **2004**, *108*, 971.
- (38) Otten, D. E.; Trevitt, A. J.; Nichols, B. D.; Metha, G. F.; Buntine, M. A. *Journal of Physical Chemistry A* **2003**, *107*, 6130.
- (39) Maselli, O. J.; Gascooke, J. R.; Kobelt, S. L.; Metha, G. F.; Buntine, M. A. *Australian Journal of Chemistry* **2006**, *59*, 104.
- (40) Horimoto, N.; Kohno, J.-y.; Mafune, F.; Kondow, T. *The Journal of Physical Chemistry A* **1999**, *103*, 9569.
- (41) Cabalo, J.; Zelenyuk, A.; Baer, T.; Miller, R. E. *Aerosol Science & Technology* **2000**, *33*, 3.
- (42) Zelenyuk, A.; Cabalo, J.; Baer, T.; Miller, R. E. *Analytical Chemistry* **1999**, *71*, 1802.
- (43) Tsuboi, Y.; Fukumura, H.; Masuhara, H. *Applied Physics Letters* **1994**, *64*, 2745.

- (44) Latifi, H.; Xie, J. G.; Ruekgauer, T. E.; Armstrong, R. L.; Pinnick, R. G. *Opt. Lett.* **1991**, *16*, 1129.
- (45) Lushnikov, A. A.; Negin, A. E. *Journal of Aerosol Science* **1993**, *24*, 707.
- (46) Puretzky, A. A.; Geohegan, D. B.; Hurst, G. B.; Buchanan, M. V.; Luk'yanchuk, B. S. *Physical Review Letters* **1999**, *83*, 444.
- (47) Zenobi, R.; Knochenmuss, R. *Mass Spectrometry Reviews* **1998**, *17*, 337.
- (48) Zhan, Q.; Wright, S. J.; Zenobi, R. *Journal of the American Society for Mass Spectrometry* **1997**, *8*, 525.
- (49) Glückmann, M.; Pfenninger, A.; Krüger, R.; Thierolf, M.; Karasa, M.; Horneffer, V.; Hillenkamp, F.; Strupat, K. *International Journal of Mass Spectrometry* **2001**, *210-211*, 121.
- (50) NoorBatcha, I.; Lucchese, R. R.; Zeiri, Y. *Journal of Chemical Physics* **1988**, *89*, 5251.
- (51) NoorBatcha, I.; Lucchese, R. R. *Journal of Chemical Physics* **1987**, *86*, 5816.
- (52) Sibold, D.; Urbassek, H. M. *Journal of Applied Physics* **1993**, *73*, 8544.
- (53) Cousins, L. M.; Levis, R. J.; Leone, S. R. *Journal of Chemical Physics* **1989**, *91*, 5731.
- (54) Elokhin, V. A.; Krutchinsky, A. N.; Ryabov, S. E. *Chemical Physics Letters* **1990**, *170*, 193.
- (55) Mowry, C. D.; Johnston, M. V. *The Journal of Physical Chemistry* **1994**, *98*, 1904.
- (56) Zhang, J. Y.; Nagra, D. S.; Li, L. *Analytical Chemistry* **1993**, *65*, 2812.
- (57) Holland, D. M. P.; Shaw, D. A.; Sumner, I.; Bowler, M. A.; Mackie, R. A.; Shpinkova, L. G.; Cooper, L.; Rennie, E. E.; Parker, J. E.; Johnson, C. A. F. *International Journal of Mass Spectrometry* **2002**, *220*, 31.

- (58) Curtis, D. M.; Murray, V. J. *Rapid Communications in Mass Spectrometry* **1993**, *7*, 569.
- (59) Ibrahim, Y. M.; Mautner, M. M. N.; Alshraeh, E. H.; El-Shall, M. S.; Scheiner, S. *Journal of the American Chemical Society* **2005**, *127*, 7053.
- (60) Kiermeier, A.; Ernstberger, B.; Neusser, H. J.; Schlag, E. W. *Journal of Physical Chemistry* **1988**, *92*, 3785.
- (61) Press, W. H.; Flannery, B. P.; Teukolsky, S. A.; Vetterling, W. T. *Numerical Recipes: The Art of Scientific Computing*; Cambridge University Press: New York, 1986.
- (62) Solca, N.; Dopfer, O. *Chemical Physics Letters* **2001**, *347*, 59.
- (63) Hansen, S. G. *Journal of Applied Physics* **1989**, *66*, 3329.
- (64) Faubel, M.; Schlemmer, S.; Toennies, J. P. *Zeitschrift Fur Physik D-Atoms Molecules and Clusters* **1988**, *10*, 269.
- (65) Knox, C. J. H.; Phillips, L. F. *Journal of Physical Chemistry B* **1998**, *102*, 10515.
- (66) Johnston, M. V. *TrAC Trends in Analytical Chemistry* **1984**, *3*, 58.
- (67) Atkins, P. W. *Physical Chemistry*, 6th ed.; Oxford University Press: Oxford, 1998.
- (68) Miller, D. R. *Atomic and Molecular Beam Methods*; Oxford University Press: New York, 1991; Vol. 1.
- (69) Tsai, S. T.; Chen, C. H.; Lee, Y. T.; Wang, Y. S. *Molecular Physics* **2008**, *106*, 239.
- (70) Kinsel, G. R.; Edmondson, R. D.; Russell, D. H. *Journal of Mass Spectrometry* **1997**, *32*, 714.
- (71) Kinsel, G. R.; Gimon-Kinsel, M. E.; Gillig, K. J.; Russell, D. H. *Journal of Mass Spectrometry* **1999**, *34*, 684.

- (72) Charvat, A.; Bogehold, A.; Abel, B. *Australian Journal of Chemistry* **2006**, *59*, 81.
- (73) Mafune, F.; Kohno, J.; Nagata, T.; Kondow, T. *Ejection of cluster ions from a liquid beam of an aniline-propanol solution following laser photoionization* **1995**, *42*, 449.
- (74) Domen, K.; Chuang, T. J. *Journal of Chemical Physics* **1989**, *90*, 3318.
- (75) Braun, R.; Hess, P. *Journal of Chemical Physics* **1993**, *99*, 8330.
- (76) Gluckmann, M.; Karas, M. *Journal of Mass Spectrometry* **1999**, *34*, 467.
- (77) Huth-Fehre, T.; Becker, C. H.; Ronald, C. B. *Rapid Communications in Mass Spectrometry* **1991**, *5*, 378.
- (78) Kelly, R.; Dreyfus, R. W. *Nuclear Instruments and Methods in Physics Research* **1988**, *B32*, 341.
- (79) Harnafi, M.; Dubreuil, B. *Journal of Applied Physics* **1991**, *69*, 7565.
- (80) Demtröder, W. Visible and Ultraviolet Spectroscopy: Physical Aspects. In *Atomic and Molecular Beam Methods*; Scoles, G., Ed.; Oxford University Press: New York, 1992; Vol. 2; pp 231.
- (81) Bernshtein, V.; Oref, I. *Journal of Physical Chemistry B* **2005**, *109*, 8310.
- (82) Bernshtein, V.; Oref, I. *Journal of Physical Chemistry A* **2006**, *110*, 1541.
- (83) Bernshtein, V.; Oref, I. *Journal of Physical Chemistry A* **2006**, *110*, 8477.
- (84) Vertes, A.; Irinyi, G.; Gijbels, R. *Analytical Chemistry* **1993**, *65*, 2389.
- (85) Akos, V.; Gijbels, R.; Levine, R. D. *Rapid Communications in Mass Spectrometry* **1990**, *4*, 228.
- (86) Parmenter, C. S.; Tang, K. Y. *Chemical Physics* **1978**, *27*, 127.
- (87) Parmenter, C. S. *Journal of Physical Chemistry* **1982**, *86*, 1735.
- (88) McCaffery, A. J.; Osborne, M. A.; Marsh, R. J.; Lawrance, W. D.; Waclawik, E. R. *Journal of Chemical Physics* **2004**, *121*, 169.

- (89) Knochenmuss, R. *Journal of Mass Spectrometry* **2002**, 37, 867.